



**HAL**  
open science

# Materials and nanostructuring processes on flexible supports for personalized security features

Manuel Alejandro Flores Figueroa

► **To cite this version:**

Manuel Alejandro Flores Figueroa. Materials and nanostructuring processes on flexible supports for personalized security features. Material chemistry. Université Jean Monnet - Saint-Etienne, 2023. English. NNT : 2023STET0023 . tel-04511332

**HAL Id: tel-04511332**

**<https://theses.hal.science/tel-04511332>**

Submitted on 19 Mar 2024

**HAL** is a multi-disciplinary open access archive for the deposit and dissemination of scientific research documents, whether they are published or not. The documents may come from teaching and research institutions in France or abroad, or from public or private research centers.

L'archive ouverte pluridisciplinaire **HAL**, est destinée au dépôt et à la diffusion de documents scientifiques de niveau recherche, publiés ou non, émanant des établissements d'enseignement et de recherche français ou étrangers, des laboratoires publics ou privés.



N°d'ordre NNT : 2023STET023

## THÈSE de DOCTORAT DE L'UNIVERSITÉ JEAN MONNET SAINT-ÉTIENNE

Membre de l'Université de LYON

École Doctorale N° 488  
Sciences, Ingénierie, Santé

Spécialité / discipline de doctorat :  
CHIMIE ET SCIENCES DES MATERIAUX

Soutenue publiquement le 04/09/2023, par :  
**Manuel Alejandro Flores Figueroa**

---

# Materials and nanostructuring processes on flexible supports for personalized security features

---

Devant le jury composé de :

<b>Plain, Jérôme</b>	Professeur des Universités, Université de Technologie de Troyes, Troyes, France	Rapporteur
<b>Soppera, Olivier</b>	Directeur de recherche, Institut de Science des Matériaux de Mulhouse, Mulhouse, France	Rapporteur
<b>Bois, Laurence</b>	Chargée de Recherches CNRS, Université de Lyon 1, Lyon, France	Examinatrice
<b>Itina, Tatiana</b>	Directrice de recherche CNRS, Université Jean Monnet, Saint-Etienne, France	Examinatrice
<b>Destouches, Nathalie</b>	Professeur des Universités, Université Jean Monnet, Saint-Etienne, France	Directrice de thèse
<b>Vocanson, Francis</b>	Professeur des Universités, Université Jean Monnet, Saint-Etienne, France	Co-directeur de thèse
<b>Grosso, David</b>	Professeur des Universités, Aix-Marseille Université, Marseille, France	Co-directeur de thèse
<b>Ayala, Stéphane</b>	Directeur senior d'ingénierie, HID Global	Invité
<b>Sharma, Nipun</b>	Responsable de l'innovation, HID Global	Invité



## **ACKNOWLEDGEMENTS**

Four years ago I embarked on this journey to obtain my PhD degree at the Laboratoire Hubert Curien in collaboration with the Institut Matériaux Microélectronique Nanosciences de Provence (IM2NP) and supported by HID GLOBAL. During this period I was able to develop myself at both personal and professional levels and for this, I would like to acknowledge and express my deepest gratitude to all the people that were involved in this journey.

First and foremost I would like to thank my supervisors, Nathalie Destouches, Francis Vocanson from the Laboratoire Hubert Curien, and David Grosso, from IM2NP. Thank you for trusting me on this multidisciplinary project and for your constant support during my time. Our long scientific discussions have greatly helped me on developing my research capabilities on different fields and led to the exciting results presented in this manuscript.

I would also like to express my gratitude to my colleagues from the “Nanoparticles” team, Nicolas Dalloz, Balint Eles, Van Doan Le, Christophe Hubert, Robin Mermillod-Blondin and Thibault Girardin. I highly appreciate the great working environment we developed during this time. I thoroughly enjoyed discussing with you regarding different topics during coffee and lunch breaks. Your support at both personal and scientific level was very valuable for me.

I’m thankful to my industrial advisors, Stéphane Ayala and Nipun Sharma from HID GLOBAL, who encouraged me continuously during my thesis to elevate my results to a real-world scenario. I’m also grateful for recruiting me with a permanent position in your engineering team and opening a door to me the industrial world. This will allow me to continue working on the project inside the company.

I would like to acknowledge a few people for their technical support during my thesis. More specifically I would like to thank Arnaud Valour, Jean-Yves Michalon, Frédéric Celle, Anthony Cazier, Yaya Lefkir and Eric Sigronde. In the administrative side, a warm thank you to Julie Diebesse, Nathalie Peritore and Patrick Vincent. I greatly appreciated your efforts on helping me out when I needed it.

On a personal note, I’m also happy to have met several persons in and out of the laboratory along the way. It allowed me to develop my cultural knowledge but also form new friendships with wonderful people.

Last but not least, I would like to give my deepest gratitude to my closest friends and family. Your continuous encouragement throughout this journey made the good days even better, and the bad days into not-so-bad days. Without your support and kindness none of this could have been achieved and I'm forever grateful for it.

A mis queridos padres, Maria y Miguel, les dedico este trabajo que culmina mi carrera académica. Gracias por creer en mí y por brindarme esta oportunidad de explorar mi espíritu crítico en las ciencias. Les agradezco de corazón todo lo que me han inculcado hasta este día. Este trabajo es fruto de su amor, dedicación y enseñanzas hacia mi persona y estaré siempre agradecido de tenerlos a mi lado. Los quiero.

## **ABSTRACT**

With the development of laser printers and copiers, document forgery is becoming more powerful. These technologies are capable of producing almost identical surface level features as the real ones. This pushes progress in the field of ID documents, a wide variety of technologies have been developed to print high quality features by using different processes that are difficult to reproduce. One of the main targets for forgers is altering the portrait of the user as it is the most noticeable and unique feature of an ID document. Therefore, a particular focus is set on developing complex technologies that can produce portraits that are easily observable by anyone but are also highly secure. The Nanoparticles team at the Laboratoire Hubert Curien have recently demonstrated the potential of plasmonic materials to produce interesting effects for anti-counterfeiting purposes. For instance, processing silver nanoparticles embedded in a semiconductor titania matrix (Ag:TiO<sub>2</sub>) with femtosecond or nanosecond laser result in the formation of well-defined nanostructures. These metasurfaces, depending on the laser processing conditions, present a wide variety of optical effects detectable in different observation and illumination conditions. These features were exploited to produce image multiplexing, which relates to encoding two or more unique images in a single print to be ultimately revealed under specific conditions. An automated process was implemented to find the best color combinations amid a wide variety of metasurfaces to produce multiplexing with two, three or even four images in a single print by using a nanosecond laser.

Despite the recent progress on the color management side, these effects have mainly been exploited on rigid transparent substrates such as glass which are not suitable for industrial applications. In fact, ID documents are mainly composed of plastic and paper supports due to their flexibility. Therefore, the goal of the work presented in this thesis revolves around implementing Ag:TiO<sub>2</sub> films in a plastic card and produce interesting color effects by laser processing. The color algorithms previously established are utilized and adapted to produce several demonstrators with full-color images easily visible with the naked eye. Additionally, multiplexing was achieved by encoding two images in a single print. This thesis is a proof-of-concept of the interest of using plasmonic materials for visual security features.



## **RESUME**

L'un des principaux objectifs des faussaires de document d'identité est de modifier le portrait de l'utilisateur, car il s'agit de la caractéristique la plus visible et unique d'un document d'identification. Par conséquent, un accent particulier est mis sur le développement de technologies complexes capables de produire des portraits facilement observables par n'importe qui, mais également hautement sécurisés. L'équipe « Nanoparticules » du Laboratoire Hubert Curien a récemment démontré le potentiel des matériaux plasmoniques pour cette application. Par exemple, le traitement de films Ag:TiO<sub>2</sub> avec un laser femtoseconde ou nanoseconde permet la formation de nanostructures bien définies. Ces métasurfaces présentent une grande variété d'effets optiques détectables dans différentes conditions d'observation. Ces caractéristiques ont été exploitées pour produire un multiplexage d'images, ce qui consiste à encoder deux images ou plus dans une seule impression, à révéler ultimement dans des conditions spécifiques. Malgré les récents progrès, ces effets ont principalement été exploités sur des substrats rigides et transparents tels que le verre. Il est nécessaire de transférer cette technologie vers des supports flexibles afin de pouvoir l'implémenter pour des applications industrielles. L'objectif du travail présenté dans cette thèse consiste à mettre en œuvre des films Ag:TiO<sub>2</sub> dans une carte en plastique et à produire des effets de couleur intéressants par traitement laser. Plusieurs démonstrations ont été produites avec des images en couleur facilement visibles à l'œil nu. De plus, le multiplexage avec deux images a été réalisé dans une seule impression.

# TABLE OF CONTENT

Acknowledgements .....	3
Abstract .....	5
Resumé .....	7
Introduction: Identity documents .....	12
<b>General presentation.....</b>	<b>12</b>
<b>Security printing techniques .....</b>	<b>13</b>
Printing techniques for static security features.....	14
Printing techniques for personalization security features.....	16
<b>Development of plasmonic colors induced by laser processing.....</b>	<b>18</b>
CHAPTER 1: State-of-the-art .....	22
<b>1.1 Sol-gel chemistry.....</b>	<b>22</b>
1.1.1. General definition .....	22
1.1.2. Preparation of mesoporous sol-gel films.....	23
1.1.2.1. Sol-gel deposition techniques .....	24
1.1.2.2. The EISA method .....	27
1.1.2.3. Soft-templating agents.....	28
1.1.3. Elaboration of titania materials .....	30
1.1.3.1. Generalities .....	30
1.1.3.2. Sol-gel approach .....	31
1.1.3.3. Aging after deposition.....	32
1.1.4. Synthesis of TiO <sub>2</sub> :Ag materials .....	34
1.1.4.1. Bottom-up approach by sol-gel methods .....	34
1.2.2.1. Top-down approach by magnetron sputtering method .....	35
<b>1.3. Optical properties of TiO<sub>2</sub>:Ag materials.....</b>	<b>36</b>
1.3.1. Plasmonic properties of metallic nanoparticles .....	36
1.3.2. Photochromic behavior of TiO <sub>2</sub> :Ag films.....	38
1.3.2.1. Photo-oxidation of silver nanoparticles .....	39
1.3.2.2. Photo-reduction .....	40

1.3.2.3.	Laser-induced metasurfaces for anti-counterfeiting applications .....	43
<b>1.4.</b>	<b>Conclusion .....</b>	<b>45</b>
 <b>CHAPTER 2: Materials and methods.....</b>		<b>46</b>
<b>2.1.</b>	<b>Material characterization methods .....</b>	<b>46</b>
2.1.1.	Spectroscopy methods .....	46
2.1.1.1.	Fourier-transform infrared spectroscopy .....	46
2.1.1.2.	UV-Visible spectroscopy.....	47
2.1.2.	Microscopy methods .....	47
2.1.2.1.	Optical microscopy.....	47
2.1.2.2.	Scanning electron microscopy .....	47
2.1.2.3.	Transmission electron microscopy.....	48
2.1.2.4.	Atomic force microscopy .....	48
2.1.3.	Ellipsometry characterizations.....	49
2.1.3.1.	Ellipsometry setup .....	49
2.1.3.2.	In-situ ellipsometry .....	49
2.1.3.3.	Environmental ellipsometric porosimetry .....	50
2.1.4.	Adhesion characterization .....	52
<b>2.2.</b>	<b>Presentation of the flexible support: Polycarbonate .....</b>	<b>52</b>
2.1.2.	PC substrate preparation .....	53
2.2.1.	PC substrate characterization .....	53
2.2.1.1.	O <sub>2</sub> plasma treatment.....	55
2.2.1.2.	PC substrates vs post-deposition treatments .....	56
<b>2.3.</b>	<b>Sol synthesis and preparation of PC:TiO<sub>2</sub>:Ag films .....</b>	<b>58</b>
2.3.1.	Chemicals .....	58
2.3.2.	TiO <sub>2</sub> sol preparation .....	59
2.3.3.	Mesoporous TiO <sub>2</sub> thin film preparation.....	60
2.3.4.	Impregnation with ammoniacal silver solution .....	60
<b>2.4.</b>	<b>PC:TiO<sub>2</sub>:Ag film characterization .....</b>	<b>61</b>
2.4.1.	Influence of the O <sub>2</sub> plasma substrate treatment on the film deposition .....	61
2.4.2.	Characterization during/after the stabilization process .....	61
2.4.2.1.	FTIR-ATR spectral characterization .....	61
2.4.2.2.	Environmental ellipsometry characterization.....	63
2.4.2.3.	Environmental ellipsometric porosimetry .....	66
2.4.3.	Characterization after impregnation .....	68
2.4.3.1.	Optical characterization .....	68
2.4.3.2.	Surface characterization .....	69

<b>2.5.</b>	<b>Preparation of TiO<sub>2</sub>:Ag PC cards</b>	<b>70</b>
2.5.1.	Lamination technique used for ID-1 PC cards	70
<b>2.6.</b>	<b>TiO<sub>2</sub>:Ag PC cards characterization</b>	<b>71</b>
<b>2.7.</b>	<b>Preparation of PC:SiO<sub>2</sub>:TiO<sub>2</sub>:Ag non-laminated samples</b>	<b>73</b>
2.7.1.	Sol synthesis and preparation of a dense SiO <sub>2</sub> protective layer	73
2.7.1.1.	Chemicals	73
2.7.1.2.	SiO <sub>2</sub> sol synthesis and film deposition	73
<b>2.8.</b>	<b>PC:SiO<sub>2</sub>:TiO<sub>2</sub>:Ag samples characterization</b>	<b>74</b>
<b>2.9.</b>	<b>Conclusion</b>	<b>75</b>

## CHAPTER 3: LASER-INDUCED COLOR PRODUCTION..... 78

<b>3.1.</b>	<b>Laser setup and color characterization</b>	<b>78</b>
3.1.1.	Laser setup	78
3.1.1.1.	Working focal plane	79
3.1.2.	Laser processing parameters	79
<b>3.2.</b>	<b>Investigation of nanostructures by TEM</b>	<b>80</b>
3.2.1.	Color measurements	82
3.2.1.1.	Camera setup and observation modes	82
3.2.1.2.	Image normalization	82
3.2.2.	Design of laser processed elements for image printing	83
3.2.2.1.	Introduction	83
3.2.2.2.	Defining pixel size and interline distance (dy)	84
3.2.2.3.	Pixel juxtaposition	87
3.2.2.4.	Image processing for color extraction	88
3.2.2.5.	Defects that alter the color extraction	89
3.2.2.6.	Color gamuts	90
3.2.3.	Color workflow for image printing	91
3.2.4.	Conclusion	94
<b>3.3.</b>	<b>Full-color image printing on PC TiO<sub>2</sub>:Ag cards</b>	<b>95</b>
3.3.1.	Selection of the observation mode for color image printing	95
3.3.1.1.	Input image database	95
3.3.1.2.	Assessment of the printed image quality	96
3.3.1.3.	Definition of the metrics	98
3.3.1.4.	Discussion about the gamuts and metrics	102
3.3.1.5.	Conclusion	104
3.3.2.	Reproducibility of laser-printed colors	105
3.3.2.1.	Drawbacks and limitations	105

3.3.2.2.	Primaries selection .....	110
3.3.2.3.	Color reproducibility assessment.....	113
3.3.2.4.	Full-color image printing .....	114
3.3.3.	Conclusion.....	116
<b>3.4.</b>	<b>Image multiplexing .....</b>	<b>117</b>
3.4.1.	Introduction .....	117
3.4.2.	Two-image multiplexing .....	118
3.4.3.	Conclusion.....	120
<b>3.5.</b>	<b>Color production on PC:SiO<sub>2</sub>:TiO<sub>2</sub>:Ag samples .....</b>	<b>120</b>
3.5.1.	Introduction: Implementation of a protective silica layer for color printing.....	120
3.5.2.	Color production on PC:SiO <sub>2</sub> :TiO <sub>2</sub> :Ag samples .....	121
3.5.2.1.	Database processing .....	121
3.5.2.2.	Investigation of diffractive gratings .....	122
3.5.2.3.	Diffractive color tuning by laser ablation .....	124
3.5.3.	Conclusion.....	126
<b>3.6.</b>	<b>Conclusion .....</b>	<b>127</b>
General conclusion & perspectives .....		130
Annexes .....		132
<b>Annex 1: FTIR spectra of the evolution of a mesoporous TiO<sub>2</sub> film.....</b>		<b>132</b>
<b>Annex 2: Spot size measurements at the focal plane <math>f_0</math> and <math>f_2</math>.....</b>		<b>132</b>
<b>Annex 3: Laser calculation formulas.....</b>		<b>133</b>
Fluence calculation formula:.....		133
Effective number calculation formulae: .....		133
<b>Annex 4: Pixel dimensions measurements .....</b>		<b>133</b>
<b>Annex 5: Color spaces .....</b>		<b>134</b>
The sRGB color space.....		134
The CIE 1976 L*a*b* color space.....		135
<b>Annex 6: Normal density values.....</b>		<b>137</b>
<b>Annex 7 : Laser parameters of 10 primaries used for halftoning test .....</b>		<b>139</b>
<b>Annex 8: Laser parameters of nanostructures for two-image multiplexing.....</b>		<b>139</b>
<b>Annex 9: AFM investigation on laser inscription parameters on PC:SiO<sub>2</sub>:TiO<sub>2</sub>:Ag samples .....</b>		<b>140</b>
<b>Annex 10: Laser parameters for image printing on PC:SiO<sub>2</sub>:TiO<sub>2</sub>:Ag samples .....</b>		<b>140</b>
References .....		142

## **INTRODUCTION: IDENTITY DOCUMENTS**

### **General presentation**

Identity authentication has been part of the human history for thousands of years as the first and most common method was identifying people by their various physical traits. As simple as it might sound, this method was often subjected to human errors as it relied on one's memory and could easily be altered. A "piece" of identification was then introduced in the form of jewelry such as beads that could determine one's cultural order, family ties or even wealth in ancient times. In the modern world, jewelry is still used for different identification purposes such as in religious groups, in the military or even in medical institutes.

Along with the development of writing and documentation systems, governments were interested in counting their population and resources giving rise to the development of census records. Several identity documentation techniques were then introduced such as birth certificates<sup>1</sup> or land record systems<sup>2</sup> in the Roman Empire. During the Ming Dynasty in the 14<sup>th</sup> century sumptuary laws were established to identify the rank of the officials in the military. They would use large embroidered badges in their clothes depicting an animal depending on the officers rank to identify them easily<sup>3</sup>. Meanwhile in Europe in the 15<sup>th</sup> century, the first passport was developed by King Henry V to identify English citizens abroad ensuring their safety in neighboring countries which is to this day the main travelling identity document worldwide. The invention of the photography was then naturally introduced along with the development of ink-based fingerprints in the 19<sup>th</sup> century, revolutionizing the identification industry and becoming core elements of secure documents. With the development of the digital era, "smart cards" were introduced encompassing now numerous identification features (text, images, alphanumeric data, logos etc.) with analog or digital information. These cards are essentially physical documents consisting of different complex layers carrying different types of information that can be used for personal authentication or to access control to a certain resource.

Nowadays, three categories of security features exist in documents:

- Level 1 or "overt" security features encompass all visible effects that are observable by the naked eye by any untrained observer such as the personal metadata, the portrait of the user, holograms or watermarks.

- Level 2 or “semi-covert” security features require an extra piece of equipment or specific knowledge/training about the document in order to observe them such as UV inks or hidden images using magnifiers.

- Level 3 or “covert” security features can be observed by using very specific and expensive laboratory equipment. Typically, the manufacturer is the only one that knows about these “secret” features.

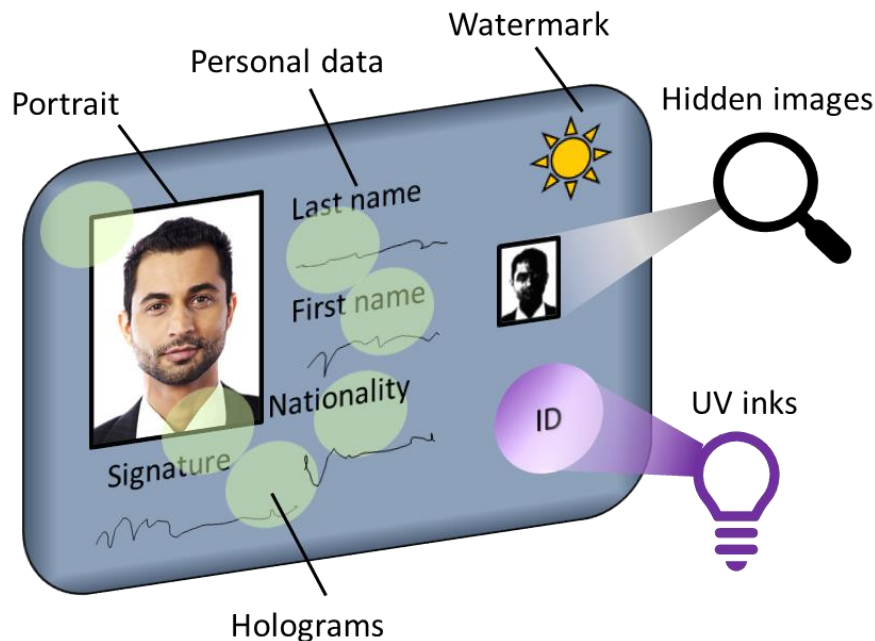


*Figure 1: Illustration of different security features found on ID documents.*

Producing documents with different levels (exemplified in figure 1) of security features seems to be “ideal” to prevent forging and counterfeiting due to their complexity. Nevertheless, it can be difficult and costly to manufacture because several elements have to be implemented in a single document, particularly for level 2 and 3 security features. In addition, these features can only be observed in very specific conditions or by trained people such as forensic document examiners (FDE), which is why it’s crucial to develop strong level 1 security features that are easily observable and can remain intact once implemented. In the following section, an overview is given on the different printing techniques used nowadays to produce security features.

### **Security printing techniques**

ID documents are generally produced by laminating (heating and pressuring) different layers of plastic or paper. Security features are often included in one of the layers of the card

construction as presented in figure 2. As a general concept, two types of features are found in ID cards, “static” or “personalization” features. The first relate to features that present a single design or pattern (figure 2.a) to be implemented generally in a card during manufacturing and are not modifiable after lamination (figure 2.b). Examples of these features are watermarks, logos, holograms, OVD (optical variable device) and guilloche patterns to name a few that are defined for each product. To produce them, the main printing techniques are flexography, offset lithography and screen printing which will be described later on.

On the other hand, personalization features encompass the metadata of the end-user produced after the manufacturing of the card. These features require versatile printing techniques since the information to be included changes from one user to the other. For this purpose, digital printing methods are the most suitable because the information can be easily introduced in a software interface, communicated to the printing machine and printed. Currently, the two main digital printing techniques are inkjet and laser printing which are widely used for both commercial and industrial applications due to their versatility and cost-efficiency.

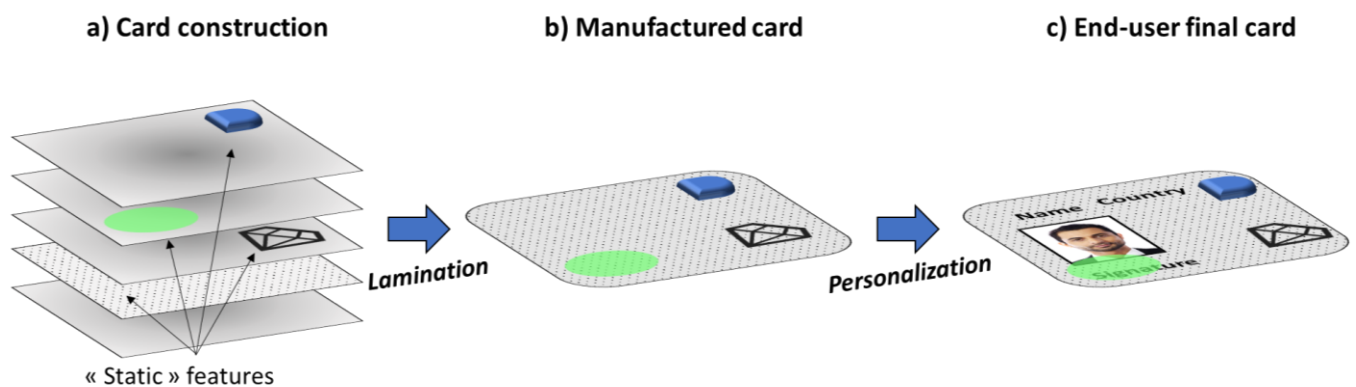


Figure 2: (a) Illustration of a card construction with different layers and “static” features. (b) The card is manufactured by laminating together the different layers. (c) “Personalization” features can then finally be added to the card.

#### Printing techniques for static security features

**Flexography** is an “indirect” technique that produces continuously predefined images or patterns using a rotational system on smooth or rough surfaces. First, the ink is transferred to an engraved cylinder known as an anilox roll. The engraved chambers are filled with ink and are put in contact with a plate cylinder, where the ink is only transferred to the relief

areas of the plate. Subsequently, the ink is transferred to the substrate to finish the process. It is widely used for security applications to deposit “invisible” inks such as UV or phosphorescent dyes on different flexible substrates (paper, cardboard or foil) as it allows the use of surfaces that are not necessarily smooth<sup>4-6</sup>. An example is illustrated in figure 3.a where a fluorescent ink is deposited by flexography and processed with different chemical treatments resulting in color changes when observed with a UV light at 365 nm. However, under day light, it remains invisible independently of the treatment.

**Offset lithography** printing is another printing technique based on a rotational system that operates on the repulsion of oil and water. Unlike flexography, this method is used to print on smooth or flat surfaces and not on rough surfaces. The image or pattern is put on thin metal plates and drenched with both water and ink using rollers. The oil-based inks adhere to the image area, while the rest is covered with water. Then, a rubber cylinder (called “offset” cylinder) is chemically pre-treated so it only accepts the ink covered areas. Finally, the ink is transferred to the substrate forming a mirror of the initial image. This technique is widely used to print high quality patterns with complexed features such as guilloche patterns or printing artwork<sup>7-9</sup>. An example is given in figure 3.b of highly detailed patterns in a banknote prepared by this technique<sup>10</sup>.

**Screen or “silkscreen” printing** is a low-cost printing method where a mesh is used to transfer ink to a substrate and form continuous patterns. First, the mesh is stenciled with the design of the pattern and placed on top of the substrate. The ink is then placed on top of the mesh and a blade (squeegee) evenly distributes it along the stencil. The ink is pressed through the stenciled areas and transferred to the underlying substrate forming a smooth pattern. This technique is commonly used to produce thick features such as optically variable devices (OVD) that change colors depending on the observation angle<sup>7-9,11,12</sup>. A recent example of an OVD is given in figure 3.c where magnetic photonic crystals are present different colors when observed under different angles<sup>13</sup>.

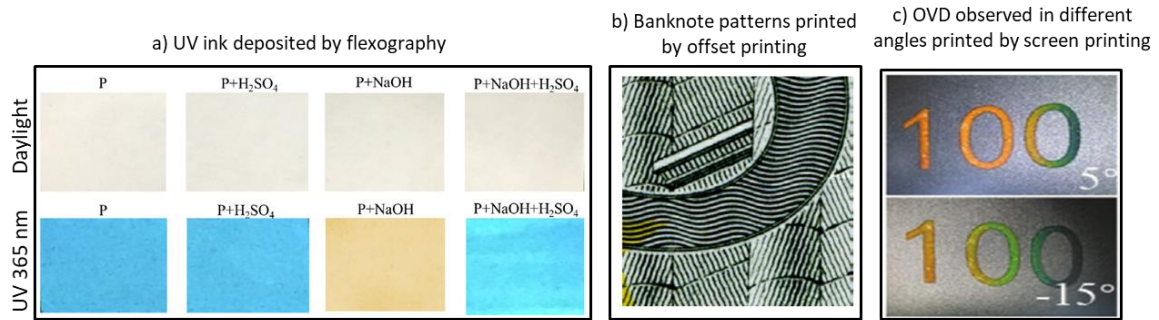


Figure 3: a) An invisible ink is deposited by flexography that reveals a fingerprint under UV light (390 nm) and is invisible under white light.<sup>4</sup> b) An example of microscale patterns printed on banknotes using offset lithography<sup>10</sup>. c) An OVD (optically variable device) is produced by screen printing magnetic crystals depicting different colors depending on the observation angle (relative angles of 5 and -15°)<sup>13</sup>.

### Printing techniques for personalization security features

**Inkjet printing** is the first digital printing method that reproduces images on flexible substrate. It is a contactless technique where droplets of ink are propelled by a nozzle via piezoelectric action, forming dots at the surface of the substrate. It is a common method used on commercial paper printers for personal or professional use to print high-quality and colorful images. For anti-counterfeiting applications, inkjet can be used to print optical devices<sup>14</sup> or colorful designs using invisible inks as presented in figure 4.a. In this example, red, green (lanthanide-based) and blue luminescent inks are used to reproduce full color images that are invisible under white light but appear under a 254 nm UV light presenting a wide variety of well saturated colors<sup>15</sup>.

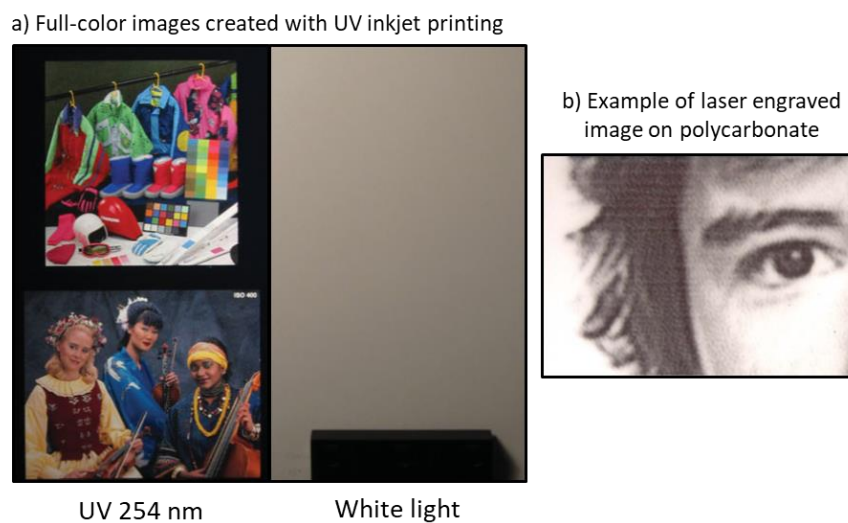


Figure 4: a) Invisible inks can also be printed by inkjet printing. Here, a combination of red, blue and green luminescent inks are used to print colorful images observed under UV light (254 nm) and disappear under white light<sup>15</sup>. b) An example of a laser-engraved image is illustrated in greyscale<sup>7</sup>.

**Laser engraving and laser marking** are two frequently used techniques to prepare security documents that do not rely on liquid inks but rather on the alteration of solid materials. Laser engraving refers to laser ablation of a material, thus removing or burning it, while laser marking implies a color change of the material after processing. Both methods allow to print high-resolution designs such as guilloche patterns, moiré patterns or images<sup>16</sup>. An example is given in figure 4.b where a polycarbonate substrate is laser engraved producing sub-micron “black” pixels and thus forming a high-resolution grey-scaled image<sup>8</sup>.

In the industrial world both laser marking and engraving are often used simultaneously to create high-quality secure images. An example of a laser-marked security document was published by Lazzari et al.<sup>17</sup> where a matrix of markable color sub-pixels is covered with an engravable layer that serves to form grey levels (figure 5.a). In fact, the laserable layer is carbonized by the laser irradiation producing black marks masking the subpixels and resulting in a well-contrasted color image. The produced image is heavily secured as it relies on two complementary printing methods. Another laser-marking strategy of producing color images is proposed by Lesur et al.<sup>18</sup> where they developed a laser-sensitive multilayer configuration (figure 5.b). Each layer is composed of at least one-color component (magenta, cyan or yellow) that can be bleached by laser irradiation at a specific wavelength without drastically modifying the remaining layers, thus producing a wide variety of colors. In addition, the images are well secured as specific layers and laser conditions are used to produce them. Both of these techniques present complex layer configurations that are difficult to counterfeit but simultaneously require complex material configurations and expensive laser-marking conditions.

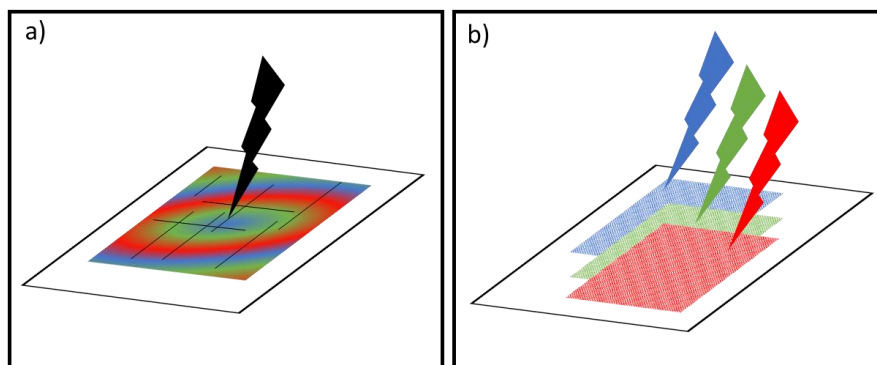


Figure 5: (a) Schematic illustration of the laser technology proposed by Lazzari et al.<sup>17</sup> where a laserable layer is carbonized to produce grey levels and mask the underlying color sub-pixels. (b) Schematic illustration of another laser-based technology developed by Lesur et

*al.<sup>18</sup> where color layers are stacked together and can be bleached independently by laser irradiation at a specific wavelength and form color gradients.*

Two types of security features were named, static or personalization features. Static features are generally produced using pattern-based methods such as flexography, offset lithography or screen printing. Flexography and offset lithography are similar techniques where ink is transferred to a substrate by using an engraved cylinder. They are great for printing different types of secure inks (UV, thermochromic or phosphorescent inks) on plastics or papers. Furthermore, screen printing is also a great printing technique on flexible supports, commonly used to produce thicker films such as OVDs. On the other hand, personalization features are produced mainly by digital printing techniques such as inkjet printing or laser printing due to their high versatility. Inkjet printing is a contactless technique equipped with a nozzle dropping ink dots at the surface of the substrate. Two types of laser printing exist, engraving and marking used to produce security features. The former relates to laser ablation of the material (plastic or paper), thus creating black dots and produce grey levels while the latter refers to color changes of the material (ink) induced by laser processing. Both techniques can be used independently or combined to produce high secure elements in industrial applications. However, they can be difficult to produce due to their complexity in terms of material preparation and/or laser setup. It is therefore interesting to develop a laser-based technology that “simplifies” the process as whole, namely having a single material and a single laser that allows the production of high-quality images.

### **Development of plasmonic colors induced by laser processing**

In recent times, the Nanoparticle team at Laboratoire Hubert Curien have had a particular focus on developing a laser-based technology that allows the production of personalization security features using plasmonic materials. To do so a sol-gel based mesoporous titania matrix embedded with silver nanoparticles is first deposited on a glass substrate. After stabilization the sample is processed by a nanosecond pulsed laser, causing a reshaping and reorganization of the silver nanoparticles and consequently producing interesting optical effects. Depending on the observation conditions under white light, each square can produce different color variations. The physical mechanisms leading to these effects have not yet been modelled but as far as it has been observed the color variety will depend mainly on the size, shape distribution of the resulting nanoparticles, their surrounding medium (thickness and

refractive index of the layers in which they are grown by laser) and the substrate. However, a practical framework was implemented by Nicolas Dalloz<sup>19</sup> to produce full-color images in a specific observation mode by introducing an original algorithm that analyze the colors produced in a considered mode and search automatically the best colors. Examples of over 250 colors produced by laser processing are depicted in figures 6.a to 6.c for respectively three different observation modes “transmission”, “frontside reflection” and “backside reflection”. Each color square corresponds to the extracted standard RGB (sRGB) color produced by a unique set of laser parameters. After selection of the best colors, an image can be printed in a selected mode. An example is given where a permanent color image (figure 6.d) is printed and observed in “backside reflection” mode (figure 6.e), highlighting the potential of the technology for color image printing.

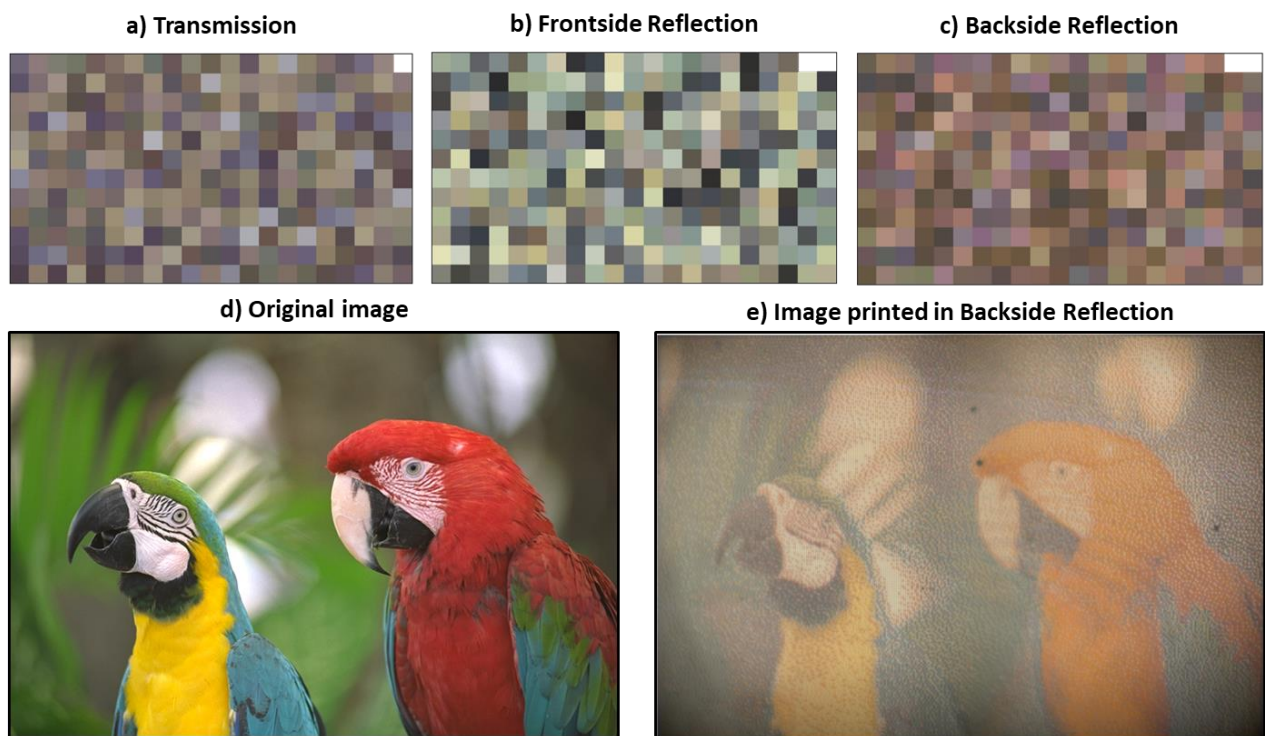


*Figure 6: The colors of over 250 squares produced by ns laser processing were recorded by a camera setup. They were detected in three specific observation conditions, namely (a) “transmission”, (b) “frontside reflection” and “backside reflection”. For each mode, each square represents the standard RGB color extracted of the color of over 250 individual sets of laser parameters. Colors can be utilized to produce high-quality image printing. An example is given where a colorful image of two birds<sup>20</sup>(d) was printed and (e) observed in backside reflection<sup>19</sup>. The size of the printed image is 23.8 mm x 15.84 mm and each printed pixel is a 72 × 72 μm<sup>2</sup> square.*

However, the technology lacks development in the material preparation side to be able to be fully implemented in an industrial application for ID documents. Such documents need to be

durable but also flexible which is why they are mainly composed of plastics or papers, yet the current processes are unsuitable for such supports, from the film preparation to the laser processing. In fact, the elaboration of these materials involves generally a thermal annealing ( $\approx 350\text{-}400\text{ }^{\circ}\text{C}$ ) that is not possible to perform on flexible supports. Alternative chemical or physical methods were developed in the group by Fanny Tricot during her PhD thesis to produce such films but are quite complex to implement in an industrial environment. Furthermore, these materials have never been embedded in a PC card, hence it is of great interest to develop a process that allows their implementation without damaging them. Therefore, inspired by her work, the first objective is to develop an alternative method to implement  $\text{TiO}_2\text{:Ag}$  films in plastic cards to replicate a real ID plastic card.

Moreover, the color production on such flexible supports has never been explored by using commercial nanosecond (ns) pulse lasers. Once included in the card, investigating their response to the laser processing is crucial to validate their interest for the application. Hence, the second objective is set on the laser processing and color production. A laser “database” was designed using several laser parameters that allows the production of a wide variety of uniform colors in different observation modes without damaging/burning the sample due to thermal effects. The third objective concerns the selection of the best colors (in a single mode) within the database that are reproducible sample to sample and utilized to produce several demonstrators, highlighting the potential of the application for color personalization. The fourth objective relate to the production of two image multiplexing using the established algorithms and the experimental results. The limitations of the work presented here are discussed for future perspectives in their full implementation on a full-scale industrial process. Finally, the fifth objective is associated to a second material configuration where a thermal barrier was implemented to produce colors on non-laminated  $\text{TiO}_2\text{:Ag}$  samples and depicting original optical features. They were characterized and utilized to produce a full color image, highlighting the versatility of the technology with different materials.

To present the different results, the manuscript is constructed as follow: in the first chapter, the concept behind the sol-gel method for material preparation is defined and highlighted for this technology. An overview is given on plasmonic materials and their properties are described. Then, the different physical mechanisms triggered by laser processing are highlighted, leading to permanent modifications of the material, revealing their interest for

secure applications. In particular, a spotlight is done on the production of colors using plasmonic structures and their use for high quality image printing. The underlying processes regarding the color production and management is described and implemented in the work presented in this thesis.

The second chapter describes the first experimental results relative to the preparation of sol-gel films on plastic supports inspired from previous works. The physico-chemical properties of the film are characterized during and after the elaboration process. After stabilizing the films, they are included in a plastic card to reproduce a real-case scenario for future industrial implementation.

The third and last chapter highlights the laser process workflow utilized to produce colors using a nanosecond pulsed laser. A study was carried to be able to understand the interaction of the material inside the card with laser irradiations by keeping the sample's integrity. A rigorous color selection was implemented that allowed to print a wide variety of colorful images in specific observation conditions. Following these results, image multiplexing was also achieved, making them great candidates for anticounterfeiting applications. Finally, non-embedded materials were laser processed in the same conditions but resulted in the production of different interesting optical properties.

## **CHAPTER 1: STATE-OF-THE-ART**

This first chapter describes in detail the context behind the thesis. It defines the different key notions, methods and latest results in literature that revolve around the technology that are necessary to be able to fully understand the work presented. First, the chemistry behind the preparation of mesoporous TiO<sub>2</sub> films that serves as a host matrix for silver nanoparticles. Then, the optical properties of these materials are described. Finally, their interaction with different laser processes are presented giving rise to unique optical features, highlighting their potential for security applications.

### **1.1 Sol-gel chemistry**

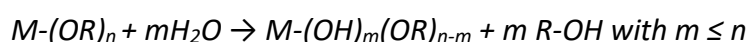
#### **1.1.1. General definition**

The sol-gel process can be defined as an inorganic polymerization procedure in which a sol, a colloidal suspension, evolves towards the formation of a gel-like diphasic system in two main steps: hydrolysis and condensation<sup>21</sup>.

A sol that is a dispersed solid phase small enough to be stable in solution, is composed of a metallic precursor, a solvent, water and additives. The most common precursors are metallic salts MX<sub>n</sub> or organometallic compounds M(OR)<sub>n</sub>, where M represents a metallic atom of n valence (Si, Ti, Al, ...), X a chloride, nitride or acetate group and R an organic ligand (alkyl, aryl,...).

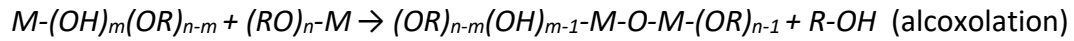
The gel is defined as a 3D solid-like system which is typically the condensed polymerized sol with small clusters forming the tridimensional network and is incorporated in a liquid phase.

The initial reaction is the hydrolysis of the precursor, which in the case of metal alkoxides, -OR ligands, substitute the organic ligands by hydroxyl groups as in the following reaction equation<sup>22</sup>:

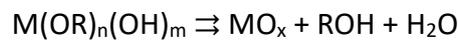


The hydrolysis of the partially hydrolyzed species may continue by replacing the rest of the ligands with hydroxyl groups depending on the experimental conditions such as the concentration and type of the metal alkoxide, pH, water/precursor molar ratio, sol-gel catalysts, among others<sup>23</sup>.

The condensation starts as soon as the first hydrolyzed species are formed and react together (oxolation) or with non-hydrolyzed alkoxides (alcoxolation) as presented respectively in the following equations<sup>22</sup>:



Both reactions are in competition and result in the growth of bigger molecules, oligomers, to ultimately form an inorganic polymer through polycondensation as simplified in the following equation<sup>24</sup>:



Understanding and controlling the kinetic of both hydrolysis and condensation reactions are crucial to obtain the desired structure and morphology of the gel. One of the most common strategies is controlling the pH of the experimental environment. As it was presented by Livage *et al.*<sup>25</sup>, there is a quantifiable pH-charge relationship during the sol-gel process, meaning that the hydrolysis and condensation kinetics highly depend on the medium's pH, hence the molecule charges. By playing with the medium's pH either the hydrolysis or condensation reactions can be promoted which can result, depending on the conditions, in materials with different structures.

For example in the case of silicates, in basic conditions, the polycondensation step is much faster than the hydrolysis reaction, favoring the nucleation, which tends to form highly branched structures with relatively large particles (colloidal gel) resulting in a porous film with higher surface areas. In acidic conditions, the rate of the hydrolysis reaction is much faster than the polycondensation step, resulting in the formation of a polymeric gel and ultimately on a denser film<sup>21</sup>.

### 1.1.2. Preparation of mesoporous sol-gel films

According to IUPAC porous materials can be classified in 3 distinct categories depending on the diameter size of the pores : micropores (< 2 nm), mesopores (2-50 nm), and macropores (> 50 nm). These materials have been widely studied as they can interact with ions, molecules, atoms and NPs within the surface but also with the bulkier part of the porous material, enhancing the physico-chemical properties of the materials and their potential applications.

Two approaches are often referred to for the preparation of such materials: A hard templating route where the material is nanostructured on the surface of a template which is later removed via physical or chemical processes; or a soft templating route which usually involves the use of organic or polymeric surfactant that assemble into supramolecular structures which are ultimately used as soft templates<sup>26</sup>. The sol-gel route belongs to the soft templating category and is widely used to prepare homogeneous porous films. The different aspects of this route are explained in the following parts.

#### 1.1.2.1. *Sol-gel deposition techniques*

The sol-gel process described previously is a well-known method to prepare homogeneous thin layers for many applications in optics (self-cleaning, anti-reflection, high reflection, filtering, coloring, etc.)<sup>27</sup>, electronics (transistors, photovoltaic solar cells, insulation)<sup>28,28,29</sup> and analysis (selective sensors)<sup>30,31</sup>. Depending on the purpose, their surface and intrinsic properties can vary as they can be dense, porous, patterned, multi-layered, composite, etcetera. The film must be identical across the whole surface of the substrate to serve its purpose and thus the thickness has to be highly controlled to obtain uniform layers. To do so, the two most common sol-gel deposition techniques across R&D are dip-coating and spin-coating where the typical thickness ranges from a few nanometers to a few micrometers. Generally speaking they follow the same sequence of successive steps: (1) formulation of chemical solution, (2) solution deposition on the surface of the substrate, (3) liquid evaporation and (4) stabilization treatment. An overview of each deposition method is given with their respective advantages and drawbacks related to their application on flexible supports.

##### 1.1.2.1.1. Dip-coating process

The principle of dip-coating deposition is immersing vertically the substrate in a solution (figure 7.a), withdrawing it at constant speed in short delay leaving a thin layer of solution in both sides (figure 7.b). Once the sample is fully withdrawn, the solvents are evaporated (figure 7.c). The thickness of the film relies on the deposition conditions namely the withdrawal speed, viscosity of the sol, temperature, relative solvent, vapor pressure, etc... At low withdrawal speed ( $< 0.1 \text{ mm}\cdot\text{sec}^{-1}$ ), solvent evaporation is faster than the motion of the drying line which induces a feeding of the upper part of the meniscus by the solution by

increasing capillarity. This phenomenon is known as a capillary regime and is illustrated in Figure 7.d.

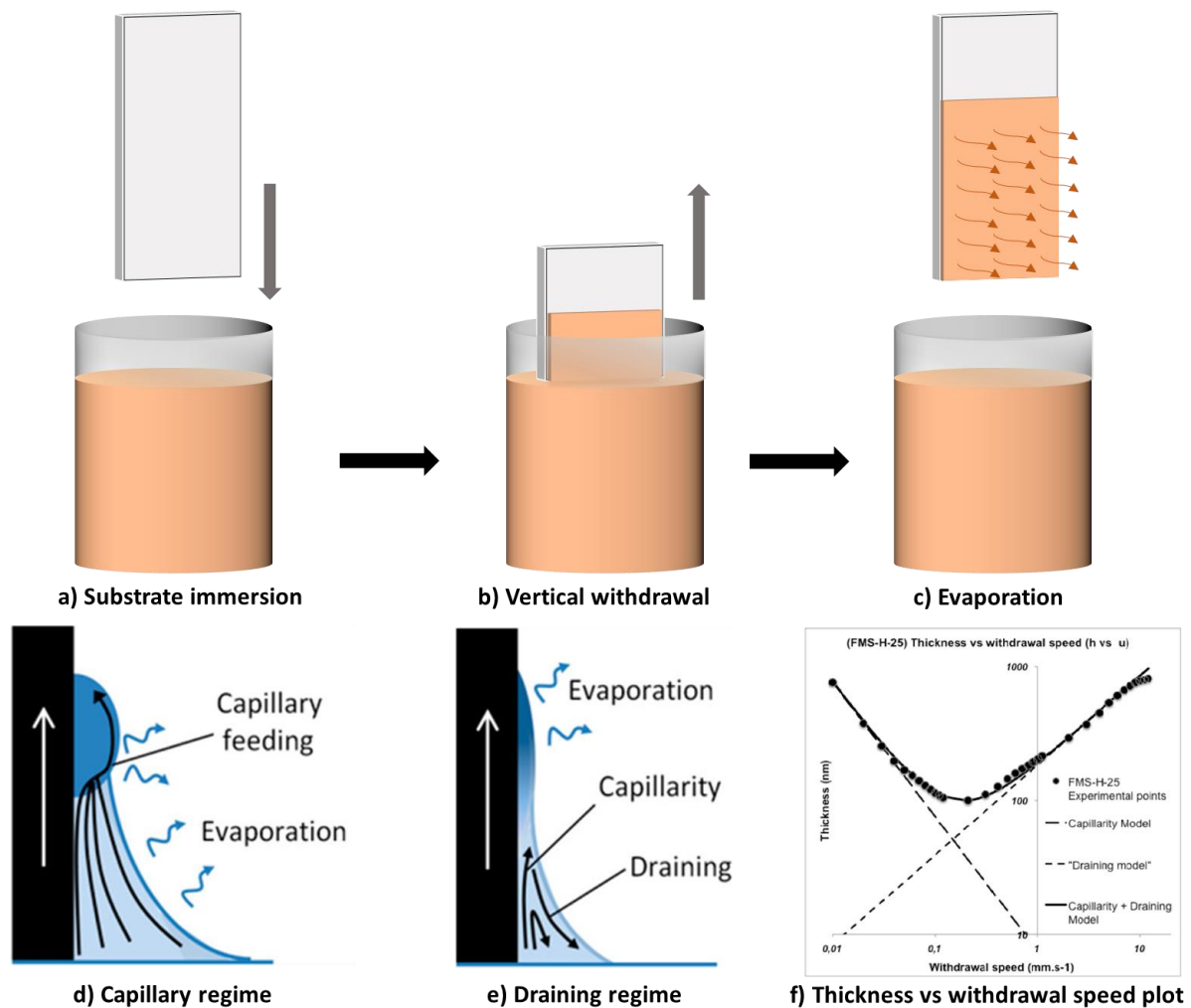


Figure 7: Schematic representation of the dip-coating process. (a) First, the substrate is vertically immersed in the sol. (b) After full or partial immersion, the substrate is withdrawn vertically at a fixed speed. (c) Once, the substrate is completely removed, the solvent content is evaporated. The evaporation rate will depend on the deposition conditions. For instance, two regimes are presented, capillary (d) and draining regime (e)<sup>33</sup>. The capillary regime is triggered when the solvent evaporation is faster than the motion drying line, triggering a continuous feeding of the meniscus. In the draining regime, the formation of the film is governed by the viscous dragging of the solution. A semi-empirical model combining both phenomena can be utilized to predict the final thickness of the film. (f) An example is given for a silica sol-gel thin film deposition by dip-coating by plotting the thickness versus withdrawal speed (log-log scale)<sup>32</sup>.

In contrast, at high withdrawal speeds the film formation follows the viscous dragging of the solution, called the draining regime as depicted in Figure 7.e. If both regimes are determined for a given solution, a semi-empirical model can be applied to predict the final film thickness

( $h_0$ ) as a function of the withdrawal speed ( $u$ ), material proportion constant ( $k_i$ ), rate of solution evaporation ( $E$ ), film width ( $L$ ) and global constant ( $D$ )<sup>32</sup>:

$$h_0 = k_i \left( \frac{E}{Lu} + Du^{\frac{2}{3}} \right) \quad (\text{Equation 1})$$

An example is given in Figure 7.f where silica-based sol-gel films were studied to determine the thickness at different speeds<sup>32</sup>.

Dip-coating is a remarkable method to produce homogeneous sol-gel films on small or large substrates with high optical quality. It's technically easy to build up and easy to control the critical conditions of deposition, namely the evaporation, with a more or less good control of the motion. Additionally, programming recipes with different withdrawal speeds can lead to efficiently produce one-directional gradients of thickness without wasting large quantities of solution. On the other hand, the main drawback of dip-coating is that all faces of the substrate are coated which is not necessarily required. This is particularly problematic for flexible supports as cleaning the undesired coated faces is difficult. Moreover, flexible supports can easily bend when dipping depending on the viscosity of the solution which can lead to inhomogeneities on the film.

#### 1.1.2.1.2. Spin-coating process

Spin-coating deposition method has been widely used to deposit uniform thin films on flat surfaces. It involves four main steps as illustrated in Figure 8. The first step (a) is depositing homogeneously a drop of the solution on top of the substrate set down on top of the spinner which is secured by a vacuum system; the second one (b) consisting in rotating the spinner at a specific angular speed allowing the solution to spread on the surface due to centrifugal force (spin-up) forming a thin film; in third step (c) the thickness of the film gradually decreases during the spin-off at constant speed due to the viscosity forces of the solution and lastly (d) during the rotation at constant speed the solvent evaporates, reducing the film thickness. The latter depends on the viscosity of the solution, the rotation speed (in rounds per minute (rpm)) and, as in dip-coating, on the environmental conditions such as relative humidity, vapor pressure and temperature of the room. To estimate the final solid thickness of the film ( $h_0$ ) a simplified model was proposed by Meyerhofer<sup>34</sup> and updated by Bornside *et al.* expressed as <sup>35</sup>:

$$h_0 = (1 - x_0) \left[ \left[ \frac{3\eta_1^0}{2\rho_1^2\omega^2} \right] \frac{p^*M}{R_gT} kx_0 \right]^{1/3} \quad (\text{Equation 2})$$

where  $x_0$  is the initial concentration of solvent,  $\eta_1^0$  and  $\rho_1^2$  are the viscosity and the density of the liquid;  $p^*$  and  $M$  are the vapor pressure and molecular weight of the pure solvent;  $R_g$  is the ideal gas constant;  $T$  is the temperature;  $k$  is the mass transfer coefficient.

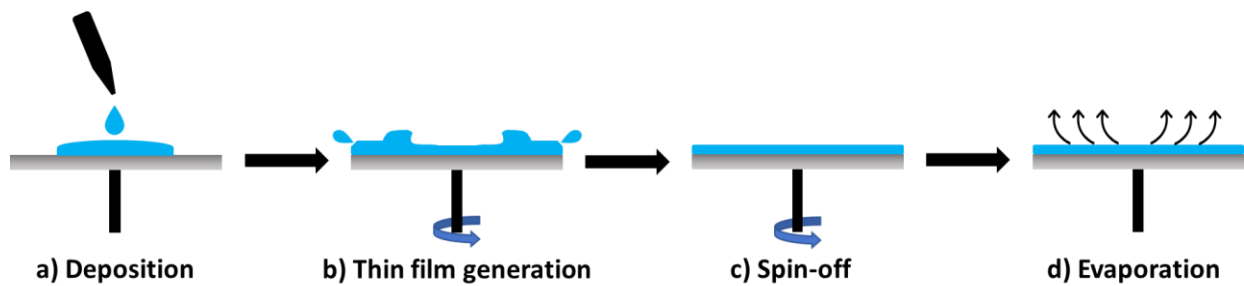


*Figure 8: Schematic representation of the four main steps of spin-coating. (a) The sol is deposited on top of the substrate correctly placed on the spinner. (b) Then the film is rotated at constant speed spreading the sol on the surface by centrifugal force (spin-up). (c) Governed by the viscosity of the solution, the thickness of the formed film gradually decreases (spin-off). (d) In the final part of the spin-coating, the solvent is evaporated, reducing even more the thickness of the film.*

This method is great for depositing on flexible substrate such as PC substrates as they are fixed in the horizontal plane during deposition thus avoiding any risk of bending the substrate. In addition, only one side of the substrate is covered with the solution, contrary to dip-coating deposition. Nevertheless, this method works well for laboratory work but is not suitable for industrial manufacturing as coating large surfaces is very difficult.

Both dip-coating and spin-coating are suitable for the production of sol-gel thin films with good optical properties. However, in the context of my PhD work, dip-coating is used for rigid flat substrates such as glass or silicon wafers and spin-coating for flexible supports.

#### 1.1.2.2. The EISA method

One of the most attractive method to prepare uniform thin films is the Evaporation-Induced Self Assembly (EISA), which combines chemical solution deposition (CSD), sol-gel chemistry, and block copolymer templating<sup>36</sup>. The self-assembly phenomenon can be described as a spontaneous organization of materials through noncovalent interactions such as hydrogen bonding, Van der Waals forces, electrostatic forces, etc. This process was first observed in the '90s by Mobil Oil researchers on the synthesis of mesoporous silica<sup>37</sup> and later reported

by the Brinker's group<sup>38</sup>. It allows the fast production of nanostructured porous materials or nanocomposites in the forms of films, fibers, or powders. Since then, many efforts have been made on understanding the self-assembly mechanism and the different steps involved in it to develop new synthetic routes to produce a wide range of porous materials.

Generally speaking the EISA process is governed by four main steps: (1) Evaporation of volatile components (mainly the solvent), (2) equilibrium of water content in the film with the moisture of the environment, (3) condensation and stabilization of the inorganic matrix and (4) network stiffening by further condensation. The first and fourth step are rather governed kinetically and the second and third step are driven by thermodynamics. This process permits control of the final structure of the material with high efficiency and reproducibility. Several experimental parameters that influence the resulting structure can be divided in two categories: chemical parameters such as the initial sol composition (precursor, solvent, structuring agent, additives), pH and aging time, and the processing parameters such as the partial vapor pressures, convection and temperature<sup>39</sup>.

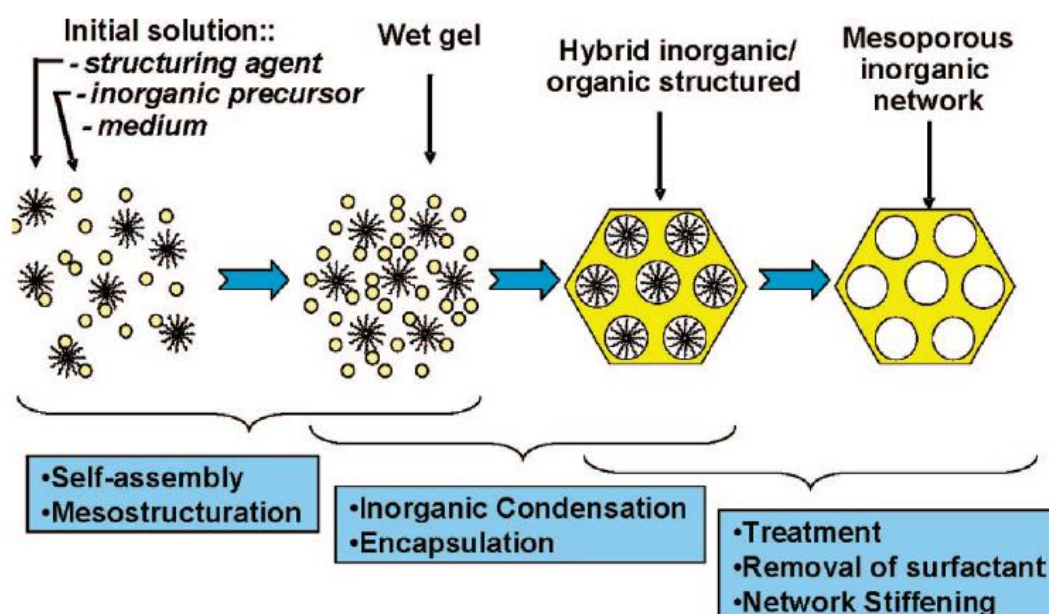


Figure 9: Schematic representation of the preparation of mesoporous materials via the EISA method adapted from Sanchez et al.<sup>40</sup>.

### 1.1.2.3. Soft-templating agents

Templating agents such as surfactants are of great interest to produce inorganic porous materials with the EISA method due to their assembling properties. These *surface-active* molecules have the unique properties of getting adsorbed at various interfaces (air-water, oil-

water, water solvent etc.) and changing their properties. Ionic surfactants were originally used to elaborate mesoporous oxide materials such as mesoporous silica films prepared using Cetyltrimethylammonium Bromide,  $[(C_{16}H_{33})N(CH_3)_3]Br$ ; CTAB) as the templating agent where small pores ranging from 2 to 10 nm were obtained with amorphous pore walls<sup>41</sup>. Their small size and restricted range of compositions limits the pore size of the nanostructured materials. To overcome these limitations non-ionic surfactants such as amphiphilic block copolymers macromolecules are being used to synthesize mesoporous materials<sup>42</sup>. Their amphiphilic properties are owed to the presence of hydrophobic (*i.e.* alkyl chains) and hydrophilic parts (ionic or polar groups) contained in the polymer blocks. Due to their unique chemical structure, such molecules in solution tend to self-assemble in the form of micelles, spherical or cylindrical structures when their concentration is greater than the Critical Micellar Concentration (CMC). As described by Nakama<sup>43</sup> and illustrated in Figure 10, depending on the synthesis temperature and the surfactant's concentration different mesophases can be obtained presenting different shapes, structures and optical properties. In addition, their physical and chemical properties can be tuned by adjusting the block length, composition or architecture of the blocks as it will consequently alter their morphology and CMC.

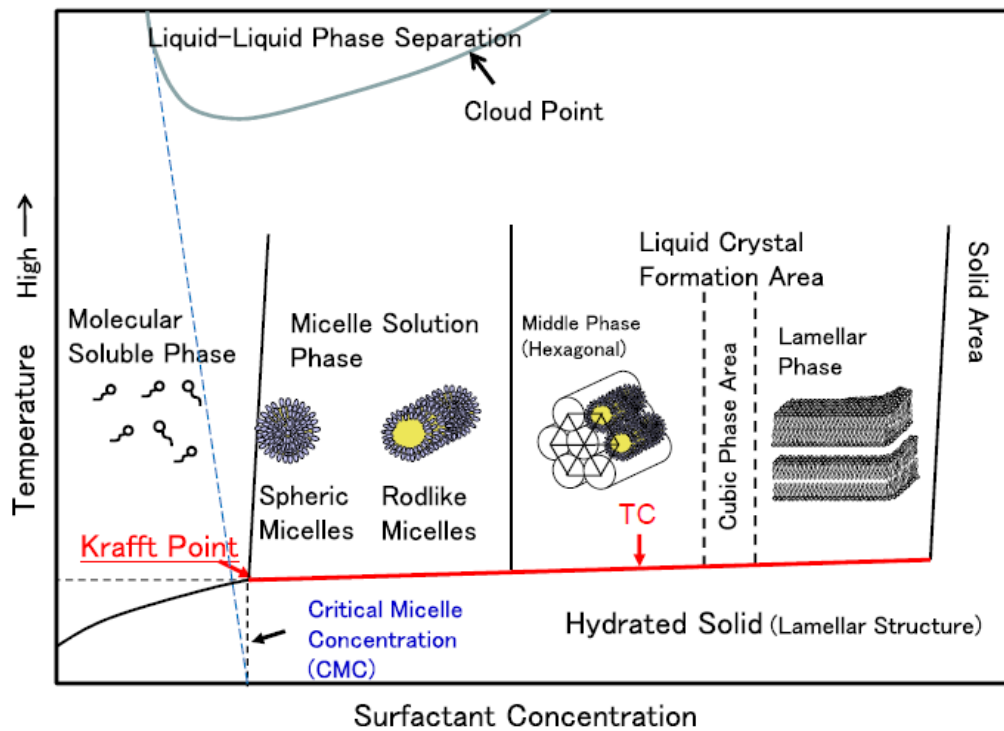


Figure 10: Conceptual scheme taken from Nakama<sup>43</sup> presenting the different forms of a surfactant in varied conditions.

### 1.1.3. Elaboration of titania materials

#### 1.1.3.1. Generalities

Metal oxide mesoporous coatings are of great interest in recent years due to their applicability as thin films and their high surface areas making them suitable for a wide range of applications such as photonics, catalysis, energy, sensing, membranes and biological sciences<sup>44</sup>. Among the transition metals, titanium (Ti) with an electronic configuration of [Ar] 4s<sup>2</sup> 3d<sup>2</sup> is one of the most studied and promising materials and more noticeably its oxide form titanium dioxide (TiO<sub>2</sub>).

Some of these properties are intrinsic to the crystalline phase of TiO<sub>2</sub> besides its amorphous phase. Titania can be found in three different crystalline phases: anatase (tetragonal, band gap of 3.21 eV), rutile (tetragonal; band gap of 3 eV) or brookite (orthorhombic, band gap of 3.3 eV) as shown in Figure 11.a<sup>46</sup>. Rutile is the most thermodynamically stable form, whereas anatase and brookite are metastable<sup>47</sup>. Initially the amorphous phase is built of TiO<sub>6</sub> octahedra, but when the synthesis' temperature (in ambient conditions) reaches 350°C to 400°C the polymorph anatase is produced by edge sharing of the TiO<sub>6</sub> octahedra. Rutile is formed starting from 500° to 800°C in air but this phase transition temperature can vary depending on the synthesis method and the precursors used as it can reach 1200 °C<sup>48</sup>. This is observed by an edge and corner sharing TiO<sub>6</sub> octahedra with a slight orthorhombic distortion<sup>47</sup>. Brookite follows an orthorhombic crystalline structure and is the least dense compared to anatase and rutile<sup>47</sup>. These distortions of the TiO<sub>6</sub> octahedra can be observed by a modification of the electronic band as the t<sub>2g</sub> and e<sub>g</sub> bands are split into sub-bands as shown in Figure 11.b<sup>49</sup>. Anatase and rutile are the most commonly synthesized polymorphs and brookite is considered more as a by-product of either or both other phases.

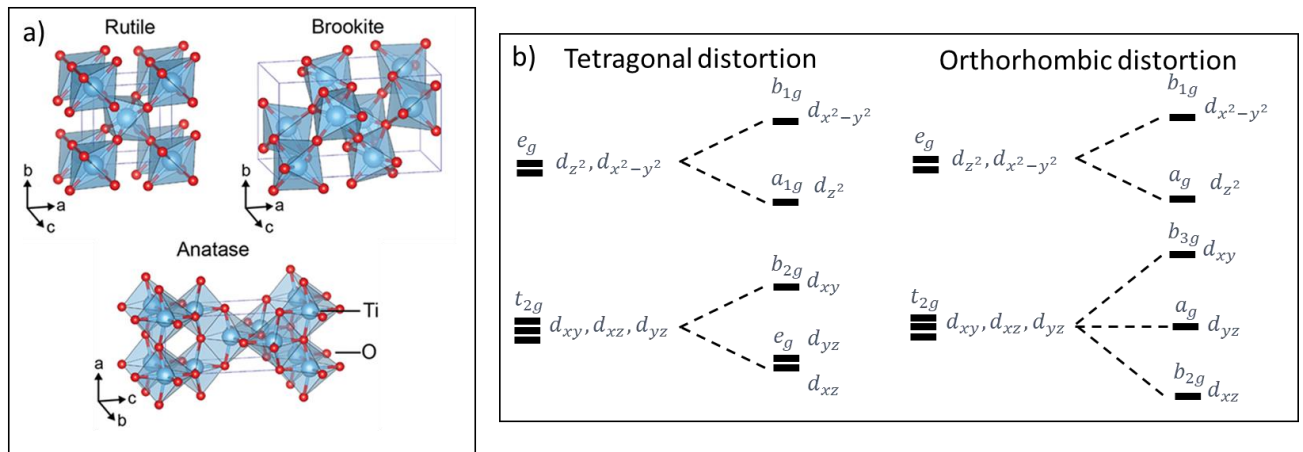


Figure 11: a) Crystal structures of TiO<sub>2</sub> rutile (tetragonal), brookite (orthorhombic) and anatase (tetragonal) polymorphs adapted from Haggerty et al.<sup>46</sup>. b) Tetragonal (anatase and rutile) and orthorhombic (brookite) distortions of TiO<sub>6</sub> result in the formation of different sub-bands in the electronic structure adapted from Tian et al.<sup>49</sup>.

This low-cost metal oxide presents exceptional chemical stability, electrochemical and photo-resistant properties with low toxicity except in nanoparticle form<sup>45</sup>. It presents a high refractive index (from 2.5 to around 3 at the wavelength of 550nm), wide band gap (3 to 3.3 eV) meaning it absorbs only ultraviolet (UV) light and thus presents excellent optical transparency in the visible and near infrared (IR) regions.

Amorphous titania along with its polymorphs are used in a wide variety of industrial domains such as optics, cosmetics, paint, and food science but also for the development of high-tech applications such as catalysis, photovoltaics, sensing and microelectronics<sup>23,37,39,40,42,44,45,50-54</sup>. For the synthesis of titania nanostructures different synthesis routes have been developed such as physical vapor deposition (PVD)<sup>55</sup>, chemical vapor deposition (CVD)<sup>56</sup>, sol-gel<sup>39,40,53</sup>, hydrothermal<sup>57</sup> or electrochemical<sup>58</sup> procedures. Depending on the desired form of TiO<sub>2</sub> and its applications, some routes are more convenient than others, since some advanced applications require thin films with highly controlled mechanical, optical and structural properties that can be produced with good homogeneity and reproducibility.

#### 1.1.3.2. Sol-gel approach

The preparation of mesoporous titania thin films (MTTF) is of great interest as the sol-gel route is in principle a promising and versatile preparation method to obtain such films with highly controlled porosity and homogeneity<sup>53</sup>. To do so the titanium precursors of choice are often alkoxides (Ti(OR)<sub>4</sub>, with RO: ethoxide, i-propoxide, n-butoxide..) or titanium chloride,

TiCl<sub>4</sub>. Alkoxides are particularly hygroscopic and reactive so a moist-free environment is needed for their operation as exposing them to damp environment can incite an undesired precipitation. These precursors are dissolved in a solvent, usually alcohols or slightly polar solvents such as THF are used, in the presence of acid or chelating agents such as acetylacetonate to stabilize them. Alternatively, TiCl<sub>4</sub> reacts aggressively with damp air and water as it promotes an exothermic hydrolysis reaction and consequently releases protons that acidify the solution, promoting the stability of positively charged Ti-oxoclusters in the sol. Depending on the chemical equilibrium, an intermediate precursor is formed that is subjected to the well-known sol-gel hydrolysis ratios  $h = [\text{H}_2\text{O}] / [\text{Ti}]$  and  $p = [\text{H}^+] / [\text{Ti}]$  as they will determine if either the hydrolysis or condensation reaction is promoted. Using various hydrolysis ratios will lead to different orderings of the mesostructure<sup>53</sup>.

#### 1.1.3.3. *Aging after deposition*

After coating of the sol on a substrate, gelation occurs as small clusters are condensed, forming a macroscopic 3D network with increasing viscosity and finally yields in a gel. However, at a microscopic level the sol (liquid phase) is still present giving certain elasticity to the solid network, the film is now aging and the evolution of the chemical processes involved will determine the final characteristics of the material<sup>40,50</sup>. During this step, the gel is at equilibrium with the environment and can either shrink or swell by adsorbing solvents and consequently modify the structure and properties of the gel. This part of the process is key to the preparation of such materials after initial assembly<sup>44</sup>.

Table 1 summarizes the most common strategies to prepare MTF in recent years, most of them involving a thermal curing over 200°C. Indeed heating boosts the removal of solvents and the templating agents which leads to the formation of pores but also induces the continuous condensation and densification of the inorganic matrix. In addition such a treatment can lead on to the crystallization of the desired titania polymorph, mainly anatase.

Table 1: Summary of different synthesis routes of MTTF in recent years

Year	Precursor	Template	Post-deposition treatment (max temperature)	Crystalline structure	Reference
2011	TTiP/Acac	P123	Thermal curing (340°C)	Amorphous	Nadar <i>et al.</i> <sup>59</sup>
2012	Ti(OBu) <sub>4</sub>	F 127	Thermal curing (260-700°C)	Amorphous; anatase	Kim <i>et al.</i> <sup>60</sup>
2013	TiCl <sub>4</sub>	CTAB; Brij-58; F127	Thermal curing (350°C)	amorphous	Bellino <i>et al.</i> <sup>61</sup>
2014	TTiP/Bzac	P123	IR annealing or Soxhlet extraction	Amorphous	Tricot <i>et al.</i> <sup>62</sup>
2014	TiCl <sub>4</sub>	Polyglycerol hyperbranched core-multishell derivatives; PEO-PB-PEO	Thermal curing (450°C)	Anatase	Bernsmeier <i>et al.</i> <sup>63</sup>
2015	TTiP	Brij-56; P123	Thermal curing (250-450°C)	Amorphous; anatase	Miyata <i>et al.</i> <sup>64</sup>
2015	TiCl <sub>4</sub>	F127; PEG6000; PB-PEO	Thermal curing (500°C)	Anatase	Faustini <i>et al.</i> <sup>65</sup>
2017	TiCl <sub>4</sub>	F127	Thermal curing(200-350°C)	Anatase	Rassu <i>et al.</i> <sup>66</sup>
2019	TiCl <sub>4</sub>	Brij 58; F127; P123	Thermal curing (200°C) + Ethanol extraction (3 days)	Amorphous	Steinberg <i>et al.</i> <sup>67</sup>
2019	TTiP/Acac	P123	Thermal (110°C) + UV curing (254nm)	Amorphous	Sharma <i>et al.</i> <sup>68</sup>

To summarize, the sol-gel route is a well-known method for the preparation of mesoporous titania films. A thermal treatment after deposition is one the most efficient and hence the most used method to create useful mesoporous titania films. Nevertheless, they have been designed to be prepared on rigid and thermal-resistant supports such as glass substrates or silicon wafers and are therefore not suitable for flexible supports that do not sustain more than 180 °C. In response, alternative strategies were developed to prepare such materials on soft materials. Tricot *et al.*<sup>69</sup> developed two alternative sol-gel routes (after annealing at 110°C) to prepare amorphous MTTFs on PET substrates. The first one involves a 24-h UV (365 nm) light treatment to decompose the TTiP/Bzac complex, combined with a chemical extraction to eliminate the remaining organic parts and produce the mesoporosity. The extraction can be done either by ultrasonication in an ethanol bath for 30 mins or by Soxhlet solid-liquid distillation lasting 18 hours. The second route involves a 30-minute infrared (IR) annealing to create the mesoporosity. Both routes yield similar results but the IR annealing is particularly more interesting as its less time-consuming (30 mins vs 24 hours for the chemical

route). However, it requires a lot of precision and skills making it prone to mistakes. More recently, Sharma *et al.*<sup>68</sup> proposed a modified version of the chemical route by using a TTiP/Acac sol to deposit on plastic substrate instead of the TTiP/Bzac complex. This way, after a 2-hour annealing at 110°C, the film is exposed to a UV treatment (254 nm) for significantly less time, 6 hours compared to 24 hours, to polymerize the TiO<sub>2</sub> film. The chemical extraction is done by sonication on an ethanol bath. This method seems convenient to develop as it was performed on flexible substrates and is significantly less time-consuming than other routes. Therefore, it was decided to further investigate and validate an adapted method to prepare mesoporous TiO<sub>2</sub> films on plastic substrates.

In the following section a description is given on the different methods to prepare TiO<sub>2</sub>:Ag films for flexible supports.

#### 1.1.4. Synthesis of TiO<sub>2</sub>:Ag materials

For the synthesis of TiO<sub>2</sub>:Ag materials two approaches are often referred to: the “bottom-up” approach which relies on colloidal/chemical synthesis or the “top-down” approach (physical methods) which refers to the cutting or slicing of a bulk material to obtain nanostructures. With top-down methods one can prepare precise and complex structures in arrays or in 3D but tend to be very expensive and time-consuming. Colloidal methods however are generally cheaper than top-down methods, nanostructures can be formed in larger quantities and are less time-consuming. However, precisely controlling the morphology, location and composition can remain a challenge for some complex nanoarchitectures. In the following part the main bottom-up and top-down methods are described.

##### 1.1.4.1. Bottom-up approach by sol-gel methods

In order to produce these nanocomposites, the general bottom-up method is to prepare first the mesoporous titania matrix and then the porosity is filled with silver salts by liquid impregnation<sup>70</sup>. To do so the dried film is immersed in ammoniacal silver nitrate (AgNO<sub>3</sub>) solution for a limited duration. Introducing ammonia (NH<sub>4</sub>OH) to the silver nitrate solution results in the formation of a positively charged silver complex, ([Ag(NH<sub>3</sub>)<sub>2</sub>]<sup>+</sup>), which neutralizes the charges at the surface and allows a rapid and homogeneous impregnation of the matrix<sup>59</sup>. The diffusion of silver ions can be further improved by using a 1:1 volume of water and ethanol as solvents due to their discrepancy in surface tension<sup>59,70–72</sup>.

Once the film is impregnated, silver ions ( $\text{Ag}^+$ ) can be reduced by optical, thermal or chemical methods to form silver nanoparticles (AgNPs) of different sizes and distributions in the host matrix<sup>59,70</sup>. It was observed that a thermal reduction leads to a slow growth of nanoparticles with a broad size distribution and a non-uniform localization. Some aggregates are formed at the surface or inside the inorganic matrix. In the contrary, a chemical reduction leads to a fast nanoparticle growth with large nanoparticles localized preferentially at the surface of the film. Finally, the optical reduction by UV irradiation leads to a homogeneous distribution of nanoparticles localized at the top part of the film. This impregnation method is suitable for plastic supports as long as they are non-porous and chemically resistant to the ammoniacal solution in order to avoid substrate impregnation or damages.

Alternative sol-gel methods were found in the literature that allows the elaboration of  $\text{TiO}_2:\text{Ag}$  materials. For example, a one-step route was developed by combining titania and silver precursors with structuring agents in a single solution to form homogeneous  $\text{TiO}_2:\text{Ag}$  films<sup>73</sup>. It was observed that the presence of templating agents such as Pluronic bloc copolymers can reduce and stabilize silver nanoparticles in solution<sup>74,75</sup>. When dispersed in a titania sol and deposited on a substrate, a calcination step can be applied to be able to simultaneously form the porosity of the titania matrix and promote the growth (reduction) of silver nanoparticles in the inorganic film<sup>73</sup>. A similar one-pot method was developed where acetonitrile is used as a chelating agent of silver in solution to avoid their agglomeration and acetylacetone is used to stabilize the Ti centers. Their implementation is needed to avoid the gelation of the sol when adding  $\text{AgNO}_3$  to the acidified titanium precursor<sup>76</sup>. Films were then stabilized by heat treatment.

#### 1.2.2.1. *Top-down approach by magnetron sputtering method*

Physical routes can also be used to prepare  $\text{TiO}_2:\text{Ag}$  materials, particularly by magnetron sputtering-based methods<sup>77-81</sup>. As a general concept, with these methods titania and silver layers are deposited independently one on top of the other to produce  $\text{Ag}/\text{TiO}_2$  or sandwiched  $\text{TiO}_2/\text{Ag}/\text{TiO}_2$  films. After deposition, the films are often stabilized by thermal annealing at 300-600 °C<sup>77-80</sup> which limits their use on flexible supports. Just one method was found to be compatible with flexible substrates as  $\text{Ag}/\text{TiO}_2$  were synthesized on PET substrates in room temperature with interesting optical properties<sup>81</sup>.

TiO<sub>2</sub>:Ag films are used to produce optical effects by a laser marking technology developed in the Hubert Curien laboratory. Liquid silver impregnation of TiO<sub>2</sub> materials was found to be the most suitable for glass and PET substrates. It is envisioned to be also used on polycarbonate substrates.

### **1.3. Optical properties of TiO<sub>2</sub>:Ag materials**

The laser marking technology used in this manuscript rely on the interaction of the light and the TiO<sub>2</sub>:Ag material resulting in permanent coloration of the film. The different mechanisms and properties to achieve this are described below.

#### **1.3.1. Plasmonic properties of metallic nanoparticles**

According to the International Standard Organisation (ISO), nanomaterials are materials possessing one, two or three external dimensions in the range between 1 and 100 nm<sup>82</sup>. Nanostructures have been a subject of scientific investigation since ancient times but have gained increasing popularity in the last century owing to the rise of nanotechnologies. Nanoscience involves understanding and controlling matter at a nanoscale and utilising the properties of these nanoscale materials that differ from their bulk counterparts to create or improve materials, devices, and systems<sup>83</sup>. The properties of nanomaterials depend directly on the nature of the material used, on their size and form, meaning that their properties can be tuned. One of the most interesting nanomaterials are nanoparticles (NPs) which possess three dimensions in the nanometric range. The smaller the particle the bigger is the ratio between surface atoms and volumes atoms and the interparticular distance is smaller compared to bulk materials.

The most common nanoparticles found in literature are prepared of metals (Ag, Au, Pd, etc.), metal oxides (SiO<sub>2</sub>, TiO<sub>2</sub>)<sup>84</sup>, polymers<sup>85</sup> or organic compounds<sup>86</sup>. Noble metals are particularly interesting on this field due to their peculiar interaction with visible light. Silver and gold nanoparticles are the most commonly studied nanoparticles both fundamental and technological studies. The conductive electrons in metals are very mobile and create an electronic cloud around metallic ions, which can be polarized by an electromagnetic source such as light. In the simple example of a spherical-shaped nanoparticle (with the diameter

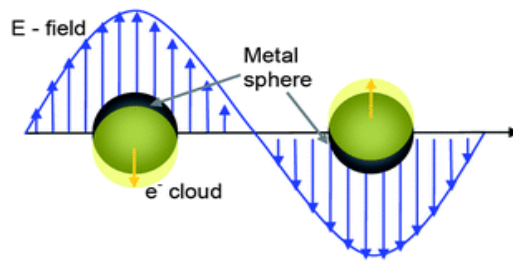


*Figure 12: Schematic representation of plasmon resonance.*

greatly inferior to the radiation's wavelength) metal free electrons oscillate collectively when they are irradiated by incident light, as seen in Figure 12, and consequently form plasmon waves at the interface between the metal and its dielectric medium, called Localized Surface Plasmon Resonance (LSPR)<sup>87</sup>. These surface resonances are often accompanied (depending on their dimensions) with remarkable scattering, absorbance, electromagnetic field enhancement and coupling properties and are observable from the visible to near infrared domain. Their optical response is directly dependent on several factors such as the composition of the metal, their size, form, and/or their dielectric environment.

An example is given in figure 13 where the optical response in the visible range was investigated for different sizes and shapes of gold and silver nanoparticles<sup>88</sup>. For instance, the response of spherical nanoparticles is blueshifted when the metal is silver (yellow curve) compared to gold (red curve). Moreover, the optical response is different when the shape of the nanoparticles changes as illustrated by the redshift for "branched gold" (blue curve) and even more for "gold nanorods" (green curve) compared to spherical gold. These properties can interest different applications such as optical sensors<sup>89</sup>, bio imaging<sup>90</sup>, drug delivery<sup>91</sup> and/or therapy<sup>92</sup>.

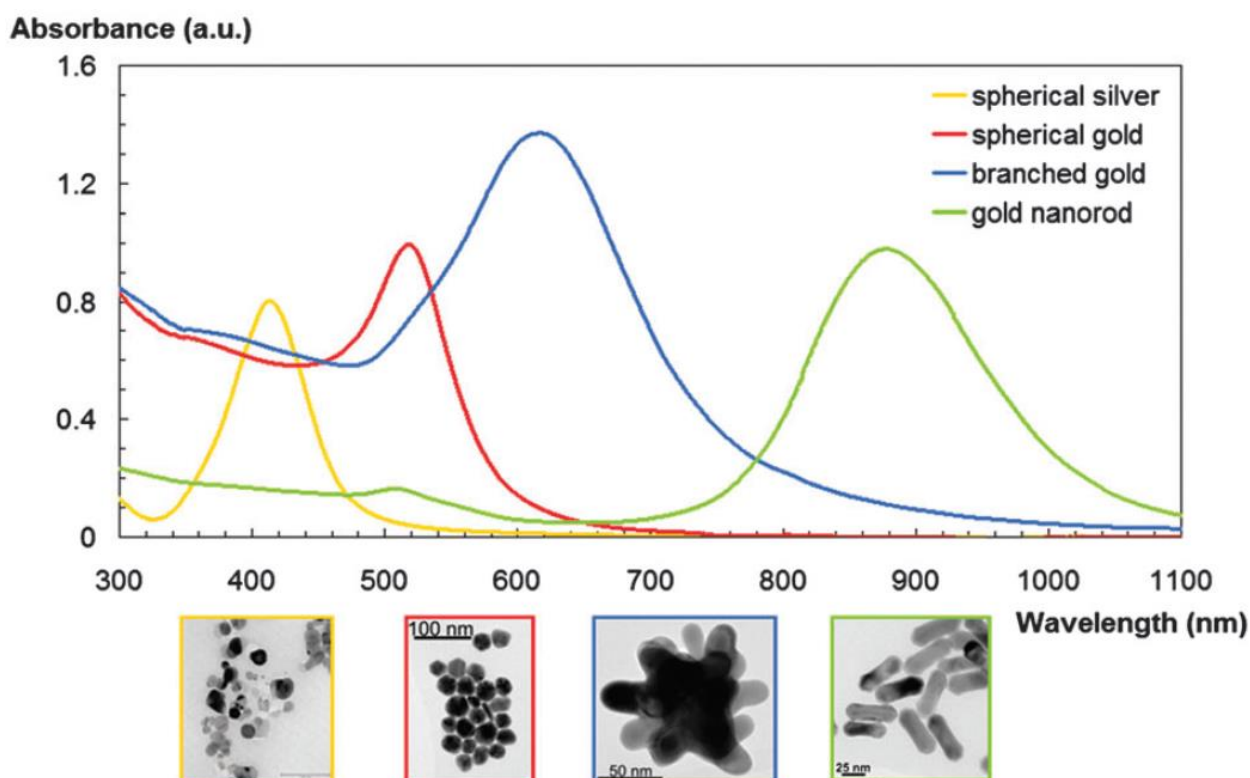


Figure 13 : Example of the plasmon resonance of metal NPs of different sizes, shapes and materials proving its dependence on all these features<sup>93</sup>.

Introducing metallic species in mesoporous titania films is particularly interesting due to their unique electronic, optical and catalytic properties. The photoresponse of TiO<sub>2</sub> in the visible and near-infrared spectral ranges is enhanced by the presence of noble metals injecting “hot electrons” in the semiconductor<sup>94</sup> and thus making them great candidates for advanced applications such as nanoelectronics<sup>95</sup> and photocatalysis<sup>71</sup>. In the scope of this manuscript, the focus is set on silver nanoparticles embedded in a titania matrix as interesting optical phenomena such as photochromism and permanent color production has been recorded. In the following part, a detailed description of the metal-semiconductor interaction which result on interesting optical effects.

### 1.3.2. Photochromic behavior of TiO<sub>2</sub>:Ag films

The photochromic behavior of a given material is defined by its reversible color transformation induced by light. Generally speaking, a chemical compound adsorbs the electromagnetic source resulting in the reversible transformation of one form (A) to another form (B) with different absorption spectra and are thermally stable under ambient conditions for a reasonable time. This phenomenon was first observed by Fritzsche in 1867 when he noticed the bleaching of an orange tetracene solution under sunlight which eventually

regained its coloration when it was kept in the dark<sup>96</sup>. This behavior was later observed in a solid material by Marckwald in 1899 when two organic compounds, anhydrous hydrochloride of benzo [c]-1,8-naphthyridine and 2,3,4,4-tetrachloro-1 (4H) -naphthalenone, became colored when exposed to light and were decolorized when kept in the dark<sup>97</sup>. Since then, organic photochromic materials have been primarily developed, more than inorganic materials, even though they present some drawbacks. Inorganic photochromic materials generally are thermally and chemically more stable than their organic counterparts. Furthermore, great efforts were put on the development of hybrid materials either being inorganic/inorganic or inorganic/organic composites in order to improve the photochromism and tune their colorations.

#### 1.3.2.1. *Photo-oxidation of silver nanoparticles*

A widely known photochromic inorganic/inorganic nanocomposite is silver nanoparticles (AgNPs) embedded in a titania (TiO<sub>2</sub>) host matrix<sup>70</sup>. The photoresponse of TiO<sub>2</sub> in the visible and near-infrared spectral ranges is enhanced by the presence of noble metals injecting “hot electrons” in the semiconductor<sup>94</sup> and thus making them great candidates for advanced applications such as nanoelectronics<sup>95</sup> and photocatalysis<sup>71</sup>. In fact, when AgNPs are in close contact with a TiO<sub>2</sub> matrix, a Schottky barrier is presented at the interface between the metal and the semiconductor<sup>98</sup>. This leads to the electron energy needed to allow electrons to leave the AgNPs to be lowered to the value of the Schottky barrier. Therefore, the excited electrons through the LSPR of the AgNPs absorb the white light and cross by injection or tunneling through the Schottky junction as presented in figure 14.a<sup>99</sup>. The injected electrons cannot escape back to the metal due to the band bending. As a result, the AgNPs are positively charged, thus unstable and consequently dissolve into Ag<sup>+</sup> ions. The possible pathways of the hot electrons are illustrated in figure 14.b as proposed by Kawahara *et al.*<sup>98</sup>. The first possibility (a) is a direct electron transfer from excited Ag to oxygen molecules in the environment. Alternatively, electrons can be transferred indirectly to the oxygen molecules via TiO<sub>2</sub> (b) or non-excited Ag (c).

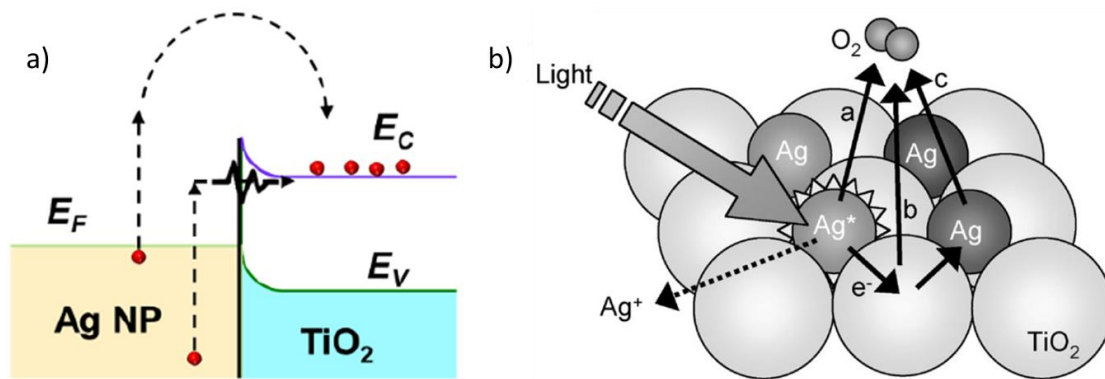


Figure 14: Schematic illustration of the Schottky junction (1) at a metallic/dielectric interface adapted from H. Ma<sup>98</sup>. The photochromic behavior of TiO<sub>2</sub>:Ag material is evidence by the absorption spectral changes (2) after every UV-Visible cycle. (wavelengths of 244 nm for the UV and 488 nm for the visible light)<sup>100</sup>.

#### 1.3.2.2. Photo-reduction

Silver ions Ag<sup>+</sup> coming from non-reduced silver content in the film or from the photo-oxidation can be converted to Ag<sup>0</sup> by a reduction process via UV irradiation<sup>59</sup>. In fact, assuming that Ag<sup>+</sup> ions are mobile enough, they can diffuse in the surrounding and recombine with electrons from the conduction band of the titania matrix (in the case when the excitation energy is superior to its band gap of 3.2 eV), or from other compounds absorbed by the film to form Ag<sup>0</sup> “monomers”<sup>101</sup>. The reduction step results in the increase of the concentration of Ag<sup>0</sup> monomers, which leads to a uniform distribution of small and monodispersed AgNPs in the titania matrix. In previous experiments, thermal diffusion was highlighted as the main initiator of NP growth driven by the following mechanisms<sup>94,102</sup>. NPs can grow by Ostwald ripening process where Ag<sup>0</sup> monomers diffuse in the material and are adsorbed at the surface of larger AgNPs. Another important mechanism is NP coalescence process where AgNPs are in contact and merge to form a single nano-object.

The different mechanisms described above are illustrated in figure 15, namely the photo-oxidation of AgNPs into Ag<sup>+</sup> ions, the reduction of Ag<sup>+</sup> to Ag<sup>0</sup> and finally both growth mechanisms, Ostwald-ripening and coalescence processes. These reactions can be controlled by the laser light and plasmon-induced temperature rise. In fact, under visible light, the excitation of the LSPR of the silver nanoparticles embedded in a titania matrix can trigger two opposite effects, either the decrease of their size due to photo-oxidation (Ag<sup>0</sup> transformed to Ag<sup>+</sup>) or their growth by in-situ heating (Ostwald-ripening and coalescence). For the latter it's been observed that strong enough irradiations in the visible range can lead to permanent

modifications of the film due to thermal effects<sup>72</sup>. The strong temperature rise induced by plasmon absorption can lead to the growth of the nanoparticles but also induce the crystallization of the surrounding TiO<sub>2</sub><sup>94</sup>. By tuning the laser processing conditions, it was demonstrated that the nanoparticle size and their self-organization can be controlled within the system resulting on interesting optical properties such as diffraction and dichroism<sup>68,102,103</sup>.

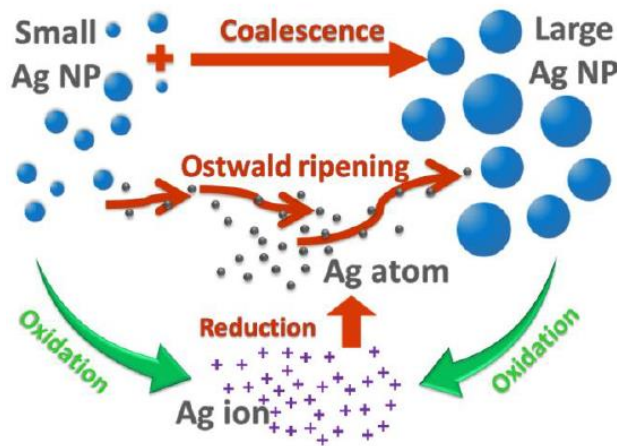


Figure 15: Illustration of the main mechanisms that control the size distribution of AgNPs embedded in a TiO<sub>2</sub> host matrix when irradiated by laser<sup>94</sup>.

Self-organization relate to the NP reshaping induced by strong laser irradiation and resulting in the formation of grating-like nanostructures containing reshaped NPs with tunable features. When the sample is illuminated by the laser, part of the electric field scattered by the initial NPs is trapped inside the film. Due to the high refractive index of the medium (titania), the film acts as waveguide, creating guided waves that interact with the incident beam and giving rise to intensity modulation and further nanoparticles growth<sup>72</sup>. An example is given in figure 16.1 where periodic nanoparticle gratings (parallel to laser polarization with  $310 \pm 5$  nm period) were formed by femtosecond laser irradiation ( $\lambda = 515$  nm) with a “low” scanning speed (LS) of  $100 \text{ mm} \cdot \text{s}^{-1}$ . Conversely, with higher scanning speeds (HS;  $1000 \text{ mm} \cdot \text{s}^{-1}$ ), laser-induced periodic surface structures (LIPSS) containing nanoparticles are formed perpendicular to the laser polarization as depicted in figure 16.2 with a period of  $490 \pm 5$  nm.

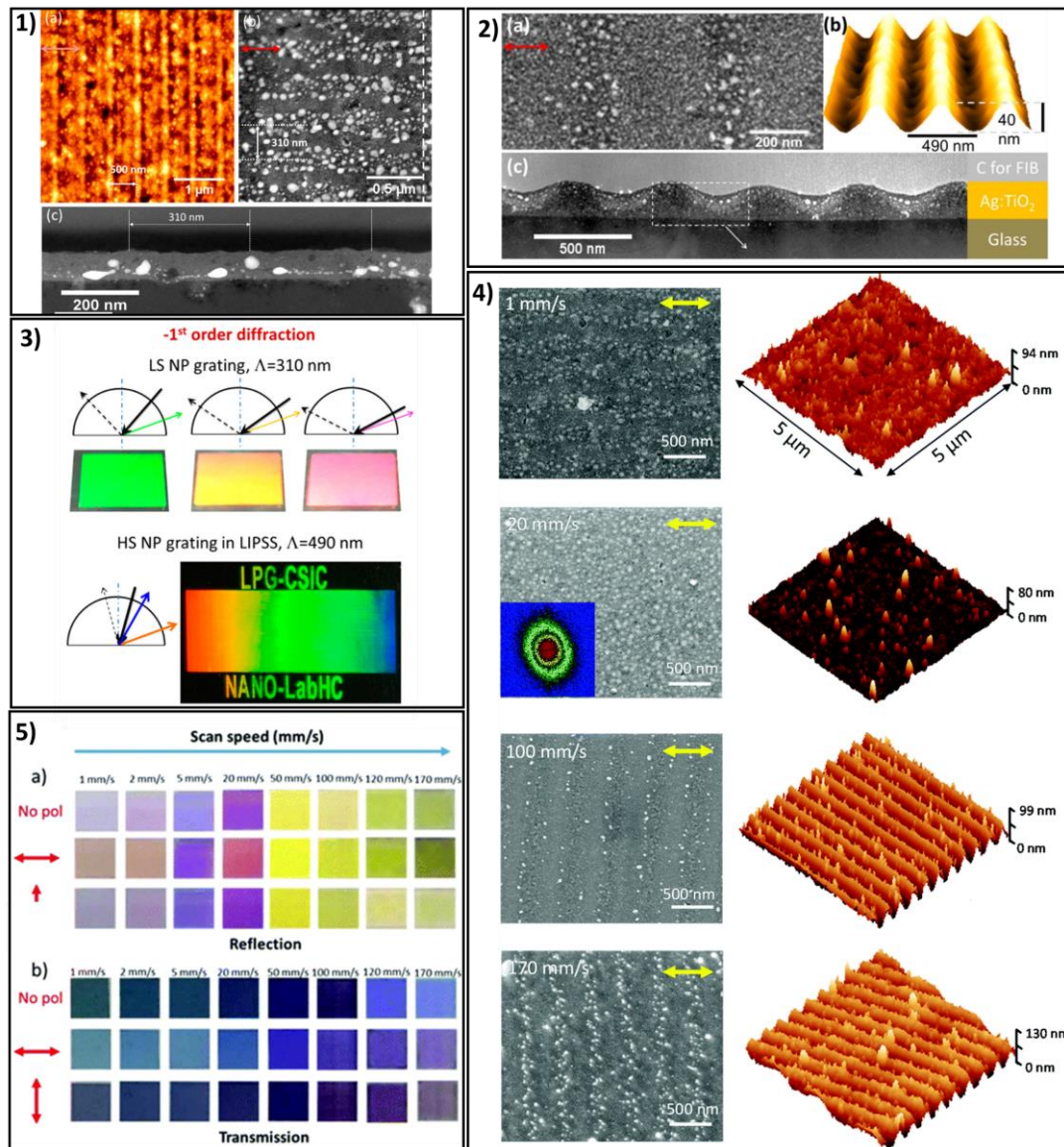


Figure 16: Nanostructures produced by fs laser processing. At “low scanning speeds”, nanoparticle periodic gratings are produced parallel to the laser polarization. The surface topography of the gratings was analyzed by AFM (a) microscopy. The top view (b) and cross section were recorded by HAADF-STEM (c) depicting structures with a period of  $310 \pm 5$  nm. On the other hand, at “high scanning” speeds (2) LIPSS with a period of  $490 \pm 5$  nm are formed perpendicular to the laser polarization as observed in the top-view (a), cross-section (c) HAADF-STEM images, and the AFM surface micrograph (b) of the sample. Such self-organized structures can diffract light under grazing angles (3), exhibiting bright colors at the  $-1^{\text{st}}$  order of diffraction<sup>102</sup>. Moreover, the evolution of the surface morphology and topography (4) of the nanocomposite structure is highlighted. Top-view SEM and AFM images were recorded of different nanostructures at different scanning speeds, namely (a)  $1 \text{ mm} \cdot \text{s}^{-1}$ , (b)  $20 \text{ mm} \cdot \text{s}^{-1}$ , (c)  $100 \text{ mm} \cdot \text{s}^{-1}$  and (d)  $170 \text{ mm} \cdot \text{s}^{-1}$ . Dichroic color changes (5) were recorded for different nanostructures on different observation conditions<sup>103</sup>. The red arrow represents the laser polarization.

Both structures exhibit strong colors in the  $-1^{\text{st}}$  back diffraction order at different incidence angles as illustrated in figure 16.3. Furthermore, in another study it was observed that varying

the laser conditions, namely the scanning speed and the laser light polarization, resulted in different configurations of nanoparticle and surface gratings as displayed in figure 16.4. They exhibit a broad range of dichroic colors as depicted in figure 16.5 due to strong local field enhancement<sup>103</sup>. The color of each nanostructure varies under unpolarized or polarized white light on either transmission or reflection observation modes.

### 1.3.2.3. *Laser-induced metasurfaces for anti-counterfeiting applications*

These metasurfaces, i.e. nanostructured photonic layers that strongly interact with light, have recently been exploited to develop optical switching devices for image multiplexing under white light. Multiplexing relates to a processing method of information or signals where separate pieces are combined and condensed in a single physical channel. In the case of image multiplexing, two or more input images are encoded in single multiplexed image. To be able to produce such an image, logical trees of colors are formed based of experimental sets of nanostructures (NS). To illustrate the concept, an example is given in figure 17.1 for the combination of two bicolor images where images A and B are displayed respectively in modes 1 and 2. Therefore,  $2 \times 2 = 4$  metasurfaces (pixels) are selected to form the color tree presented in figure 17.1.c that display the specific two-dimensional colors visualized in figure 17.1.d. In mode 1, nanostructures NS1 and NS2 display blue (■) and nanostructures NS3 and NS4 display yellow (■), while in mode 2, nanostructures NS1 and NS3 display purple (■) and nanostructures NS2 and NS4 display green (■). The resulting image is printed in a support and to observe (or demultiplex) the output images, they are revealed independently under very specific observation and illumination conditions (mode 1 or 2). An example of an experimental result is given in figure 17.2 where three unique images are encoded in a single multiplexed image. The latter is reproduced on the sample by processing a single print using a femtosecond laser. To observe or demultiplex each output image, the laser processed area is observed in different modes (1, 2 or 3) using polarizers<sup>104</sup>.

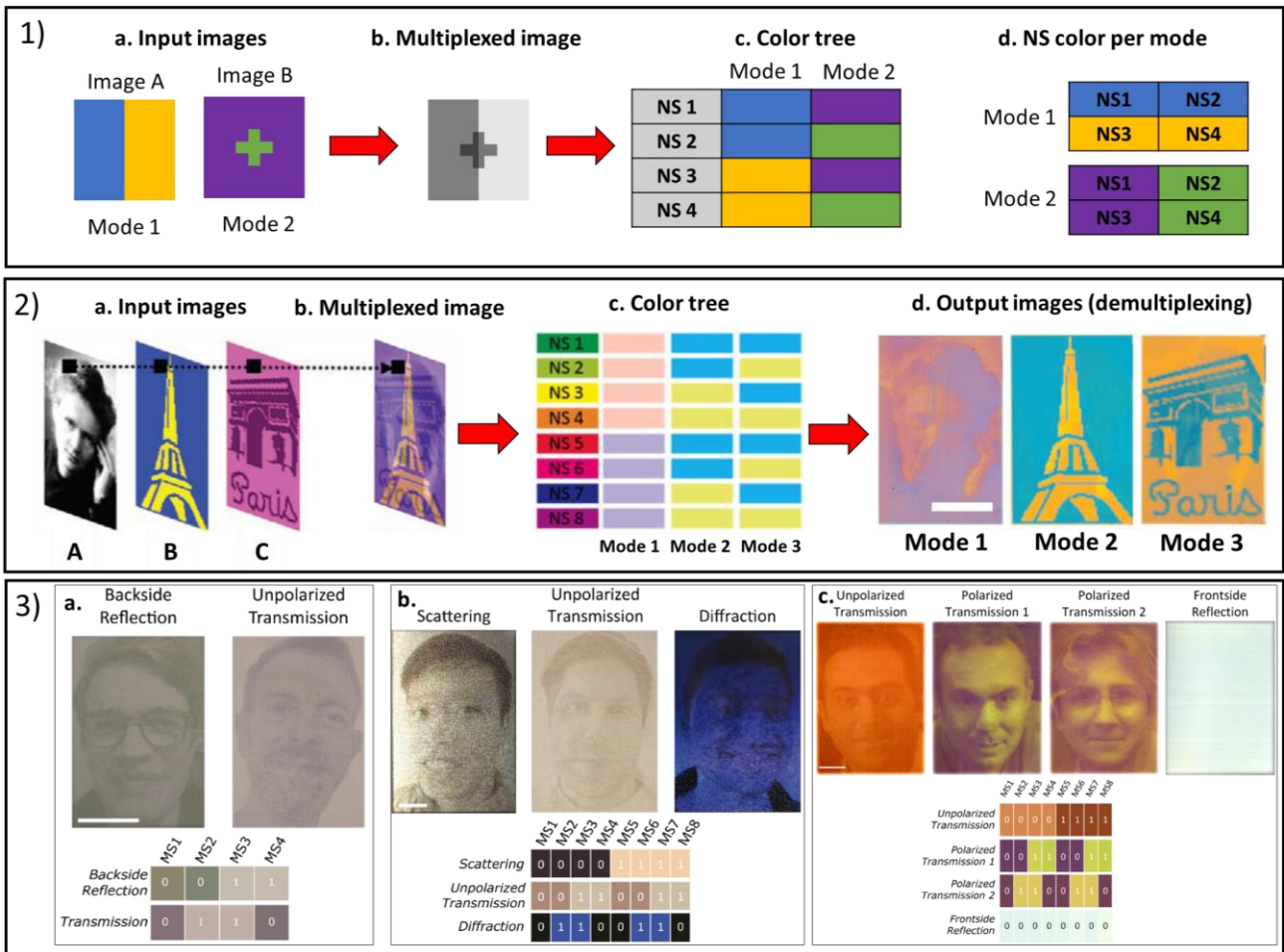


Figure 17: (1) Schematic representation of two-image multiplexing using two colors per observation mode, therefore using 4 nanostructures (NS1 to NS4). First (a) the input images (A and B) are presented for each mode with their respective colors to create a multiplexed image (b). Then, four nanostructures are selected of the database that fulfill the color tree for multiplexing (c). Each nanostructure will depict a specific color (d) on the corresponding mode. (2) This method can be implemented for three-image multiplexing by fs laser processing nanostructures on TiO<sub>2</sub>:Ag films as presented by the experimental results. (3) Furthermore, examples of (a) two, (b) three and (c) four-image multiplexing are presented on the same material but using industrial ns laser processing.

Implementing expensive and time-consuming femtosecond lasers to create the images and polarizers to observe them seem difficult to implement in industrial applications. Therefore, more recently, to produce image multiplexing a nanosecond laser was implemented that produces efficiently nanostructures with a broad range of colors detected in different observation conditions<sup>105</sup>. A color search algorithm was developed that identifies all the possible color combinations to construct logical trees that allows two (a), three (b) and four (c) image multiplexing as illustrated in figure 17.3 that are easily observable by untrained users leveraging the potential of this technology for overt security features.

#### **1.4. Conclusion**

The thesis revolves completely around laser processing a titania-based film hosting silver nanoparticles. The optical properties of these nanocomposites are particularly interesting as they can interact with light triggering different physical mechanisms and leading to permanent modifications of the material. These effects can be interesting for security applications. Therefore, it is of great interest to develop this technology on flexible supports.

To be able to produce these effects, a TiO<sub>2</sub>:Ag thin film is elaborated by sol-gel method. The host titania host matrix is deposited on a substrate followed by a stabilization process. For rigid and thermally resistant substrates such as glass, a thermal treatment at 340°C is the most efficient method to stabilize the matrix to amorphous titania and create the porosity. However, this method is not suitable for flexible supports. Recently, alternative methods were developed at low synthesis temperatures to stabilize such materials on plastic and paper that will serve as the basis for the preparation of materials in the thesis. Once the matrix has been stabilized, silver is introduced by liquid impregnation mainly in the form of ions Ag<sup>+</sup>, Ag<sup>0</sup> and small AgNPs. Mesoporous titania being a semiconductor can act as a host to grow metallic nanoparticles inside it leading to a photochromic behavior due to photo-oxidation and photo-reduction mechanisms when exposed to white and UV light respectively. Moreover, if the laser irradiation is strong enough, heat-assisted mechanisms are triggered namely Ostwald ripening and/or coalescence leading to the formation of bigger NPs. It also induces significant changes to the surrounding medium such as the crystallization of TiO<sub>2</sub>. These modifications are permanent and can lead to interesting visual effects such as color production in different illumination conditions that can be utilized to produce images. The most recent results were produced by ns pulsed laser ( $\lambda=532$  nm) where a color search algorithm was developed to automatically choose the best colors from a laser database and produce anticounterfeiting features such as image multiplexing. It relates to encoding at least two images in a single print and are observed independently on specific observation conditions as seen in figure 17.

The objective is to utilize the results and know-how presented in this chapter to develop a process to prepare the different materials on plastic substrates before laser processing. Therefore, in the next chapter the different materials and methods are presented followed by a deep characterization of the as-prepared films on flexible supports.

## **CHAPTER 2: MATERIALS AND METHODS**

In this chapter, the objective is to develop an alternative low-thermal preparation of mesoporous titania films is developed and impregnated with silver salts. Inspired by Tricot *et al.* past work<sup>69</sup>, further steps were taken to optimize the stabilization process of mesoporous titania films embedded with silver nanoparticles. Three different configurations were prepared on polycarbonate samples illustrated in figure 18:

- “**PC:TiO<sub>2</sub>:Ag**”: The first configuration relate to a mesoporous titania film is deposited on a clear PC substrate which is then impregnated with silver to form AgNPs in the host matrix.
- “**TiO<sub>2</sub>:Ag PC card**”: the second configuration relates to a PC:TiO<sub>2</sub>:Ag that is laminated to form a PC card and emulate a real document.
- “**PC:SiO<sub>2</sub>:TiO<sub>2</sub>:Ag**”: the third and last configuration relate to the introduction of a dense silica layer between the PC and the TiO<sub>2</sub>:Ag film to protect the PC substrate.

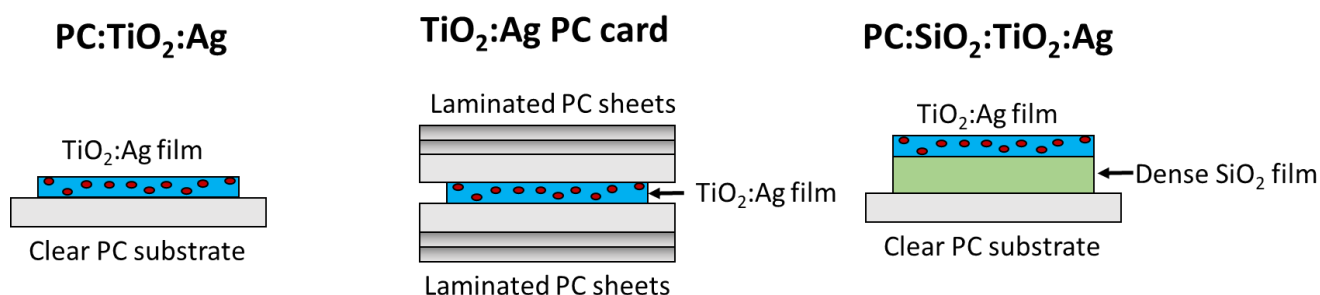


*Figure 18: Illustration of the three configurations developed in the manuscript.*

Before describing the different steps taken to prepare these materials, the characterization methods are described in the following section.

### **2.1. Material characterization methods**

Different chemical and physical characterizations are made on the different elaborated thin films presented in figure 18. In the following section, the different methods are described.

#### **2.1.1. Spectroscopy methods**

##### *2.1.1.1. Fourier-transform infrared spectroscopy*

Fourier-transform infrared spectroscopy (FTIR) is a non-destructive characterization technique to obtain an absorption spectrum of a sample in the infrared (IR) range, typically between 4000 and 400 cm<sup>-1</sup>. This technology relies on atomic vibrations of molecules that

only absorbs at specific frequencies and energies of IR irradiation. The FTIR spectrometer uses an interferometer to record the energy that is being transmitted or reflected by the sample over a broad spectrum. The resultant signal passing through the detector represents a molecular “fingerprint” of the sample with dips at frequencies that characterize the presence of specific functional groups.

FTIR were carried out with an attenuated total reflectance module (FTIR-ATR). Here the IR irradiation passes through the diamond until it reaches the diamond/sample interface where light is totally reflected at least once and creating an evanescent wave. In regions where the sample absorbs energy, this evanescent wave will be attenuated or altered. The resultant signals are passed to the detector in the spectrometer and finally to the system to generate an IR spectrum. These measurements were done with a Nicolet iS20 FTIR spectrometer from Thermo Fisher Scientific (LabHC) where the sample is placed in contact with a diamond crystal.

#### *2.1.1.2. UV-Visible spectroscopy*

UV-Visible spectroscopy relies on the absorption or reflection of ultraviolet or visible light by a material. To perform these measurements a Cary 5000 spectrophotometer from Agilent was used to measure the transmittance of the different samples at a 0° incident angle.

### **2.1.2. Microscopy methods**

#### *2.1.2.1. Optical microscopy*

The samples were observed using an BX51M microscope with a 10X/0.25 objective both from Olympus. In order to take images in transmission, the setup was equipped with a uEye camera controlled with uEye cockpit software from IDS-imaging placed at the top of the microscope following the plane of the objective. Additionally, a Marzhauser Wetzlar motorized stage is placed between the objective and the light source to move the sample.

#### *2.1.2.2. Scanning electron microscopy*

Scanning electron microscopy (SEM) is a type of electron microscopy to produce images of a sample by scanning the surface with a focused beam of electrons under vacuum. The atoms present at the surface interact with atoms resulting in various signals that reveal information about the topography or composition of the surface at the nanometric scale. Various types of

signals, depending on the detector, can be measured such as secondary electrons (SE), back scattering electrons (BSE) and x-rays or light for cathodoluminescence (CL). In this manuscript, a JSM-IT200HL electron microscope from JEOL with a helix detector is used to characterize the morphology of the materials by collecting the secondary electrons signals under low vacuum at 5kV. Working in these conditions, any damage or deterioration of the sample is avoided, especially for plastic substrates and AgNPs which are sensitive to intense energy scanning.

#### 2.1.2.3. *Transmission electron microscopy*

Transmission electron microscopy (TEM) imaging was performed by using a JEOL NeoARM 200F electron microscope in “scanning” mode (STEM) where the beam is focused at larger angle and is converged into a focal point. Chemical mapping of the samples was performed with a STEM HAADF Gatan detector.

#### Sample preparation for cross-section imaging

To observe the cross-section of the films embedded in plastic (TiO<sub>2</sub>:Ag PC card) the samples are prepared by ultramicrotomy using a LEICA EM UC7 ultramicrotome. For this a small piece of the card is cut in the shape of a tip and included in an epoxy resin. After solidification, the samples are cut in ambient conditions with the ultramicrotome. The cut section is then placed in a copper grid to be able to observe it by TEM. It is important to note that it is difficult to assess what is the top and bottom part of the film as we have residual polycarbonate on both sides.

#### 2.1.2.4. *Atomic force microscopy*

Atomic force microscopy (AFM) is a scanning microscopy used to probe the topography of the surface of a sample by measuring the movement of a cantilever with a sharp tip raster-scanning over a surface. In the manuscript, the AFM measurements are carried in tapping mode over 20µm x 20µm areas of the surface of the film using a Bruker ICON AFM controlled with Nanoscope software in ambient conditions.

### 2.1.3. Ellipsometry characterizations

#### 2.1.3.1. Ellipsometry setup

Ellipsometry is a non-destructive characterization method based on the measurement of depolarization of a light beam after being reflected by a material. It provides valuable information about the optical properties (refractive index,  $n$ , extinction coefficient,  $k$ ) and thickness ( $T$ ) of the material. Here a J.A. Woollam M200V ellipsometer is used and equipped with a source (1.2x0.3 cm<sup>2</sup> spot size at 70°) and a detector as illustrated in figure 19. The relative changes in amplitude  $\Delta$  and phase  $\psi$  of the reflected beam are measured as a function of the wavelength of the incident beam ( $\psi, \Delta = f(\lambda)$ ). To determine the contribution of  $n$ ,  $k$  and  $T$ , the experimental measurements are fitted to a model built to represent the stack (substrate + film(s)) by using the software “Wase 32” from Woollam. If the studied material is dielectric and transparent in the visible range, which is the case here, it can be modeled following a simple Cauchy dispersion model where  $n \approx A + B/\lambda^2$ .

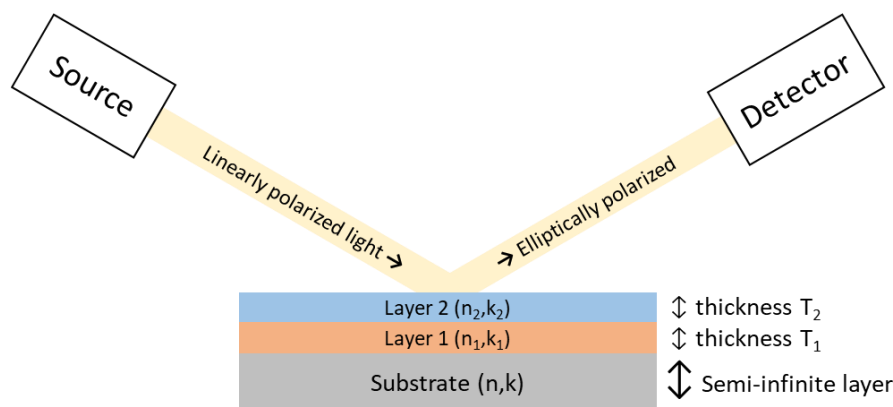


Figure 19: Schematic representation of an ellipsometer.

#### 2.1.3.2. In-situ ellipsometry

In-situ ellipsometry can provide valuable information about the evolution of optical properties ( $n$ ) and thickness ( $T$ ) of thin films in time. During aging of a material, chemical reactions occur within the system leading to changes of refractive index and thickness. In this manuscript, a thermal treatment followed by a UV exposure of the film were investigated. For this purpose, a programmable heating stage (Linkam T96-HT with temperature range 10 – 750 °C) is mounted on the ellipsometer used above to reproduce the thermal treatment. For the UV exposure, a 254 nm UV LED (4W) is mounted on the ellipsometer to irradiate the sample during measurement.

### 2.1.3.3. Environmental ellipsometric porosimetry

Changes in the properties of a material can occur due to equilibrium with the atmosphere. Solvent vapors (water, organic solvents) potentially present in the environment can thus absorb (as-prepared films) or adsorb (rigid porous films) and lead to modifications of the film thickness (shrinkage or contraction) and refractive index. In the case of mesoporous films, when the relative solvent pressure increases, adsorption and capillary condensation occur in the pores. By carefully programming the atmosphere conditions and monitoring the film evolution, it is possible to determine the percentage of porosity and the pore size. This method is named Environmental Ellipsometric Porosimetry (EEP). For this purpose, a home-made ellipsometry chamber was designed where gas (vapor containing air) is injected accordingly to the programmed relative solvent vapor pressure  $P/P_0$  (solvent pressure / saturation vapor pressure). Mass flow controllers deliver a flow of dry air ( $P/P_0 = 0$ ) mixed with a flow of air containing a solvent or water ( $P/P_0 = 1$ ) to control precisely the relative solvent vapor pressure inside the chamber. In this manuscript, isopropanol (iPrOH) was used as solvent in ambient conditions. During the adsorption, pores containing air ( $n=1$ ) are progressively filled with solvent ( $n_{iPrOH} = 1.383$ ), resulting in an increase of the overall refractive index. Once the partial pressure reaches  $P/P_0 = 1$ , desorption is carried by progressively decreasing the relative vapor pressure until the atmosphere is completely dried ( $P/P_0=0$ ). The combination of the adsorption and desorption curves depicts an isotherm of the evolution of the refractive index (here at 600nm) versus the solvent partial pressure ( $P/P_0$ ) inside the chamber that can be treated like all other volumetric methods to determine pore characteristics. To do so, the volume of solvent absorbed is calculated with the Bruggeman effective medium approximation (BEMA) model as depicted in Equation (3) for two components, with  $\tilde{\epsilon}_1$  and  $\tilde{\epsilon}_2$  the respective dielectric functions of the material and pores and  $f$  the volume fraction of each. The dielectric constant of the overall transparent composite coating, experimentally measured, is  $\tilde{\epsilon} = n^2$ <sup>106</sup>.

$$f \frac{\tilde{\epsilon}_1 - \tilde{\epsilon}}{\tilde{\epsilon}_1 + 2\tilde{\epsilon}} + (1 - f) \frac{\tilde{\epsilon}_2 - \tilde{\epsilon}}{\tilde{\epsilon}_2 + 2\tilde{\epsilon}} = 0 \quad (\text{Equation 3})$$

The porous volume of the film  $V_p$  is measured in dry atmosphere ( $P/P_0=0$ ) and  $\tilde{\epsilon}_2 = 1$ . By collecting the refractive index of the film at each solvent relative partial pressure, the adsorption-desorption isotherm  $V_{\text{adsorbed}}/V_{\text{film}}$  vs. relative vapor pressure can then be

experimentally obtained as in figure 20.a as  $V_{adsorbed}/V_{film}$  is considered to be equal to the product of the porous volume and the volumetric fractions of the solvent-saturated mesoporous film:

$$V_{adsorbed}/V_{film} = fV_P \quad (\text{Equation 4})$$

The pore size distribution is determined from the isotherm with the Kelvin equation (Equation 5) based on the curvature of the meniscus inside pores. The expression relates the partial pressure  $P/P_0$ , the surface tension  $\gamma$ , the molar volume of the liquid  $V_L$ , the contact angle  $\theta$  between the solid and the adsorbate, and  $dS/dV$  as the geometric function to express the variation of surface of the pores with the variation of their volume.

$$RT \ln \frac{P}{P_0} = \gamma V_L \cos \theta \frac{dS}{dV} \quad (\text{Equation 5})$$

It is important to note that capillary condensation does not occur directly on the pore itself but rather in the adsorbed layer, creating a cavity with a smaller radius, called the kelvin radius  $r_k$ . To implement this in the Kelvin equation, a Tolman correction is applied that considers the geometry of the pores by computing a geometrical factor,  $G$ , with values of 1 for cylindrical pores and 2 for spherical pores, and the bond length,  $\delta$ , of an isopropanol molecule set at  $2.10^{-10}$  m. This leads to the following relation<sup>106</sup>:

$$r_k = G \left( \frac{-\gamma_0 V_L \cos \theta}{RT \ln(P/P_0)} + \delta \right) \quad (\text{Equation 6})$$

From this the diameter of the pores can be determined with equation 7, considering the thickness of the adsorbed layer,  $h_{ads}$ , and the kelvin radius  $r_k$ . It is therefore possible to change  $P/P_0$  axis in dimension of the pore  $D$  and plot the derivative of the isotherm ( $dV/dD$ ) vs.  $D$ , providing the pore size distribution as presented in figure 20.b for both adsorption (blue) and desorption (red) curves. The pore size distribution is determined with the adsorption curve.

$$D = 2 (h_{ads} + r_k) \quad (\text{Equation 7})$$

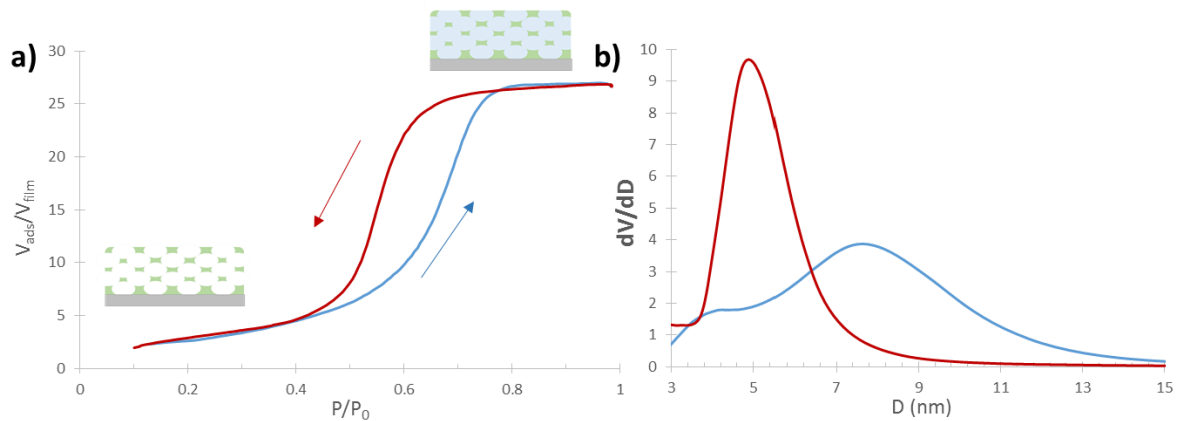


Figure 20: (a) Adsorption (blue) and desorption (red) curves as a function of the relative water vapor pressure. (b) Extraction of the pore size distribution based on (a). Taken from T. Bottein thesis<sup>24</sup>.

#### 2.1.4. Adhesion characterization

The adhesion of the prepared film was characterized by a scotch test following the technique D3359-97 of “the American Society for Testing and Materials”. A multi cross cutter from *Ericksen* (model 295) is used to perform a grid in the film. A standardized tape (Scotch 2525) is stuck at the surface of the film for 30 seconds and pulled in a fast-single motion. The region around the grid is analysed by optical microscope to determine the percentage of film removed with the tape.

The different material characterization methods have been presented that allow us to investigate the physical and chemical properties of the substrates and films that are described below.

## 2.2. Presentation of the flexible support: Polycarbonate

In this manuscript, the plastic support used is polycarbonate ( $-\text{[CO-O-pPh-C(CH}_3\text{)}_2\text{-pPh-O]}_n$ ). It is a thermoplastic that is widely used for electronic identity documents with great optical and physical properties. A full PC card is made of different PC sheets that fuse together to form a uniform and flexible solid material. It presents exceptional non-delaminable properties compared to other plastics (PVC or PET) in the security industry, meaning that all the security features that are included in the various layers are “trapped”, hence protected, in the card providing enhanced anti-counterfeiting properties. They can endure real use situations in different climatic conditions and even intense physical and chemical lab tests without diminishing its properties. The lifespan of a PC card is at least of 10 years of real use. Additionally, PC is environment-friendly as its decomposition does not release toxic waste but

mostly carbon dioxide and water when combusted. Moreover, it has excellent transparency as its light transmission percentage is around 90%, ideal for multimodal plasmonic coloring.

### 2.1.2. PC substrate preparation

100  $\mu\text{m}$  “non laserable” PC sheets with a matte finish were provided by *Exim* (product reference: JS1501T) for this project. To produce transparent and rigid substrates that are easier to manipulate, two of these 100  $\mu\text{m}$  thick PC sheets are laminated together. After lamination, 200 $\pm$ 5  $\mu\text{m}$  transparent PC sheets are cut in 4x4 cm squared PC substrates. Before any deposition both surfaces of the substrates were cleaned thoroughly. To do so they were first cleaned with soapy water by gently brushing each surface with a clean brush. Then, they were placed in a container with anhydrous ethanol for 10 minutes. The same process was repeated in deionized water and then the substrates were dried using gaseous  $\text{N}_2$ . Finally, before any deposition the surface was treated with a two-minute plasma  $\text{O}_2$  treatment to improve its adhesion properties. For this, the samples are put in a vacuum chamber attached to a Pico plasma system by *Diener Electronic*. Air is pumped out for roughly 30 seconds until it reaches a chamber pressure of 0.06 mbar. Then,  $\text{O}_2$  gas is supplied in the chamber at a flow rate of 50 sccm (standard cubic centimeter per minute) for a minute. After filling the chamber, the plasma process is performed at 50% power (100% power = maximum power) for two minutes. The remaining  $\text{O}_2$  in the chamber is flushed out for 5 seconds, the vacuum is released and the substrates can be finally removed.

### 2.2.1. PC substrate characterization

As-prepared 200  $\mu\text{m}$  PC substrates were characterized before any deposition. The FTIR-ATR spectra of the sample is depicted in figure 21 revealing the main characteristic chemical bonds of its molecular architecture (displayed inset). These are mono-bonds carbon-carbon (C-C) and carbon-hydrogen (C-H), as well as double bonds carbon=carbon (C=C), carbon=oxygen (C=O). Table 2 summarizes the vibrational bands of the different functional groups that are carbonyl, phenyl and methyl groups in accordance with literature<sup>107</sup>.

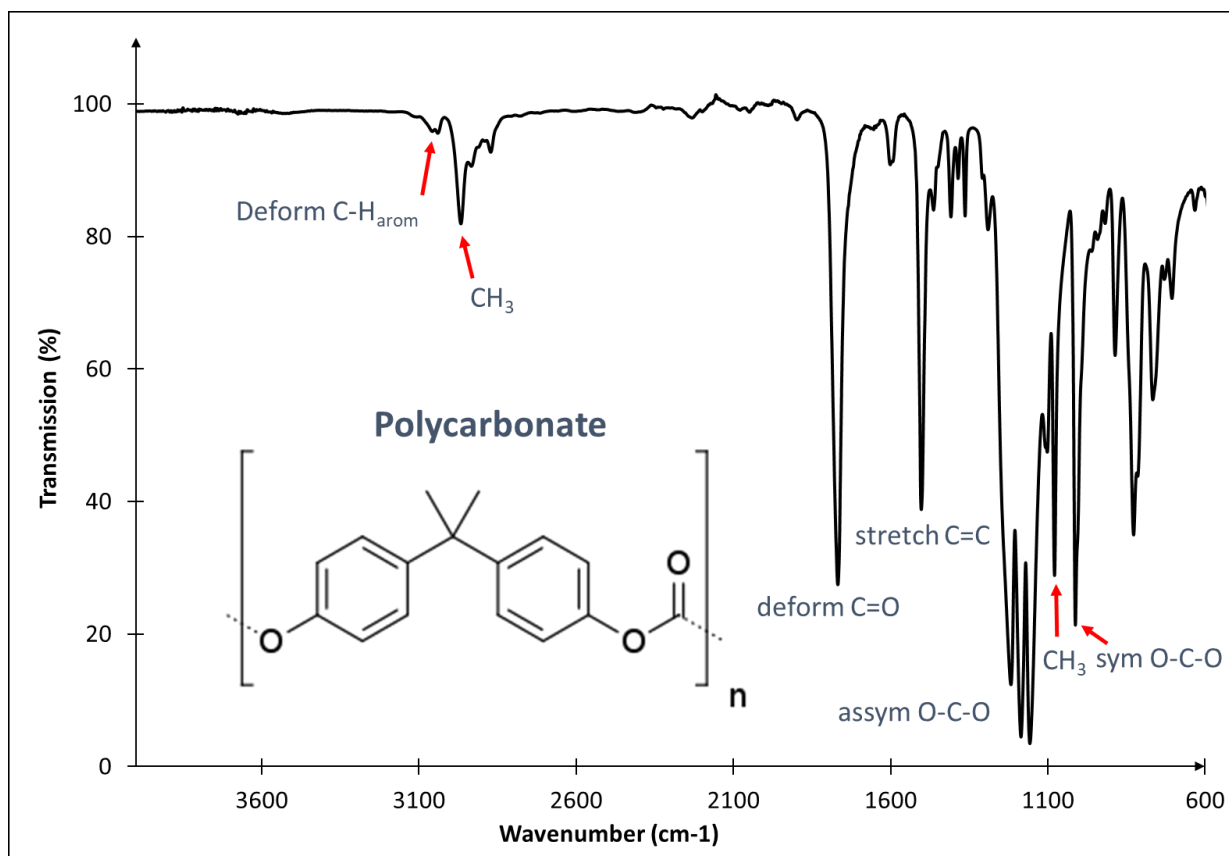


Figure 21: FTIR transmission spectra of a polycarbonate substrate. Inset the semi-developed formula of PC is displayed.

Table 2: Chemical bonds recorded by FTIR of a polycarbonate substrate.

Chemical bonds	Wavenumber (cm <sup>-1</sup> )
Aromatic C-H ring deformation	3040
CH <sub>3</sub> vibrations	2966
C=O deformation	1770
C=C stretching vibrations	1503
Assymmetric O-C-O deformations	1217-1157
CH <sub>3</sub> vibrations	1079
Symmetric O-C-O deformations	1013

PC substrates are transparent in the visible range as shown in the UV-Visible transmission spectra in figure 22 where 80% is transmitted between 350 and 800 nm. A sharp decrease near 350 nm to 0% is observed covering the UV domain until 200nm, typical of a transparent polycarbonate substrate due to the presence of aromatic parts<sup>107</sup>.

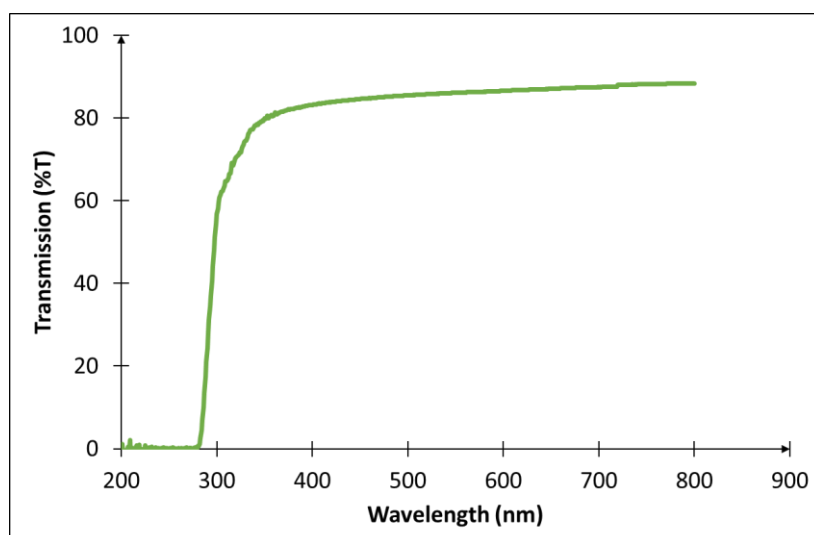


Figure 22: UV-Vis transmission (%T) spectra of a PC substrate between 200 and 800 nm wavelength.

#### 2.2.1.1. $O_2$ plasma treatment

$O_2$  plasma treatment of plastic supports is a well-known concept to improve the adherence of coating deposition<sup>108</sup>. Plasma partially ionizes oxygen into different components such as  $O^+$ ,  $O^-$ ,  $O_2^-$ ,  $O_3$ , ionized ozone, metastable  $O_2$  and free electrons. Their recombination releases energy and photons, mainly in the UV range. These UV photons bombard the surface with enough energy to break the polymer's carbon-carbon and carbon-hydrogen bonds present at the surface and increases the oxygen content, thus increasing the surface energy. Not only the surface chemistry can be altered but also the roughness of the surface. For polycarbonate in particular it was found that an  $O_2$  plasma treatment can reduce the “macroscopic” roughness of a PC surface leading to a better overall contact area between the liquid and the substrate<sup>109</sup>.

A PC substrate was investigated before and after a 2-minute oxygen plasma treatment. First, a decrease of the overall roughness of the surface was observed after treatment as depicted by the AFM micrographs in figure 23.a. This demonstrated a smoothing of the surface as the mean roughness ( $S_a$ ) is reduced by a factor of 2 going from 11.25 nm to 5.59 nm. Additionally, an improvement in hydrophilicity of the surface was evidenced in figure 23.a (bottom) where the contact angle of DI water droplets greatly decreases after the treatment. This was attributed to partial surface chemistry modifications with the formation of -OH groups<sup>109</sup> even if it was difficult to conclude with FTIR characterization in figure 23.b due to

the limit of sensibility of the technique. The influence of this treatment on film deposition is later described in part 2.4.1.

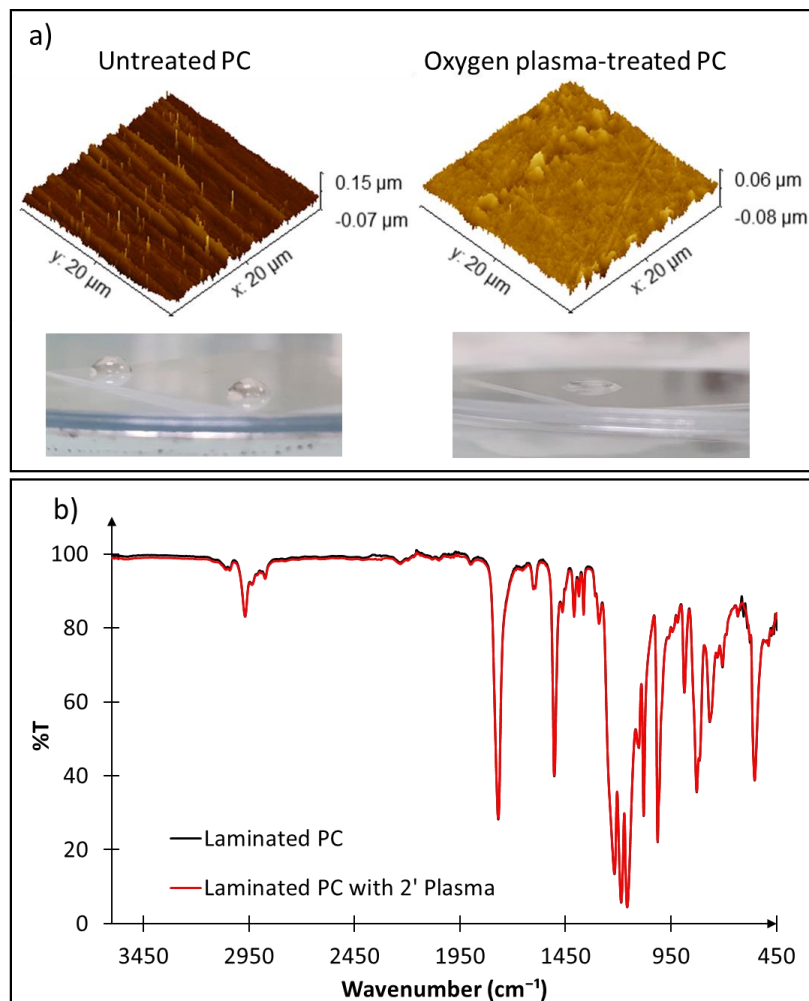


Figure 23: (a) Before and after oxygen plasma treatment, 20x20 μm 3D AFM micrographs were recorded showcasing the surface roughness modifications (upper part). In parallel, images of DI water droplets on top of the surface were taken by a phone camera demonstrating an improvement in hydrophilicity after treatment (bottom part). (b) No significant chemical changes were observed after treatment as illustrated in the FTIR-ATR spectra measurements.

#### 2.2.1.2. PC substrates vs post-deposition treatments

It is envisioned to utilize a combination of thermal and UV treatments to prepare TiO<sub>2</sub> films as developed by Nipun *et al.*<sup>68</sup>. The behavior of PC substrates to the thermal (130°C) and UV (254 nm; 50 mW.cm<sup>-2</sup>) treatment used for the elaboration of sol-gel film. PC samples were cleaned and treated separately by each process for 4 hours. The substrates were characterized by FTIR-ATR spectroscopy as depicted in figure 24 where the untreated PC

substrate is represented by the black curve, PC substrates treated separately by the thermal and UV treatments are depicted respectively in red and blue curves.

Regarding the thermal treatment no visual modifications or deformations were observed as long as the temperatures is below 130°C, otherwise they start bending/melting as the glass transition of PC is around 145°C. Additionally, the FTIR spectra in figure 24 (red curve) do not present significant chemical changes even after 4 hours of treatment at 130°C.

Conversely, after a 4-hour UV treatment the substrate presents a slight yellowish color. This is due to the photo-Fries reaction of polycarbonate under short UV radiation as energy is adsorbed by the polymer and promotes the scission of carbonate linkage<sup>110</sup>. The break of the carbonate bonds leads to the production of free radicals which are then rearranged to form primarily phenylsalicylates or hydroxybenzophenones, as well as ether derivate groups<sup>107</sup>. The photo-products formed are ortho-dihydroxybenzophenone and diphenoquinone that adsorb in the blue range thus responsible for the yellowing of the substrate<sup>111</sup>. These structure changes are revealed by the blue FTIR curve in figure 24. A slight broad band starts to appear at 3400 cm<sup>-1</sup> indicating the presence of hydroxyl groups corresponding to the rearranged species. An increase of the transmission at 1770 cm<sup>-1</sup> is sign of carbonate sites acting as initiators for the photo-Fries reaction. This is accompanied by a transmission decrease of peaks at 1592, 1615 and 1683 cm<sup>-1</sup> (carbonyl region at 1760-1550 cm<sup>-1</sup>) and are attributed to the formed photoproducts containing substituted phenols, aromatic esters, aromatic aldehydes, carboxylic acids<sup>111</sup>.

In summary, the FTIR spectra supports that the PC substrate can withstand long thermal treatments as long as the temperature does not exceed 130°C. On the other hand, long UV irradiation ( $\approx$  4 hours) can lead to photo-Fries reaction of the polymer's surface as evidenced in the structural changes depicted in the FTIR spectra. This is observed a very slight yellowing of the substrate's color, consequently diminishing the transparency of the sample and potentially its mechanical properties. Regarding the sample preparation it is then envisioned to not exceed these constraints, mainly for the UV exposure (less than 4 hours), to not deteriorate the substrates and only affect the film. The methods of sol-gel film preparation are described in the following section.

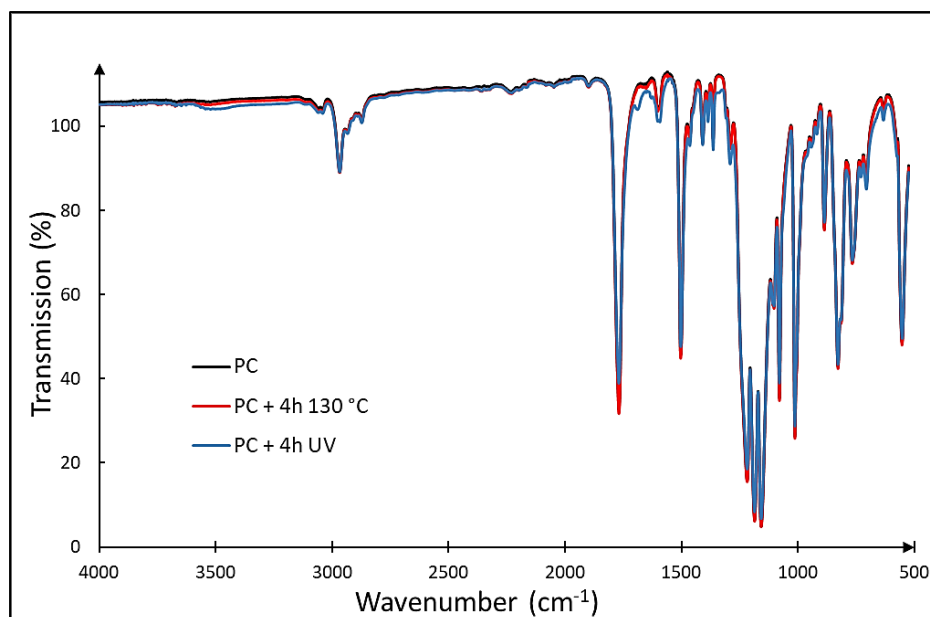


Figure 24: FTIR-ATR spectral measurements of a PC substrate (black curve) treated 4 hours at 130 °C (red curve) and 4 hours exposed to UV light (254nm; blue curve).

### 2.3. Sol synthesis and preparation of PC:TiO<sub>2</sub>:Ag films

The preparation of TiO<sub>2</sub>:Ag films is described in this part. First, the titania matrix is elaborated by sol-gel method and followed by liquid impregnation of silver salts. Below, the chemicals and methods are detailed.

#### 2.3.1. Chemicals

The titania sol synthesis is inspired by previous works on the preparation of mesoporous films on plastic supports<sup>68</sup>. It follows a typical formulation but with the addition of acetylacetone (AcAc) to complex the inorganic titania precursors and form either titania mono-adducts or bis-adducts as depicted in figure 25. This moderates the hydrolysis and condensation of inorganic species, preserving the TiO<sub>2</sub> nanocrystal size to a minimum as it was observed that without complexants, large nanocrystals are formed. This could lead to light scattering making the material unsuitable for optical applications. Additionally, AcAc molecules can be photodegraded by UV exposure at 254 nm leading to a controlled polymerization of the amorphous titania matrix without needing high thermal treatments<sup>112</sup>.

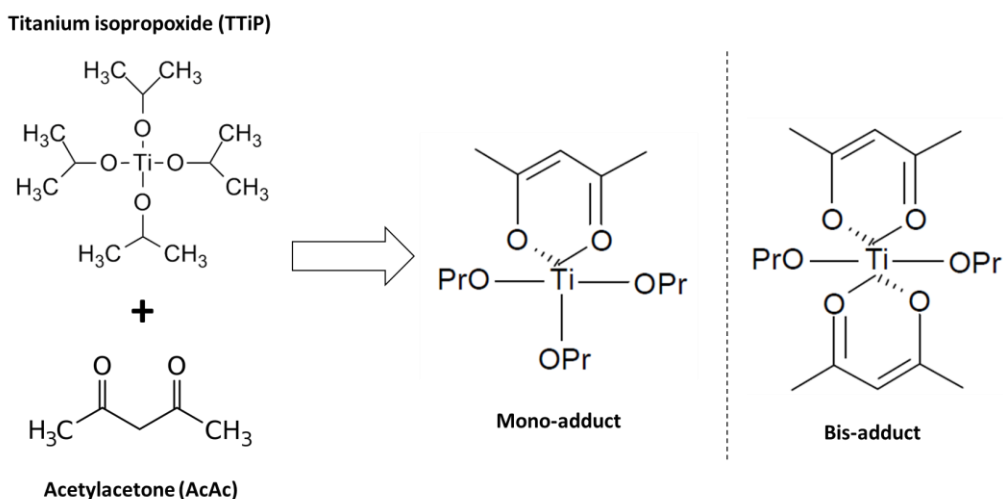


*Figure 25: Illustration of the reaction of metallic precursors, titanium isopropoxide (TTiP), mixed with complexing agent acetylacetonone (AcAc) resulting in the formation of titania mono-adducts and bis-adducts.*

The chemicals involved in this synthesis are titanium tetraisopropoxide (TTiP; 97%), acetylacetonone (AcAc, 99%), poly(ethylene oxide)-poly(propylene oxide)-poly(ethylene oxide) block copolymer (Pluronic P123, molecular weight: 5800 g.mol<sup>-1</sup>), all purchased from Merck Group, hydrochloric acid (HCl; 37%) and absolute anhydrous ethanol (EtOH) bought respectively from Carl Roth and Carlos Elba. Deionized water (DI water) is also involved in the sol synthesis. The sol was prepared in a clean room (class 100, RH%= 50±5 %; temperature= 22±2 °C) to maintain reproducibility of the synthesis.

### 2.3.2. TiO<sub>2</sub> sol preparation

TiO<sub>2</sub> films were prepared by sol-gel process using titanium tetraisopropoxide (TTiP) as the titania precursor, AcAc as a stabilizing agent, absolute ethanol (EtOH) as the main solvent, block copolymer P123 as the templating agent, hydrochloric acid (HCl) as the acidifying agent and deionized water (DI water) to promote the hydrolysis. The molar ratio of each chemical is set to: TTiP:P123:EtOH:HCl:H<sub>2</sub>O:AcAc :: 1:0.025:72:0.015:29.97:0.5. In a 100 mL round flask (1), 2.55g of P123 were dissolved in EtOH (23.08g) under stirring for 15 minutes before adding two drops of HCl (37%; 0.028g) and stirred for 30 more minutes. In another 100 mL round flask (2), 5g of TTiP are mixed with 0.88g AcAc under stirring for 15 minutes. Once the mixtures are ready, the content of flask (2) is added dropwise to flask (1) while stirring and followed by the addition of 9.5 g of DI water. The solution was then stirred for 7 hours and a transparent yellow solution is obtained. A final 35.5g of EtOH was added to the solution to dilute it by a 1:1 factor in volume.

### 2.3.3. Mesoporous TiO<sub>2</sub> thin film preparation

The sol described above is deposited in ambient conditions (22°C; 36%RH) on the PC substrate using a syringe equipped with a filter to remove impurities (25mm Acrodisc syringe filter with 0.2 µm PVDF from Sigma Aldrich). The deposited solution is spin coated at a turning speed of 2000 rounds per minute (RPM) for 60 seconds (acceleration of 500 RPM) using a Laurell “WS400A 6TFM/LITE” spin-coater placed under the hood. After this process, the opposite side of the coated surfaces was thoroughly cleaned with a clean room pad soaked in EtOH to remove sol excess. The samples were then placed in a stove (Mettler-100) with a controlled temperature of 130°C for 2 hours. This was followed by a 2-hour UV exposure at 254nm using a 15W lamp (intensity of roughly 25 mW.cm<sup>-2</sup>) from Vilber (CN-15.CC UV darkroom). The films were then washed with absolute ethanol for 2 minutes and finally heated for an hour at 120°C to remove any remaining organic parts and solvent from the film. A 95±5 nm mesoporous titania film is obtained and named “PC:TiO<sub>2</sub>”.

### 2.3.4. Impregnation with ammoniacal silver solution

After stabilization of the mesoporous films, their porosity was filled with silver nanoparticles as described elsewhere<sup>59</sup>. For this, an ammoniacal silver nitrate solution [Ag(NH<sub>3</sub>)<sub>2</sub>]<sup>+</sup>NO<sub>3</sub><sup>-</sup> (1.5M) was prepared by adding silver nitrate (AgNO<sub>3</sub>) in an equivalent 1:1 molar ratio solution of EtOH and deionized water and stirred for 5 mins. Ammonia (NH<sub>3</sub>) was then added until the initially brown solution turned transparent (≈12 g of 5N NH<sub>4</sub>OH solution). Just before soaking, the samples were dried in a stove at 130°C to remove any VOCs (volatile organic compounds) or humidity present in the pores. After one hour of drying, they were rapidly placed in a Petri dish and soaked in the silver nitrate solution in the dark. After one hour of soaking, they were rinsed with DI water to remove silver excess on the surface and dried with nitrogen gas. The resulting films were transparent and colorless at this stage and contained mainly silver ions (Ag<sup>+</sup>). The formation of silver NPs was induced photocatalytically under UV exposure. The samples were exposed to a 254 nm UV light (50 mW.cm<sup>-2</sup>) for 1 hour and a brownish color was obtained due to AgNPs growth. For reference, these samples are called “PC:TiO<sub>2</sub>:Ag” samples. They contain a blend of Ag<sup>+</sup> ions, Ag<sup>0</sup> atoms and Ag NPs whose size is comprised between 10 and 40 nm.

## 2.4. PC:TiO<sub>2</sub>:Ag film characterization

### 2.4.1. Influence of the O<sub>2</sub> plasma substrate treatment on the film deposition

As previously presented an oxygen plasma treatment was performed on PC substrates in order to improve the adherence of sol-gel films. To support this mesoporous TiO<sub>2</sub> films were prepared (as described in part 2.3.3) on untreated and treated PC substrates, and characterized in transmission by optical microscopy. As observed in figure 26.a the film presents heavy cracking and delamination, contrary to what is observed in figure 26.b where a crack-free film is obtained when pretreating the PC with a fast O<sub>2</sub> plasma treatment. The adhesion of the film was evaluated by the scotch test described in part 2.1.4, presenting good adherence

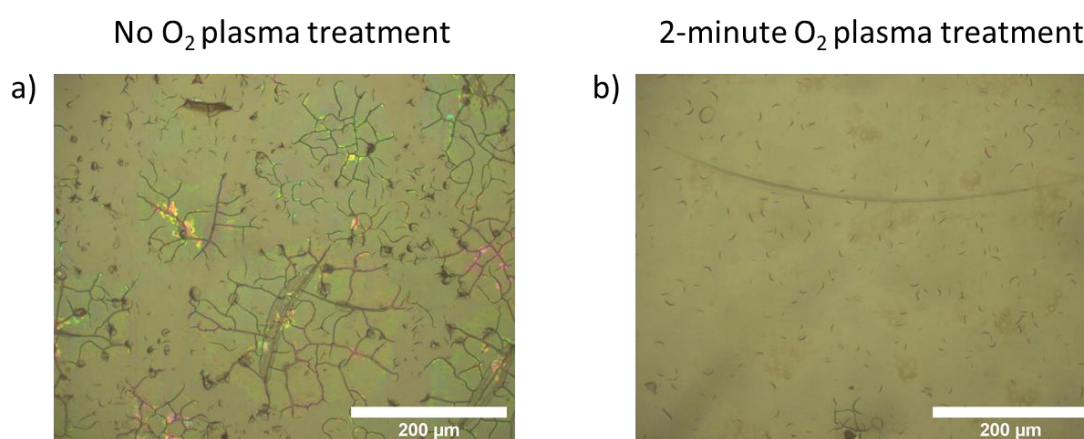


Figure 26: Optical microscope images of the surface of a PC:TiO<sub>2</sub> substrate untreated (a) and treated with an oxygen-plasma treatment for 2 minutes (b).

### 2.4.2. Characterization during/after the stabilization process

The preparation of mesoporous TiO<sub>2</sub> films on PC substrates can be divided into two key steps after formulation of the sol: the deposition, ensuring the homogeneity of the film, and the post-deposition treatments, consolidating the inorganic matrix while simultaneously emptying the porosity. In this manuscript three post-deposition treatments are performed: a thermal treatment at 130°C for 2 hours for solvent evaporation, followed by a 2-hour 254 nm UV treatment that breaks “Ti-Acac” complexes and a chemical extraction with EtOH to remove any residual organic parts. The performance of each step is investigated.

#### 2.4.2.1. FTIR-ATR spectral characterization

During the film preparation, FTIR-ATR spectral measurements can reveal information, in theory, about three different chemical changes: (1) the consolidation of the inorganic titania

matrix, (2) the elimination of the stabilizing agent AcAc and lastly (3) the elimination of the templating agent, P123, and thus creating the porosity. Unfortunately, PC presents a large number of vibrational bands that overwhelm the different vibrational bands, thus limiting the extraction of accurate information as depicted in the FTIR spectra in Annex 1. The only vibrational band not present in the PC FTIR spectrum is for methylene groups (-CH<sub>2</sub>) of the block co-polymer P123 and acetylacetone around at 2870 cm<sup>-1</sup>. Therefore, the focus is set in the measurements in the 3800-2500 cm<sup>-1</sup> range depicted in figure 27.

The apparition of a broad band at 3400 cm<sup>-1</sup> is attributed to stretching vibrations of water and -(OH) groups<sup>113</sup>. Another peak is noted at 2868 cm<sup>-1</sup> for the symmetric stretching of (-CH<sub>2</sub>) groups<sup>113</sup> related to the presence of AcAc and P123 compounds after the thermal treatment. This is logical as the thermal treatment reaches only a temperature of 130°C and P123<sup>114</sup> and AcAc<sup>115</sup> start decomposing at 150 °C and higher. However, this band is significantly reduced after the UV<sub>254</sub> treatment, which is a sign of photocatalytic elimination of P123 by the titania film. Furthermore, the remaining organic parts are washed by ethanol followed by a final drying step. This suggests that the surfactant is eliminated leading to the formation of pores are formed in the material. To verify this hypothesis, ellipsometric characterizations were performed.

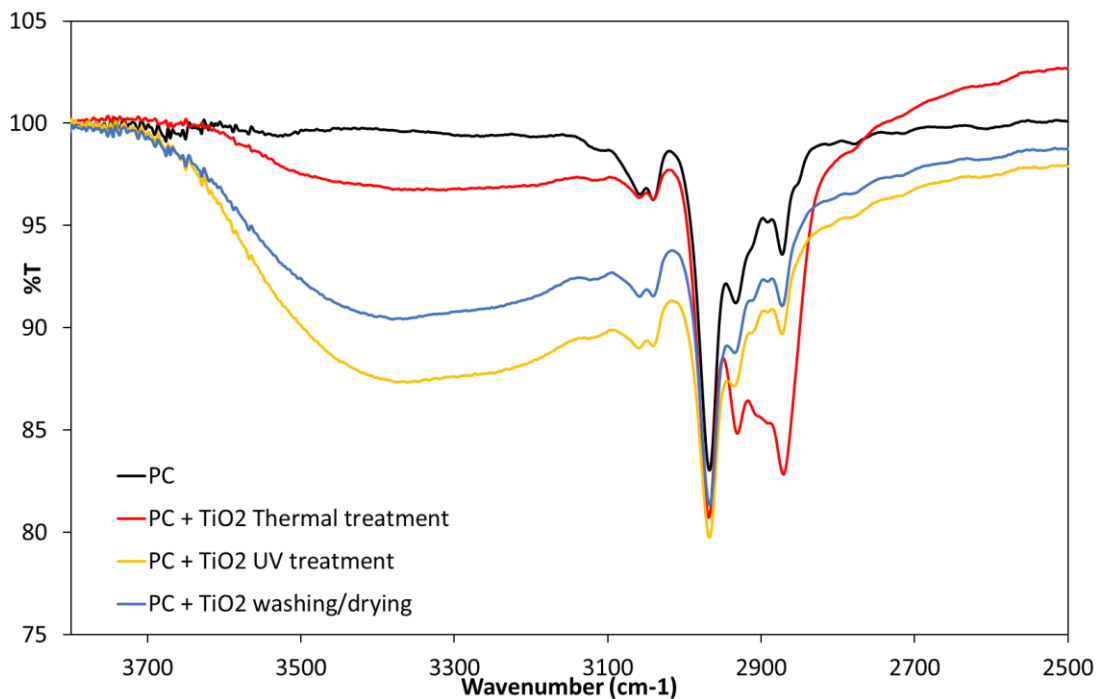


Figure 27: FTIR-ATR spectra measurements of the evolution of a TiO<sub>2</sub> film over the course of the stabilization process. The thermal, UV and washing steps are illustrated by the red, blue and yellow curves respectively. The black curve is related to a virgin PC substrate.

#### 2.4.2.2. *Environmental ellipsometry characterization*

During the post-deposition treatments, the refractive index and thickness of a layer vary over time due to chemical reactions taking place within the system. Here these modifications were followed by in-situ environmental ellipsometry (in-situ EE) of the TiO<sub>2</sub> film during the thermal and UV treatment as previous FTIR-ATR measurements (figure 27) suggest a significant change in chemical composition. To avoid measurement aberrations due to the anisotropy of polycarbonate substrates, the characterization was carried on silicon wafers. Before coating, the silicon wafers were thoroughly cleaned with acetone, water and ethanol. The TiO<sub>2</sub> sol is deposited in ambient conditions by dip-coating using an ACE-dip from Solgelway with a pulling speed of 5 mm.s<sup>-1</sup> to adjust the final thickness to 95±5 nm. After deposition, the sample is quickly placed in the thermal chamber mounted on the ellipsometer and heated at 130°C (120 °C/min ramp) for 2 hours. The evolution of the refractive index (n) at 600 nm wavelength and thickness (T) are recorded every 10 seconds of the treatment as presented in figure 28. The interpretation of the ellipsometry data variation for mesostructured films can be fairly complex as different chemical mechanisms can take place. For instance, three regimes are depicted: film before (0), during (1) and after (2) treatment. During the annealing (1), the refractive index starts to increase progressively accompanied with a progressive decrease of the thickness, sign of film densification. This is attributed to dehydration of the inorganic matrix (ethanol, water) and thus densification of the film<sup>44</sup>. After the end of the treatment (2), the refractive index increases significantly going from 1.536 to 1.581 and the thickness decreases from 251±5 to 240±5 nm. This is due to relaxation of the film from its thermal expansion, resulting in the contraction of the material.

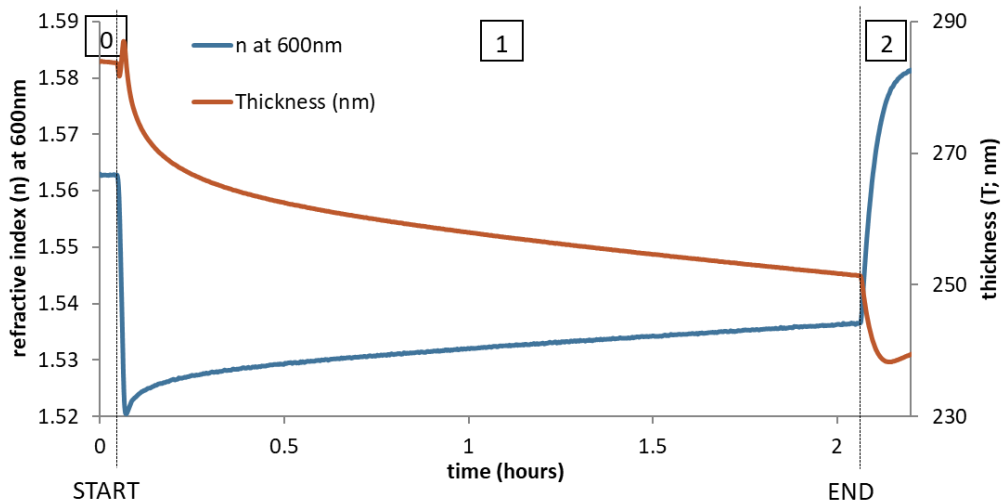


Figure 28: In-situ ellipsometric behavior of a xerogel  $\text{TiO}_2$  film on Si wafer during a 2-hour thermal treatment at  $130^\circ\text{C}$ . The refractive index ( $n$  at 600 nm; blue curve) and the thickness ( $T$ ; red curve) of the film are presented as a function of time.

The sample was then exposed to a UV treatment for several hours as the power of the lamp mounted in the ellipsometer is significantly lower than the one described in part 3.2 (4W vs 15 W). The in-situ EE measurements were performed every 10 seconds of treatment and are depicted in figure 29 where three regimes are presented. During the first hour of treatment (1), the film is greatly densified as the refractive index of the film increases (1.607 to 1.690) and the thickness ( $T$ ) decreases considerably (234 to 115 nm). After roughly 100 minutes of treatment (2), the refractive index drops considerably alongside a partial decrease of the thickness of the film. This is attributed to the templating agent ( $n > 1$ ) being eliminated from the film, forming pores which are filled with air ( $n = 1$ ). Consequently, the overall refractive index of the system drops while the thickness slowly decreases. Lastly, after 5 hours of UV exposure (3) the film is stable as no significant changes were observed where  $n = 1.515 \pm 0.1$  and  $T = 103 \pm 5$  nm.

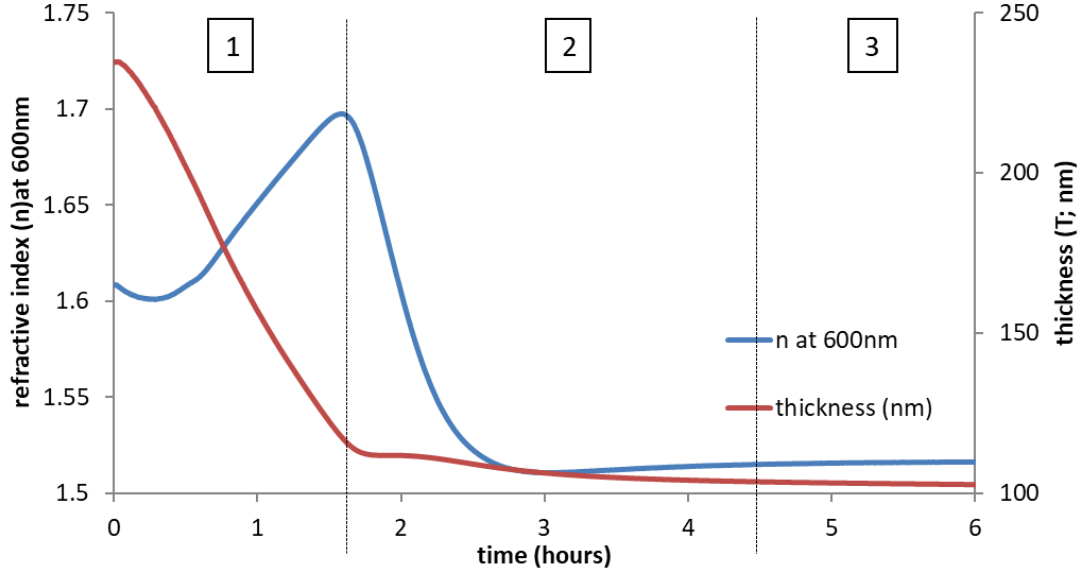


Figure 29: In-situ ellipsometric behavior of a xerogel  $\text{TiO}_2$  film on Si wafer during a 6-hour 254 nm UV treatment. The refractive index ( $n$  at 600 nm; blue curve) and the thickness ( $T$ ; red curve) of the film are presented as a function of time.

The final step was EtOH washing and drying of the film for an hour at  $130^\circ\text{C}$  to dry and remove the remaining organic parts and characterized ex-situ by environmental ellipsometry (ex-situ EE). The sample was placed in the chamber for 5 minutes in dried conditions ( $P/P_0=0$ ) to remove potential adsorbed VOC and its properties were determined as  $n_1(@600\text{nm}) = 1.546$  and  $T = 91.91$  nm, sign of a densification of the film. The same measurement in a solvent-saturated environment was carried ( $P/P_0= 1$ ) with iPrOH resulting in an increase of the refractive index to  $n_2 = 1.726$  and a constant thickness of 92.2 nm, confirming the presence of pores where air ( $n_{\text{air}}=1$ ) is replaced by iPrOH ( $n_{\text{iPrOH}} = 1.383$ ) and consequently increasing the overall refractive index of the film from ( $n_1$ ) 1.546 to ( $n_2$ ) 1.726 without altering its thickness ( $\approx 92$  nm). From these results, the porosity ( $f_p$ ) can be estimated to 40%v if the following equations are considered:

$$n_1 = n_{\text{air}}f_p + n_{\text{TiO}_2}(1 - f_p) \quad (\text{Equation 8})$$

and

$$n_2 = n_{\text{iPrOH}}f_p + n_{\text{TiO}_2}(1 - f_p) \quad (\text{Equation 9})$$

results in

$$f_p = \frac{n_1 + n_2}{n_{\text{air}} - n_{\text{iPrOH}}} \quad (\text{Equation 10})$$

Conclusively, in-situ EE measurements reveals that the thermal treatment induces primarily the evaporation of excess of ethanol and water, subsequently densifying the film. This densification process is carried on by the UV treatment until the templating agent is being progressively eliminated and the porosity is created illustrated by a drop of the refractive index of the film and a partial stabilization of the thickness in the in-situ EE results. Ex-situ EE measurements carried after the last treatment, washing and drying, confirms the presence of pores in the material as suggested by the previous FTIR-ATR spectral study showing the elimination of the templating agent. Figure 30 summarizes the evolution of the refractive index (@600nm) and thickness after each post-deposition treatment. The porosity represents 40% of the volume of the film.

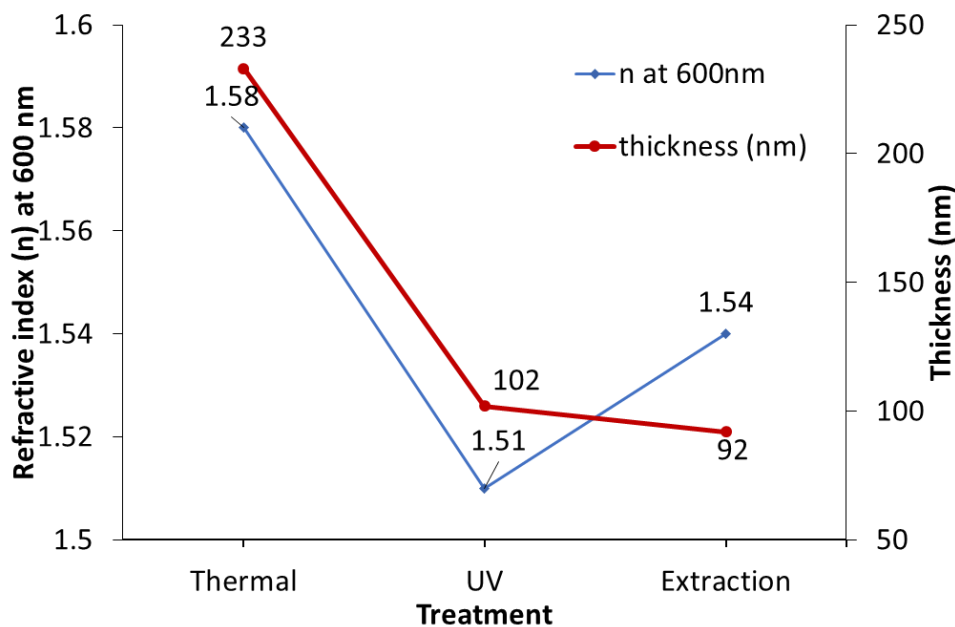


Figure 30: Summary of the ex-situ ellipsometric behavior after each stabilization step. The refractive index ( $n$  at 600 nm; blue curve) and the thickness ( $T$ ; red curve) of the film are presented after each step.

#### 2.4.2.3. Environmental ellipsometric porosimetry

Environmental ellipsometric porosimetry (EEP) measurements were carried on a stabilized  $\text{TiO}_2$  film on Si wafer to extract information about the porosity of the film. The refractive index and thickness of the film are recorded every 60 seconds as the solvent ( $i\text{PrOH}$ ;  $n_{i\text{PrOH}} = 1.383$ ) partial pressure is varied in the chamber at ambient temperature. The adsorption curve is measured from  $P/P_0 = 0$  to 1 with an increment of 0.033 succeeded by the recording of the desorption from  $P/P_0 = 1$  to 0. The resultant adsorption-desorption isotherms of  $n$ ,  $T$ , and  $V_{\text{ads}}/V_{\text{film}}$  as a function of  $P/P_0$  are depicted in figure 31.a, b and c respectively. Adsorption

starts at low adsorbate pressure ( $P/P_0 \leq 0.4$ ) attributed to the presence of a small amount of micropores in the film followed by a marked step around  $P/P_0 \approx 0.6$ , typical of capillary condensation of mesopores filling with solvent (type IV isotherm). The desorption course leads to a hysteresis loop of type H2 with two diagonal sloping branches. In parallel, in figure 31.c, the thickness of the film suddenly drops around  $P/P_0 \approx 0.6-0.7$ , attributed to capillary stress during the desorption course. At low adsorbate pressure until the end of the desorption, the film regains its original thickness suggesting a relaxation of the material, evidence of structural elasticity. However, the refractive index at the end of the desorption in figure 31.a is slightly higher (1.580) than the original refractive index (1.561) implying that the desorption is not fully completed since despite a relative long waiting time between each point, the equilibrium has not been reached.

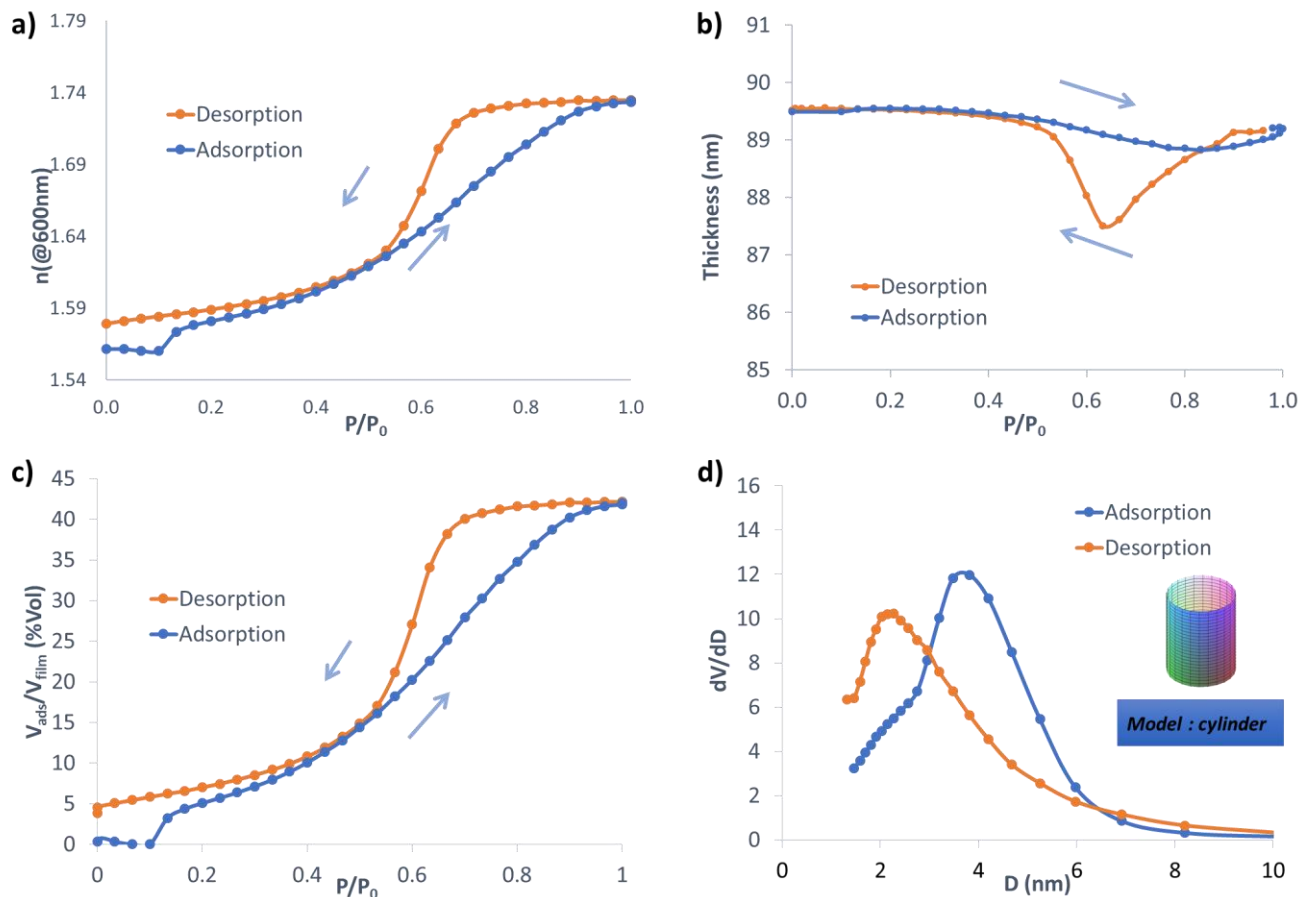


Figure 31: Adsorption-desorption isotherm of a stabilized mesoporous  $\text{TiO}_2$  film of  $n$  (a),  $T$  (b) and  $V_{\text{ads}}/V_{\text{film}}$  (c) as a function of the vapor solvent pressure ( $P/P_0$ ). The pore size distribution (d) is determined for a contact angle of  $10^\circ$  and by considering the pore shape as cylindrical as illustrated inset.

The porosity volume  $f_p$  was determined, in dry atmosphere, at 42%vol. The pore size distribution is calculated with the method described in part 2.2.3.3 or a contact angle of  $10^\circ$

and considering the pore shape as cylindrical. It was determined to 3-4 nm as presented in figure 31.d. This is in good agreement with the estimation made previously with the EE In-situ measurements with a porosity of 40%vol. Furthermore, it is in agreement for the formation of silver nanoparticles in an inorganic titania matrix for their optical properties utilized in the literature<sup>59,62,70,94,100</sup>.

The sequence of treatment applied to the film leads to a fairly good mechanical stability since the film is mesoporous and remain so even after deformation induce by the capillary stress. Moreover, the film is well adapted for optical applications as the surface is fairly smooth. Therefore, it is thus ready for silver infiltration in liquid phase.

### 2.4.3. Characterization after impregnation

#### 2.4.3.1. *Optical characterization*

Once the mesoporous titania film is prepared, silver is introduced in the matrix by liquid impregnation. The detailed process is given in part 2.3.4. In summary, dried TiO<sub>2</sub> films are soaked in an ammoniacal silver solution ( $[\text{Ag}(\text{NH}_3)_2]^+$ ) for an hour, washed with water and dried. Silver ions ( $\text{Ag}^+$ ) are then reduced into  $\text{Ag}^0$ , forming silver nanoparticles (AgNPs) by optical reduction. The optical evolution of the film is characterized by UV-Vis spectroscopy in the visible range (350-750 nm) as presented in figure 32.a. After impregnation (green curve), silver is primarily in its ionic form but the overall transmission of the sample decreases due the presence of a limited number of nanoparticles absorbing in the visible range. After reduction (blue curve), the transmission drops considerably due to the formation of a large variety of AgNPs. The sample obtained has a brownish color as illustrated in figure 32.b, typical of a TiO<sub>2</sub> film with embedded silver nanoparticles.

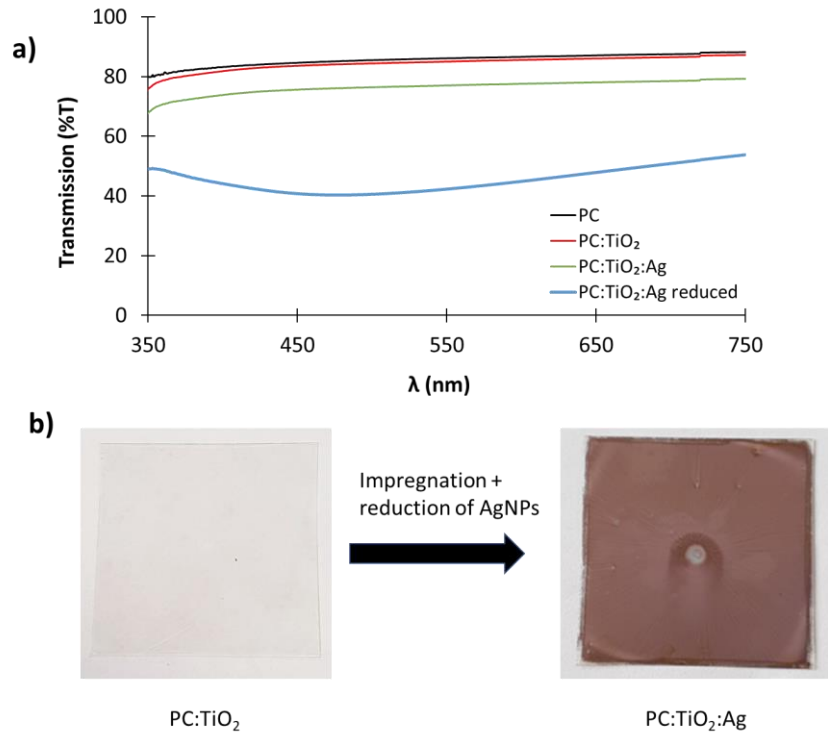


Figure 32: UV-Visible transmission spectrum (a) of a virgin PC substrate (black), a mesoporous TiO<sub>2</sub> film on PC (red) which was then impregnated with silver ions (green) and reduced by UV exposure (blue). The PC:TiO<sub>2</sub> sample is initially transparent (b) and gains a brownish color after the impregnation of silver salts and their reduction to silver nanoparticles.

#### 2.4.3.2. Surface characterization

The surface of TiO<sub>2</sub> films before (PC:TiO<sub>2</sub>) and after silver impregnation (PC:TiO<sub>2</sub>:Ag) was characterized by AFM method presented in figure 33.a and b respectively. A 10x10 $\mu$ m area of each film was scanned to plot the 3D micrograph showcasing elevation variations in the range of tens of nanometers. The mean roughness  $S_a$  was determined to 4.1 nm for PC:TiO<sub>2</sub> and 4.9 nm for PC:TiO<sub>2</sub>:Ag, similarly observed for the PC substrate alone ( $S_a$ = 5.6 nm).

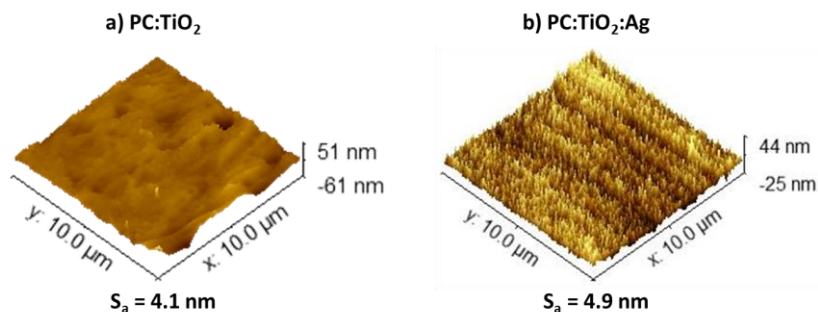


Figure 33: 3D AFM 10 $\mu$ m x 10 $\mu$ m micrographs of the surface of (a) a stabilized TiO<sub>2</sub> film deposited on polycarbonate and (b) after silver impregnation and reduction.

PC:TiO<sub>2</sub>:Ag samples present good optical and mechanical properties, thus ready for lamination.

## **2.5. Preparation of TiO<sub>2</sub>:Ag PC cards**

Manufacturing ID cards have to follow very specific characteristics in order to be recognized as such for international interchange. These specifications are compiled in the standard ISO/IEC 7810:2019 that includes the card materials, constructions, characteristics and physical dimensions. Polyvinyl chloride (PVC), polyethylene terephthalate (PET) and PC are common materials used to produce ID cards. Four different card sizes are described in the standard: ID-1 (85.6x53.98mm), ID-2 (105x74mm), ID-3 (125x88mm) and ID-000 (25x15mm) with all of them having a thickness between 0.68 mm and 0.84 mm. ID-1 are the most commonly used as payment cards, driver licenses or personal identity cards across numerous countries. ID-2 format is an “old” and larger format used mainly for visas and identity cards. In the past years they have been replaced by ID-1 cards, for example since August 2021 the French ID cards are issued in the ID-1 format. The ID-3 size is mainly used for passport booklets and the ID-000 for SIM cards (subscriber identity modules). Each format has to pass standardized tests to evaluate namely their resistance to bending, chemicals, temperature and humidity in order to be recognized as ID cards.

In the scope of the project we focused on the production of color images for ID-1 personal identity documents. In the following section the lamination process is described to produce ID-1 PC cards while including the laser-engravable films.

### **2.5.1. Lamination technique used for ID-1 PC cards**

PC ID cards are made by laminating together stacks of thin PC sheets with different properties and thicknesses. This process involves different heat and pressure steps in order to merge homogeneously the different sheets. It's a delicate process that requires experimental knowledge to define both the card configuration and lamination conditions (depending on the equipment) to avoid potential flaws such as warping, bubbling, delamination or crushing the sample.

The designed card configuration is illustrated in figure 34.a containing 8 A4 PC sheets (800 µm thick stack) with different properties and thicknesses: 100 µm thick clear non laserable PC sheets with or without artwork (C, NL); 100 µm thick clear laserable PC sheets (C, L) and 100

$\mu\text{m}$  thick white PC sheets (W), all provided by Exim. A 2x2cm clear window was cut off the white sheets where the sample is placed. The samples are originally 4x4cm squares but were cut in 4 equal squares of 2x2cm to maximize the card sampling. Once the stacks are prepared they are carefully placed between two lamination plates and introduced in the press. To produce the PC cards a BGi167 laminator press (A4 format) from BG INGENIERIE is used following the lamination recipe presented in the table of figure 34.b. The recipe follows a 6-step process with each step configured with a defined temperature (T in  $^{\circ}\text{C}$ ), pressure (P in  $\text{N}\cdot\text{cm}^{-2}$ ) and time (t in seconds). After the lamination process, the cards are removed from the press and plotted as ID-1 cards (85.6x53.98mm) as seen in figure 34.c. For future reference, cards containing  $\text{TiO}_2$  films are referenced as “ $\text{TiO}_2\text{:Ag}$  PC card”.

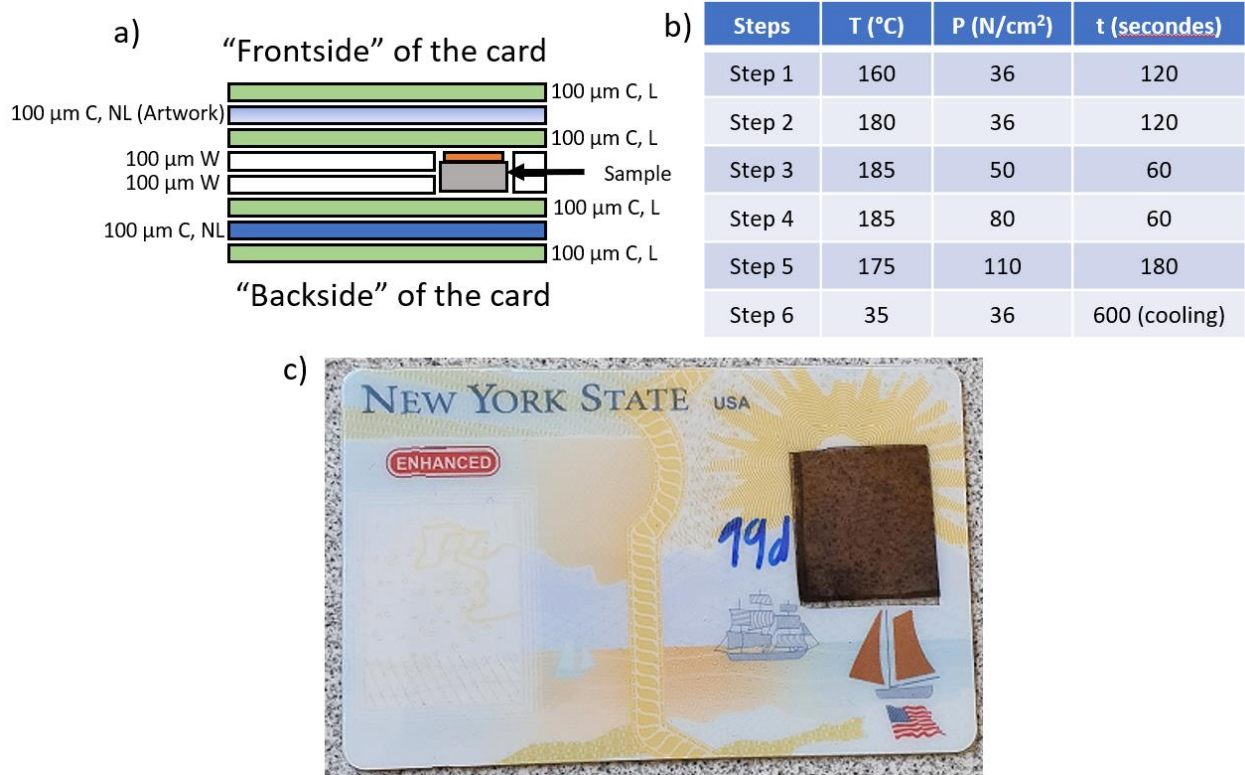


Figure 34: (a) Sketch of the card configuration with a stack of 8 PC sheets for sample lamination, (b) lamination program with 6 steps with varied temperatures, pressures and times. (c) Image taken with a camera phone of the “frontside” of a laminated card containing a 2x2cm sample.

## 2.6. $\text{TiO}_2\text{:Ag}$ PC cards characterization

After reduction of AgNPs,  $\text{PC}:\text{TiO}_2\text{:Ag}$  samples are laminated inside a card for laser inscription. Details on the lamination process are given in part 3.2.6 to prepare “ $\text{PC TiO}_2\text{:Ag}$  cards”. After lamination, the state of the film was observed by optical microscopy as depicted in figure 35.a

showcasing slight cracking of the film. This is due to the high pressure exercised during the lamination process. Additionally, the transmission spectral behavior of the sample was recorded in the visible range and compared to a non-laminated sample (PC:TiO<sub>2</sub>:Ag) as illustrated in figure 35.b. Despite having more or less a 600 μm layer of PC in the PC TiO<sub>2</sub>:Ag card and being submitted to a lamination process, the transmission behavior remains the same between 550 and 750 nm compared to the non-laminated sample. However, in the 350-550 nm region a blue-shifted decrease in transmission is observed peaking at 430 nm suggesting the formation of small nanoparticles. This is likely due to the thermal treatment endured during the lamination process as temperature reaches 185°C. To verify this, the sample was characterized by STEM imaging of the film's cross section as presented in figure 35.c where it is observed spherical-like silver nanoparticles with 5 to 20 nm in diameter. Moreover, the lamination induced as well the contraction of the system with a thickness of 55±5nm compared to the original thickness of 95±5 nm before lamination.

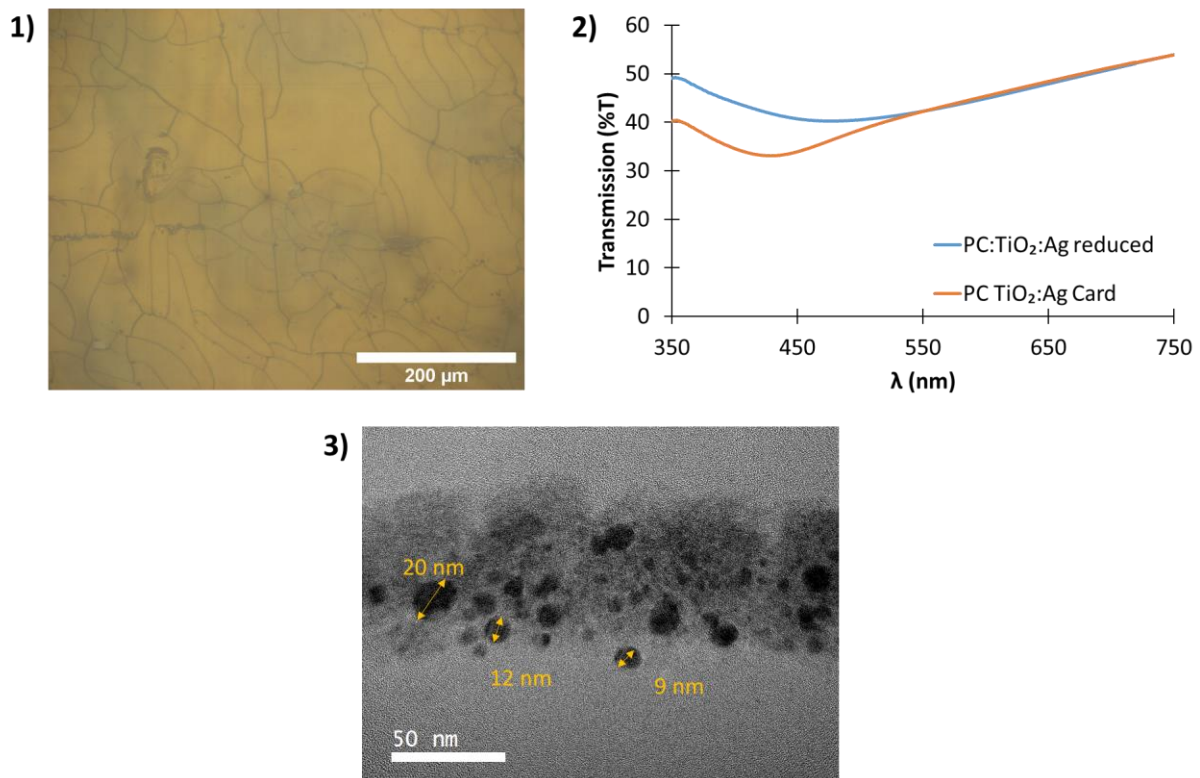


Figure 35: (a) Optical microscope image of a PC TiO<sub>2</sub>:Ag card after lamination presenting slight cracking. (b) UV-Vis spectral curves of the sample before (in blue) and after lamination (in orange). (c) STEM image of the cross section of PC TiO<sub>2</sub>:Ag card depicting small AgNPs with diameter ranging from 5 to 20 nm in the titania matrix.

The lamination process leads to significant changes in the material as it shrinks to roughly  $75\pm 5$  nm and induces cracking of the film. In parallel, small silver nanoparticles are formed (5-20 nm in diameter) according to the UV-Vis spectroscopy and STEM characterization. The samples are therefore available for laser processing.

## **2.7. Preparation of PC:SiO<sub>2</sub>:TiO<sub>2</sub>:Ag non-laminated samples**

### **2.7.1. Sol synthesis and preparation of a dense SiO<sub>2</sub> protective layer**

Silica coatings are known to be resistant to high temperatures due to their low thermal conductivity<sup>116</sup> and have been used to enhance the binding between polymer substrates and inorganic layers<sup>117</sup>. Therefore, an intermediate dense SiO<sub>2</sub> layer was prepared to protect the substrate from thermal effects due to laser processing of the TiO<sub>2</sub>: Ag film and produce PC:SiO<sub>2</sub>:TiO<sub>2</sub>:Ag samples. For clarity's sake, these samples are not included in a PC card and laser processed directly, hence non-laminated samples.

#### *2.7.1.1. Chemicals*

The sol preparation follows the synthesis process described elsewhere with some modifications<sup>118</sup>; instead of ethanol as the main solvent, isopropanol was used as it improved the adherence of the sol to the surface of the PC substrate. Additionally, the silica precursors are a 50/50 mix instead of 40/60 of tetraethyl orthosilicate (TEOS;  $\geq 99\%$ ) and triethoxymethylsilane (MTEOS;  $\geq 99\%$ ). Both precursors were purchased from Sigma-Aldrich, isopropanol (iPrOH) was bought from Fisher Scientific and glacial acetic acid (CH<sub>3</sub>COOH) from Sigma-Aldrich is used as a catalyser diluted in DI water.

#### *2.7.1.2. SiO<sub>2</sub> sol synthesis and film deposition*

To prepare the SiO<sub>2</sub> sol the different molar ratios of TEOS:MTEOS:iPrOH:CH<sub>3</sub>COOH:H<sub>2</sub>O were defined to 1:1.5:47:0.3:4.6 respectively. In a flask, 2.9 g of TEOS are mixed with 3.8 g of MTEOS in 39.9 g of isopropanol. After the solution is stirred for 30 minutes, 1.2 g of 0.1 M acetic acid are then added dropwise. The 0.1M solution is prepared by diluting the glacial acetic acid ( $17.47 \text{ mol.L}^{-1}$ ) in DI water. Finally, the flask containing the sol is placed in a water bath at a constant temperature of 40 °C and stirred for 2 hours before any deposition.

The film deposition follows the method described in part 2.3.3 where the sol is filtered in usual conditions and deposited on a PC substrate and spin coated at 2000 RPM for 60 seconds

in ambient conditions. After deposition the opposite side of the substrate is cleaned off sol excess and is placed in a stove at 130 °C for stabilization for 2 hours. Mesoporous titania thin films are then deposited following the procedure as described in 2.3.3 and impregnated with silver to obtain PC:SiO<sub>2</sub>:TiO<sub>2</sub>:Ag samples.

## 2.8. PC:SiO<sub>2</sub>:TiO<sub>2</sub>:Ag samples characterization

Due to the complexity of the system (anisotropy PC substrate and stacking layers), in-situ ellipsometry characterization was not possible to perform during the stabilization process. However, a single measurement was made after stabilization in dried conditions ( $P/P_0=0$ ), revealing the thickness of the silica layer at  $255\pm 5$  nm with a refractive index of 1.51 at  $\lambda=600$  nm (Cauchy law with  $A=1.468$ ;  $B = 0.0152$ ) and the top TiO<sub>2</sub> layer presenting a thickness of  $91\pm 5$  nm and the refractive index (@600nm) to 1.58 (Cauchy law with  $A=1.515$ ;  $B = 0.02379$ ). The latter is in agreement to the properties of mesoporous TiO<sub>2</sub> film investigated in part 2.4.2. Its optical behavior was investigated by UV-Vis spectroscopy. Figure 36 displays the transmission measurements performed on PC:SiO<sub>2</sub> (red curve) and PC:SiO<sub>2</sub>:TiO<sub>2</sub> (green curve) systems in the visible range. Less than 5% of the transmission is lost when a silica layer is implemented similar to what is observed in a “PC:TiO<sub>2</sub>” system in figure 32.a, thus the optical transparency of the sample is well kept. Furthermore, the sample was soaked with silver salts by liquid impregnation and nanoparticles were produced by exposing the sample to UV(254 nm) for an hour. The sample obtained PC:SiO<sub>2</sub>:TiO<sub>2</sub>:Ag (blue curve) presents similar optical behavior as PC:TiO<sub>2</sub>:Ag (blue dotted curve) in the visible range. The sample is ready to be laser processed.

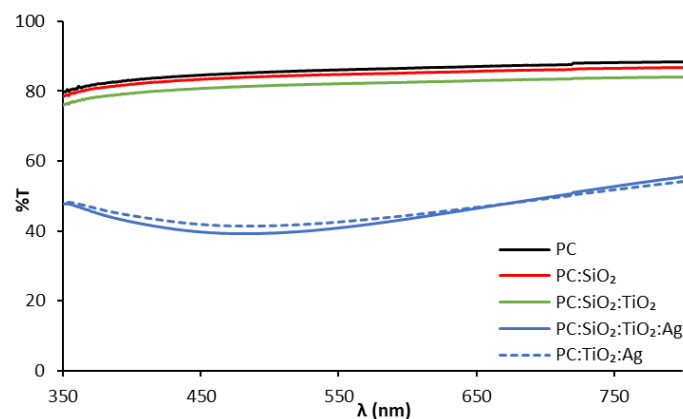


Figure 36: UV-Visible transmission spectrum of a virgin PC substrate (black curve) and with a silica film deposited at the surface of the PC (red curve) depicting high transparency. On top of the silica film a mesoporous TiO<sub>2</sub> was deposited (green curve) which was then impregnated with silver (green) and reduced by UV exposure (blue).

## 2.9. Conclusion

In this chapter, it was presented the development of TiO<sub>2</sub>:Ag films on polycarbonate supports by sol-gel methods. First, the plastic substrates resistance to different treatments were studied, namely the O<sub>2</sub> plasma, thermal and UV treatment, to be able to identify the optimal working conditions for them. It was determined that a 2-minute oxygen plasma process of the surface changes the surface properties as the roughness decreased, going from mean roughness ( $S_a$ ) of 11.25 nm to 5.59 nm. Moreover, the surface becomes hydrophilic as the contact angle of DI water droplets significantly decreases after the treatment due to the presence of -OH groups. Consequently, the adherence of the sol-gel films is heavily improved because they are crack-free.

Regarding the preparation of mesoporous TiO<sub>2</sub> films, a titanium-based sol was deposited at the surface of PC. A 2-hour thermal treatment at 130°C was performed to densify the film due to evaporation of the solvents as depicted by the in-situ EE measurements without damaging the substrate. This is followed by a 2-hour UV (254 nm) treatment to polymerize the titanium into TiO<sub>2</sub> as Ti/Acac complexes are progressively eliminated. In parallel, the templating agents are eliminated. A final solvent extraction is performed in ethanol that allows to eliminate the residual organic parts and create the porosity as evidenced by the ex-situ EE and EEP measurements.

The samples are then soaked in ammoniacal silver solution to fill the pores with mainly Ag<sup>+</sup> but also Ag<sup>0</sup> and AgNPs. A 1-hour exposure to UV (254 nm) allows the reduction of Ag<sup>+</sup> to Ag<sup>0</sup> and form ultimately AgNPs. The prepared PC:TiO<sub>2</sub>:Ag samples are then included in a PC card by means of a lamination process. This results in a slight cracking of the TiO<sub>2</sub>:Ag film as observed in the optical microscope images of the sample. Moreover, a shrinkage of the material is highlighted, going from 90±5 nm thick film to 55±5 nm evidenced by the TEM images of the sample cross-section. This is due to the pressure and temperature applied to the sample during the lamination process. Despite this significant change, the overall absorption in the visible range remains similar compare to non-laminated samples, thus ready for laser processing.

Lastly, for processing experiments on non-laminated samples an intermediate silica layer was implemented to protect the PC from damaging due to heat accumulation induced by the

irradiation as silica presents low thermal conductivity. A MTEOS/TEOS sol was formulated and deposited on top of a PC substrate and stabilized with a thermal treatment to produce a  $255\pm 5$  nm dense thick silica layer. On top of this film, a mesoporous  $\text{TiO}_2$  film is prepared and impregnated with silver NPs depicting similar optical behavior than PC: $\text{TiO}_2$ :Ag samples.

In the following chapter, the laser processing of  $\text{TiO}_2$ :Ag PC cards and PC: $\text{SiO}_2$ : $\text{TiO}_2$ :Ag samples is investigated.



## **CHAPTER 3: LASER-INDUCED COLOR PRODUCTION**

As described in Chapter 1, exciting plasmonic systems by laser processing can lead to strong localized heat deposition. This can be problematic for polymer-based samples such as polycarbonate ( $T_{\text{fusion,PC}} = 140^{\circ}\text{C}$ ) as they can be easily burned when laser processed. Taking this into account the first task is to establish the best conditions of laser processing within the sample's limitations. To date there are no models that are able to predict the physical or optical properties of laser-induced nanostructures on such substrates due to their complexity. To overcome this limitation an empirical approach is followed, inspired by the recent work of other colleagues, namely Nicolas Dalloz<sup>105</sup>, Van Doan Le and Robin Mermillod-Blondin (unpublished results) who developed several tools to be able to produce nanostructures, extract their color values and utilized them for high quality image printing. For this,  $\text{TiO}_2:\text{Ag}$  PC cards are first investigated to produce well-controlled colors for full-color image printing. Then, the collected experimental knowledge is then translated to non-laminated  $\text{PC}:\text{SiO}_2:\text{TiO}_2:\text{Ag}$  samples. Finally, demonstrators are printed to highlight their potential for high-quality and secure image printing.

### **3.1. Laser setup and color characterization**

#### **3.1.1. Laser setup**

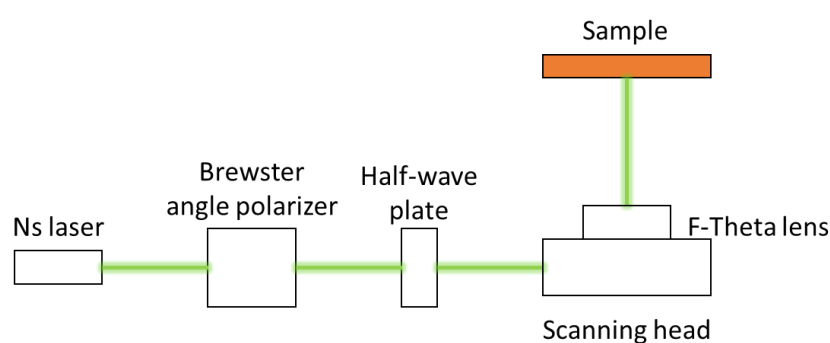


*Figure 37 : Schematic representation of the nanosecond laser setup.*

The laser setup is composed of an industrial fibered laser (*IPG Photonics*) with a wavelength of 532 nm and pulse duration of 1.3 ns; a Brewster angle polarizer paired with a half-wave plate for polarization rotation and finally a galvanometric mirror scan head from *Sunny Technology* as depicted in figure 37. The latter consists of two galvanometric mirrors which can rotate in order to control the beam angle in both horizontal and vertical directions. To focus the laser beam in the sample a 16cm F-Theta lens converts the angle given by the

mirrors into a displacement on the sample located in the image focal planes of the lens. The radius of the spot at the focal plane (named “ $f_0$ ”) was determined by image profiling using a CMOS camera from Thorlabs, where the smallest circular-like spot is observed in Annex 2.a. The vertical optical intensity profile passing through the middle of the spot was plotted and fitted to a Gaussian model ( $I(r) = I_0 \cdot e^{-2r/r_{1/e^2}}$ ). The beam radius where the optical intensity drops to  $1/e^2$  of the maximum intensity value was determined to  $r_{1/e^2} = 13.74 \mu\text{m}$ .

#### 3.1.1.1. Working focal plane

Laser processing at the focal plane  $f_0$  induces severe damage on the samples due to overwhelming heat accumulation as the samples are either burned or bubbles were created inside the PC cards even when working in the lowest power range of the laser (figure 38). Therefore, to avoid this, samples were placed 2 mm after the focal plane  $f_0$  relative to the scanner head and named “ $f_2$ ” plane. The spot size was imaged at this position as displayed inset in Annex 2.b where an elliptical spot size is obtained due to the astigmatism of the laser beam. Therefore, both vertical and horizontal intensity profiles passing through the middle of the spot were plotted and fitted separately to a Gaussian profile following the same model presented previously. The horizontal,  $r_{h,1/e^2}$ , and vertical,  $r_{v,1/e^2}$ , radii were determined respectively to  $26.2 \mu\text{m}$  and  $34.5 \mu\text{m}$ . This allows to increase the beam size, thus reducing the fluence (energy deposited per area;  $\text{mJ}\cdot\text{cm}^{-2}$ ) of the laser inscription.

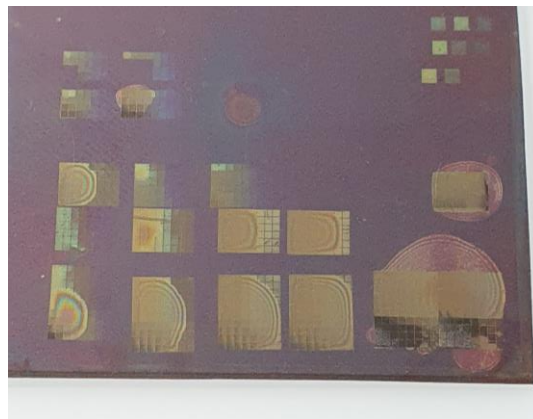


Figure 38: Image taken by a phone camera of laser inscriptions made at the focal plane  $f_0$  on a  $\text{TiO}_2:\text{Ag}$  PC card presenting bubbles due to intense irradiation.

#### 3.1.2. Laser processing parameters

The laser and scanner head are controlled by the software *CS Mark*. The laser movements follow a virtual vector drawing interface that defines the path of the laser beam to draw dots,

lines and any kind of geometric object. Each object is assigned to different laser parameters namely the repetition rate (kHz), laser power (written in % of the maximum laser power and converted in fluence,  $\text{mJ}\cdot\text{cm}^{-2}$ , in the manuscript using the formula in Annex 3). In the case of “dots”, the laser is turned on statically for a given exposure time (in  $\mu\text{s}$ ). For lines, the laser is continuously scanned along a line at a given speed (in  $\text{mm}\cdot\text{s}^{-1}$ ). These parameters are defined by the user and during marking they are automatically changed by the software. In addition, the laser polarization can be tuned manually with the half-wave plate and was kept at  $0^\circ$  (horizontal plane) across every inscription in this work.

Laser processing on plastic supports is delicate due to the thermal heating induced by the Ag nanoparticle absorption that can burn the plastic. The laser repetition and power must be limited to a maximum value and very low scanning speeds are prohibited. The parameters used to create the database are presented in the following table, leading to 480 different combinations of laser parameters:

*Table 3: Database laser parameters*

<b>Repetition rate (kHz)</b>	<b>Laser power</b>		<b>Fluence (<math>\text{mJ}/\text{cm}^2</math>)</b>	<b>Scan speeds (mm/s)</b>
	<b>(%)</b>	<b>(mW)</b>		
10	6	18	33.3	30
20	8	20.4	37.9	40
40	10	23.8	41.9	50
50	12	25.3	45.8	60
	14	28.5	50.1	80
	16	33.4	55.3	100
	18	36.5	60.1	150
	20	38.2	64.2	600
	22	43.5	71.9	700
	25	45.2	77.5	800
				1000
				1500

### **3.2. Investigation of nanostructures by TEM**

As described in the literature, laser processing  $\text{TiO}_2\text{:Ag}$  films induces different modifications of the film. However, investigating them when the material is embedded in a plastic card is a difficult task as the surface is not available for observation due to the presence of a thick PC layer on top of it. This makes it impossible to observe the plain view of the sample without

completely destroying it. Nevertheless, the cross-section can be observed by TEM by preparing the sample by ultramicrotomy as described in part 2.1.2.3. The untreated sample is presented in figure 39.a whereas two laser conditions were investigated, one at 10 kHz and another at 40 kHz, in figures 39.b and 39.c respectively. For each sample, a chemical mapping was performed to identify the silver (green), titanium (blue) and oxygen (red) atoms present in the film. Initially the diameters of the nanoparticles vary between 5 to  $20\pm 2$  nm (figure 39.a). After laser processing at 10 kHz (figure 39.b), nanoparticles grow as large spherical ones are formed with a diameter comprised between 20 to  $45\pm 2$  nm embedded in the material. Furthermore, nanoparticles grow even more when laser processed at 40 kHz (figure 39.c) as larger spheroidal nanoparticles are formed with a diameter comprised between 40 and  $70\pm 2$  nm. They are located preferentially at the surface of the titania film rather than embedded. However, it is difficult to assess if they migrate to the “top” (irradiation side) or the “bottom” of the film as polycarbonate is present on both sides.

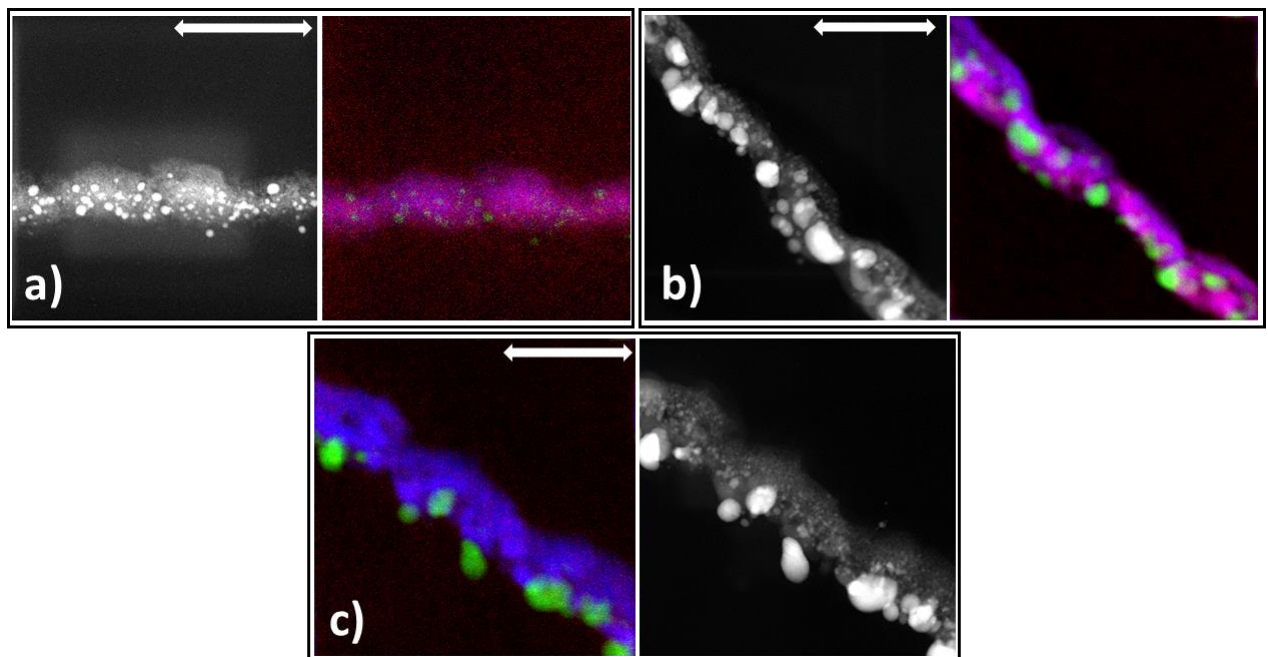


Figure 39: (a) Cross-section TEM images of the untreated  $\text{TiO}_2\text{:Ag}$  film embedded in a PC card and the film laser-processed at 10 kHz (b) and at 40 kHz (3) with a laser power  $28.5 \text{ mW}$  and scanning speed of  $50 \text{ mm}\cdot\text{s}^{-1}$ . For each condition, the chemical mapping is illustrated on the right side where silver (green), titanium (blue) and oxygen (red) are highlighted. The scale bar represents  $200 \text{ nm}$  for every chemical mapped image.

### 3.2.1. Color measurements

#### 3.2.1.1. Camera setup and observation modes

Four different observation modes with non-polarized light have been considered for this study: “frontside reflection” (FR), “backside reflection” (BR), “transmission” (T) and “diffraction” (Diff). The color measurement setup is presented in Figure 40 where images are taken using an RGB camera (*Basler ac2500-14gc*), two 15 cm wide LED light sources placed accordingly for “reflection” and “transmission” measurements of a given sample. The latter can rotate around a perpendicular axis to the incidence plane allowing to freely vary the observation angles. For both transmission and reflection measurements, the incidence angle of the sample is  $0^\circ$  and  $15^\circ$ , respectively. For diffraction measurements, the  $-1^{\text{st}}$  diffraction order was observed using the same camera and source configuration as for the reflection mode but the incidence angle was set at  $55^\circ$ .

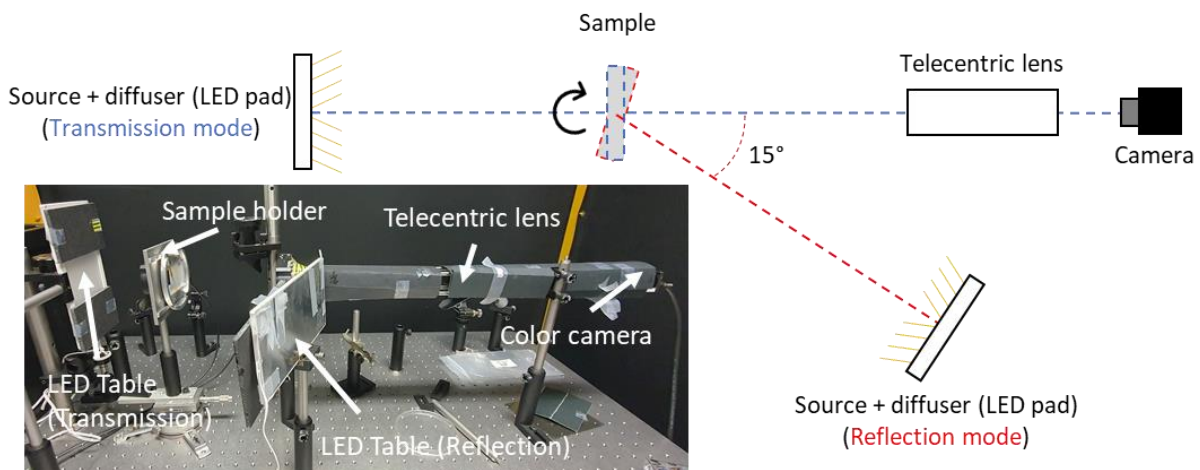


Figure 40: Sketch and picture of the image acquisition setup.

#### 3.2.1.2. Image normalization

To overcome the lightness homogeneity on the camera field of view, the images are normalized by dividing them with an image of the light source taken without the sample. This step is done for every image in “transmission” and “reflection” modes taken with this camera setup before extraction. An example is given with a transmission image of a laser processed database, figure 41.a, is normalized. The lightness inhomogeneity is corrected as illustrate in figure 41.b.

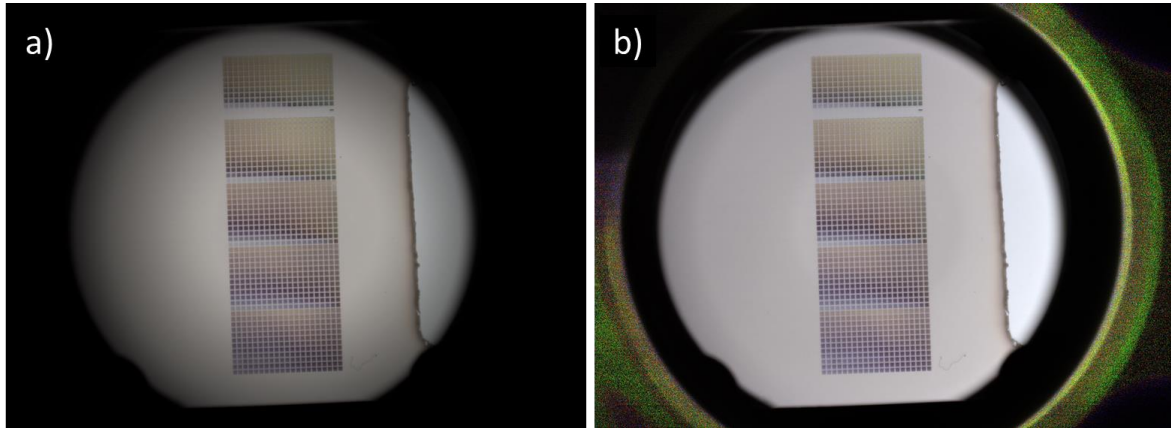


Figure 41: (a) Image of a sample taken with the same setup in “transmission” mode depicting lightness decay from the center to the borders. (b) Normalized image of the sample, correcting the lightness decay of the lens.

### 3.2.2. Design of laser processed elements for image printing

#### 3.2.2.1. Introduction

To be able to print an image each pixel is assigned a vectorized element (series of lines or dot) which controls the laser path used to print it. The pixel color depends on the laser parameters, but also on the design of the vectorized element and the size of the printed pixel. The numerical methodology and the software used to control the laser process was elaborated by Nicolas Dalloz during his PhD work<sup>105</sup>. Each pixel is a “square” made of parallel laser lines separated by an interline spacing distance ( $dy$ ) which fill the vectorized area. The lines can be drawn in the same direction or following a serpentine direction, illustrated in figure 42.a, and are all inclined at a certain angle relative to the pixel position, for example at  $0^\circ$  or at  $45^\circ$  as depicted in figure 42.b.

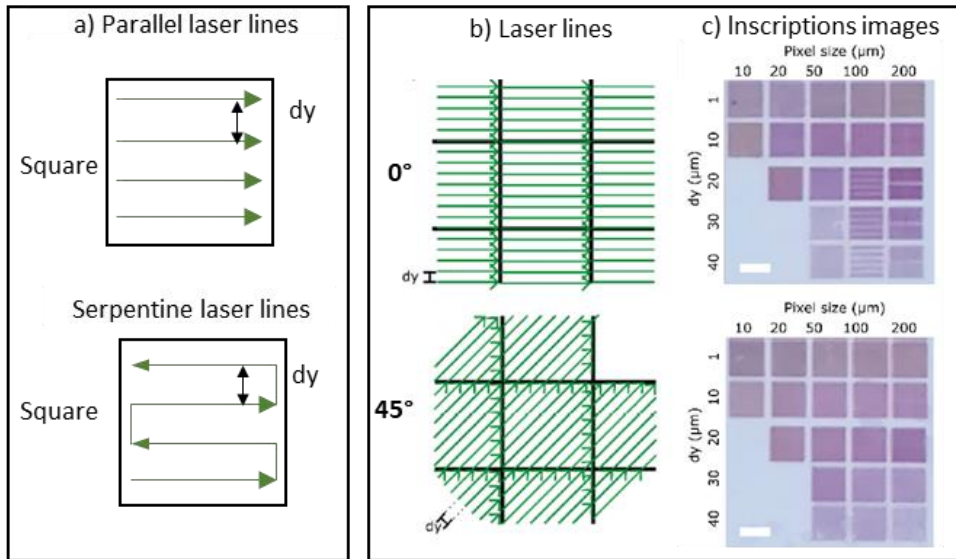


Figure 42: (a) Illustration of horizontal laser lines and serpentine laser lines in a square with an arbitrary interline distance  $dy$ . (b) Illustration of squares filled with lines at  $0^\circ$  relative to the square edge (top) or at  $45^\circ$  (bottom). (c) Image taken with a camera setup of  $500 \times 500 \mu\text{m}^2$  squares filled with pixels of different sizes (10 to  $200 \mu\text{m}$ ) and different interline distances (1 to  $40 \mu\text{m}$ ). In the top image squares are written at  $0^\circ$  while in the bottom image the inscriptions are made with  $45^\circ$  lines. The scale bar is  $500 \mu\text{m}$ .

A study was carried on the influence of using either  $0^\circ$  and  $45^\circ$  lines on the color production with different pixel sizes and interline distances. In figure 42.c, an image was taken of squares inscribed at the focal plane  $f_0$  on  $\text{TiO}_2:\text{Ag}$  films deposited on glass. Each square is filled with either  $0^\circ$  or  $45^\circ$  parallel laser lines with juxtaposed pixels having sizes (10 to  $200 \mu\text{m}$ ) and different  $dy$  values (1 to  $40 \mu\text{m}$ ). It is observed that with  $0^\circ$  laser lines some color discrepancies can be observed, particularly for 100 and  $200 \mu\text{m}$  square size with 20, 30 and  $40 \mu\text{m}$   $dy$  values. This is due the spacing of the horizontal lines being disproportional to the pixel size and leaving unmarked areas. However, in the case of  $45^\circ$  lines every square presents uniform color as the inscription is done homogeneously and do not leave unmarked areas. Based on these results, laser lines with a  $45^\circ$  hatching orientation appear to be the best candidates for homogeneous color production and image printing.

### 3.2.2.2. Defining pixel size and interline distance ( $dy$ )

In the *Cs Mark* software, a line defines the movement of the laser line distance but does not represent the real width of the inscribed line. In fact, the laser width at  $1/e^2$  is significantly higher than the vectorized line and will vary depending on the laser conditions. To illustrate this, lines were inscribed at the plane  $f_2$  with different powers and scanning speeds. The repetition rate was set at 40 kHz, the laser powers at 18; 33.4 and 45.2 mW, and the scanning

speeds at 30, 500 and 1500 mm.s<sup>-1</sup>. After inscription, optical microscope images were taken of the different lines depicted in figure 43.

First, it can be observed that increasing the laser power increases the width of the inscribed line. This is logical as higher power means higher fluence, thus more energy is adsorbed by the silver NPs which is then dissipated in the surrounding area. The width variations are more noticeable with lower scanning speed (30 mm.s<sup>-1</sup>) as the line width for powers of 18, 33.4 and 45.2 mW increase respectively to 25, 30 and 46.5 μm. For intermediate scanning speed (500 mm.s<sup>-1</sup>) this effect is less noticeable as the line width is comprised between 22 and 28 μm and the uniformity of the laser lines is hindered. This effect is more visible with laser inscriptions at high scanning speed (1500 mm.s<sup>-1</sup>) where dots are observed instead of a continuous laser line. This can be explained by the high scanning speed that translates to a low effective number of pulses of 1.6 per spot diameter (formula annex 3) that is not sufficient to create a homogenous modification of the material even with high power.

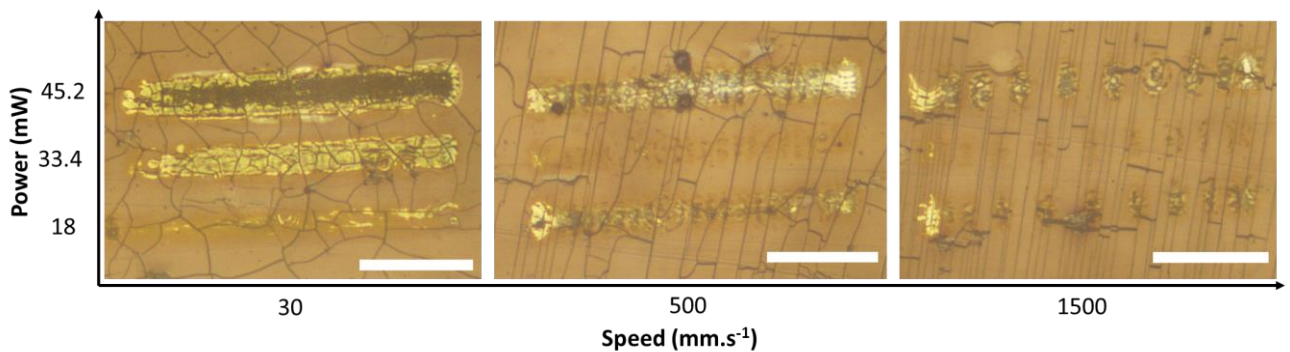


*Figure 43: Microscope images of laser lines inscribed in a TiO<sub>2</sub>:Ag PC card with different laser conditions. The repetition rate was fixed at 40 kHz, the power varied to 18,33.4 and 45.2 mW, and the scanning speed varied to 30, 500 and 1500 mm.s<sup>-1</sup>. The scale bar is 100 μm for every image.*

This study shows that varying the laser conditions influences heavily on the shape of the printed laser line. However, as presented in figure 38, pixels are printed by filling the area with several parallel lines separated by a fixed interline distance. These squares are usually in the range of 25 to 80 μm, depending on the desired size and resolution of the printed image. It is therefore interesting to investigate the formation of pixels with different sizes and interline distance values.

For this several pixels were printed using four different pixel sizes, 25, 35, 50 and 65 μm, and four different dy values of 5, 10, 20 30 μm as illustrated in figure 44.a. Each pixel was printed

on a TiO<sub>2</sub>:Ag PC card by keeping the power and scanning speed constant at respectively 33.4 mW and 500 mm.s<sup>-1</sup>, however the repetition rate was varied to 10, 30 and 50 kHz to have an overview of the pixels in different laser processing conditions. After laser marking, they were observed under the microscope as presented in figure 44.b for each repetition rate. The real dimensions, i.e. height and length (μm), were measured for each pixel and summarized in Annex 4.

As a general observation, the real pixel size is between 1.5 and 1.8 times bigger than the intended size independently of the laser conditions. This can be explained by the laser lines at the borders of the pixels, having a beam radius of  $r_{h,1/e^2}$ , and vertical,  $r_{v,1/e^2}$  at respectively 26.2 μm and 34.5 μm at the  $f_2$  plane, inducing the “oversizing” of the pixels in both vertical and horizontal directions. Moreover, pixels with dy values of 20 or 30 μm present unmarked areas within the square independently of the repetition rate, while for 5 and 10 μm dy values, the pixels are fairly homogeneous. The latter is attributed to the significant line overlapping occurring within each pixel that is responsible on producing a uniform nanostructure independently of the intended pixel size. This is not the case for pixels with dy values of 20 or 30 μm as single lines are detected.

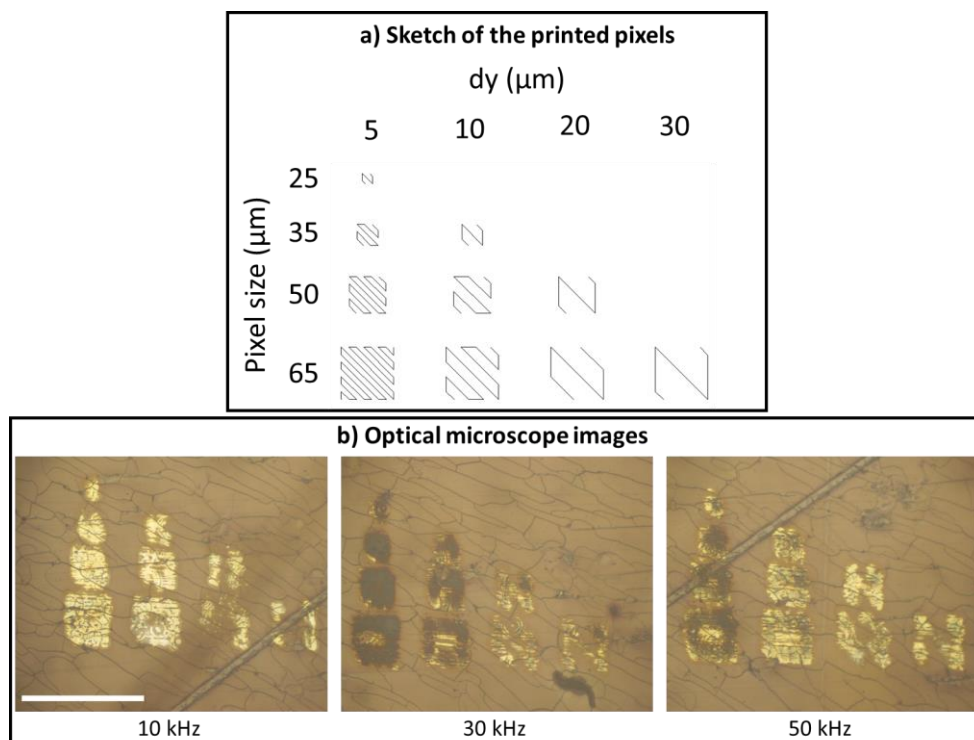


Figure 44: (a) Design of pixels with different sizes (25-65 μm) and different dy values (5-30 μm). These pixels were printed in a PC:TiO<sub>2</sub>:Ag card at three different repetition rates (10,

30 and 50 kHz) and (b) observed under the microscope. The scale bar is 200  $\mu\text{m}$  for the three images.

Conclusively, pixel structures using low high interlines values lead to uniform marking and are suitable for image printing due to consistent line overlapping. However, the oversizing of the pixels remains an issue as it is intended to juxtapose pixels to produce images. This issue is tackled in the following section. To simplify the task, among the different pixel designs presented in figure 44.a, a pixel size of 50  $\mu\text{m}$  and interline distance value of 10  $\mu\text{m}$  will be the only pixel configuration utilized from now on in this manuscript.

### 3.2.2.3. Pixel juxtaposition

As previously stated the pixels are oversized 1.5 to 1.8 bigger than the intended size. This means that in the case where juxtaposing pixels it could lead to overlapping pixels. An example of this phenomenon is depicted in figure 45.a where 50x50  $\mu\text{m}^2$  binary pixels are juxtaposed, creating a 400x400  $\mu\text{m}^2$  square of 8x8 pixels, displayed in the laser software interface. Each pixel contains 45° serpentine lines with a dy of 10  $\mu\text{m}$ . Two sets of laser conditions were used, on one hand the parameters for pixels highlighted in “black” are 45.2 mW power and 30  $\text{mm}\cdot\text{s}^{-1}$  speed while “pink” pixels were inscribed with the same scanning speed but with a lower power of 33.4 mW. The inscription is then observed under the microscope where “black” pixels overlap completely the “pink” pixels as their real size is well above 50  $\mu\text{m}$  to an average of 80  $\mu\text{m}$  due to a significantly larger processed area. To answer to this problem an additional parameter is introduced, the pixel “margin” noted  $m$ , that allows to separate the juxtaposed pixels by a fixed distance and reduce their size in the software interface. An example is given in figure 45.b where “50x50  $\mu\text{m}^2$ ” pixels are separated by a margin of 15  $\mu\text{m}$ . This results in the shrinking of the pixels to a size of 35  $\mu\text{m}$  in the software interface and are thus separated by a distance of 15  $\mu\text{m}$ . This way the oversizing of the pixels can be diminished. “Black” and “pink” pixels are inscribed in these conditions using the same laser parameters as before. The inscription is observed in the microscope in figure 45.b revealing the real size of the inscribed pixels to an average of 50  $\mu\text{m}$  and without presenting overlapping. This margin is therefore necessary to juxtapose pixels and diminish laser processing errors.

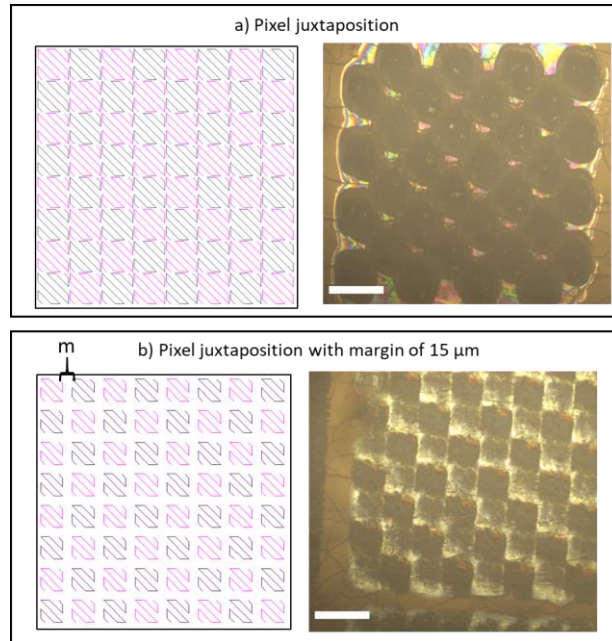


Figure 45: (a) A  $400 \times 400 \mu\text{m}^2$  square containing  $8 \times 8$   $50 \mu\text{m}^2$  binary pixels is inscribed in a  $\text{TiO}_2:\text{Ag}$  PC card and observed under the microscope depicting severe pixel overlapping. (b) Introducing a margin of  $15 \mu\text{m}$  between the pixels and reducing their size to  $35 \mu\text{m}$  results in a homogenous inscription as no overlapping was observed. The scale bar of the images is  $100 \mu\text{m}$ .

#### 3.2.2.4. Image processing for color extraction

To anticipate the fact that images will be printed pixel by pixel, and in order to estimate the color gamut that can be printed by the ns laser on the samples elaborated in this thesis, a color database is created in the form of squares where each square is made of  $7 \times 7$  pixels with the laser parameters given in Table 3 (part 3.1.2). The printed database in the  $\text{TiO}_2:\text{Ag}$  PC card is displayed in figure 46.a, the image was taken with a smartphone camera. For the color extraction, the matrices are imaged by the setup depicted above and normalized. The average sRGB values of each square, as presented in figure 46.b and c, is extracted and saved in a database with the corresponding laser parameters. The sRGB values extracted are then transformed into CIE 1976  $L^*a^*b^*$  coordinates. The CIE 1976  $L^*a^*b^*$  color space is a well-known color appearance model, used noticeably in the printing industry, where color values are compared by following a chromatic adaptation regarding the white point coordinates. For each mode, the white point is chosen among the database. The computational part of this chromatic adaptation is described by Nicolas D. in his thesis<sup>19</sup>.

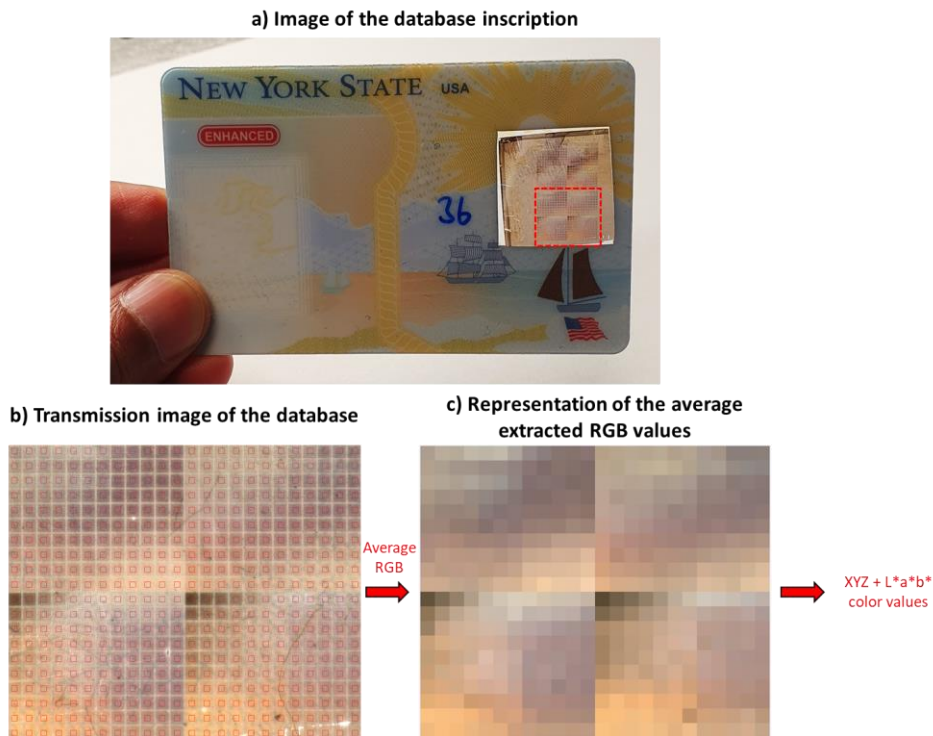


Figure 46: (a) Picture by a phone camera of the database consisting of 480 squares as highlighted in red. The image processing method for color extraction is presented. First, an image is taken of the database with the camera setup, normalized and the colors are averaged at the center of each square as delimited by the red square. The extracted sRGB values (c) are transformed to CIE XYZ values and then converted to CIE  $L^*a^*b^*$  coordinates.

### 3.2.2.5. Defects that alter the color extraction

Very often the samples can present defects that can distort the colors extracted from a square and then be at the origin of a false primary. Figure 47 depicts several examples of common artefacts and their influence on the color extraction on 6 different squares. The first type of artefact is depicted in square (1) where a black spot darkens the real color orange to brown. Another artefact is depicted in squares (2) and (5) where the presence of threads can also darken the real color. The last defects observed are cracks in the film as depicted in squares (4), (5) and (6) that do not darken the averaging area but can bleach them, misrepresenting the real luminance of the color.

These defects certainly appear during the material preparation or the lamination process as they are not performed under well-controlled environments. For instance, the samples before lamination are subjected to different stabilization steps that require manual handling to be able to elaborate the film  $TiO_2:Ag$ , thus can be scratched in the process. Moreover, the samples are prepared in a chemical laboratory where a dust-free environment is not guaranteed, making them prone to have impurities in the film. This is also the case for the

lamination process which is done in an uncontrolled environment and can collect impurities in the process. All of these issues can be certainly diminished if they were prepared in a clean room where the temperature, humidity and dust-free conditions can be well-controlled for both the material and lamination preparation. Unfortunately, such process is not yet developed therefore to avoid distortions of the color extraction of each square, they were manually scrutinized. If the color averaging area for a square contained artefacts they were excluded from the color selection.

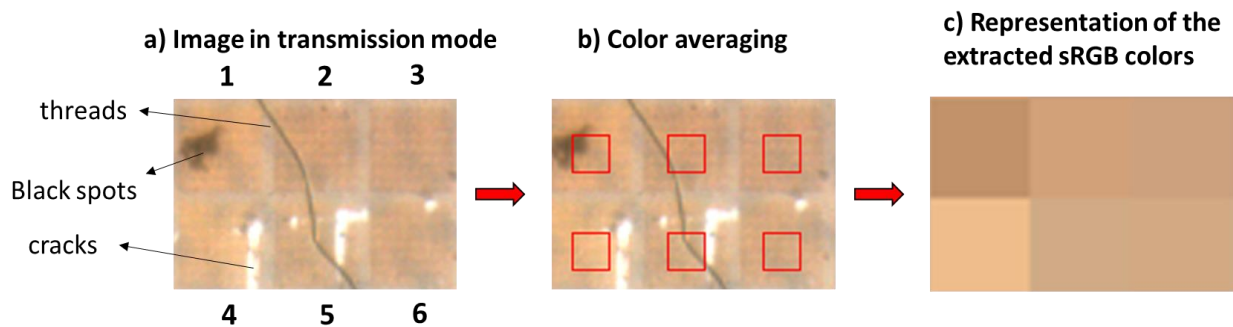


Figure 47: 6 nanostructures are printed on a PC TiO<sub>2</sub>:Ag card (a) presenting several artefacts, such as threads, black spots, holes and lamination artwork. The color averaging for each nanostructure is highlighted in a red square (b). In some cases, the presence of artefacts can hinder the color extraction, resulting in erroneous color values (c).

### 3.2.2.6. Color gamuts

To be able to easily visualize the colors of the database, the corresponding color gamut can be illustrated in a 2D projection. An example is given in figure 48 depicting the colors of the database recorded in “transmission” observation mode. The extracted color values converted into CIE L\*a\*b\* color values are displayed in the a\*b\* plane and L\*C\* plane. Each colored dot represents the color of a unique square. The a\*b\* color gamut represents the color values (chromaticity) of each nanostructure by neglecting their luminance L\* which allows to observe the range of the attainable colors by laser processing. The L\*C\* color gamut represents the luminance L\* as function of the chroma C\* ( $C^* = \sqrt{a^{*2} + b^{*2}}$ ) that grants information about the lightness and color saturation of each nanostructure, essential to determine the laser-printed colors that will be considered as the “white” and “black” colors of the database when gamut mapping will be implemented to print any kind of image with a realistic rendering.

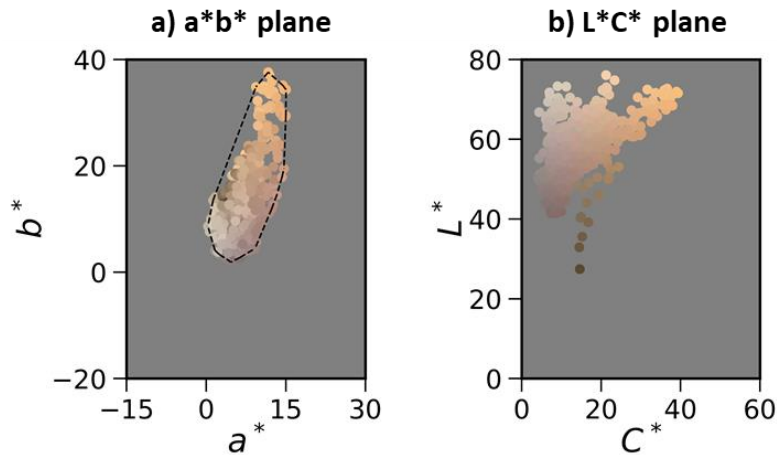


Figure 48: 2D projections of the colors of the database recorded in transmission mode. The colors are illustrated in the  $a^*b^*$  plane with the dashed black line depicting the convex hull of the points, representing the attainable colors, and in the  $L^*C^*$  plane. Each colored point represents the color of a square.

### 3.2.3. Color workflow for image printing

This part describes the workflow elaborated by Nicolas Dalloz and further improved by Van Doan Le, which has been applied in this thesis. It consist in finding the best “white” and “black” color among the printed color gamut, map the gamut of any original image to the one that can be printed by laser in order to provide a final color rendering that approaches at best the one of the original image, extract a limited selection of colors named “primaries”, and implement half-toning to convert the mapped image into an image printed with only the laser printed primaries. The motivation for such an image processing comes from the fact that the volume of the color gamut of original images is substantially larger than the one of the database. Therefore, each original color has to be transformed to be able to enter in the gamut to the database. This algorithmic transformation is called gamut mapping. The color spaces utilized are described in Annex 5.

#### Chromatic adaptation

Once the white and black points are selected among the clusters, the whole printed database gamut is distorted in order to align the grey line between the black and white colors to the zero chroma axis (figure 49.a).

The distorted database gamut is cut into sub-volumes in which the colorimetric distance between any two colors is lower than the minimum perceptible color difference (or a value fixed by the user when the latter wants to reduce the number of primaries to fasten the

printing). A single color per sub-volume is selected to define the primaries color set. The volume in the CIE 1976 L\*a\*b\* color space of the convex hull containing the primaries is very close to the one of the full color database.

### Gamut mapping

First, the lightness of the original gamut is compressed to fit with the maximum lightness variations of the printed gamut defined by the white and black colors (Figure 49.b).

Second, the primaries gamut is densified virtually by calculating a large number of halftones in order to get a quasi-continuous gamut. This step, is a transient step required only to numerically implement the next one. These virtual halftones will not be considered when implementing laser printing.

Third, the two gamuts (original gamut compressed in lightness and distorted printed gamut) are sliced along the lightness axis (Figure 49.c) and, for each slice, the chroma of the original gamut compressed in lightness is compressed using a linear homothetic to enter in the distorted database gamut (Figure 49.d). Each color of the original image is now associated to a color that can be printed by laser (in the distorted gamut).

Finally, in order to display the mapped image using the color that can be effectively printed, the database gamut is distorted back to its original position.

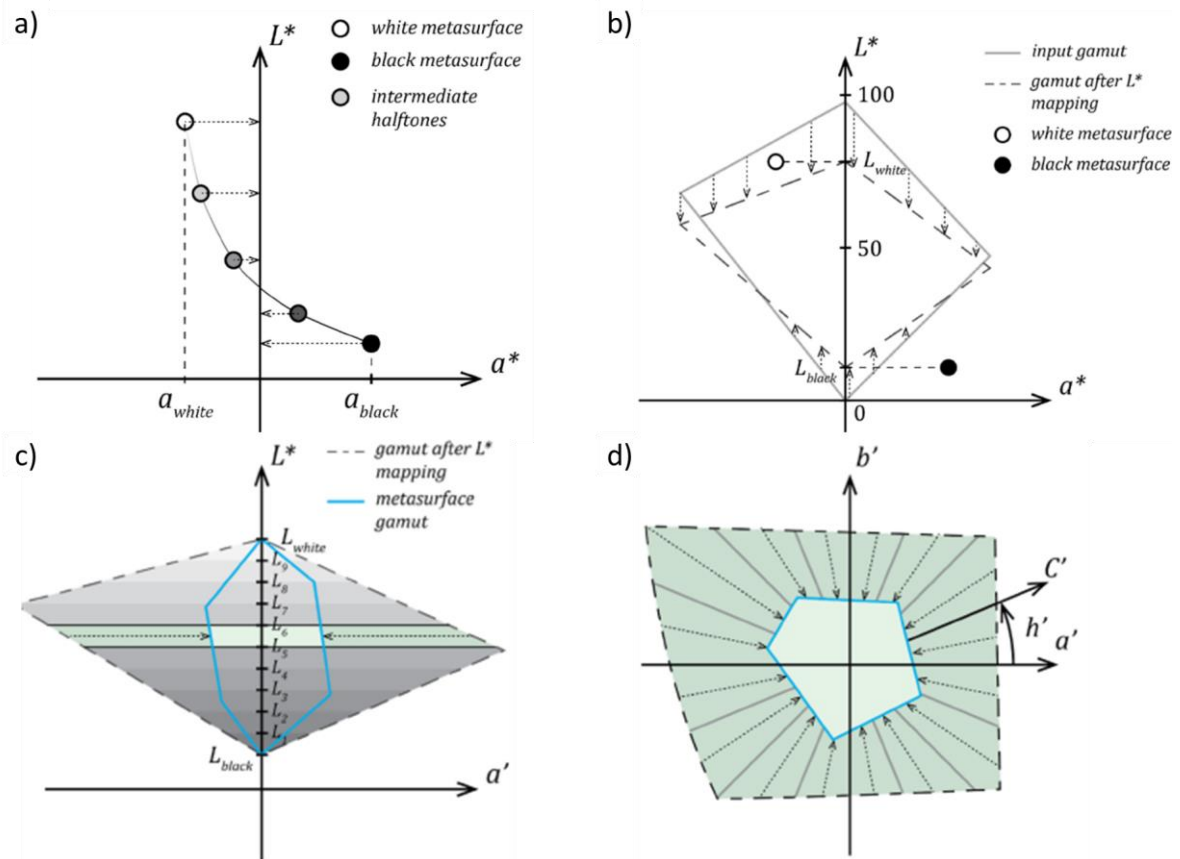


Figure 49: (a) Luminance mapping of the input image to the luminance of a database projected on the  $L^*a^*$  plane. (b) Alignment of the gray axis of the database to the CIE 1976  $L^*a^*b^*$  color space. (c) After alignment, the luminance of the gamut is divided in multiple sections. For each section, the colors of the input gamut are translated linearly to the database (metasurface) gamut as depicted in the  $L^*a'$  plane. The same translation is carried for the mapping of the chroma (d) in the  $a'b'$  plane.

### Error diffusion dithering for halftoning

As the mapped colors of the original image do not necessarily correspond exactly to primaries, especially when the number of primaries is intentionally reduced, the error diffusion dithering technique is used to create halftones and provide a good color rendering. Halftoning is a printing technique of continuous color gradients that rely on the spatial averaging properties of the human sight where the halftones, for example dots, are small enough that, at a certain distance, the patterns patterned areas are interpreted by the eye as smooth tones. This optical illusion can be created by either superposition or juxtaposition of the halftones. In this our case, the halftoning is produced by juxtaposing laser-processed pixels (primaries) and relying on their quantized diffusion error distributed to neighboring pixels. For this a simple error diffusion algorithm called Floyd-Steinberg dithering is used to print the images. that this algorithm is known to works well for low resolution images and a small number of primaries.

## Software laser instructions (vectorization)

Once each pixel of the gamut image is assigned to a laser parameter set by the algorithm, the information needs to be readable by the *CsMark* software. For this a python script was developed to first create the “physical” aspect of the pixels (shape, size, pixel distance) of the image. Then, the laser parameters for each pixel is attributed while respecting the maximum limit of pixels in a single file (100 000) and the number of maximum unique sets of parameters (254, which is the maximum number of primaries that can be chosen finally).

### 3.2.4. Conclusion

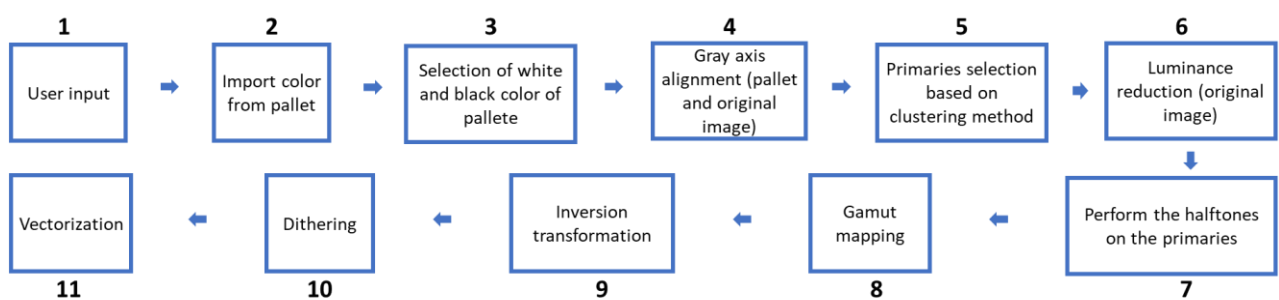


Figure 50: Schematic representation of the color workflow depicting the 11 distinctive steps to produce a printable image from a laser processed database.

The color printing workflow, which includes the recording of the printed database in one mode of observation, is summarized in figure 50. Figure 51.a illustrates an image that can be simulated from an original one after gamut mapping when using all virtual halftones (Figure 51.b), after implementing the error diffusion dithering when using only the primaries selected from printing (Figure 50.c), and after vectorization and assignment of a set of laser parameters to be able to print with the *CSMark* software (figure 50.d).

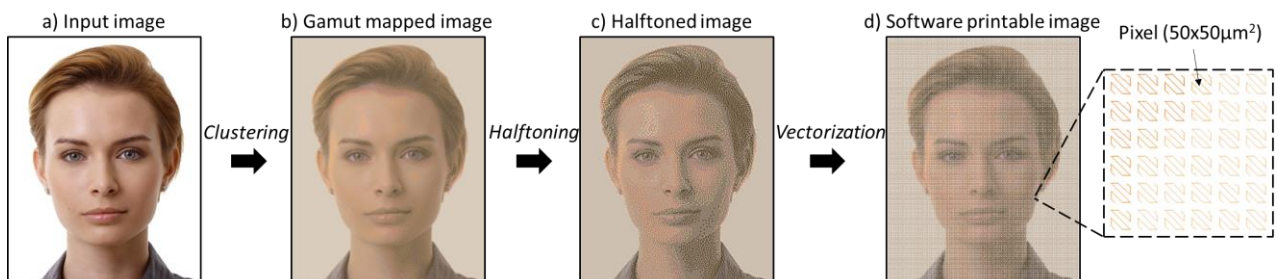


Figure 51: The color printing workflow is summarized in 4 main steps. a) Extraction of the colors of the input image in sRGB color space. b) The image is gamut mapped with the attainable colors of the database gamut. c) An error diffusion algorithm is applied using 10 primaries. d) The resulting image is vectorized in the *CSMark* software. The pixel size is  $50 \times 50 \mu\text{m}^2$  with an interline distance ( $dy$ ) of  $10 \mu\text{m}$ .

### 3.3. Full-color image printing on PC TiO<sub>2</sub>:Ag cards

#### 3.3.1. Selection of the observation mode for color image printing

In order to define the best observation mode that should be chosen to display the printed image, it should be defined a process to assess the quality of the expected printed image in the different modes. Different image quality assessment methods have been developed so far, which can be classified as subjective or objective. Subjective methods are based on the assessment of different criteria by an observer panel whereas objective methods use metrics values to classify the images. The metrics that can be found in the literature have been mostly defined for printing techniques that provide a color gamut that is not very far from the sRGB color gamut and they appeared to be irrelevant for our printing technology. In this part, a work is introduced that will be carried out in another PhD study, to identify relevant metrics to rank the quality of images simulated in different modes of observation with this laser processing technique with some explanations on why this evaluation is only subjective in the present work.

##### 3.3.1.1. *Input image database*



*Figure 52: Input image database composed of 16 distinctive portraits.*

The objective of the project is to develop this laser technology for security applications in ID documentation. Therefore, 16 different portraits with different skin tones and hair colors were chosen as input images as presented in figure 52. Establishing the input images is important as, depending, on the “type” of images such as human/animal portraits, logos or landscape images, the selection of the observation mode can change. Indeed, as different input images might not require the same color values and the colors of the database can vary depending on the observation mode.

### 3.3.1.2. *Assessment of the printed image quality*

The software described previously allows to simulate the 16 portraits expected in three observation modes, “transmission” (T), “frontside reflection” (FR) and “backside reflection” (BR) in figure 53 using 10 primaries from the knowledge of the color database printed in the card and recorded in each observation mode. My own perception of these images allows me to conclude that the simulated images are more faithful to the original ones in the transmission mode and will be used in the following to optimize the printing process. However, a discussion rose on the selection process as it is based on personal assessment of the image quality and does not follow an objective approach. Therefore, to avoid this a process for an automatic selection of the “best” mode is presented by assessing the quality of the simulated images. The process involves three criteria, namely the contrast and variety of colours recorded for each observation mode that lead to a third one relative to the color fidelity to the different images. For each one of them, a metric is defined to compare and evaluate the performance of the simulated images for each observation mode. The color spaces utilized are described in Annex 5.

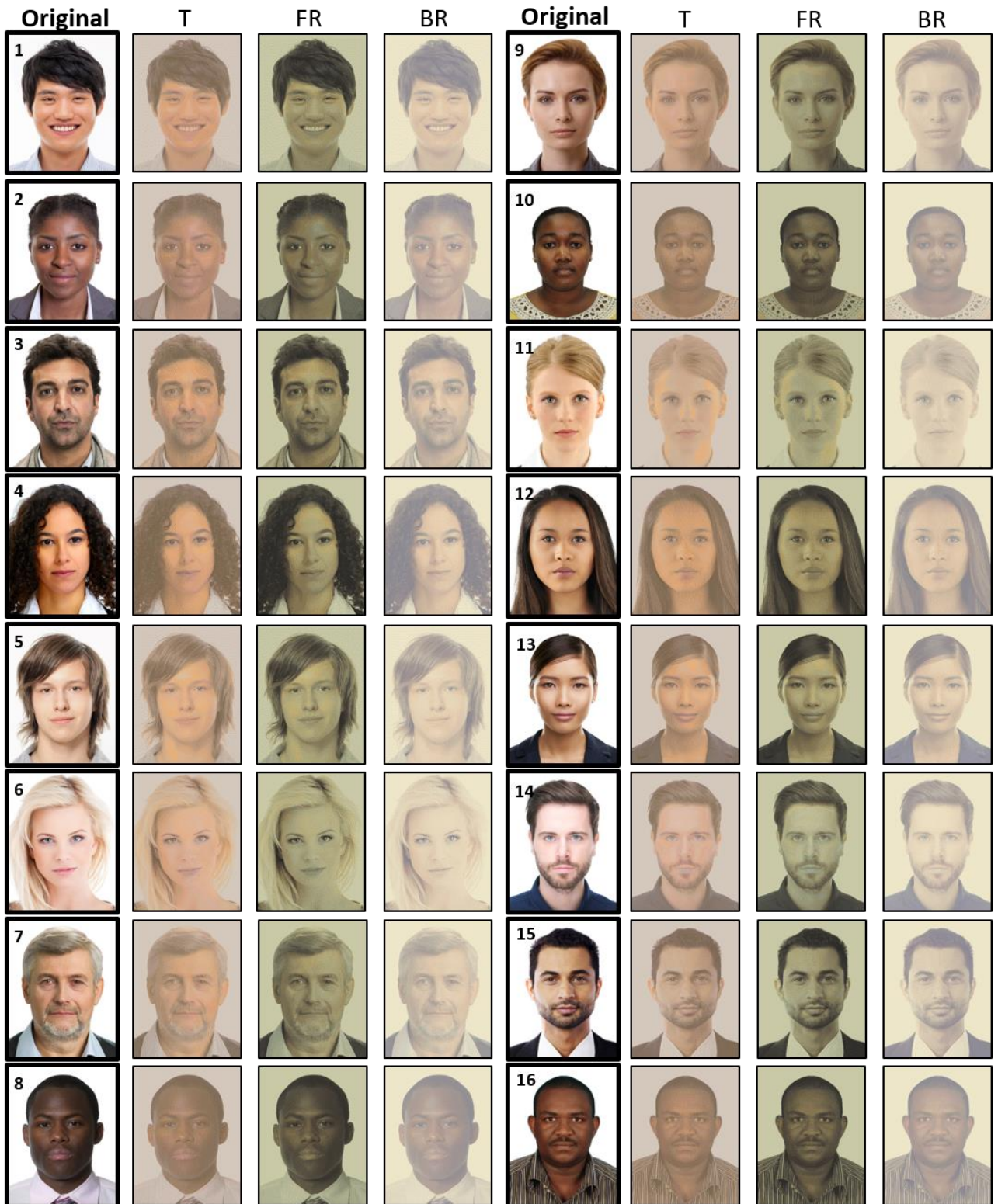


Figure 53: 16 portraits and their respective simulations are divided in two columns. From left to right, for each portrait, the first image is the original one, the second to fourth ones are the virtual mapped image after halftoning using 10 primaries for transmission (T), frontside reflection (FR) and backside reflection (BR).

### 3.3.1.3. Definition of the metrics

The criteria used in this process relate to metrics that can be quantified from the knowledge of the color gamut. Figure 54 depicts the color gamuts recorded in (a) transmission, (b) frontside reflection and (c) backside reflection modes in a 2D representation. For each mode, the gamut is projected in the  $L^*C^*$  and  $a^*b^*$  plane that are utilized to define the following metrics.

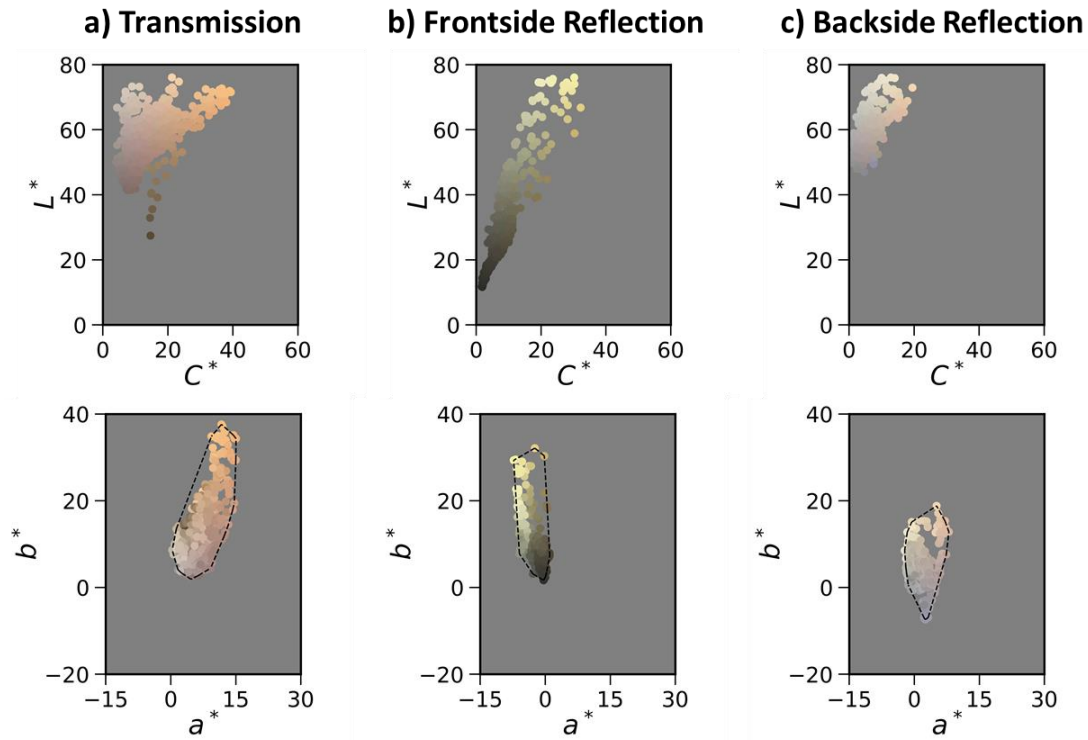


Figure 54: The database colors detected in “transmission” (a), “frontside reflection” (b) and “backside reflection” are illustrated in a 2D representation. On one hand the color’s luminance  $L^*$  is plotted as a function of the chroma ( $C^*$ ). Each colored point represents a nanostructure. On the other hand, in the  $a^*b^*$  plane with the dashed black line depicting the convex hull of the points, which represents the attainable colors.

The first metric relates to evaluating the contrast of the images by determining the maximum variation of lightness in the image. For this, the lightness distance, named  $\Delta L^*$ , between the black and white colors found in the database are visualized in the  $L^*C^*$  projections for each mode and is calculated as followed:

$$\Delta L^* = L_{white} - L_{black} \quad (\text{Equation 11})$$

The second criterion is the variety of colors which corresponds to the “gamut volume” metric, i.e. to the minimum volume that contains all the data points in the CIE1976, or to the area of

the projection of this gamut in the  $a^*b^*$  plane depicted in figure 54. The different metrics extracted from the color gamuts are summarized in table 4.

*Table 4: Main features of the color gamut in the CIE1976  $L^*a^*b^*$  color space for the printed database observed in three different observation modes.*

<b>Observation mode</b>	<b>Transmission</b>	<b>Frontside reflection</b>	<b>Backside reflection</b>
<b><math>\Delta L^*</math> (distance between black and white)</b>	46	53	30
<b>LAB volume (CIE <math>L^*a^*b^*</math> units)</b>	8300	3680	2945
<b>Area in <math>a^*b^*</math> (CIE <math>a^*b^*</math> units)</b>	309	189	171

However, one has to pay attention to the fact that the database gamuts measured in the three modes are not centred on the ( $a^*=0, b^*=0$ ) axis and can be localized in a part of the  $a^*b^*$  plane. It means that the number of hues can be limited and this can be a problem when assessing the color fidelity. Thus, one must also consider a metric related to the diversity of colors and their proximity to the colors present in the original image. This leads to the third and final metric called “density difference” to characterize this property. All numerical tools used for this have been elaborated by a master 1 student, Aldi Wista Fadhilah.

To evaluate it, the distorted gamuts measured for (a) each observation mode and (b) the 16 portraits are calculated after selecting the white and black colors of the gamut and shifting them to ( $a^*=0, b^*=0$ ) axis as presented in figure 54. The ( $a^*, b^*$ ) plane is then divided in 36 sectors (pie portion) of  $10^\circ$  each and we define a normalized density  $n_{Density}$  of color points per sector using the following formula:

$$n_{Density}^s = \frac{\text{number of points in a sector } s}{\text{total number of colors in the sample}} \quad (\text{Equation 12})$$

The measured  $n_{Density}$  of the 16 portraits are given in Annex 6 for each sector, while the values extracted for each observation mode are summarized below in table 5.

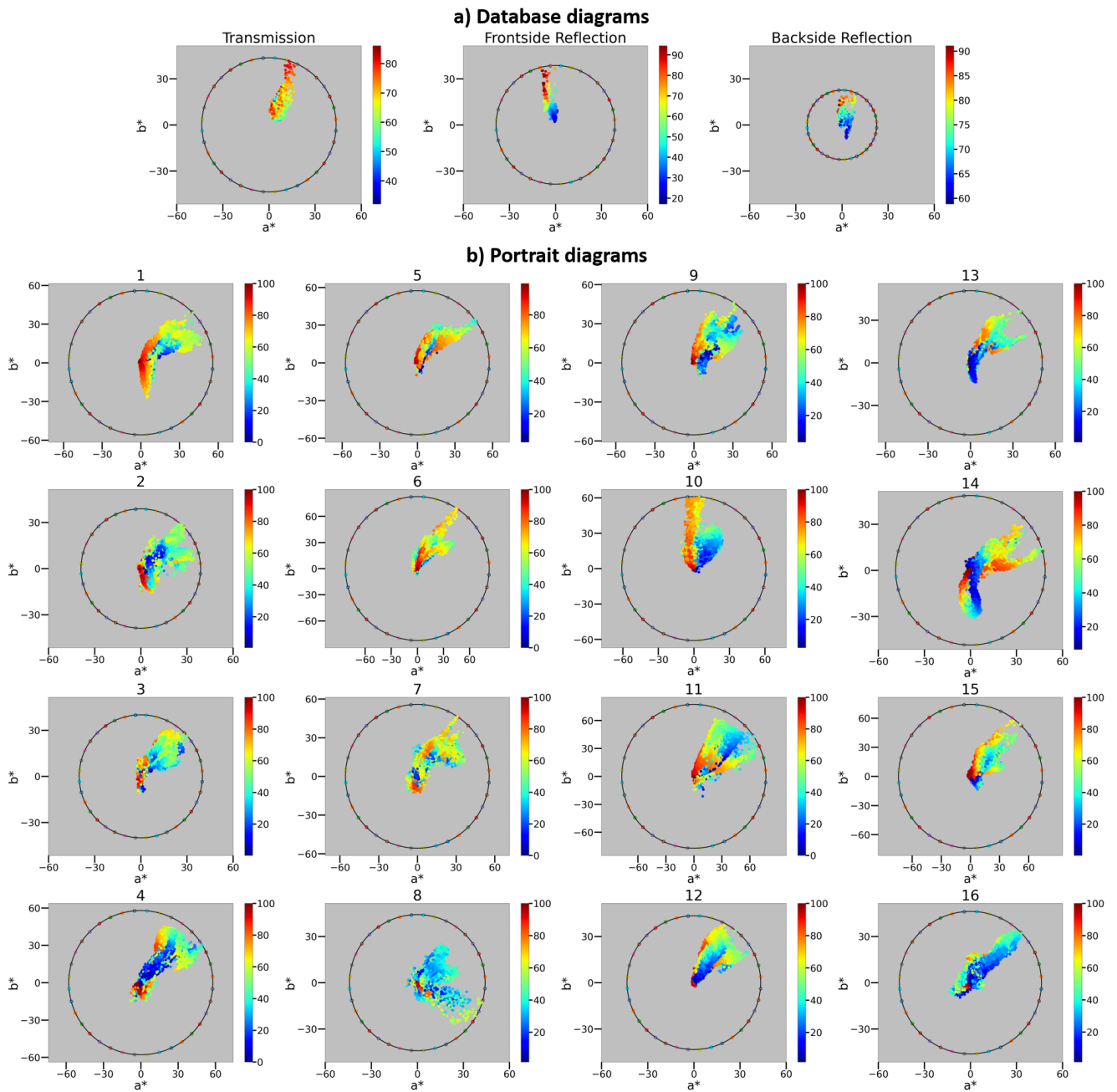


Figure 55: (a) 2D  $C^*h^*$  circular diagrams projected in the  $a^*b^*$  plane of the database (a) observed in transmission, frontside reflection and backside reflection, and for the 16 portraits (b). Each point corresponds to the color extracted of a nanostructure and are color-coded based on their luminance ( $L^*$ ). Additionally for every projection the diagram is divide into 36 sectors.

Table 5: Normal density values extracted for each sector based on the hue diagrams of the colors of the database observed in different observation modes.

Sector	Transmission	Frontside Reflection	Backside Reflection
1			0.00833
2			0.00417
3	0.00417		0.00625
4	0.08958		0.00417
5	0.12708		0.00625
6	0.13750		0.00208
7	0.21875		0.02083
8	0.33125		0.01667
9	0.08750	0.01875	0.00833
10	0.00417	0.20000	0.01667
11		0.47500	0.03333
12		0.25208	0.02083
13		0.04792	0.00833
14		0.00625	0.00833
15			0.00625
16			0.00625
17			0.00625
18			0.00417
19			0.03333
20			0.13542
21			0.17083
22			0.08333
23			0.03542
24			0.02292
25			0.01042
26			0.01042
27			0.00625
28			0.03750
29			0.10208
30			0.06875
31			0.04792
32			0.02083
33			0.01042
34			0.01250
35			
36			0.00417

The “density difference” allows to compare the normalized density of two gamuts, sector per sector, and to give a total number as follows:

$$D_{n_{Density,i,x}} = \sum_{s=1}^{36} |n_{Density,i}^s - n_{Density,x}^s| \quad (\text{Equation 13})$$

Where  $i$  relates to the gamut of an original image and  $x$  to the gamut of the selected mode for the image to be printed.  $s$  is the number of sectors. The lower the value of the density

difference, the better the performance of the mode in terms of color fidelity. The calculated density differences are summarized in table 6.

*Table 6: Density difference values calculated between every input image (16 portraits) and each observation mode. The average distance values is given for every mode.*

<b>Portrait</b>	<b><math>D_{Transmission}</math></b>	<b><math>D_{Frontside Reflection}</math></b>	<b><math>D_{Backside Reflection}</math></b>
1	1.43	1.89	1.50
2	1.13	1.87	1.78
3	1.14	1.79	1.68
4	1.29	1.86	1.62
5	1.28	1.68	1.72
6	0.88	1.84	1.80
7	1.24	1.89	1.65
8	1.02	1.86	1.82
9	0.94	1.80	1.63
10	0.66	1.80	1.77
11	0.92	1.79	1.75
12	0.85	1.82	1.62
13	1.03	1.79	1.76
14	1.36	1.89	1.70
15	1.26	1.88	1.66
16	1.25	1.89	1.58
<b>Average</b>	<b>1.10</b>	<b>1.79</b>	<b>1.69</b>

#### 3.3.1.4. Discussion about the gamuts and metrics

Based on the results in table 4, and if the features are considered independently, one could conclude that the mode with the biggest gamut volume (T mode) is the best one, which correlates with what was concluded from the visual observation. Moreover, the gamut area ( $a*b^*$ ) metric ranks the modes in the same manner. However, the mode presenting the highest contrast is the FR mode, which does not correlate. In BR mode, the color variation and contrast present the lowest values among the three modes, thus qualified as the least interesting one.

The hue diagrams in figure 55 confirm that the printed database has always a smaller color gamut than the original image, as already assumed when describing the gamut mapping method. This figure also highlights the fact that the printed database gamut may contain hue ranges that are very limited and completely different from the one of the original gamut.

Despite T mode presenting the highest  $a^*b^*$  surface, the colors are condensed in a portion of the hue diagram as seen in figure 55.a. The same can be said for FR mode where the colors are limited in a different area of the hue diagram. This statement is supported by the normalized density values measured for both modes, covering only a few sectors, while the original images cover the majority of the diagram as seen in figure 55.b. Therefore, the color variation is not as important as previously suggested for both T and FR mode. On the other hand, in BR mode the colors are well distributed in the hue diagram of figure 55.a. However, the chromaticity (color saturation) and luminance (lightness) are rather limited compared to both T and FR modes. The calculated “density differences” presented in table 6 correlate the color gamuts of the database to each of the 16 portraits. In T mode, the density difference is the lowest compared to both FR and BR mode, making it the best one for this specific set of images thus correlating to the preliminary observation.

Obviously, correlation does not mean causality and this simple study cannot allow to conclude about the relevance of these metrics for ranking any kind of image. However, this first investigation suggests that several metrics could be considered to assess objectively the quality of the simulated images in different modes of observation by considering the limited color (lightness, hue, chroma-saturation) range produced in various modes of observation by ns laser processing of our plasmonic nanocomposite films inside the PC cards.

An example that shows that, if the database or input images are changed, the results might differ is presented in figure 56. An image with different saturated colors is considered here, printed with the same database as previously and simulated in the three observation modes T, FR and BR. With this image the metrics “density difference” ranks the BR mode first ( $D_{Backside\ reflection} = 1.13$ ) ahead of modes FR and T ( $D_{Transmission} = 1.54$ ;  $D_{Frontside\ reflection} = 1.23$ ). One can see that even if the colors indeed look closer in R mode to the ones of the original image in this mode the contrast is poor and may cause an observer to prefer the other images.

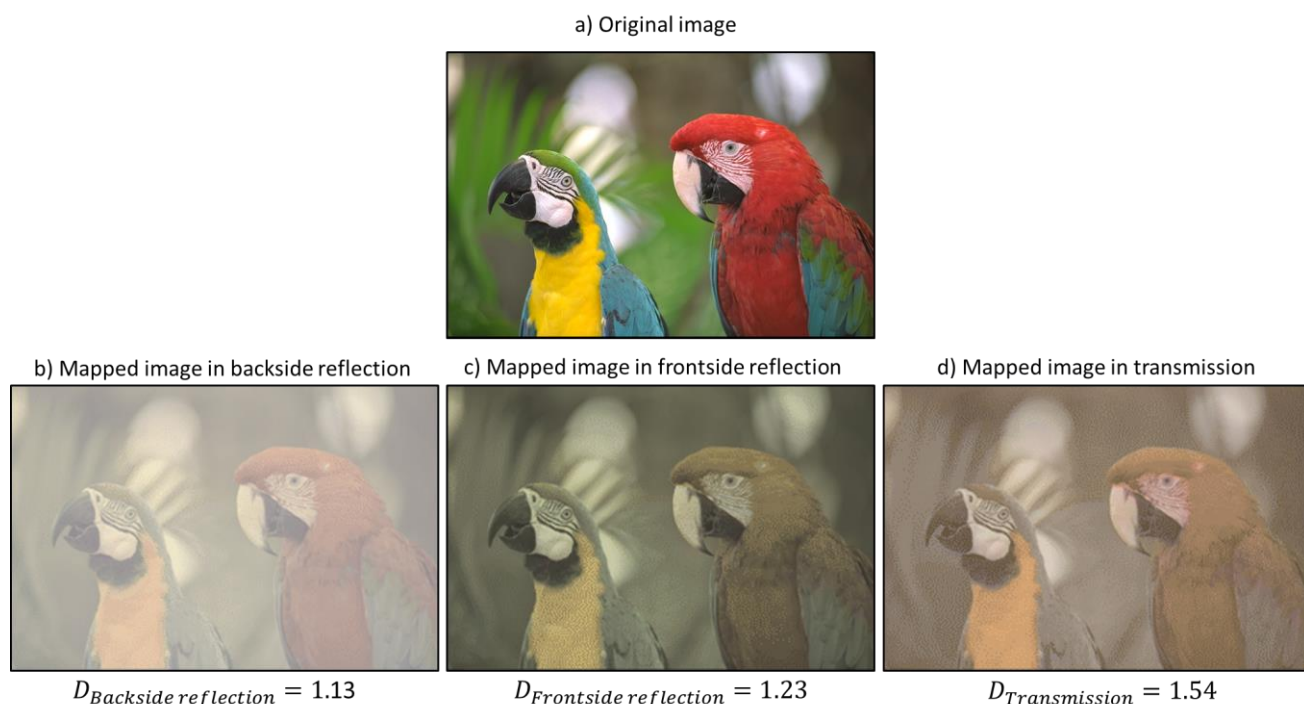


Figure 56: (a) Image of two colorful parrots are gamut mapped in three observation modes, backside reflection (b), frontside reflection (c) and transmission (d). For each mode, the distance differences of the normal density of the image versus the mode is given.

Further study should consider a larger library of different kinds of images, subjective assessment by an observer panel and not only one observer, statistical evaluation of different criteria, and correlations with weighted linear combination of metrics.

### 3.3.1.5. Conclusion

Quality image assessment for such a technology requires developing specific metrics and assessment procedures and cannot be automated easily at this stage. For industrialization purpose, proposing an automatic optimization of the whole printing process with quantified assessment of the results will make sense. Further investigation must be done in this direction to support the development of this technology.

However, to progress in the development of the elaboration process of the materials, which was the main objective of this PhD work, subjective assessments of image quality have been used. In the following steps, the colors in T mode will be used to produce high quality image printing.

### 3.3.2. Reproducibility of laser-printed colors

The following numerical tools used in this section were developed by Robin Mermillot-Blondin, PhD student.

#### 3.3.2.1. *Drawbacks and limitations*

The reproducibility of colors is difficult to achieve in a sample and more so from sample to sample, which hinders the efficiency of this technology. This can be attributed to both the material and the laser setup as they present some drawbacks.

Local defects due to dusts, scratches or impurities are also largely present on the final cards. These defects can strongly affect not only the selection of the primaries as stated in part 3.1.4.5 but also the final printed image when the defects are present in the printed area.

Thickness variations within a film strongly can influence the printed colors. In the case of this manuscript, the titania matrix is prepared by spin-coating on flexible substrates. During this process, the support is maintained on the stage by vacuum suction, producing a slight bending of the sample in some cases and leading to inhomogeneities, namely on the edges of the sample. Unfortunately, due to the nature of the substrates, it was not possible to measure systematically the film thickness variations. Additionally, working with silver nanoparticles makes also the reproducibility tricky. Introducing silver salt in the mesoporous TiO<sub>2</sub> film by soaking and rinsing the silver overload on the surface before drying is done manually and requires to reproduce accurately the know-how. Varying the silver load in the film can strongly affect the Ag NPs size and density after laser processing and the resulting colors. Before lamination, when the silver loaded films are exposed to ambient conditions, the size and density of Ag NPs can evolve in time as it was demonstrated by N. Sharma in his thesis<sup>119</sup>. The time and the storage condition of these films must be well controlled until lamination, which is why it was done in the first 48 hours after silver loading. The stability of the materials embedded in a PC card was investigated by UV-Visible spectroscopy presented in figure 57. On one hand the ageing of the film (black curve) over time was evaluated after 9 months (dotted black curve), depicting a fairly good stability. On the other hand, two additional materials from different batches were investigated after lamination (red and green curves) depicting slightly different optical behaviour.

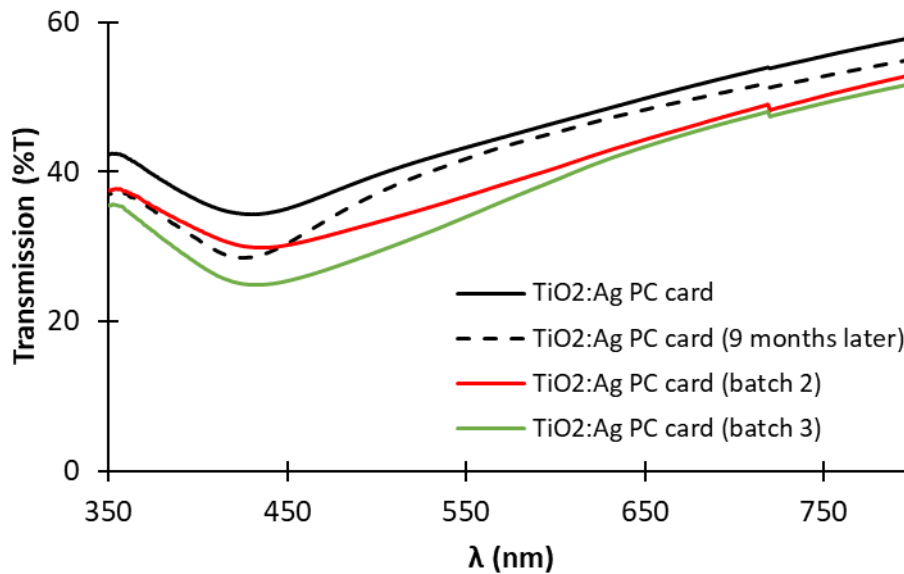


Figure 57: UV-Visible transmission spectra of TiO<sub>2</sub>:Ag PC cards. The solid black curve represents the measurements carried after laminating a TiO<sub>2</sub>:Ag PC card (batch 1) and the dotted curve represents the same sample after 9 months. Other samples prepared in the same manner are characterized and illustrated by the red and green curves, belonging to different sample batches (2 and 3).

On the three samples presented above, the database was inscribed and the colors were measured with the camera setup. Figure 58 illustrates the sRGB color values extracted for each square in the database in a 2D representation following the scheme. For each square (nanostructure), the extracted sRGB colors are represented following the scheme presented on the right of the figure. In summary, the database is divided in 4 parts based on the repetition rate (10, 20, 40 and 50 kHz), each section contains the same power variations (10) and scanning speeds (12) as described in part 3.1.2. It is evident that color discrepancies occur from batch to batch as the colors are different for some sets of laser parameters. However, it is worth noting that despite the color differences, some color trends were detected for some groups of laser parameters. For example, for the three samples, at low power, low scanning speeds and at 40 and 50 kHz, yellowish colors are produced, while at high scanning speeds, some brownish colors are produced.

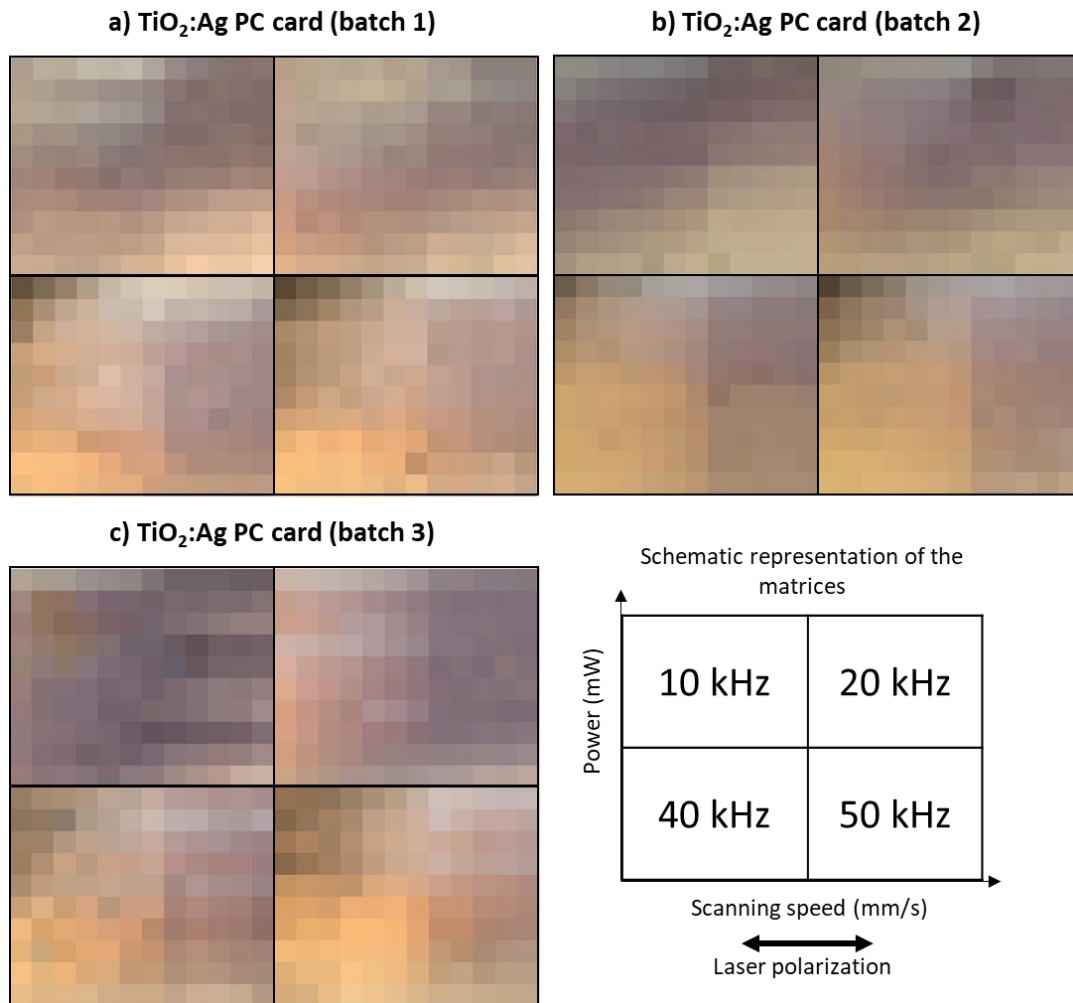


Figure 58: The database was printed in three different samples belonging to three different sample batches (a, b and c). The colors were characterized in transmission and represented in a 2D projection following the scheme.

These discrepancies can also be related to the laser processing, as the samples are placed in a sample holder for laser marking. After the inscription the cards are removed from it and placed in the camera setup for the color extraction. Then, the sample is placed back in the holder of the laser setup but not necessarily at the same exact position which could lead to slight displacements of the surface and thus affect the produced colors. To solve this issue, it would be advantageous to build the camera and laser setups together to avoid moving the sample.

The pixel size after laser processing varies with the processing parameters (power, scan speed, repetition rate) and juxtaposing a small pixel with a larger pixel may change the expected halftone color despite the addition of the margin. One has to pay attention to the color mixing result when involving very different parameter values in an image. To illustrate this phenomenon, a palette selected by the color gamut algorithm consisting of 10 primaries

is used with the laser parameters described in Annex 7. This can be quantified by calculating the color differences of a halftoning matrix by printing “50/50” patches coupling the nanostructures in the palette. Figure 59.a illustrates an example where pixels with parameters “A” and “B” are alternated homogeneously to create a 50%/50% halftone. Figure 59.b depicts the resulting print characterized with the camera setup using the 10 primaries of the palette. The color values of each nanostructure “100” patches are extracted independently and a theoretical average of every “50/50” patch is calculated in the CIE 2000 color space. These theoretical average values are compared to the experimental “50/50” measured colors by calculating the color difference, “ $\Delta E_{2000}$ ”, in the CIE 2000 color space. The lower the values of  $\Delta E_{2000}$ , the closer the experimental colors are to the expected ones. In figure 59.c, the sRGB colors values of the “100” and the “50/50” patches are represented in a 2D plane.  $\Delta E_{2000}$  values in the “50/50” patches are depicted in green if the values are lower than 5, which relate to colors considered perceptually similar. Values above 5 are depicted in red, highlighting a bad color mixing between the two nanostructures. It is observed that all the nanostructures can mix fairly well with values comprised between 1 and 5, except for the nanostructure (8) that does not mix well as high  $\Delta E$  values are detected (in red). For instance, here, nanostructure (8) has a high laser power and low scanning speed compared to others, resulting in larger processed areas compared to others despite adding a margin to separate the pixels accordingly. To visualize this, figure 59.d depicts pixels printed together and the red dotted square represents 4 neighboring pixels. The “black” squares (nanostructure 8) are significantly larger than the “yellow” pixels (nanostructure 7) resulting in an overlapping of the pixels, thus having a bigger color contribution. To be able to avoid this, developing a model that predicts the processed areas based on the laser parameters would be beneficial. This way the pixels could be designed accordingly to the laser parameters and obtain consistently good halftoning. One can imagine that pixels with high fluence and low scanning speed would have a “smaller” theoretical size in the *CsMark* software compared to pixels with lower fluences and/or lower scanning speeds to avoid overlapping.

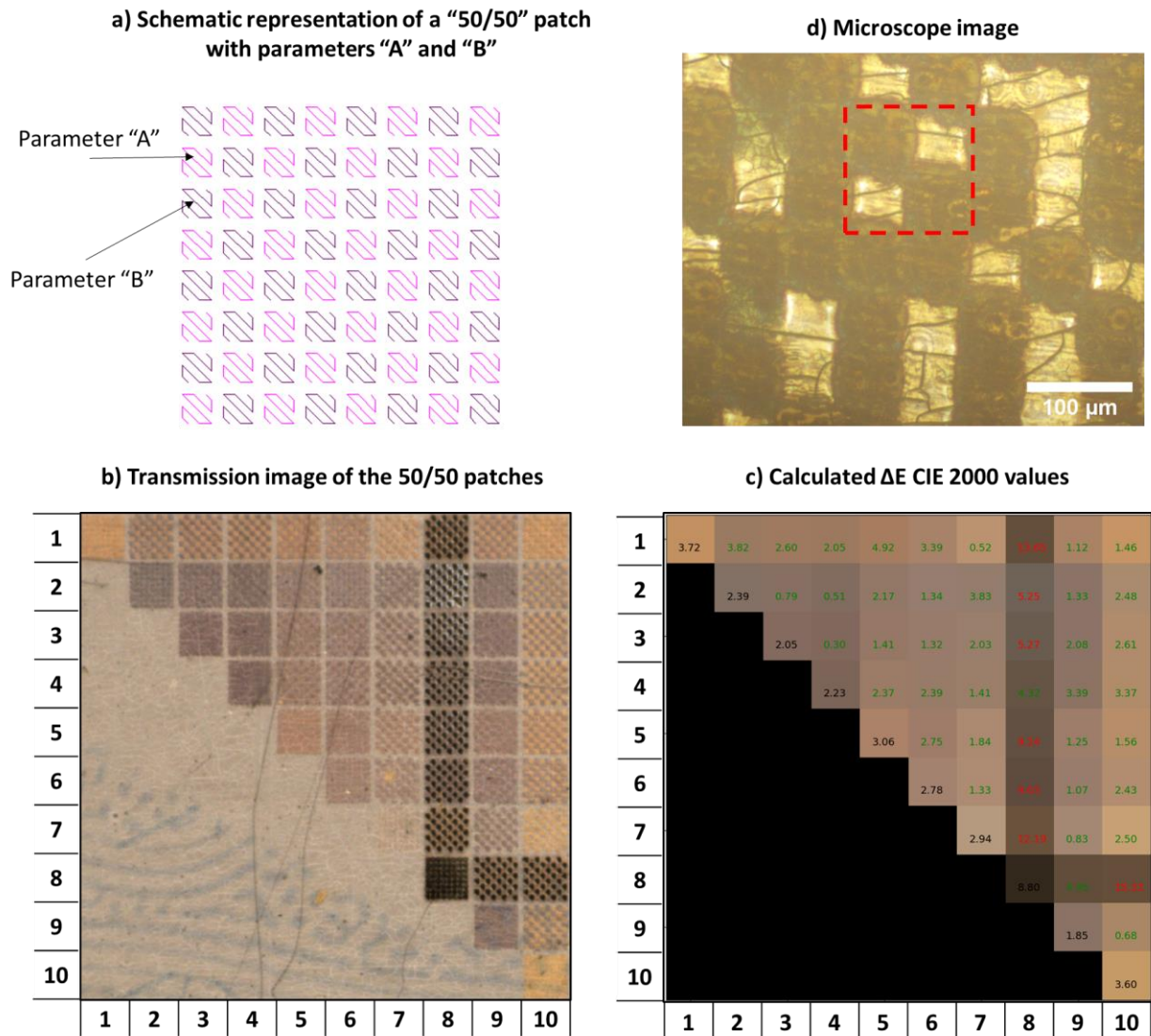


Figure 59: “50/50” patches (a) were constructed by coupling the nanostructures of the palette and (b) printed in a  $\text{TiO}_2\text{:Ag}$  PC card. The calculated color differences  $\Delta E_{2000}$  values (c) of the “50/50” patches are extracted and highlighted in green if the difference values are below 5. Values higher than 5 are depicted in red, sign of bad color mixing. (e) Optical microscope image of laser-processed pixels ( $50 \times 50 \mu\text{m}^2$ ) showcasing bad halftoning. The red dotted square represents four neighbouring pixels. The “black” squares (nanostructure 8) cover larger areas compared to the “yellow” squares (nanostructure 7) even though they should be similar for the halftoning to work.

Figure 60 displays an example where a printed portrait that does not look as expected from the simulation (in transmission mode). The bad color reproduction in Figure 60.c makes the traits of the face difficult to recognize. This bad result may come from a combination of the issues listed above. An empirical methodology has been implemented to overcome this kind of issues and improve the results whatever the state of the fabricated card.

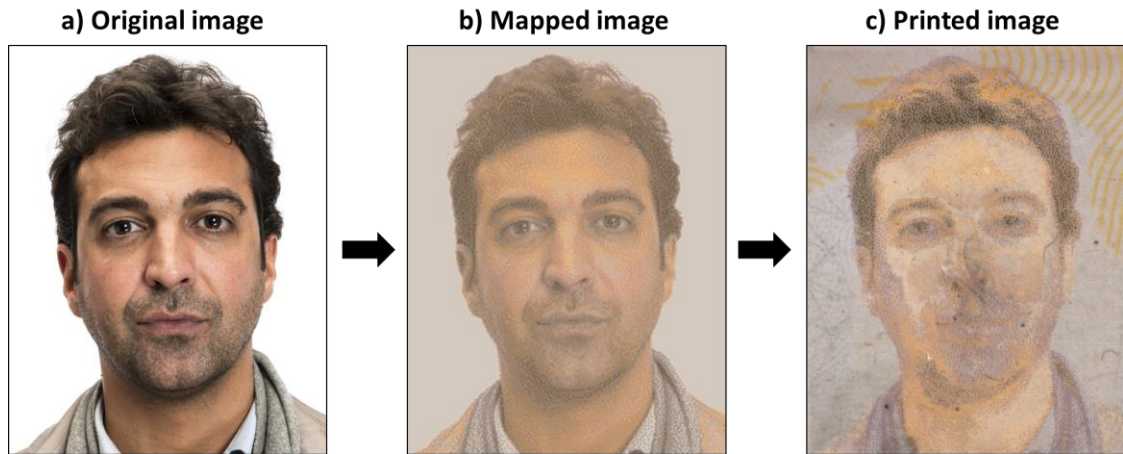


Figure 60: (a) Original image is gamut mapped in transmission mode (b), vectorized and printed on a PC TiO<sub>2</sub>:Ag card (c) depicting several printing errors.

### 3.3.2.2. Primaries selection

As previously said the samples inhomogeneities lead to color discrepancies from batch to batch. Therefore, the following study was performed on a single batch (batch 1 in figure 58) and then evaluated on other batches.

The color selection during the clustering step is a crucial part of the printing result. The primaries selection of the primaries is purely based on the color values and not on the laser parameters. In the following section, a strategy is described where a compromise is made between the most optimal laser parameters and the color values to select a primary, ensuring a good reproducibility of colors with relatively low color variations.

The first step is to investigate the distribution of color clusters of the database relative to the laser parameters of each nanostructure. Each nanostructure has three characteristic parameters, the laser power, scanning speed and the repetition rate, thus a 3D plot of each color would be ideal to be presented. However, visualizing them in 3D can be quite tricky and difficult to appreciate, therefore the nanostructures are illustrated in a 2D representation of the database observed in transmission mode as depicted in figure 61. To highlight the clusters, each square is tagged with a small square whose color corresponds to a specific cluster, thus 10 distinctive colors are used to highlight the 10 clusters. To better visualize the clusters, the palette containing the primary of each cluster is illustrated at the bottom of the figure.

## Representation of the extracted sRGB colors of the database

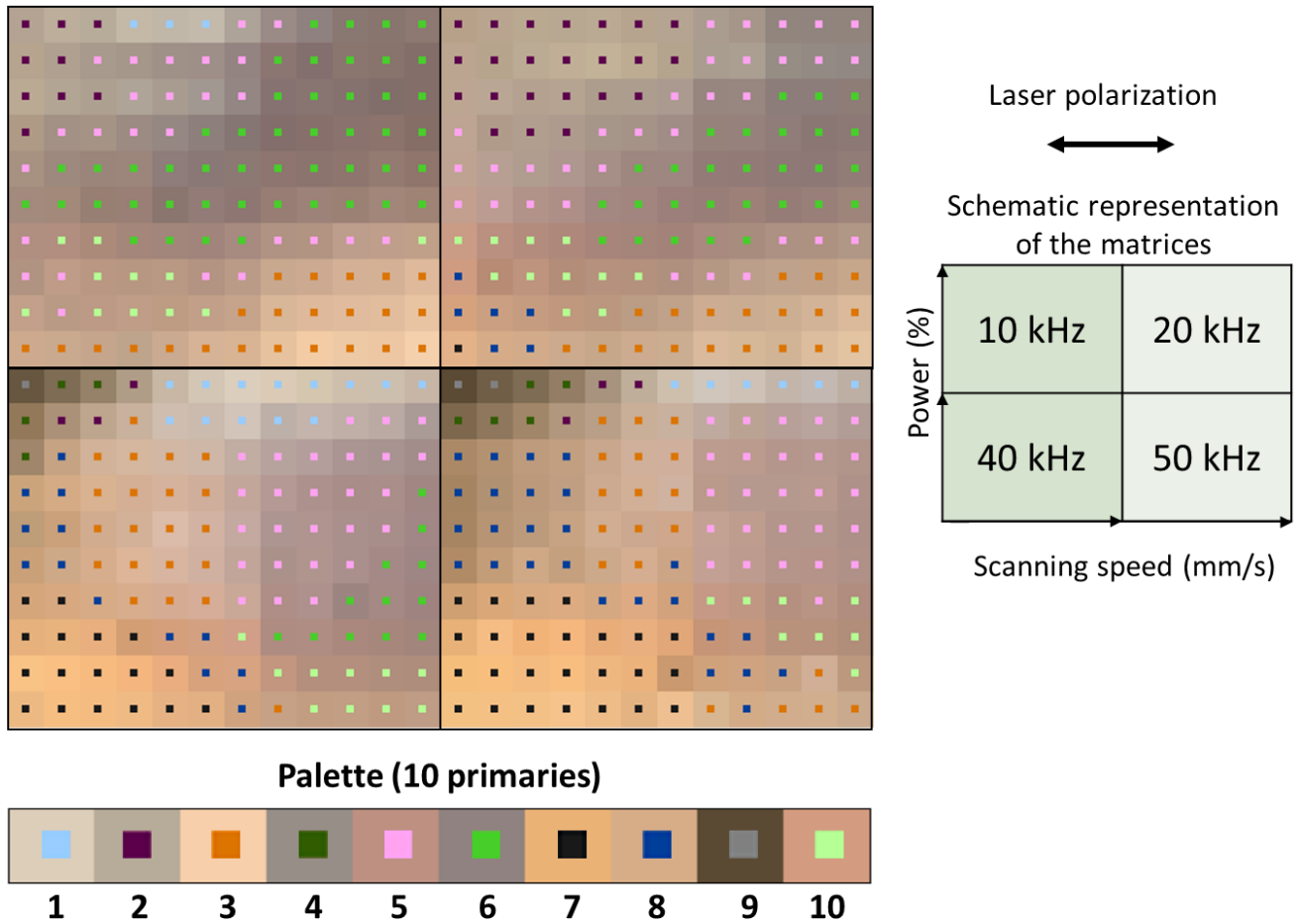


Figure 61: On the left, the database observed in transmission mode is represented by the extracted sRGB color values of each square. Each of them is marked with a color coded small square which relates to their affiliation to one of the 10 clusters as highlighted by the color palette. On the right, a schematic representation of the database is given with their corresponding laser parameters.

It is observed that similar color gradients can be produced using different repetition rates, laser powers and/or scanning speeds. For example, for repetition rates of 10, 40 and 50 kHz colors belonging to cluster (2) coded in purple are produced using a few powers and scanning speeds. However, for 20 kHz, the same colors can be generated using 22 different neighbouring sets of laser parameters. This means that for a wide range of laser powers and scanning speeds the color variation is quite limited. This can be beneficial to improve the reproducibility of the color if it is produced by an “intermediate” set of laser parameters. If there were any processing errors due to small laser power fluctuations, the color would still be consistent, as either a smaller or higher power can result in the same color according to the database. To showcase this an example is given in figure 62 with cluster (2) colors present

in both 50 (a) and 20 kHz (b) sections. In figure 62.a, the nanostructure with 22% laser power and a 60 mm.s<sup>-1</sup> scanning speed at 50 kHz is surrounded with colors associated to different color clusters as depicted with the red arrows. Therefore, if any processing errors occur the color produced could certainly be different. However, in figure 62.b, with a repetition rate of 20 kHz, same laser power and scanning speed the nanostructure is surrounded with colors from the same cluster hence, despite any potential processing errors, the color generated would likely be reproducible. Therefore, this nanostructure is selected as the primary for cluster (2).

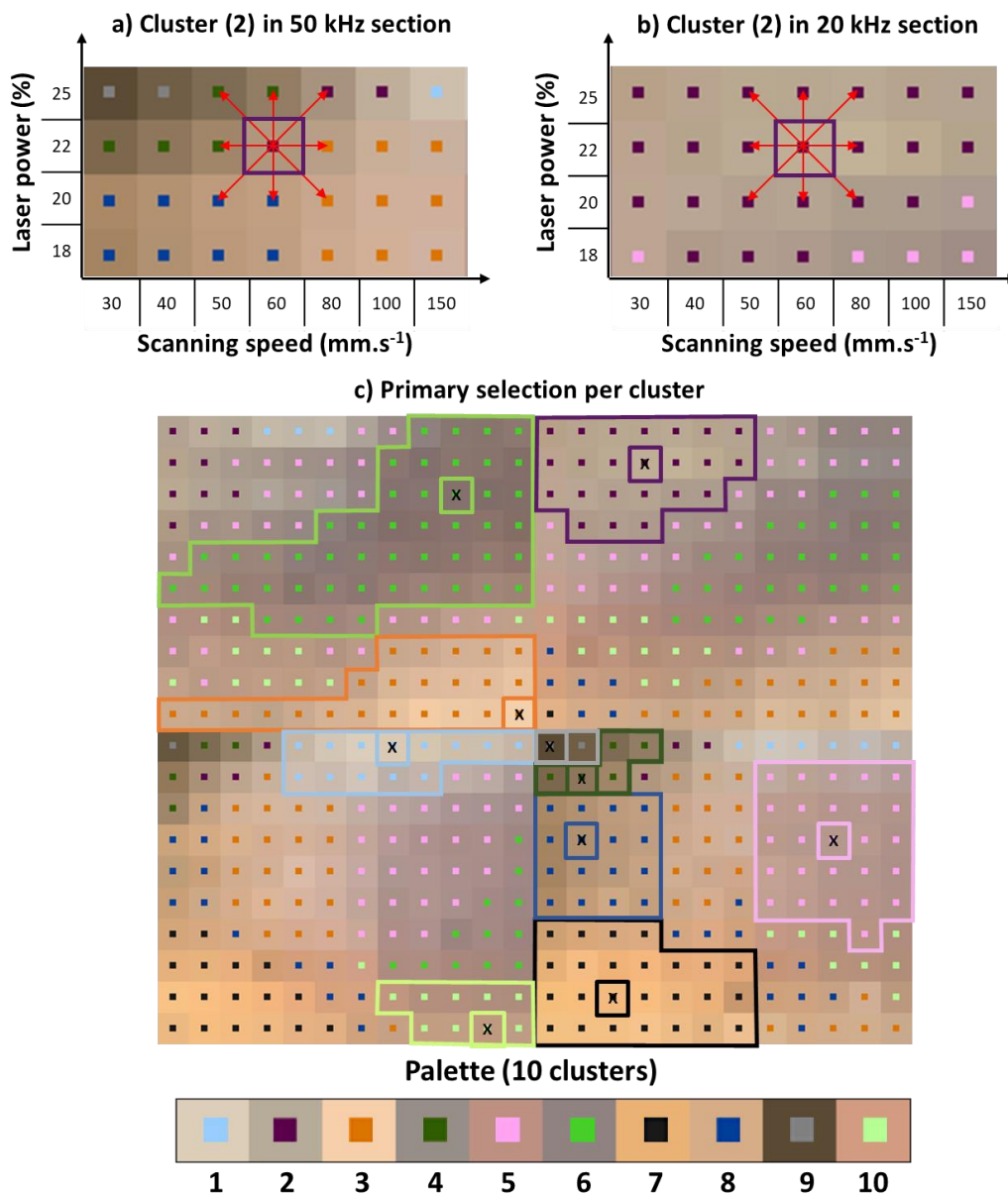


Figure 62: Nanostructures with colors belonging to cluster (2) are depicted in the (a) 50 kHz and (b) 20 kHz sections. For each repetition rate, a nanostructure and their neighboring squares are highlighted. In the 50 kHz section (a), the nanostructure is surrounded with

*nanostructures with similar laser parameters but very different colors. Whereas in the 20 kHz section (b), the nanostructure highlighted is surrounded with identical colors using similar laser parameters. (c) For the selection of the primary for each cluster, the largest area is highlighted in the corresponding color code. Then, within the area, the primary is selected at the center of it as highlighted with an (X).*

The same strategy can be applied to other clusters containing a variety of laser parameters such as clusters (1), (4), (5), (6), (7), (8) and (10) as depicted in figure 62.c. For each of these clusters, the selected nanostructure is highlighted with an (X) and their corresponding laser parameters are given in table 7. The selection for clusters (3) and (9) is quite particular as they represent respectively the white and black colors so the priority was on the most achromatic nanostructures with the highest luminance for the white color (brightest) and the lowest one for the black color (darkest).

*Table 7: Laser parameters of the final 10 selected primaries*

<b>Primary n°</b>	<b>Repetition rate (kHz)</b>	<b>Laser power</b>		<b>Fluence (mJ/cm<sup>2</sup>)</b>	<b>Scan speeds (mm/s)</b>
		<b>(%)</b>	<b>(mW)</b>		
<b>1</b>	40	25	45.2	77.5	600
<b>2</b>	20	22	43.5	71.9	60
<b>3</b>	10	6	18	33.3	1500
<b>4</b>	50	22	43.5	71.9	40
<b>5</b>	50	18	36.5	60.1	800
<b>6</b>	10	20	38.2	64.2	800
<b>7</b>	50	8	20.4	37.9	50
<b>8</b>	50	18	36.5	60.1	40
<b>9</b>	50	25	45.2	77.5	30
<b>10</b>	40	6	18	33.3	1000

### 3.3.2.3. Color reproducibility assessment

The reproducibility of the 10 selected primaries is investigated by calculating the color differences between several prints of each primary. Each one of them is printed at least 5 times following the laser parameters described in table 7. The sRGB color values of each nanostructure is extracted and converted to the CIE 1976 L\*a\*b\* color space. Then, the color difference,  $\Delta E$ , is calculated between a single inscription and the average of all inscriptions for every primary. The results are depicted in table 8 where for every primary  $\Delta E$  values are calculated between the color values of an inscription and the average of them all. Subsequently, the average  $\Delta E$  value is calculated for every primary. The average  $\Delta E$  values are comprised between 1 and 3 with the highest recorded  $\Delta E$  value being for primary (9) at 2.75.

Therefore, the color differences between inscriptions are barely perceptible unless observed at close observation meaning that the reproducibility of the colors is correct within a sample.

The same process was carried on a different sample (2) from the same batch where the average  $\Delta E$  values are also mostly comprised between 1 and 2  $\Delta E$  values as presented in table 8 (right column), reinforcing the good reproducibility of the selected colors.

*Table 8:  $\Delta E$  values of each inscription versus their average. The average  $\Delta E$  values are given for each primary for two different samples.*

Primary n°	Inscription ( $\Delta E$ value of a color vs average)					Average $\Delta E$	Average $\Delta E$ (sample (2))
	1	2	3	4	5		
1	2.45	2.13	1.43	2.91	2.50	<b>2.28</b>	<b>1.04</b>
2	0.63	1.75	1.24	0.68	0.99	<b>1.06</b>	<b>1.15</b>
3	0.86	0.71	0.43	0.58	0.45	<b>0.61</b>	<b>1.76</b>
4	1.86	1.37	2.17	2.16	1.65	<b>1.84</b>	<b>1.71</b>
5	0.98	1.08	1.32	2.20	1.32	<b>1.38</b>	<b>1.54</b>
6	0.83	0.97	1.47	1.35	2.79	<b>1.48</b>	<b>1.69</b>
7	1.17	0.81	0.67	1.22	0.43	<b>0.86</b>	<b>2.00</b>
8	1.06	1.17	2.06	0.33	2.14	<b>1.35</b>	<b>1.75</b>
9	0.77	2.52	2.30	3.69	4.48	<b>2.75</b>	<b>2.86</b>
10	2.16	2.29	2.37	0.49	1.63	<b>1.79</b>	<b>0.66</b>

#### 3.3.2.4. Full-color image printing

Now that the reproducibility of the color palette has been verified, six images of the 16 portraits are gamut mapped and printed in different samples as depicted in figure 63. For each set of images (1 to 6), the original image is presented on the left, the mapped image in the middle and the printed image on the right. To print, the mapped image is vectorized in the CSmark software into a printable image consisting of 210x269 pixels (50x50  $\mu\text{m}^2$ ) resulting in a 10.5x13.45  $\text{mm}^2$  printed image. The processed image is observed with the usual color setup and normalized. Overall the color reproduction is good despite the presence of artefacts hindering the quality of the print.

### Palette in T mode (10 primaries)

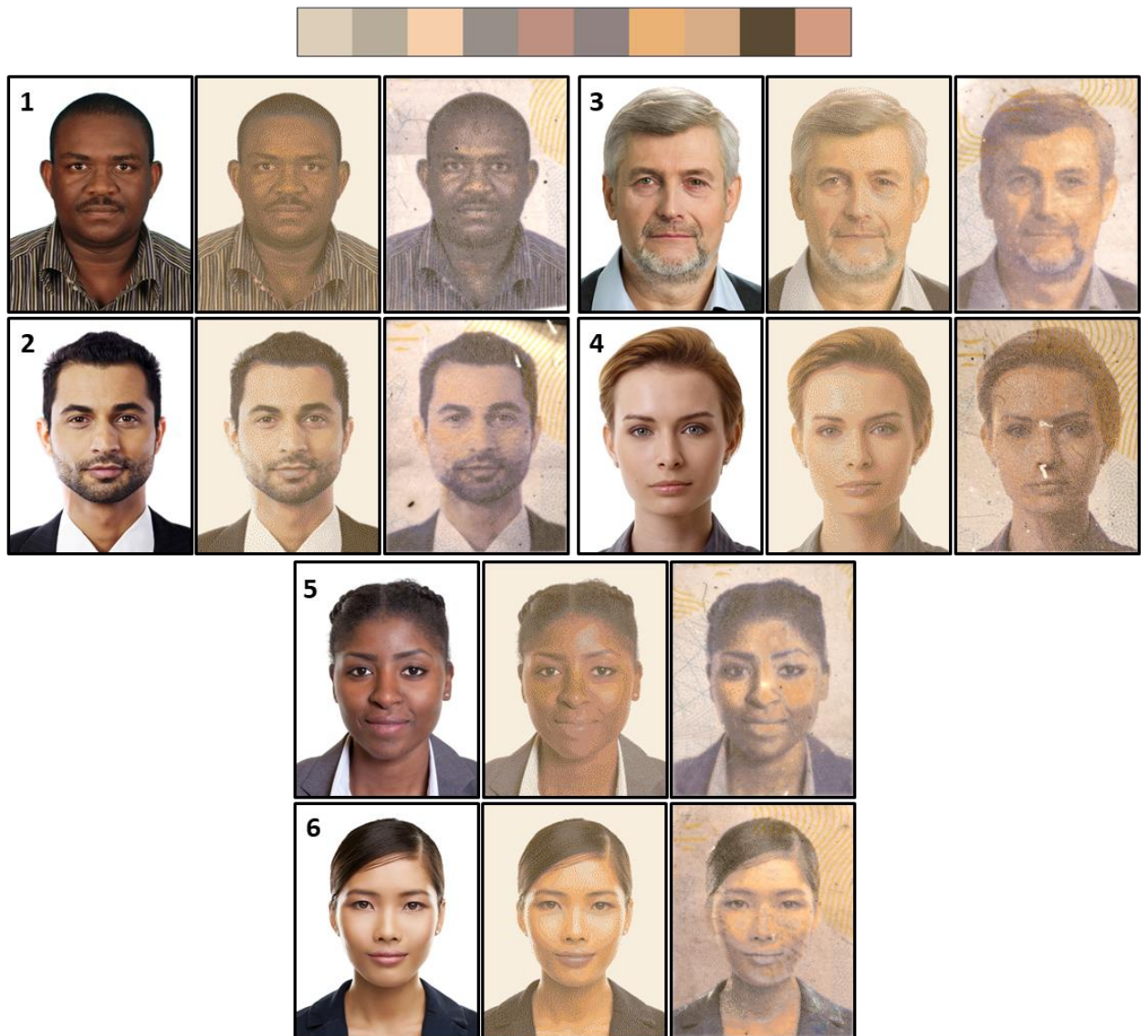


*Figure 63: 6 portraits are gamut mapped, vectorized and printed in different PC TiO<sub>2</sub>:Ag cards using the 10 primaries observed in transmission mode as depicted on top of the figure. The dimensions of every printed image are 10.5x13.45 mm<sup>2</sup>.*

Furthermore, the reproducibility of a single image was tested on different samples depicted in figure 64. The original image (a) is mapped in transmission mode (b) and printed in three different samples from the same batch (c, d and e). The printed images present similar results in terms of color reproducibility and high quality.

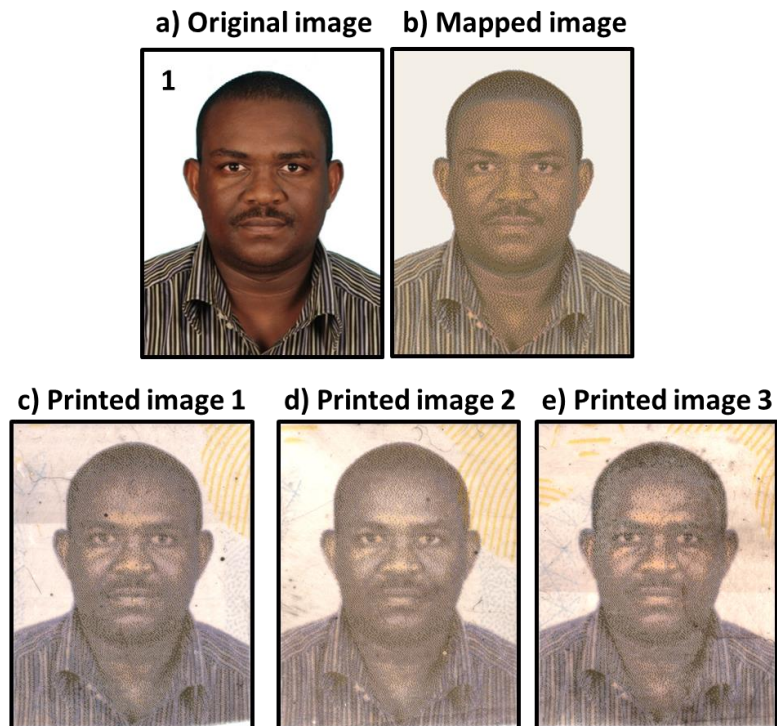


*Figure 64: The original portrait (a) is gamut mapped (b) using 10 primaries in transmission mode. The resulting image is printed in three different samples (c, d and e) and detected in transmission.*

These results confirm the good reproducibility of the selected primaries without needing any further optimizations that can be translated from one sample to another and using different input images. Furthermore, it consolidates the interest of using this technology for full color image printing for security applications inside plastic cards.

### 3.3.3. Conclusion

This laser-based technology presents different technical limitations in the color selection workflow making it difficult to print images consistently without needing long and tedious optimizations. Here, some criteria were implemented to improve the reproducibility of the printed colors that can be printed correctly within in a batch. On one hand, the color extraction of the database was investigated as several artefacts are present in the material that hinder the real color values of the nanostructures. Therefore, each square of the database was manually scrutinized to verify their color uniformity. On the other hand, the primary selection is based on the color values and does not necessarily consider their laser parameters. Hence, an assessment was made on each cluster where the representative (primary) is selected based on the most optimal laser parameters. After selection of the 10 primaries, their color reproducibility was verified within a sample and from sample to sample

presenting fairly good results. To illustrate this, 6 demonstrators were produced by printing full color images using this palette in different samples, revealing its potential for high-quality image marking.

### **3.4. Image multiplexing**

#### **3.4.1. Introduction**

The flexibility of this laser-based technology allows to produce a large number of complexed nanostructures with varied optical properties making them ideal for visual security features. Recently, laser-processed TiO<sub>2</sub>:Ag materials were used to encode several images into a single print with each image observed independently under specific conditions<sup>105,104</sup>. This concept is known as image multiplexing where images are fully mingled, where modifying one of them would also alter the others, thus making it a great anticounterfeiting feature. An example of the most recent results are depicted in Figure 65 where multiple image multiplexing under white light is achieved by processing TiO<sub>2</sub>:Ag films deposited on glass with the same nanosecond pulsed laser ( $\lambda=532$  nm)<sup>19,105</sup>. The principle is given for two bicolor images in figure 65.a. Each image is to be reproduced in an observation mode (mode 1 or 2) when processing the multiplexed image illustrated in figure 65.b (nanostructure = metasurface). For two bicolor image multiplexed images, four nanostructures (MS1 to MS4) have to be properly selected to form the color combinations presented in the logical color tree depicted in figure 65.c. Each nanostructure would need to display exactly one of the two colors on each mode (color 0 or 1). From this principle, an automatic colorimetric algorithm was developed to find all the possible solutions of nanostructure combinations that enable multiplexing for two images. An examples is presented in figure 65.d where a butterfly is observed in “unpolarized” transmission mode while a racoon is depicted in diffraction mode<sup>105</sup>. Needless to say, it is of great interest to be able to transfer this technology on PC cards to pave the way for their implementation on advanced security documents.

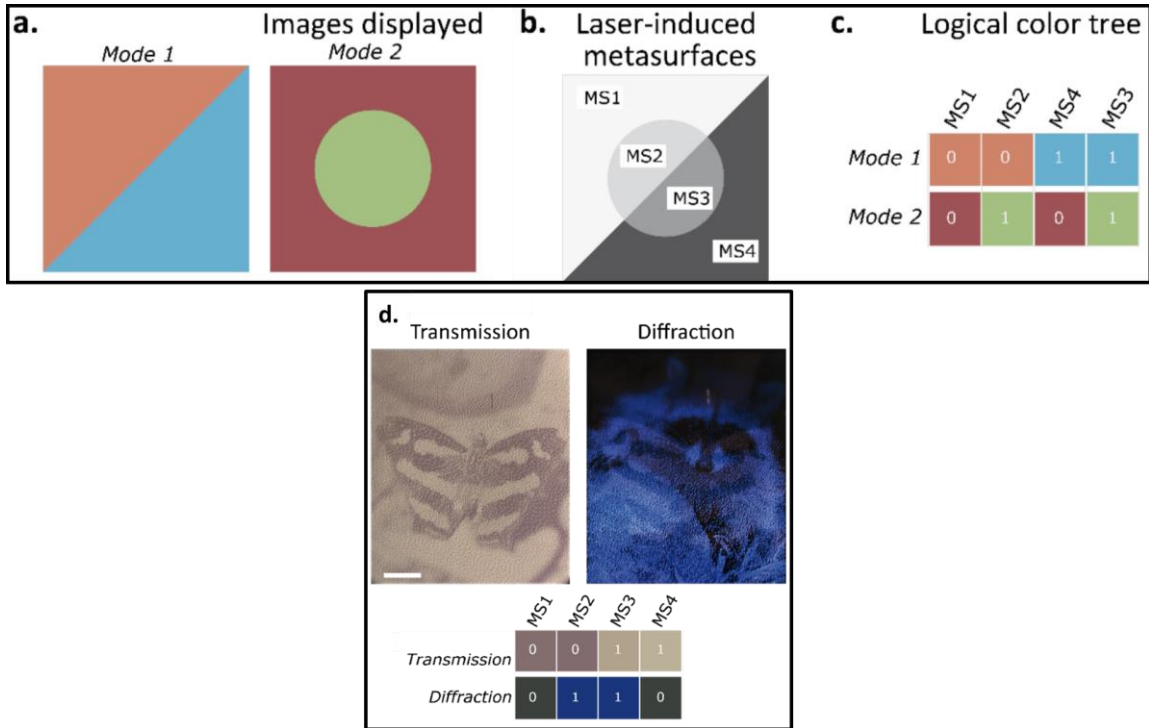


Figure 65: The principle of two-image bicolor multiplexing is presented. Input images are assigned to a chosen observation mode (a) to be able to print a multiplexed image (b). The latter is composed of 4 nanostructures (metasurfaces) that provide the colors depicted in the logical color tree (c). An example of two-image multiplexing is given (d) where a butterfly is observed in “transmission” and a racoon is observed in “diffraction” mode.

### 3.4.2. Two-image multiplexing

For binary images the most important aspect of the color selection is the contrast i.e. the perceptual distance  $\Delta L^*$  of the two colors for each mode, while the chromatic discrepancies are usually disregarded. Therefore, the clustering process here is based purely on cutoff distances of luminance differences ( $\Delta L^*$ ) to find a “bright” color and a “dark” color on each mode.

To find the most suitable multiplexing solution different cutoff distances were tested to form clusters in transmission and backside reflection modes. As a reminder, the colors are extracted from the palette described in part 3.3.2.3. consisting of 10 nanostructures. Among them, three interesting simulated results were obtained with cutoff distance values of 5, 10 and 20 (on both modes) producing three different multiplexing solutions. The resulting simulated multiplexed images are given in figure 66 observed in transmission mode and backside reflection. Each color pixel is represented by the color of the nanostructures of the solution in the given mode. When using a low cutoff value of 5, the contrast is quite low. This is due to having a relatively low cutoff distance, meaning several small clusters are formed

with similar color values, obtaining multiplexing solutions with similar colors, thus with a relatively low contrast. However, if the cutoff value is heavily increased, the size of the clusters increases grouping different nanostructures with larger luminance differences, which can produce artifacts when colors that are expected to be similar are actually perceptually different at a glance. For instance, here, using a cutoff value of 20 results in noticeable luminance differences for colors expected to be similar as observed in figure 66 that create slight image “ghosting”. As a result, a tradeoff needs to be found between the contrast and the uniformity of the images. In the present case, the most optimal solution was found at a cutoff distance of 10 presenting a well-rounded contrast in both modes and do not present any type of ghosting.

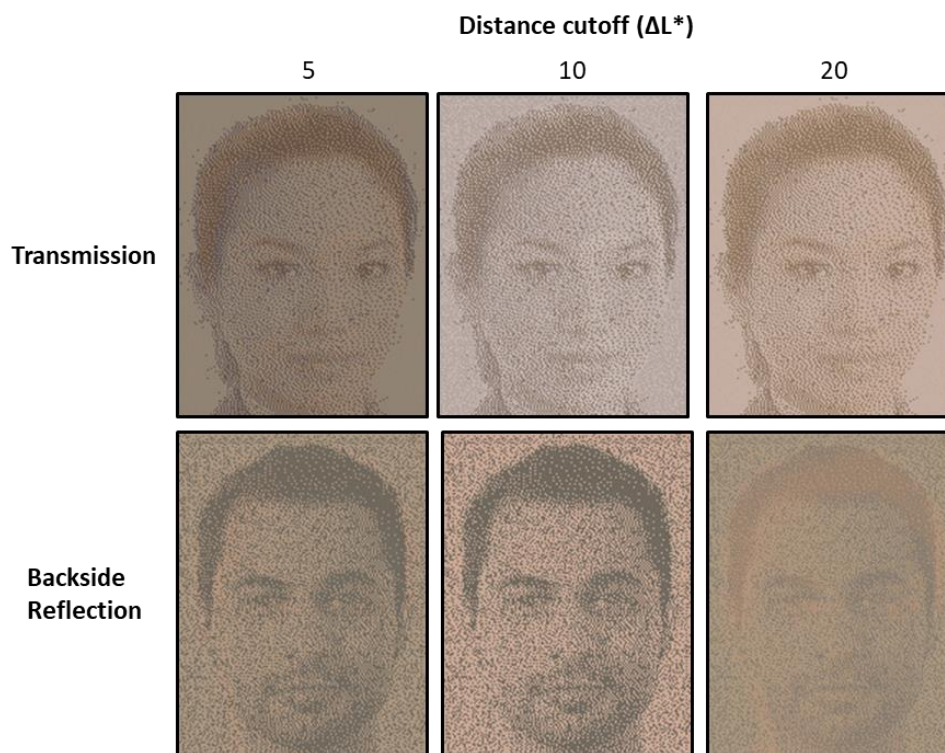


*Figure 66: Comparison of two-image multiplexing solutions using two colors in transmission and backside reflection modes (four in total) using different cutoff distances of  $\Delta L^*$  (5, 10 and 20). For each cutoff distance, the simulated images in each mode of observation are displayed.*

To be able to print the multiplexed image, each pixel of the image is vectorized with the laser parameters of the selected nanostructure as depicted in the color tree in figure 66.a. The laser parameters of each nanostructure are given in Annex 8. The real size of the image is 9.7 mm x 7.5 mm with a pixel size of 50 $\mu$ m. The multiplexed image is printed in a sample and observed with the camera setup in transmission and back reflection modes depicted in figure 67.b and

67.c respectively. Both images are easily observable with the naked eye under white light with a good contrast. To support this, several untrained users at the laboratory were able to identify the faces without having any prior information, hence illustrating the potential of this technology for anti-counterfeiting applications.

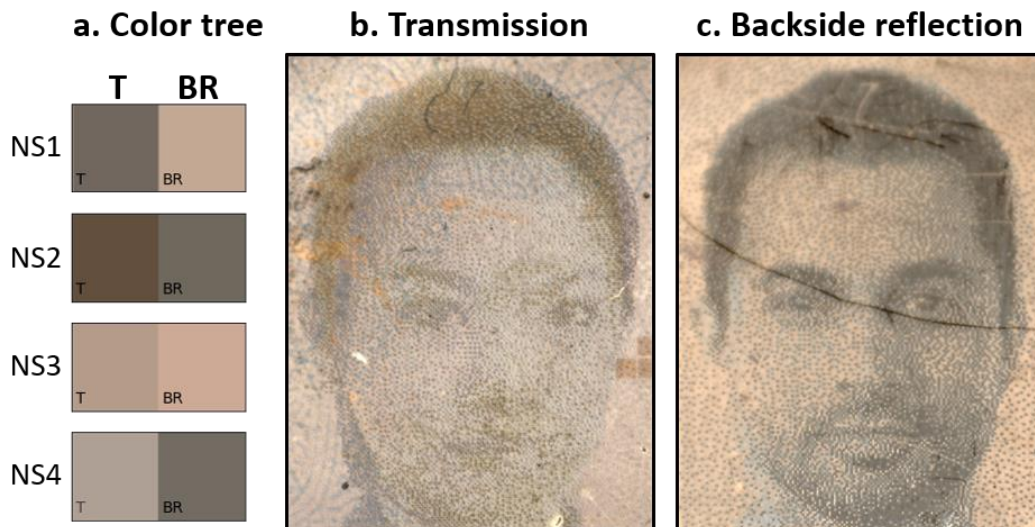


Figure 67: Experimental result of two-color image multiplexing. The color tree (a) consists of 4 nanostructures (NS1 to NS4) depicting different colors in transmission (T) and backside reflection (BR). The multiplexed image is printed and characterized with the camera setup in transmission (b) depicting a woman and in backside reflection (c) depicting a man.

### 3.4.3. Conclusion

The conditional gamut algorithm implemented allows to find multiplexing solutions within the reproducible palette introduced in part 3.3.1. The resulting multiplexed image is printed on a PC card showcasing a good reproducibility despite the pixel overlapping. It provides a first glimpse to the potential of this technology to be able to print multiplexed images inside PC cards, with similar results to what has been previously observed on glass substrates<sup>104,105</sup>. The future steps would be to first expand the color gamut in the different modes to improve the quality of the print and investigate the possibility of three or more image multiplexing.

## 3.5. Color production on PC:SiO<sub>2</sub>:TiO<sub>2</sub>:Ag samples

### 3.5.1. Introduction: Implementation of a protective silica layer for color printing

Laser processing directly on TiO<sub>2</sub>:Ag films without lamination are of great interest as the surface is accessible for observation and characterization. However, when irradiating non-laminated PC:TiO<sub>2</sub>:Ag samples the material is ablated independently of the laser conditions (same as described in part. 3.1.2). An example is depicted by the SEM images in figure 68

where pixels with 45° laser lines ( $175 \text{ mJ}\cdot\text{cm}^{-2}$ ;  $30 \text{ mm}\cdot\text{s}^{-1}$ ) were drawn illustrating ablation of the material. Therefore, an intermediate protective silica layer was introduced to be able to modify the material by laser processing without damaging the film. This transparent silica-based film has been previously used as a laser-damage resistant coating for optics applications<sup>118</sup>. The film preparation is described in part 2.7.1.

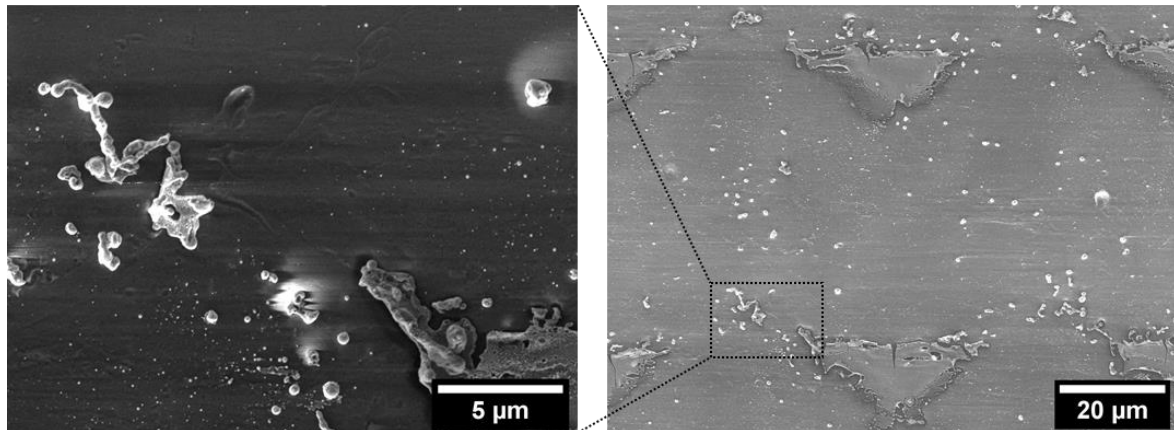


Figure 68: SEM images of a laser-processed PC:TiO<sub>2</sub>:Ag film depicting severe delamination of the material.

### 3.5.2. Color production on PC:SiO<sub>2</sub>:TiO<sub>2</sub>:Ag samples

#### 3.5.2.1. Database processing

The color database is produced using the same laser conditions performed on PC TiO<sub>2</sub>:Ag cards with over 450 unique sets of laser parameters described in part 3.1.2. Colors were observed in four observation modes, transmission, frontside reflection, backside reflection and “diffraction”. The latter relates to the -1<sup>st</sup> order diffraction observed at an incidence angle of 25° perpendicular to the laser polarization. The L\*a\*b\* color values are visualized for each mode in figure 69, the database is projected in the a\*b\* and L\*C\* planes with each nanostructure represented by a color point. Compared to PC TiO<sub>2</sub>:Ag cards the color production is quite different, especially for transmission and backside reflection modes. In transmission the color variation is limited to blue and white shades while in backside reflection the color diversity is significantly higher consisting of greens, blacks, whites, yellows and oranges. Meanwhile, in diffraction mode not only the color variation is by far the biggest one in terms of a\*b\* surface but also presents the highest contrast ( $\Delta L^* \approx 80$ ).

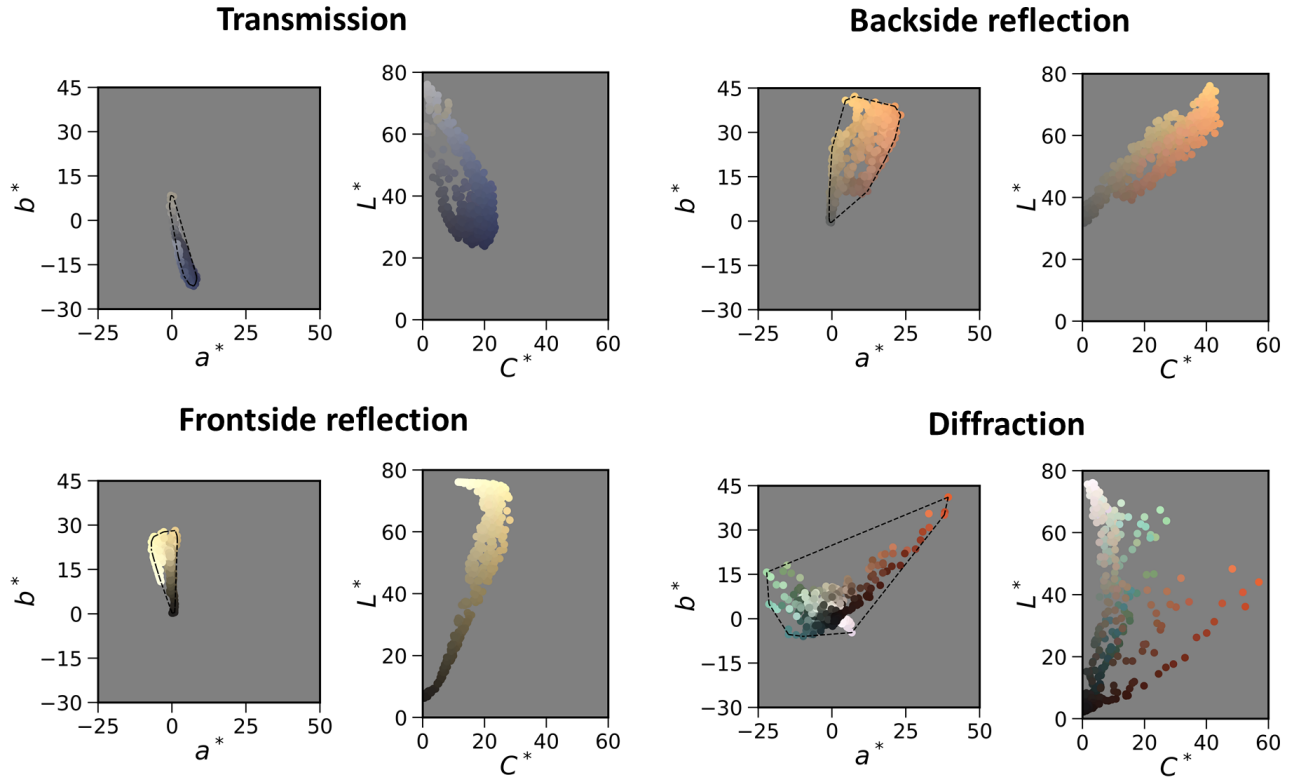


Figure 69: The color production of the database on a PC:SiO<sub>2</sub>:TiO<sub>2</sub>:Ag sample was investigated. Four observation modes were identified : transmission, frontside reflection, backside reflection and diffraction. To illustrate the color gamut, for each mode, the colors of the nanostructures are projected in the  $a^*b^*$  and  $L^*C^*$  planes for each mode. Each point represents a nanostructure and is color coded accordingly to their sRGB values. In the  $a^*b^*$  plane, the gamut is highlighted by the black-dotted outline.

### 3.5.2.2. Investigation of diffractive gratings

Such diffractive properties were first observed by laser processing TiO<sub>2</sub>:Ag materials on glass and flexible supports (PET) with femtosecond lasers<sup>68,102–105</sup>. This is due to self-organization mechanisms triggered by ultrafast laser excitation that generate periodic ripples at the surface, also known as laser-induced periodic surface structures (LIPSS). Their periodicity and direction are thus controlled by the laser processing conditions, generating interesting optical properties. With femtosecond lasers, it was observed that surface gratings were produced perpendicularly to the laser polarization<sup>68,102–104</sup>, while with the same nanosecond laser used here, surface gratings were formed parallel to the laser polarization<sup>105</sup>. For the latter, a single diffractive color was detected in the -1<sup>st</sup> order which relates to self-organized gratings with an average period of 320 nm.

However here on PC:SiO<sub>2</sub>:TiO<sub>2</sub>:Ag samples, three “main” colors (white, green and red) were detected besides “black” which relates to the absence of grating formation. To understand

their origin, nanostructures producing these colors were investigated by SEM and AFM profiling. The laser parameters used to produce green, red and white are given respectively in annex 9 and depicted on top of figure 70 (1 to 4). SEM images and AFM topographic profiles (20µm x 20µm) of the initial film (1) and the three nanostructures (2 to 4) formed by laser were recorded perpendicularly to the laser polarization (red arrow). For each micrograph a 2D “Fast Fourier transform (2D FFT) was performed using *Gwyddion* software (depicted inset) to be able to determine the periodicity of the surface grooves if any are present. The initial film presents a smooth surface with small elevation variations up to 35 nm which can be attributed to nanoparticles placed at the surface of the material and supported by the SEM image. According to the 2D FFT image, no periodicity was detected which explains the absence of diffractive color. However, periodic surface gratings are observed for both green and red nanostructures (2 and 3) perpendicularly to the laser polarization but with different periodicity. The periodicity of both grooves was determined by measuring the vertical profile of the 2D FFT images. For the nanostructure (2), the period of the gratings was determined to  $430 \pm 20$  nm that is consistent to the green color captured ( $\lambda \approx 530$  nm) in these observation conditions if the following periodic grating equation is considered for a diffraction order of -1:

$$\Lambda = \frac{\lambda}{\sin(\theta_i) + \sin(\theta_o)} \quad (\text{Equation 14})$$

where  $\Lambda$  is the period of the grating,  $\lambda$  is the wavelength of light (color detected),  $\theta_i$  is the incidence angle (55°) and  $\theta_o$  is the observation angle (25°).

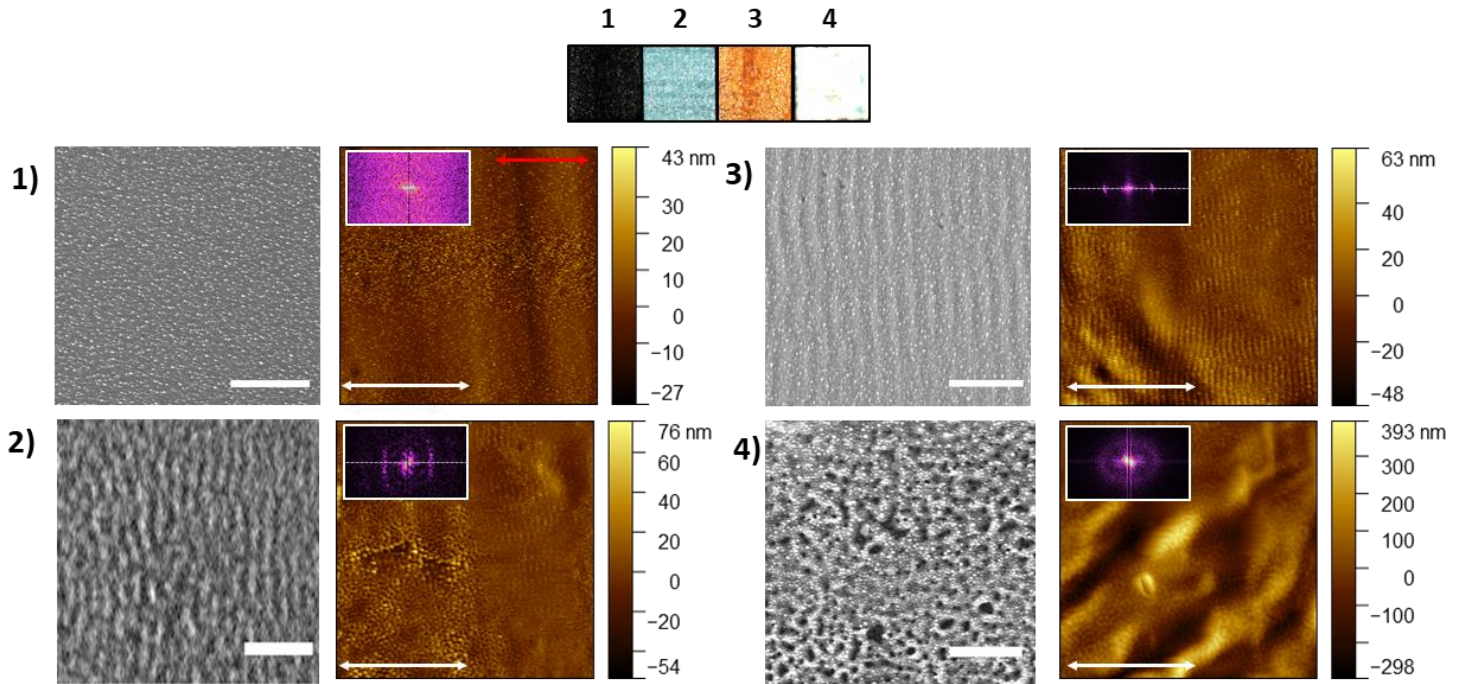


Figure 70: Four nanostructures (a to d) presenting different colors in diffraction mode are presented on top. For each sample, a  $20^2 \mu\text{m}^2$  AFM micrograph was recorded parallel to the laser polarization depicted with the red arrow. The scalebar is  $10 \mu\text{m}$  illustrated by the white arrows. The 2D Fast Fourier Transform (FFT) of the surface was measured by using Gwyddion software as depicted inset. The grey-dotted lines represent the measured horizontal profile to be able to determine the period of the surface grooves in nanostructures (2) and (3),  $\Lambda = 430 \pm 20 \text{ nm}$  and  $\Lambda = 500 \pm 20 \text{ nm}$  respectively.

For the nanostructure (3) surface gratings present a higher period at  $500 \pm 20 \text{ nm}$ . If equation (14) is considered, the color detected corresponds well in the red range ( $\lambda \approx 600 \text{ nm}$ ). On the other hand, for the white nanostructure (4) the surface is heavily altered by the laser processing as drastic variations of hundreds of nanometres in elevation are observed without detecting any periodicity. This is due to the strong laser conditions as 95 effective number of pulses are deposited with high fluence ( $68 \text{ mJ}\cdot\text{cm}^{-2}$ ;  $10 \text{ kHz}$ ) inducing significant changes to the material due to intense thermal plasmon absorption. Thus, the white color presented relates to the processed surface modifications of the material scattering the white light source of the camera setup. This phenomenon is discussed in the following part and its influence on the color production.

### 3.5.2.3. Diffraction color tuning by laser ablation

The material is rather sensitive to strong laser excitation as different alterations occur, resulting in interesting optical properties, namely diffraction, scattering or the combination of both. To be able to illustrate these phenomena, three samples were investigated by SEM

microscopy as presented in figure 71. They were processed with the same repetition rate and fluence ( $10\text{ kHz}$ ;  $68.0\text{ mJ.cm}^{-2}$ ) but with different scanning speeds,  $1500$  (a),  $150$  (b) and  $30$  (c)  $\text{mm.s}^{-1}$ , that present respectively a green, light green and white color in diffraction mode. First thing it was observed that for either laser process a first type of ablation appears as “nanovoids” are formed in the material. They become bigger and more prominent as the scanning speed is decreased.

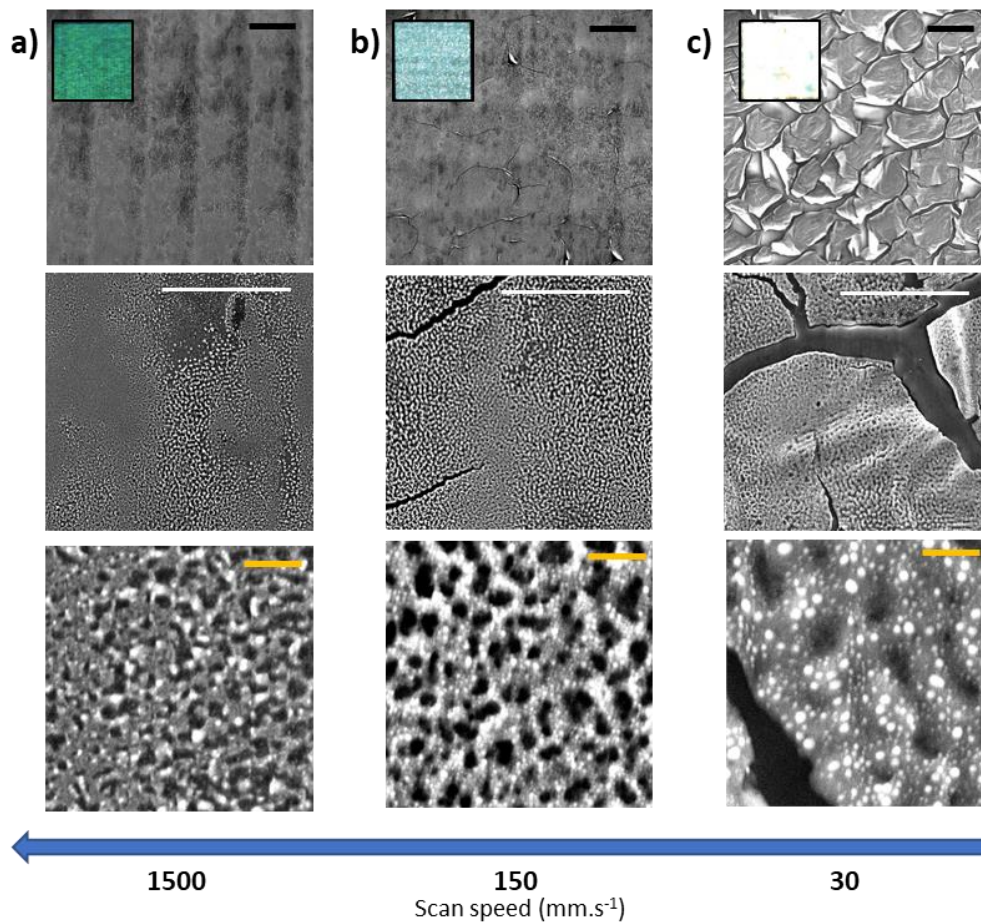


*Figure 71: Investigation of surface modulations by SEM microscopy. Three nanostructures (a, b and c) were produced by using the same repetition rate and fluence ( $10\text{ kHz}$ ;  $68.0\text{ mJ.cm}^{-2}$ ) but with different scanning speeds,  $1500$  (a),  $150$  (b) and  $30$  (c)  $\text{mm.s}^{-1}$ . The black scalebars of the top figures are of  $50\mu\text{m}$ , the white scalebars in the middle figures are of  $10\mu\text{m}$  and the yellow scalebars of the bottom figures is of  $200\text{ nm}$ .*

Furthermore, spallation occurs as cracks start to appear in the film with intermediate scanning speeds ( $150\text{ mm.s}^{-1}$ ) and become heavily prominent with lower scanning speeds ( $30\text{ mm.s}^{-1}$ ) at which the film starts peeling off while still attached. The higher the degradation of the film is, the stronger the scattering and the color bleaching in the diffraction observation mode. A well-defined green is observed when the film is crack-free (a), light green is obtained when cracks start to appear (b) to ultimately obtain a white color (c) as the peeled off areas

scatter the white light. By taking this into consideration, it is possible to tune the “paleness” of the diffractive color by varying the laser parameters. To highlight these colors an image was mapped as presented in figure 71.1 using nanostructures depicting red, black, white and different shades of green (6 primaries in total). The set of laser parameters of each nanostructure is described in Annex 10. The image was vectorized with  $35\mu\text{m}\times 35\mu\text{m}$  size pixels where each one was assigned to a set of laser parameters and printed in a sample. The resulting printed image was observed in diffraction with the camera setup as depicted in figure 71.2. It presents a fairly good color reproduction that confirms the interest of using diffractive colors to print high quality colored images with outstanding contrast and color saturation.

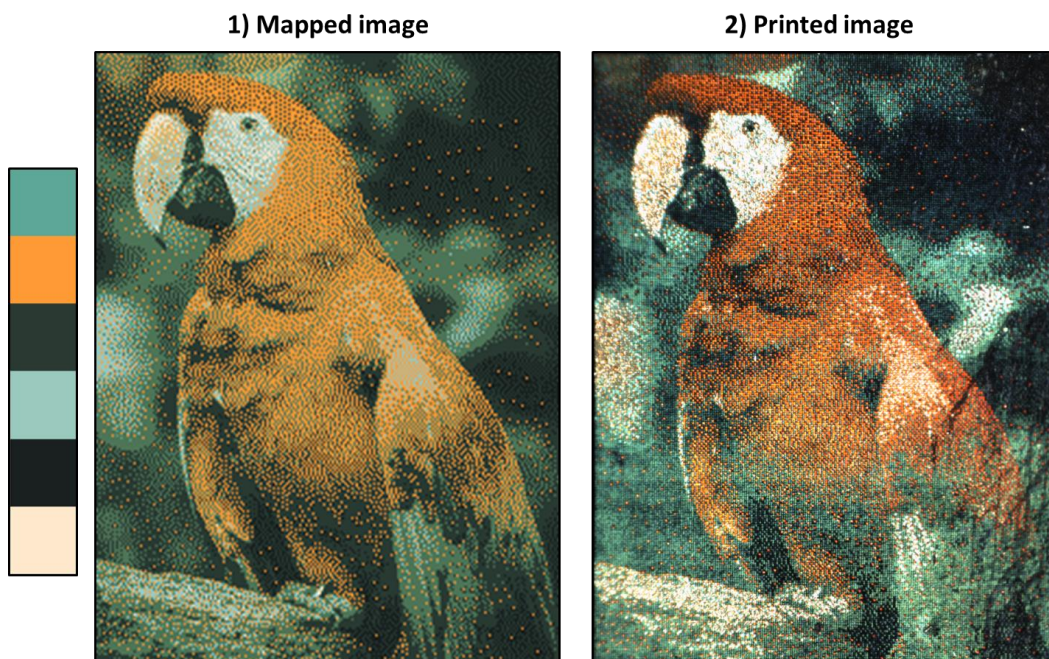


*Figure 72: Full-color image printing in diffraction mode. The mapped image (1) is simulated by using 6 primaries depicted at the left of the figure. It is then vectorized and printed on a sample. The resulting image was produced by using  $35\times 35\ \mu\text{m}^2$  pixels and has a real size of  $10.6\times 13.2\ \text{mm}^2$ . The image is observed with the camera setup in diffraction mode (2).*

### 3.5.3. Conclusion

In conclusion, different surface modifications were observed such as the formation of LIPPS, voids and cracks that result in different optical features. The formation of LIPPS with two different periods in one direction is particularly unique to this sample as previous studies show only surface gratings with a single period<sup>68,102–105</sup>. Moreover, laser ablation is usually something that is avoided as the material is damaged or delaminated leading to undesired

features. In this case, the partial peeling off of the material is presented by cracks is exploited to be able to tune the shading of the detected colors and utilized to be able to print high quality images. To summarize this section, 2D parameters regimes were defined to be able to obtain the different diffractive/scattering properties on PC:SiO<sub>2</sub>:TiO<sub>2</sub>:Ag samples, presented in Figure 72.

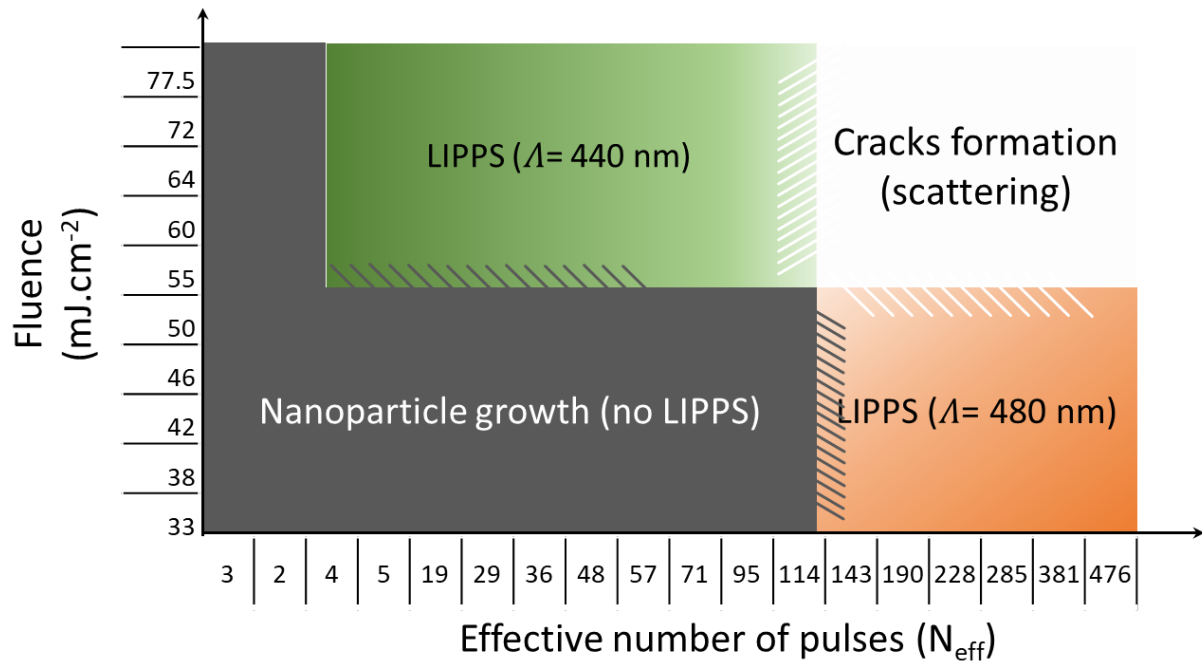


Figure 73: Parameters regime of laser-induced surface modifications of a database of 480 unique sets of parameters with varied fluences (20-74 mJ.cm<sup>-2</sup>) and effective number of pulses (2-476).

### 3.6. Conclusion

In this chapter, the laser-induced color production was investigated inside PC cards using TiO<sub>2</sub>:Ag materials. First, the best laser conditions were established to avoid sample burning or damaging due to strong heat accumulation. It was found out that working with weak parameter range (low powers and repetition rates) and out of the focal plane of the laser would allow the production of interesting colors without damaging the samples. Then, the design of the most optimal pixel was scrutinized to be able to print uniform colors as 35x35μm<sup>2</sup> pixel size with interline distance of 10μm results in consistent color production. The database was then created and their colors were extracted in different observations modes. An assessment was developed that automatically selects the optimal mode to print color images based on a selection of input images. Here, transmission mode presents the most optimal color variations for portrait printing.

The color workflow was discussed as some inconsistencies were highlighted, particularly for the color extraction and the selection of the primaries, that are at the root of poor color reproducibility. Here, an empirical process was implemented to select the primaries based primarily on the laser parameters to anticipate color discrepancies. After selection, the reproducibility of the primaries was verified in terms of colors as they present good color uniformity with all  $\Delta E$  values lower than 3. Furthermore, the palette was used to map and print several demonstrators of full color images in one mode but also multiplexed images illustrating the great potential of this efficient technology for secure applications.

Finally, the laser-induced color production was investigated on non-laminated samples on PC samples. For this, a protective layer of dense silica was implemented to be able to produce colors without damaging the sample. The colors obtained are quite different to what is observed on laminated samples as diffractive colors were detected depicting well-defined and saturated colors. These diffractive properties were investigated by AFM and SEM microscopy. It was found out that periodic gratings were produced at two different periodicities (440 or 480 nm) parallel to the laser polarization. Additionally, laser ablation was observed when processing with strong irradiation, which results in light scattering effect that is detected as “white” in diffraction mode. The peeling off of the material can be controlled by the laser processing conditions and can be used to tune the luminance of the detected colors. To illustrate this an image was produced using different shades of green, red, white and black colors that present good color fidelity.



## **GENERAL CONCLUSION & PERSPECTIVES**

In the grand scheme, the works presented here relate to the development of visual features that could potentially be implemented in ID security applications, particularly for image printing. Here a solution is proposed based on a laser marking technology developed at the Hubert Curien laboratory using plasmonic materials on plastic supports.

The first step was to develop a synthesis process to obtain TiO<sub>2</sub>:Ag thin films by sol-gel method that is suitable for plastic supports. To avoid high temperature annealing, the inorganic matrix was prepared by a multi-step process that allows obtaining homogeneous mesoporous titania films. The surface of polycarbonate substrates is pre-treated by a fast oxygen plasma treatment that improves the mechanical stability of deposited sol-gel materials as crack-free films were obtained. To stabilize such materials after deposition, the samples are exposed to low temperature that densifies the inorganic matrix, followed by a UV exposure and solvent extraction that eliminates the organic parts, namely the templating agent, to ultimately form the porosity in the film ( $\approx 40\%$ vol) with a final thickness of  $95\pm 5$  nm. The as-prepared films are then impregnated with silver salts by liquid method and form nanoparticles embedded in the matrix with good reproducibility. The resulting TiO<sub>2</sub>:Ag films on PC are then included on a plastic card without damaging the samples during the laminating process.

The as-prepared samples were irradiated by a nanosecond laser. The best working laser conditions were studied to be able to produce a variety of colors without damaging/burning the sample. Once the laser conditions were defined, an exploratory work was carried on selecting the best colors for a certain type of images, highlighting the importance of developing an automated method to select the appropriate colors among the attainable ones. Once the colors were selected, several demonstrators were printed in a selected observation mode, depicting high quality details and features. Additionally, two-image multiplexing was investigated and achieved as well-defined and contrasted results were showcased.

Materials not embedded in a PC card were also investigated by laser processing. A protective silica layer between the substrate and the TiO<sub>2</sub>:Ag film was implemented to avoid damages of the substrate or the material during laser processing. It allows to produce a wide variety of optical effects different to what was observed in PC cards. In particular, it was observed that diffractive colors were produced due to the formation of surface gratings parallel to the

laser polarization. Two types of gratings were detected as a period of  $440 \pm 10$  nm to produce a green color or with a period  $480 \pm 10$  nm to produce a bright red color. The shade of the colors can be tuned by laser ablation as the strong irradiation would lead to spallation of the material. This leads to producing a scattering effect by the damaged areas and are thus detected as “white” in these observation conditions. To highlight this effect an image was produced with different shades of green, red white and black colors.

Following these results, some future perspectives can be proposed:

- Regarding the material preparation, despite the successful inclusion of a  $\text{TiO}_2\text{:Ag}$  material inside a PC card, it still needs development to be able to be fully implemented in an industrial application. For this, a route can be considered where titanium silver precursors are mixed together and form a sol. This would allow to produce the film in one step without needing to first produce a mesoporous film and then include the silver by liquid impregnation. The deposition could first be tested in the same conditions as presented here and further develop a deposition process with another method such as inkjet or flexography which are widely used in the industry.

- Regarding the laser processing, it would be of major interest to investigate the physical mechanisms taking place inside the card during laser irradiation. By understanding the different these mechanisms, we could potentially improve the color variety.

- Finally, a third perspective would revolve around the image processing part. The “best” colors and images are always subjective to personal assessment. Thus, it would ideal to develop a complete and automated process to select the best conditions.

## ANNEXES

### Annex 1: FTIR spectra of the evolution of a mesoporous TiO<sub>2</sub> film

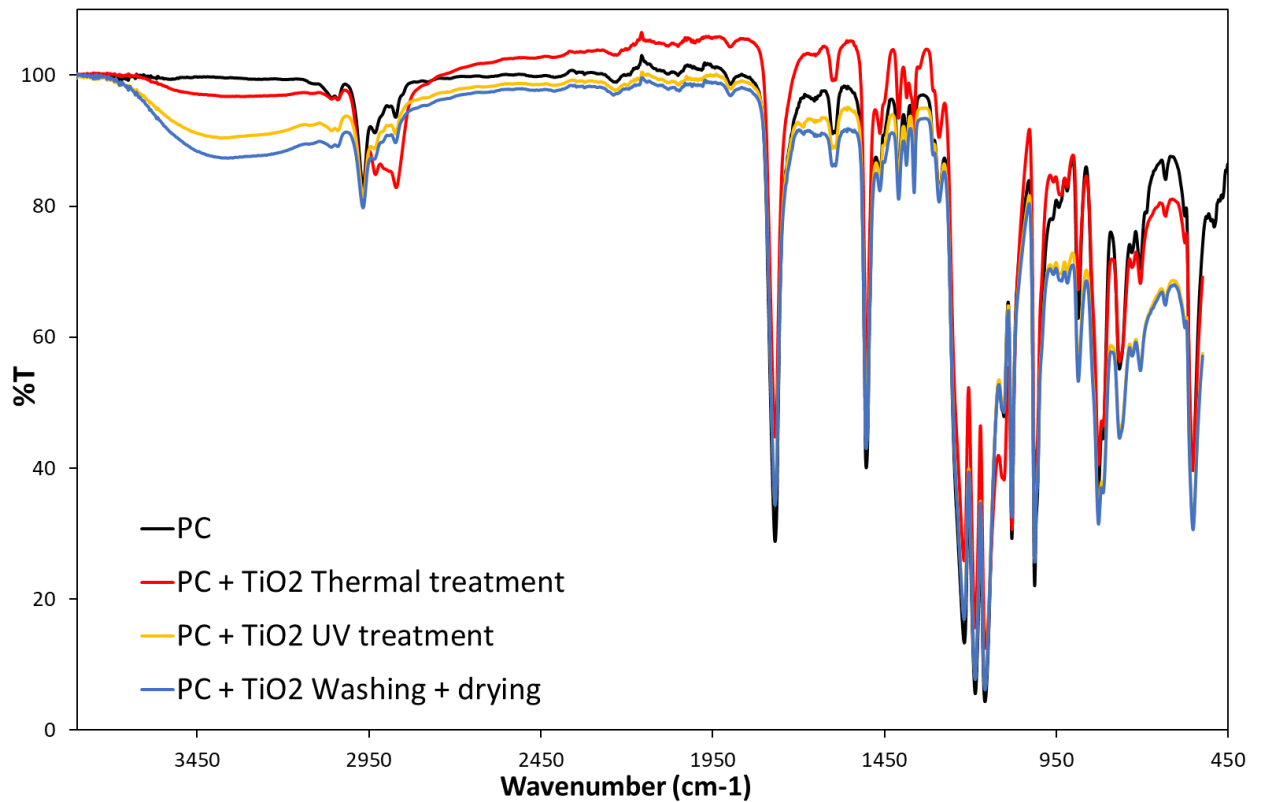
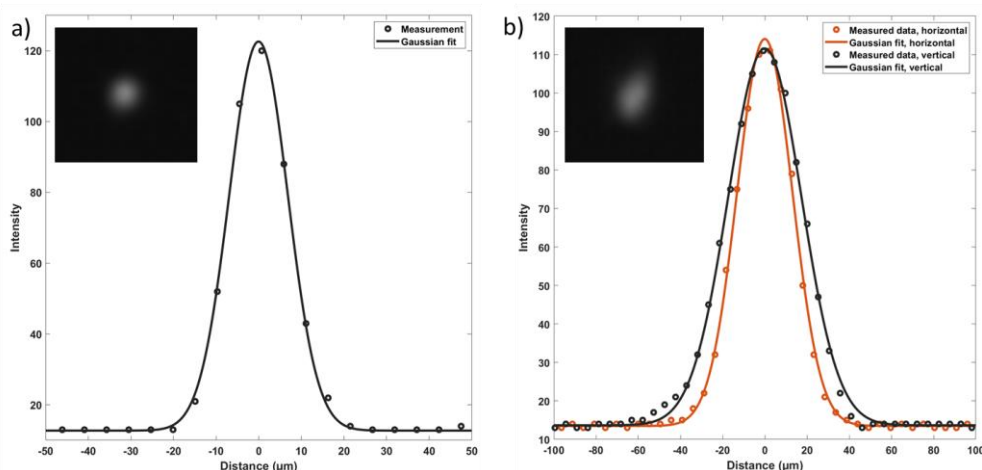


Figure: FTIR-ATR measurements of a TiO<sub>2</sub> film during the stabilization process. The spectra is extracted after the thermal treatment (red curve), UV treatment (yellow curve) and finally washing/drying (blue curve). The black curve represents a PC substrate without any deposition.

### Annex 2: Spot size measurements at the focal plane $f_0$ and $f_2$



a) Spot size captured by the camera (inset) at the focal plane " $f_0$ " and the fitted gaussian profile for the vertical profile. b) Spot size captured by the camera at the plane " $f_2$ " fitted to a Gaussian profile for both vertical and horizontal profiles. Every profile was fitted with a

$$\text{simple gaussian equation: } I(r) = I_0 \cdot e^{-2r/r_{1/e^2}}.$$

### **Annex 3: Laser calculation formulas**

Fluence calculation formula:

To calculate the fluence in  $\text{mJ.cm}^{-2}$  the following formula was used by taking into account the elliptical shape of the beam spot:

$$F (\text{mJ.cm}^{-2}) = 1000 \times \frac{2 \frac{\text{Power (W)}}{\text{Repetition rate (Hz)}}}{\pi \times r_{h,1/e^2}(\text{cm}) \times r_{v,1/e^2}(\text{cm})}$$

Effective number calculation formulae:

To calculate the effective number of pulses of a single line the following equation was used described by Florian *et al.*<sup>120</sup>:

$$N_{eff,1D} = \frac{\left( r_{h,1/e^2}(\text{cm}) + r_{v,1/e^2}(\text{cm}) \right) \times \text{Repetition rate (Hz)}}{\text{Scanning speed (cm.s}^{-1}\text{)}}$$

For parallel lines the formula presented above is modified to include the interline distance ( $dy$ ) and results in the following formula:

$$N_{eff,2D} = \frac{\pi \times \left( r_{h,1/e^2}(\text{cm}) \times r_{v,1/e^2}(\text{cm}) \right) \times \text{Repetition rate (Hz)}}{\text{Scanning speed (cm.s}^{-1}\text{)} \times dy (\text{cm})}$$

### **Annex 4: Pixel dimensions measurements**

The dimensions of the pixels presented in figure 40 were measured for every repetition rate. The height x length of the pixels in  $\mu\text{m}$  were extracted and are summarized in the following table:

		<b>dy (<math>\mu\text{m}</math>)</b>				
		<b>Original</b>	<b>5</b>	<b>10</b>	<b>20</b>	<b>30</b>
<b>pixel size (<math>\mu\text{m}</math>)</b>	<b>25x25</b>	36x26				
	<b>35x35</b>	52x42	51x43			
	<b>50x50</b>	68x60	70x60	65x58		
	<b>65x65</b>	85x74	84x75	84x76	77x73	

**30 kHz**

		<i>dy</i> ( $\mu\text{m}$ )			
		5	10	20	30
<i>pixel size</i> ( $\mu\text{m}$ )	Original				
	25x25	36x25			
	35x35	48x43	56x44		
	50x50	67x58	66x58	68x57	
	65x65	88x78	85x70	84x73	82x70

**50 kHz**

		<i>dy</i> ( $\mu\text{m}$ )			
		5	10	20	30
<i>pixel size</i> ( $\mu\text{m}$ )	Original				
	25x25	40x31			
	35x35	52x42	51x43		
	50x50	66x58	68x59	65x57	
	65x65	85x73	82x70	84x72	83x72

**Annex 5: Color spaces**

The sRGB color space

The red green blue (RGB) color space is a well-known method to encode the colors of each pixel (gamut) of an image in a specific device. However, every digital device, such as monitors, televisions, printers or presentation devices, have their own individual color space and range of colors that it can print or display. To be able to interchange and communicate color between devices, “standard” color spaces have been developed in the imaging industry such as such as the “standard” red green blue (sRGB) space that belongs to the Commission Internationale de l’Eclairage” (CIE) 1931 XYZ color space<sup>121</sup>. For instance, sRGB values can be transformed to three linear primaries, X, Y and Z values back and forth by a matrix ( $M$ ) multiplication:

$$\begin{bmatrix} X \\ Y \\ Z \end{bmatrix} = M \begin{bmatrix} R \\ G \\ B \end{bmatrix}$$

To be able to interchange the information in color spaces under different lightings, standard spectral power distributions (SPDs) were developed by the CIE. They are called also “illuminants” and are inspired of different light sources such as incandescent light (A series),

daylight (D series), fluorescent lightings (F series), and LEDs. In the graphical and paper industry, illuminants D50 and D65 are mainly used as they correspond respectively to the horizon and noon daylight spectra. In the present case, illuminant D65 is utilized and defines the matrix as follow<sup>122</sup>:

$$M = \begin{bmatrix} 0.4124564 & 0.3575761 & 0.1804375 \\ 0.2126729 & 0.7151522 & 0.0721750 \\ 0.0193339 & 0.1191920 & 0.9503041 \end{bmatrix}$$

The CIE 1976 L\*a\*b\* color space

Once the CIE 1931 XYZ tristimulus values of a color are calculated, they can be represented in the CIE 1976 L\*a\*b\* three-dimensional color system. This model allows to provide perceptually more uniform spacing (differentiation) of colors with similar luminance. It expresses colors with three values, L\* for luminance, a\* represents the red-green axis and b\* represents the blue-yellow. For this, a color is defined as the reference "white" with the tristimulus values of X<sub>n</sub>, Y<sub>n</sub> and Z<sub>n</sub> and perform a chromatic adaptation and calculate the L\*a\*b\* coordinates as follow:

$$\begin{aligned} L^* &= 116 f(Y/Y_n) - 16 \\ a^* &= 500[f(X/X_n) - f(Y/Y_n)] \\ b^* &= 200[f(Y/Y_n) - f(Z/Z_n)] \end{aligned}$$

With

$$f(q) = \begin{cases} q^{1/3} & \text{if } q \geq 0.008856 \\ 7.787q + \frac{16}{116} & \text{if } q \leq 0.008856 \end{cases}$$

The two coordinates a\* and b\* can describe the "chroma" (C\*) and "hue" (h\*) of a given color according to the following correlations:

$$C^* = \sqrt{a^{*2} + b^{*2}} \quad ; \quad h^* = \arctan \frac{b^*}{a^*}$$

The CIE 1976 model allows to estimate the perceptual difference between two colors, called  $\Delta E_{ab}^*$ . It follows a simple Euclidean distance formula for colors "1" and "2":

$$\Delta E_{ab}^* = \sqrt{(\Delta L^*)^2 + (\Delta a^*)^2 + (\Delta b^*)^2}$$

with

$$\Delta L^* = L_1^* - L_2^* ; \Delta a^* = a_1^* - a_2^* ; \Delta b^* = b_1^* - b_2^*$$

A newer color difference metric was developed in 2000, the CIE DE 2000 or  $\Delta E_{00}$ , that proposes to correct the perceptual non-uniformity by following a more complex formula:

$$\Delta E_{00} = \sqrt{\left(\frac{\Delta L'}{k_L S_L}\right)^2 + \left(\frac{\Delta C'}{k_C S_C}\right)^2 + \left(\frac{\Delta H'}{k_H S_H}\right)^2 + R_T \frac{\Delta C'}{k_C S_C} \frac{\Delta H'}{k_H S_H}}$$

With

$$L' = L^*$$

$$\Delta L' = L'_1 - L'_2$$

$$\bar{L} = \frac{(L'_1 + L'_2)}{2}$$

$$\bar{C} = \frac{(L_1^* + C_2^*)}{2}$$

$$a' = a^* + \frac{a^*}{2} \left( 1 - \sqrt{\frac{\bar{C}^7}{\bar{C}^7 + 25^7}} \right)$$

$$b' = b^*$$

$$C' = \sqrt{a'^2 + b'^2}$$

$$\Delta C' = C'_1 - C'_2$$

$$\bar{C}' = \frac{(C'_1 + C'_2)}{2}$$

$$h' = \arctan\left(\frac{b'}{a'}\right) \text{ mod}(360^\circ)$$

$$\Delta h' = h'_1 - h'_2$$

$$\bar{h}' = \frac{(h'_1 + h'_2)}{2}$$

$$\Delta H' = 2\sqrt{C'_1 C'_2} \sin\left(\frac{\Delta h'}{2}\right)$$

$$S_L = 1 + \frac{0.015(\bar{L} - 50)^2}{\sqrt{20 + (\bar{L} - 50)^2}}$$

$$S_C = 1 + 0.045 C'$$

$$S_C = 1 + 0.015 C'T$$

$$T = 1 - 0.17 \cos(\bar{h} - 30) + 0.24 \cos(2\bar{h}) + 0.32(3\bar{h} + 6) - 0.20 \cos(4\bar{h} - 63)$$

$$R_T = -2 \sqrt{\frac{(\bar{C}')^7}{(\bar{C}')^7 + 25^7}} \sin \left[ 60^\circ \exp \left[ - \left( \frac{\bar{h}' - 275^\circ}{25^\circ} \right)^2 \right] \right]$$

$$k_L = k_C = k_H = 1$$

## **Annex 6: Normal density values**

Based on the hue diagrams presented in figure 54 (part 3.2.1), the extracted normal density values were calculated for every sector of each portrait. The results are summarized in the following table:

Sector	Image number															
	1	2	3	4	5	6	7	8	9	10	11	12	13	14	15	16
1	0.01 835	0.00 953	0.00 016	0.00 595	0.00 027	0.00 004	0.00 034	0.00 271	0.00 234	0.00 004	0.00 127	0.00 014	0.00 007	0.00 287	0.00 618	0.00 407
2	0.01 676	0.01 739	0.00 012	0.00 353	0.00 011		0.00 021	0.00 718	0.00 202	0.00 004	0.00 337		0.00 020	0.00 694	0.00 945	0.00 427
3	0.03 591	0.03 173	0.00 418	0.01 878	0.00 595	0.00 037	0.00 257	0.01 346	0.00 362	0.00 075	0.01 366	0.00 475	0.00 263	0.01 214	0.01 808	0.00 807
4	0.03 873	0.09 627	0.00 541	0.02 798	0.00 632	0.00 461	0.00 361	0.01 973	0.00 736	0.00 179	0.01 110	0.00 716	0.01 354	0.08 230	0.02 948	0.00 844
5	0.05 821	0.26 209	0.01 935	0.09 344	0.02 498	0.00 666	0.01 393	0.08 848	0.03 424	0.02 651	0.05 408	0.02 892	0.01 962	0.22 526	0.05 933	0.11 014
6	0.24 578	0.08 537	0.12 506	0.24 679	0.14 656	0.01 578	0.08 693	0.21 308	0.29 156	0.17 211	0.25 614	0.15 288	0.06 576	0.12 603	0.08 354	0.27 478
7	0.03 679	0.00 825	0.32 354	0.27 055	0.37 281	0.20 696	0.22 768	0.07 454	0.21 383	0.13 608	0.17 041	0.37 863	0.32 586	0.02 724	0.10 433	0.04 244
8	0.00 373	0.00 257	0.09 503	0.06 422	0.12 774	0.23 234	0.11 249	0.02 321	0.02 996	0.03 955	0.23 286	0.17 934	0.04 203	0.00 886	0.09 201	0.07 705
9	0.00 267	0.00 175	0.01 428	0.02 255	0.01 867	0.10 125	0.11 371	0.00 448	0.00 552	0.01 368	0.05 697	0.01 062	0.00 543	0.00 327	0.00 101	0.04 733
10	0.00 126	0.00 104	0.02 255	0.01 103	0.00 944	0.00 589	0.02 405	0.00 700	0.00 205	0.02 283	0.01 321	0.00 852	0.00 199	0.00 175	0.00 037	0.02 596
11	0.00 039	0.00 046	0.01 682	0.00 432	0.00 482	0.00 227	0.00 671	0.00 314	0.00 093	0.03 556	0.00 894	0.00 161	0.00 092	0.00 114	0.00 014	0.00 480
12	0.00 359	0.00 280	0.00 491	0.00 545	0.02 271	0.00 323	0.00 409	0.00 753	0.00 630	0.03 876	0.01 109	0.00 575	0.00 197	0.00 287	0.00 397	0.00 818
13	0.23 615	0.36 230	0.35 651	0.13 365	0.23 925	0.40 036	0.31 408	0.35 614	0.36 680	0.50 686	0.16 038	0.20 562	0.42 313	0.39 479	0.39 190	0.32 991

14	0.00 025	0.00 054	0.00 037	0.00 027	0.00 127	0.00 020	0.00 070	0.00 091	0.00 043	0.00 241	0.00 059	0.00 021	0.00 020	0.00 036	0.00 030	0.00 130
15	0.00 099	0.00 139	0.00 077	0.00 146	0.00 164	0.00 079	0.00 134	0.00 111	0.00 189	0.00 105	0.00 084	0.00 102	0.00 039	0.00 105	0.00 126	0.00 330
16				0.00 002		0.00 005	0.00 007	0.00 011		0.00 009						0.00 032
17	0.00 023	0.00 071	0.00 012	0.00 082	0.00 023	0.00 025	0.00 353	0.00 071	0.00 039	0.00 012	0.00 002	0.00 005	0.00 004	0.00 016	0.00 011	0.00 216
18	0.00 002	0.00 016	0.00 004	0.00 066	0.00 004		0.00 029	0.00 014	0.00 007	0.00 002				0.00 005	0.00 004	0.00 136
19	0.00 151	0.00 009	0.00 191	0.00 587	0.00 007	0.00 009	0.00 123	0.00 032			0.00 004	0.00 009	0.00 112	0.00 139	0.00 012	0.00 100
20	0.00 172	0.00 032	0.00 218	0.01 048	0.00 046	0.00 230	0.01 318	0.00 102	0.00 004	0.00 009	0.00 014	0.00 191	0.00 160	0.00 277	0.00 068	0.00 105
21	0.00 004		0.00 045	0.00 486		0.00 016	0.01 644	0.00 012					0.00 039	0.00 187		0.00 057
22	0.00 022	0.00 011	0.00 021	0.00 669	0.00 011	0.00 046	0.01 880	0.00 023	0.00 005	0.00 002	0.00 002	0.00 032	0.00 060	0.00 171	0.00 027	0.00 161
23	0.00 002	0.00 005	0.00 014	0.00 487		0.00 029	0.01 393	0.00 004		0.00 004		0.00 002	0.00 012	0.00 066	0.00 005	0.00 211
24			0.00 009	0.00 387		0.00 014	0.00 432	0.00 002					0.00 002	0.00 025		0.00 511
25				0.00 323		0.00 011	0.00 057	0.00 002						0.00 014	0.00 002	0.00 589
26	0.00 233	0.00 162	0.00 125	0.00 936	0.00 157	0.00 337	0.00 377	0.00 164	0.00 466	0.00 064	0.00 121	0.00 227	0.00 066	0.00 232	0.00 215	0.00 957
27				0.00 059		0.00 002	0.00 016	0.00 002								0.00 150
28	0.00 771	0.00 029	0.00 068	0.00 646	0.00 021	0.00 798	0.00 532	0.00 064			0.00 009	0.00 104	0.00 475	0.00 291	0.00 028	0.00 129
29	0.03 367	0.01 184	0.00 104	0.00 593	0.00 005	0.00 071	0.00 116	0.00 105			0.00 018	0.00 043	0.06 665	0.07 868	0.00 073	0.00 021
30	0.14 317	0.00 811	0.00 100	0.00 637	0.00 561	0.00 320	0.00 304	0.00 480	0.00 070	0.00 041	0.00 089	0.00 507	0.01 856	0.00 534	0.02 595	0.00 196
31	0.01 267	0.02 480	0.00 004	0.00 398	0.00 202		0.00 039	0.04 171	0.00 016		0.00 048	0.00 039	0.00 108	0.00 066	0.08 912	0.00 018
32	0.02 097	0.03 892	0.00 020	0.00 293	0.00 102	0.00 002	0.00 043	0.05 031	0.00 225	0.00 005	0.00 023	0.00 059	0.00 023	0.00 095	0.02 768	0.00 048
33	0.02 515	0.00 987	0.00 096	0.00 391	0.00 207	0.00 011	0.00 059	0.05 613	0.00 727	0.00 027	0.00 062	0.00 155	0.00 025	0.00 116	0.01 807	0.00 189
34	0.01 319	0.00 828		0.00 150	0.00 005		0.00 007	0.00 980	0.00 511	0.00 002	0.00 025		0.00 004	0.00 050	0.01 337	0.00 155
35	0.02 212	0.00 548	0.00 045	0.00 427	0.00 316		0.00 018	0.00 593	0.00 655	0.00 011	0.00 032	0.00 096	0.00 014	0.00 087	0.01 218	0.00 541
36	0.01 570	0.00 587	0.00 018	0.00 336	0.00 079		0.00 011	0.00 254	0.00 391	0.00 012	0.00 059	0.00 014	0.00 004	0.00 071	0.00 783	0.00 473

### **Annex 7 : Laser parameters of 10 primaries used for halftoning test**

<i>Nanostructure</i>	<i>Repetition rate (kHz)</i>	<i>Laser power (mW)</i>	<i>Scanning speed (mm.s<sup>-1</sup>)</i>
1	40	20.4	50
2	80	38.2	16
3	20	28.5	1000
4	10	36.5	800
5	20	45.2	10
6	50	33.4	600
7	10	36.5	1500
8	50	45.2	30
9	20	20.4	1000
10	40	18	30

### **Annex 8: Laser parameters of nanostructures for two-image multiplexing**

Table summarizing the laser parameters of the four nanostructures used for two-image multiplexing:

<i>Nanostructure n°</i>	<i>Repetition rate (kHz)</i>	<i>Laser power</i>		<i>Fluence (mJ/cm<sup>2</sup>)</i>	<i>Scanning speeds (mm.s<sup>-1</sup>)</i>
		<i>(%)</i>	<i>(mW)</i>		
NS1	10	20	38.2	64.2	800
NS2	50	25	45.2	77.5	30
NS3	10	6	18	33.3	1500
NS4	40	25	45.2	77.5	600

### **Annex 9: AFM investigation on laser inscription parameters on PC:SiO<sub>2</sub>:TiO<sub>2</sub>:Ag samples**

Table summarizing of laser parameters used to produce three different nanostructures with diffractive properties:

<i>Nanostructure n°</i>	<i>Fluence (mJ/cm<sup>2</sup>)</i>	<i>Repetition rate (kHz)</i>	<i>Scanning speed (mm.s<sup>-1</sup>)</i>
2 (green)	68.0	10	150
3 (red)	74.3	40	30
4 (white)	68.0	10	30

### **Annex 10: Laser parameters for image printing on PC:SiO<sub>2</sub>:TiO<sub>2</sub>:Ag samples**

Table summarizing the laser parameters of the six nanostructures used to create the palette for colourful image printing

<i>Nanostructure n°</i>	<i>Fluence (mJ/cm<sup>2</sup>)</i>	<i>Repetition rate (kHz)</i>	<i>Scanning speed (mm.s<sup>-1</sup>)</i>
1	68.0	10	30
2	33.3	10	1500
3	68.0	10	150
4	50.5	10	1500
5	74.3	40	30
6	68.0	10	1500



## **REFERENCES**

- (1) Schulz, F. Roman Registers of Births and Birth Certificates. Part II. *J. Roman Stud.* **1943**, 33, 55–64. <https://doi.org/10.2307/296627>.
- (2) Bagnall, R. S. Landholding in Late Roman Egypt: The Distribution of Wealth. *J. Roman Stud.* **1992**, 82, 128–149. <https://doi.org/10.2307/301288>.
- (3) Cammann, S. The Development of the Mandarin Square. *Harv. J. Asiat. Stud.* **1944**, 8 (2), 71–130. <https://doi.org/10.2307/2717953>.
- (4) Muthamma, K.; Sunil, D.; Shetty, P.; Kulkarni, S. D.; Anand, P. J.; Kekuda, D. Eco-Friendly Flexographic Ink from Fluorene-Based Schiff Base Pigment for Anti-Counterfeiting and Printed Electronics Applications. *Prog. Org. Coat.* **2021**, 161, 106463. <https://doi.org/10.1016/j.porgcoat.2021.106463>.
- (5) Bhagya, R. S.; Sunil, D.; Muthamma, K.; Shetty, P.; Kulkarni, S. D. Water-Based Invisible Green Flexographic Ink for Anti-Counterfeit Applications. *Prog. Org. Coat.* **2022**, 173, 107212. <https://doi.org/10.1016/j.porgcoat.2022.107212>.
- (6) Lorenz, A.; Senne, A.; Rohde, J.; Kroh, S.; Wittenberg, M.; Krüger, K.; Clement, F.; Biro, D. Evaluation of Flexographic Printing Technology for Multi-Busbar Solar Cells. *Energy Procedia* **2015**, 67, 126–137. <https://doi.org/10.1016/j.egypro.2015.03.296>.
- (7) Bozhkova, T.; Spiridonov, I.; Shterev, K. Overview of Security Printing Types and Trends in Its Future Development; Special Issue L; The Bulgarian Academy of Sciences; The Union of Chemists in Bulgaria: Sofia, Bulgaria, 2016; Vol. 49.
- (8) Borota, C. M. PRINTING TECHNIQUES USED TO SECURE BORDER CROSSING DOCUMENTS. *Int. J. Crim. Investig.* **2012**, 2 (1), 31–40.
- (9) Pranav Y. Dave. Short Review on Printing Ink Technology to Prevent Counterfeit of the Products. *J. Adv. Chem. Sci.* **2020**, 6 (4), 693–697. <https://doi.org/10.30799/jacs.227.20060401>.
- (10) Pfeifer, A.; Gillich, E.; Lohweg, V.; Schaede, J. Detection of Commercial Offset Printing in Counterfeited Banknotes; Reconnaissance International: San Francisco, CA, 2016; Vol. 5.
- (11) Wu, W. H.; Yang, W. K.; Cheng, S. H.; Kuo, M. K.; Lee, H. W.; Chang, C. C.; Jeng, G. R.; Liu, C. P. Optical Security and Anti-Counterfeiting Using 3D Screen Printing. In *Display Technologies and Applications for Defense, Security, and Avionics*; SPIE, 2007; Vol. 6558, pp 195–201. <https://doi.org/10.1117/12.719167>.
- (12) Phillips, R. W. Optically Variable Films, Pigments, and Inks; Seddon, R. I., Ed.; San Diego, CA, 1990; p 98. <https://doi.org/10.1117/12.22377>.
- (13) Li, G.; Luo, W.; Che, Z.; Pu, Y.; Deng, P.; Shi, L.; Ma, H.; Guan, J. Lipophilic Magnetic Photonic Nanochains for Practical Anticounterfeiting. *Small* **2022**, 18 (21), 2200662. <https://doi.org/10.1002/sml.202200662>.
- (14) Yin, Z.; Li, H.; Xu, W.; Cui, S.; Zhou, D.; Chen, X.; Zhu, Y.; Qin, G.; Song, H. Local Field Modulation Induced Three-Order Upconversion Enhancement: Combining Surface Plasmon Effect and Photonic Crystal Effect. *Adv. Mater.* **2016**, 28 (13), 2518–2525. <https://doi.org/10.1002/adma.201502943>.

- (15) Andres, J.; Hersch, R. D.; Moser, J.-E.; Chauvin, A.-S. A New Anti-Counterfeiting Feature Relying on Invisible Luminescent Full Color Images Printed with Lanthanide-Based Inks. *Adv. Funct. Mater.* **2014**, *24* (32), 5029–5036. <https://doi.org/10.1002/adfm.201400298>.
- (16) Schott, J. H. Optical Security Features for Plastic Card Documents. In *Optical Security and Counterfeit Deterrence Techniques II*; SPIE, 1998; Vol. 3314, pp 294–298. <https://doi.org/10.1117/12.304698>.
- (17) Lazzari, J. P.; Lazzari, J. M. Procédé De Formation D'une Image Laser Couleur Observable Selon Des Couleurs Variables, Et Document Sur Lequel Une Telle Image Laser Couleur Est Ainsi Réalisée. FR2987156B1, January 30, 2015.
- (18) Lesur, J.-L.; Larina, N.; Nikkila, J. Color Laser Marking of Security Document and a Method for Producing Such Security Document. US11084315B2, August 10, 2021.
- (19) Dalloz, N. Multiplexage d'images Par Marquage Laser Pour Applications Dans Le Domaine Des Documents de Sécurité et d'identité, Université Jean Monnet, 2022. <http://www.theses.fr/s216289>.
- (20) *Kodak Image 23*. <https://r0k.us/graphics/kodak/kodim23.html> (accessed 2023-05-30).
- (21) Peterson, D. S. Sol–Gel Technique. In *Encyclopedia of Microfluidics and Nanofluidics*; Li, D., Ed.; Springer US: Boston, MA, 2014; pp 1–7. [https://doi.org/10.1007/978-3-642-27758-0\\_1432-2](https://doi.org/10.1007/978-3-642-27758-0_1432-2).
- (22) Audebert, P.; Miomandre, F. Procédé sol-gel de polymérisation. **2005**, 15.
- (23) Malucelli, G. Hybrid Organic/Inorganic Coatings Through Dual-Cure Processes: State of the Art and Perspectives. *Coatings* **2016**, *6* (1), 10. <https://doi.org/10.3390/coatings6010010>.
- (24) Bottein, T. Synergetic Combination of Top-down and Bottom-up Lithography Processes for Large Scale Nanostructures Applied to Photonics, Aix Marseille Université, Marseille, 2018.
- (25) Livage, J.; Henry, M.; Sanchez, C. Sol-Gel Chemistry of Transition Metal Oxides. *Prog. Solid State Chem.* **1988**, *18* (4), 259–341. [https://doi.org/10.1016/0079-6786\(88\)90005-2](https://doi.org/10.1016/0079-6786(88)90005-2).
- (26) Iqbal, P.; Preece, J. A.; Mendes, P. M. Nanotechnology: The “Top-Down” and “Bottom-Up” Approaches. In *Supramolecular Chemistry*; John Wiley & Sons, Ltd, 2012. <https://doi.org/10.1002/9780470661345.smc195>.
- (27) Biswas, P. K. Sol–Gel Thin Films for Optics and Photonics. *J. Sol-Gel Sci. Technol.* **2011**, *59* (3), 456–474. <https://doi.org/10.1007/s10971-010-2368-5>.
- (28) Sharma, A.; Pal, B. N. Sol-Gel Derived High Performance Low-Voltage Thin Film Transistor. *Mater. Today Proc.* **2022**, *48*, 573–575. <https://doi.org/10.1016/j.matpr.2021.04.466>.
- (29) Pettit, R. B.; Brinker, C. J. Use of Sol-Gel Thin Films in Solar Energy Applications. *Sol. Energy Mater.* **1986**, *14* (3), 269–287. [https://doi.org/10.1016/0165-1633\(86\)90053-5](https://doi.org/10.1016/0165-1633(86)90053-5).
- (30) Alberti, S.; Jágerská, J. Sol-Gel Thin Film Processing for Integrated Waveguide Sensors. *Front. Mater.* **2021**, *8*.

- (31) Figueira, R. B.; Almeida, J. M. de; Ferreira, B.; Coelho, L.; Silva, C. J. R. Optical Fiber Sensors Based on Sol–Gel Materials: Design, Fabrication and Application in Concrete Structures. *Mater. Adv.* **2021**, *2* (22), 7237–7276. <https://doi.org/10.1039/D1MA00456E>.
- (32) Faustini, M.; Louis, B.; Albouy, P. A.; Kuemmel, M.; Grosso, D. Preparation of Sol–Gel Films by Dip-Coating in Extreme Conditions. *J. Phys. Chem. C* **2010**, *114* (17), 7637–7645. <https://doi.org/10.1021/jp9114755>.
- (33) Bindini, E.; Naudin, G.; Faustini, M.; Grosso, D.; Boissière, C. Critical Role of the Atmosphere in Dip-Coating Process. *J. Phys. Chem. C* **2017**, *121* (27), 14572–14580. <https://doi.org/10.1021/acs.jpcc.7b02530>.
- (34) Meyerhofer, D. Characteristics of Resist Films Produced by Spinning. *J. Appl. Phys.* **1978**, *49* (7), 3993–3997. <https://doi.org/10.1063/1.325357>.
- (35) Bornside, D. E.; Brown, R. A.; Ackmann, P. W.; Frank, J. R.; Tryba, A. A.; Geyling, F. T. The Effects of Gas Phase Convection on Mass Transfer in Spin Coating. *J. Appl. Phys.* **1993**, *73* (2), 585–600. <https://doi.org/10.1063/1.353368>.
- (36) Krins, N.; Faustini, M.; Louis, B.; Grosso, D. Thick and Crack-Free Nanocrystalline Mesoporous TiO<sub>2</sub> Films Obtained by Capillary Coating from Aqueous Solutions. *Chem. Mater.* **2010**, *22* (23), 6218–6220. <https://doi.org/10.1021/cm102524u>.
- (37) Kresge, C. T.; Leonowicz, M. E.; Roth, W. J.; Vartuli, J. C.; Beck, J. S. Ordered Mesoporous Molecular Sieves Synthesized by a Liquid-Crystal Template Mechanism. *Nature* **1992**, *359* (6397), 710–712. <https://doi.org/10.1038/359710a0>.
- (38) Brinker, C. J.; Lu, Y.; Sellinger, A.; Fan, H. Evaporation-Induced Self-Assembly: Nanostructures Made Easy. *Adv. Mater.* **1999**, *11* (7), 579–585. [https://doi.org/10.1002/\(SICI\)1521-4095\(199905\)11:7<579::AID-ADMA579>3.0.CO;2-R](https://doi.org/10.1002/(SICI)1521-4095(199905)11:7<579::AID-ADMA579>3.0.CO;2-R).
- (39) Grosso, D.; Cagnol, F.; Soler-Illia, G. J. de A. A.; Crepaldi, E. L.; Amenitsch, H.; Brunet-Bruneau, A.; Bourgeois, A.; Sanchez, C. Fundamentals of Mesostructuring Through Evaporation-Induced Self-Assembly. *Adv. Funct. Mater.* **2004**, *14* (4), 309–322. <https://doi.org/10.1002/adfm.200305036>.
- (40) Sanchez, C.; Boissière, C.; Grosso, D.; Laberty, C.; Nicole, L. Design, Synthesis, and Properties of Inorganic and Hybrid Thin Films Having Periodically Organized Nanoporosity. *Chem. Mater.* **2008**, *20* (3), 682–737. <https://doi.org/10.1021/cm702100t>.
- (41) Zhang, X.; Cresswell, M. Chapter 4 - Silica-Based Amorphous Drug Delivery Systems. In *Inorganic Controlled Release Technology*; Zhang, X., Cresswell, M., Eds.; Butterworth-Heinemann: Boston, 2016; pp 93–137. <https://doi.org/10.1016/B978-0-08-099991-3.00004-1>.
- (42) Danks, A. E.; Hall, S. R.; Schnepf, Z. The Evolution of ‘Sol–Gel’ Chemistry as a Technique for Materials Synthesis. *Mater. Horiz.* **2016**, *3* (2), 91–112. <https://doi.org/10.1039/C5MH00260E>.
- (43) Nakama, Y. Surfactants. In *Cosmetic Science and Technology*; Elsevier, 2017; pp 231–244. <https://doi.org/10.1016/B978-0-12-802005-0.00015-X>.

- (44) Bass, J. D.; Grosso, D.; Boissiere, C.; Sanchez, C. Pyrolysis, Crystallization, and Sintering of Mesostructured Titania Thin Films Assessed by in Situ Thermal Ellipsometry. *J. Am. Chem. Soc.* **2008**, *130* (25), 7882–7897. <https://doi.org/10.1021/ja078140x>.
- (45) Bagheri, S.; Mohd Hir, Z. A.; Yousefi, A. T.; Abdul Hamid, S. B. Progress on Mesoporous Titanium Dioxide: Synthesis, Modification and Applications. *Microporous Mesoporous Mater.* **2015**, *218*, 206–222. <https://doi.org/10.1016/j.micromeso.2015.05.028>.
- (46) Haggerty, J. E. S.; Schelhas, L. T.; Kitchaev, D. A.; Mangum, J. S.; Garten, L. M.; Sun, W.; Stone, K. H.; Perkins, J. D.; Toney, M. F.; Ceder, G.; Ginley, D. S.; Gorman, B. P.; Tate, J. High-Fraction Brookite Films from Amorphous Precursors. *Sci. Rep.* **2017**, *7* (1), 15232. <https://doi.org/10.1038/s41598-017-15364-y>.
- (47) Ali, I.; Suhail, M.; Alothman, Z. A.; Alwarthan, A. Recent Advances in Syntheses, Properties and Applications of TiO<sub>2</sub> Nanostructures. *RSC Adv.* **2018**, *8* (53), 30125–30147. <https://doi.org/10.1039/C8RA06517A>.
- (48) Li, J.-G.; Ishigaki, T. Brookite→rutile Phase Transformation of TiO<sub>2</sub> Studied with Monodispersed Particles. *Acta Mater.* **2004**, *52* (17), 5143–5150. <https://doi.org/10.1016/j.actamat.2004.07.020>.
- (49) Tian, M.; Liu, C.; Ge, J.; Geohegan, D.; Duscher, G.; Eres, G. Recent Progress in Characterization of the Core–Shell Structure of Black Titania. *J. Mater. Res.* **2019**, *34* (07), 1138–1153. <https://doi.org/10.1557/jmr.2019.46>.
- (50) Grosso, D.; Boissière, C.; Nicole, L.; Sanchez, C. Preparation, Treatment and Characterisation of Nanocrystalline Mesoporous Ordered Layers. *J. Sol-Gel Sci. Technol.* **2006**, *40* (2–3), 141–154. <https://doi.org/10.1007/s10971-006-8990-6>.
- (51) Wang, S.; Ding, Z.; Chang, X.; Xu, J.; Wang, D.-H. Modified Nano-TiO<sub>2</sub> Based Composites for Environmental Photocatalytic Applications. *Catalysts* **2020**, *10* (7), 759. <https://doi.org/10.3390/catal10070759>.
- (52) Promnopas, W.; Promnopas, S.; Phonkhokkong, T.; Thongtem, T.; Boonyawan, D.; Yu, L.; Wiranwetchayan, O.; Phuruangrat, A.; Thongtem, S. Crystalline Phases and Optical Properties of Titanium Dioxide Films Deposited on Glass Substrates by Microwave Method. *Surf. Coat. Technol.* **2016**, *306*, 69–74. <https://doi.org/10.1016/j.surfcoat.2016.04.078>.
- (53) Soler-Illia, G. J. A. A.; Angelomé, P. C.; Fuertes, M. C.; Grosso, D.; Boissiere, C. Critical Aspects in the Production of Periodically Ordered Mesoporous Titania Thin Films. *Nanoscale* **2012**, *4* (8), 2549. <https://doi.org/10.1039/c2nr11817c>.
- (54) Karthick, S. N.; Hemalatha, K. V.; Suresh Kannan Balasingam; Manik Clinton, F.; Akshaya, S.; Kim, H. Dye-Sensitized Solar Cells: History, Components, Configuration, and Working Principle. In *Interfacial Engineering in Functional Materials for Dye-Sensitized Solar Cells*; Pandikumar, A., Jothivenkatachalam, K., Bhojanaa, K., Eds.; Wiley, 2019; pp 1–16. <https://doi.org/10.1002/9781119557401.ch1>.
- (55) Giolli, C.; Borgioli, F.; Credi, A.; Fabio, A. D.; Fossati, A.; Miranda, M. M.; Parmeggiani, S.; Rizzi, G.; Scrivani, A.; Troglio, S.; Tolstoguzov, A.; Zoppi, A.; Bardi, U. Characterization of TiO<sub>2</sub> Coatings Prepared by a Modified Electric Arc-Physical Vapour Deposition System. *Surf. Coat. Technol.* **2007**, *202* (1), 13–22. <https://doi.org/10.1016/j.surfcoat.2007.04.043>.

- (56) Wang, W. B.; Yanguas-Gil, A.; Yang, Y.; Kim, D.-Y.; Girolami, G. S.; Abelson, J. R. Chemical Vapor Deposition of TiO<sub>2</sub> Thin Films from a New Halogen-Free Precursor. *J. Vac. Sci. Technol. Vac. Surf. Films* **2014**, *32* (6), 061502. <https://doi.org/10.1116/1.4894454>.
- (57) Rehan, M.; Lai, X.; Kale, G. M. Hydrothermal Synthesis of Titanium Dioxide Nanoparticles Studied Employing in Situ Energy Dispersive X-Ray Diffraction. *CrystEngComm* **2011**, *13* (11), 3725. <https://doi.org/10.1039/c0ce00781a>.
- (58) Anandgaonker, P.; Kulkarni, G.; Gaikwad, S.; Rajbhoj, A. Synthesis of TiO<sub>2</sub> Nanoparticles by Electrochemical Method and Their Antibacterial Application. *Arab. J. Chem.* **2019**, *12* (8), 1815–1822. <https://doi.org/10.1016/j.arabjc.2014.12.015>.
- (59) Nadar, L.; Sayah, R.; Vocanson, F.; Crespo-Monteiro, N.; Boukenter, A.; Sao Joao, S.; Destouches, N. Influence of Reduction Processes on the Colour and Photochromism of Amorphous Mesoporous TiO<sub>2</sub> Thin Films Loaded with a Silver Salt. *Photochem. Photobiol. Sci.* **2011**, *10* (11), 1810. <https://doi.org/10.1039/c1pp05172e>.
- (60) Kim, C. W.; Pal, U.; Park, S.; Kim, Y. H.; Kim, J.; Kang, Y. S. Crystallization Induced Porosity Control and Photocatalytic Activity of Ordered Mesoporous TiO<sub>2</sub>. *RSC Adv.* **2012**, *2* (31), 11969–11975. <https://doi.org/10.1039/C2RA21391E>.
- (61) Bellino, M. G.; Golbert, S.; Marzi, M. C. D.; Soler-Illia, G. J. A. A.; Desimone, M. F. Controlled Adhesion and Proliferation of a Human Osteoblastic Cell Line by Tuning the Nanoporosity of Titania and Silica Coatings. *Biomater. Sci.* **2013**, *1* (2), 186–189. <https://doi.org/10.1039/C2BM00136E>.
- (62) Tricot, F.; Vocanson, F.; Chaussy, D.; Beneventi, D.; Reynaud, S.; Lefkir, Y.; Destouches, N. Photochromic Ag:TiO<sub>2</sub> Thin Films on PET Substrate. *RSC Adv.* **2014**, *4* (106), 61305–61312. <https://doi.org/10.1039/C4RA08804B>.
- (63) Bernsmeier, D.; Ortel, E.; Polte, J.; Eckhardt, B.; Nowag, S.; Haag, R.; Kraehnert, R. Versatile Control over Size and Spacing of Small Mesopores in Metal Oxide Films and Catalytic Coatings via Templating with Hyperbranched Core–Multishell Polymers. *J Mater Chem A* **2014**, *2* (32), 13075–13082. <https://doi.org/10.1039/C4TA01842G>.
- (64) Miyata, H.; Fukushima, Y.; Kanno, Y.; Hayase, S.; Hara, S.; Watanabe, M.; Kitamura, S.; Takahashi, M.; Kuroda, K. Mesoporous TiO<sub>2</sub> Films with Regularly Aligned Slit-like Nanovoids. *J. Mater. Chem. C* **2015**, *3* (16), 3869–3875. <https://doi.org/10.1039/C4TC02932A>.
- (65) Faustini, M.; Grenier, A.; Naudin, G.; Li, R.; Grosso, D. Ultraporous Nanocrystalline TiO<sub>2</sub>-Based Films: Synthesis, Patterning and Application as Anti-Reflective, Self-Cleaning, Superhydrophilic Coatings. *Nanoscale* **2015**, *7* (46), 19419–19425. <https://doi.org/10.1039/C5NR06466J>.
- (66) Rasso, P.; Malfatti, L.; Carboni, D.; Casula, M. F.; Garroni, S.; Zampetti, E.; Macagnano, A.; Bearzotti, A.; Innocenzi, P. Mesoscale Organization of Titania Thin Films Enables Oxygen Sensing at Room Temperature. *J. Mater. Chem. C* **2017**, *5* (45), 11815–11823. <https://doi.org/10.1039/C7TC03397D>.
- (67) Steinberg, P. Y.; Zalduendo, M. M.; Giménez, G.; Soler-Illia, G. J. A. A.; Angelomé, P. C. TiO<sub>2</sub> Mesoporous Thin Film Architecture as a Tool to Control Au Nanoparticles Growth and Sensing Capabilities. *Phys. Chem. Chem. Phys.* **2019**, *21* (20), 10347–10356. <https://doi.org/10.1039/C9CP01896D>.

- (68) Sharma, N.; Vangheluwe, M.; Vocanson, F.; Cazier, A.; Bugnet, M.; Reynaud, S.; Vermeulin, A.; Destouches, N. Laser-Driven Plasmonic Gratings for Hiding Multiple Images. *Mater. Horiz.* **2019**, *6* (5), 978–983. <https://doi.org/10.1039/C9MH00017H>.
- (69) Tricot, F.; Vocanson, F.; Chaussy, D.; Beneventi, D.; Reynaud, S.; Lefkir, Y.; Destouches, N. Photochromic Ag:TiO<sub>2</sub> Thin Films on PET Substrate. *RSC Adv.* **2014**, *4* (106), 61305–61312. <https://doi.org/10.1039/C4RA08804B>.
- (70) Bois, L.; Chassagneux, F.; Battie, Y.; Bessueille, F.; Mollet, L.; Parola, S.; Destouches, N.; Toulhoat, N.; Moncoffre, N. Chemical Growth and Photochromism of Silver Nanoparticles into a Mesoporous Titania Template. *Langmuir* **2010**, *26* (2), 1199–1206. <https://doi.org/10.1021/la902339j>.
- (71) Andersson, M.; Birkedal, H.; Franklin, N. R.; Ostomel, T.; Boettcher, S.; Palmqvist, A. E. C.; Stucky, G. D. Ag/AgCl-Loaded Ordered Mesoporous Anatase for Photocatalysis. *Chem. Mater.* **2005**, *17* (6), 1409–1415. <https://doi.org/10.1021/cm0485761>.
- (72) Destouches, N.; Crespo-Monteiro, N.; Vitrant, G.; Lefkir, Y.; Reynaud, S.; Epicier, T.; Liu, Y.; Vocanson, F.; Pigeon, F. Self-Organized Growth of Metallic Nanoparticles in a Thin Film under Homogeneous and Continuous-Wave Light Excitation. *J. Mater. Chem. C* **2014**, *2* (31), 6256–6263. <https://doi.org/10.1039/C4TC00971A>.
- (73) Ismail, A. A. Facile Synthesis of Mesoporous Ag-Loaded TiO<sub>2</sub> Thin Film and Its Photocatalytic Properties. *Microporous Mesoporous Mater.* **2012**, *149* (1), 69–75. <https://doi.org/10.1016/j.micromeso.2011.08.030>.
- (74) Lei, Z.; Fan, Y. Preparation of Silver Nanocomposites Stabilized by an Amphiphilic Block Copolymer under Ultrasonic Irradiation. *Mater. Lett.* **2006**, *60* (17), 2256–2260. <https://doi.org/10.1016/j.matlet.2005.12.136>.
- (75) Sakai, T.; Alexandridis, P. Ag and Au Monometallic and Bimetallic Colloids: Morphogenesis in Amphiphilic Block Copolymer Solutions. *Chem. Mater.* **2006**, *18* (10), 2577–2583. <https://doi.org/10.1021/cm051757y>.
- (76) Page, K.; Palgrave, R. G.; Parkin, I. P.; Wilson, M.; Savin, S. L. P.; Chadwick, A. V. Titania and Silver–Titania Composite Films on Glass—Potent Antimicrobial Coatings. *J. Mater. Chem.* **2006**, *17* (1), 95–104. <https://doi.org/10.1039/B611740F>.
- (77) Jiang, T.; Miao, L.; Tanemura, S.; Tanemura, M.; Xu, G.; Wang, R. P. Tunable Ag Surface-Plasmon-Resonance Wavelength and Its Application on the Photochromic Behavior of TiO<sub>2</sub>–Ag Films. *Superlattices Microstruct.* **2009**, *46* (1), 159–165. <https://doi.org/10.1016/j.spmi.2008.10.043>.
- (78) Dahmen, C.; Sprafke, A. N.; Dieker, H.; Wuttig, M.; von Plessen, G. Optical and Structural Changes of Silver Nanoparticles during Photochromic Transformation. *Appl. Phys. Lett.* **2006**, *88* (1), 011923. <https://doi.org/10.1063/1.2163268>.
- (79) Okumu, J.; Dahmen, C.; Sprafke, A. N.; Luysberg, M.; von Plessen, G.; Wuttig, M. Photochromic Silver Nanoparticles Fabricated by Sputter Deposition. *J. Appl. Phys.* **2005**, *97* (9), 094305. <https://doi.org/10.1063/1.1888044>.
- (80) Zuo, J.; Keil, P.; Grundmeier, G. Synthesis and Characterization of Photochromic Ag-Embedded TiO<sub>2</sub> Nanocomposite Thin Films by Non-Reactive RF-Magnetron Sputter

- Deposition. *Appl. Surf. Sci.* **2012**, *258* (18), 7231–7237. <https://doi.org/10.1016/j.apsusc.2012.04.054>.
- (81) Diop, D. K.; Simonot, L.; Destouches, N.; Abadias, G.; Pailloux, F.; Guérin, P.; Babonneau, D. Magnetron Sputtering Deposition of Ag/TiO<sub>2</sub> Nanocomposite Thin Films for Repeatable and Multicolor Photochromic Applications on Flexible Substrates. *Adv. Mater. Interfaces* **2015**, *2* (14), 1500134. <https://doi.org/10.1002/admi.201500134>.
- (82) ISO/DIS 80004-1(En), Nanotechnologies – Vocabulary — Part 1: Core Terms and Definitions, 2021. <https://www.iso.org/obp/ui/#iso:std:iso:80004:-1:dis:ed-1:v1:en>.
- (83) Venkatesh, N. Metallic Nanoparticle: A Review. *Biomed. J. Sci. Tech. Res.* **2018**, *4* (2). <https://doi.org/10.26717/BJSTR.2018.04.0001011>.
- (84) Stankic, S.; Suman, S.; Haque, F.; Vidic, J. Pure and Multi Metal Oxide Nanoparticles: Synthesis, Antibacterial and Cytotoxic Properties. *J. Nanobiotechnology* **2016**, *14* (1), 73. <https://doi.org/10.1186/s12951-016-0225-6>.
- (85) Lu, X.-Y.; Wu, D.-C.; Li, Z.-J.; Chen, G.-Q. Polymer Nanoparticles. *Prog. Mol. Biol. Transl. Sci.* **2011**, *104*, 299–323. <https://doi.org/10.1016/B978-0-12-416020-0.00007-3>.
- (86) Ng, K. K.; Zheng, G. Molecular Interactions in Organic Nanoparticles for Phototheranostic Applications. *Chem. Rev.* **2015**, *115* (19), 11012–11042. <https://doi.org/10.1021/acs.chemrev.5b00140>.
- (87) Rivera, V. a. G.; Ferri, F. A.; Jr, E. M. *Localized Surface Plasmon Resonances: Noble Metal Nanoparticle Interaction with Rare-Earth Ions*; IntechOpen, 2012. <https://doi.org/10.5772/50753>.
- (88) Boken, J.; Khurana, P.; Thatai, S.; Kumar, D.; Prasad, S. Plasmonic Nanoparticles and Their Analytical Applications: A Review. *Appl. Spectrosc. Rev.* **2017**, *52* (9), 774–820. <https://doi.org/10.1080/05704928.2017.1312427>.
- (89) Wang, C.; Luconi, M.; Masi, A.; Fernandez, L. Silver Nanoparticles as Optical Sensors. In *Silver Nanoparticles*; Pozo, D., Ed.; InTech, 2010. <https://doi.org/10.5772/8517>.
- (90) Chen, J.; Saeki, F.; Wiley, B. J.; Cang, H.; Cobb, M. J.; Li, Z.-Y.; Au, L.; Zhang, H.; Kimmey, M. B.; Li, X.; Xia, Y. Gold Nanocages: Bioconjugation and Their Potential Use as Optical Imaging Contrast Agents. *Nano Lett.* **2005**, *5* (3), 473–477. <https://doi.org/10.1021/nl047950t>.
- (91) De Jong, W. H.; Borm, P. J. Drug Delivery and Nanoparticles: Applications and Hazards. *Int. J. Nanomedicine* **2008**, *3* (2), 133–149. <https://doi.org/10.2147/IJN.S596>.
- (92) Siddique, S.; Chow, J. C. L. Gold Nanoparticles for Drug Delivery and Cancer Therapy. *Appl. Sci.* **2020**, *10* (11), 3824. <https://doi.org/10.3390/app10113824>.
- (93) Jans, H.; Huo, Q. Gold Nanoparticle-Enabled Biological and Chemical Detection and Analysis. *Chem. Soc. Rev.* **2012**, *41* (7), 2849–2866. <https://doi.org/10.1039/C1CS15280G>.
- (94) Liu, Z.; Destouches, N.; Vitrant, G.; Lefkir, Y.; Epicier, T.; Vocanson, F.; Bakhti, S.; Fang, Y.; Bandyopadhyay, B.; Ahmed, M. Understanding the Growth Mechanisms of Ag Nanoparticles Controlled by Plasmon-Induced Charge Transfers in Ag-TiO<sub>2</sub> Films. *J. Phys. Chem. C* **2015**, *119* (17), 9496–9505. <https://doi.org/10.1021/acs.jpcc.5b01350>.

- (95) D. Martínez, E.; Granja, L.; G. Bellino, M.; A. Soler-Illia, G. J. A. Electrical Conductivity in Patterned Silver –Mesoporous Titania Nanocomposite Thin Films: Towards Robust 3D Nano- Electrodes. *Phys. Chem. Chem. Phys.* **2010**, *12* (43), 14445–14448. <https://doi.org/10.1039/C0CP00824A>.
- (96) Fries, K.; Fink-Straube, C.; Mennig, M.; Schmidt, H. Photochromic Coatings. In *Sol-Gel Technologies for Glass Producers and Users*; Aegerter, M. A., Mennig, M., Eds.; Springer US: Boston, MA, 2004; pp 251–259. [https://doi.org/10.1007/978-0-387-88953-5\\_33](https://doi.org/10.1007/978-0-387-88953-5_33).
- (97) Marckwald, W. Ueber Phototropie. *Z. Für Phys. Chem.* **1899**, *30U* (1), 140–145. <https://doi.org/10.1515/zpch-1899-3007>.
- (98) Kawahara, K.; Suzuki, K.; Ohko, Y.; Tatsuma, T. Electron Transport in Silver-Semiconductor Nanocomposite Films Exhibiting Multicolor Photochromism. *Phys. Chem. Chem. Phys.* **2005**, *7* (22), 3851–3855. <https://doi.org/10.1039/B511489F>.
- (99) Ma, H. Numerical Study of Laser Micro- and Nano-Processing of Nanocomposite Porous Materials. arXiv March 12, 2021. <https://doi.org/10.48550/arXiv.2103.07334>.
- (100) Nadar, L.; Destouches, N.; Crespo-Monteiro, N.; Sayah, R.; Vocanson, F.; Reynaud, S.; Lefkir, Y.; Capoen, B. Multicolor Photochromism of Silver-Containing Mesoporous Films of Amorphous or Anatase TiO<sub>2</sub>. *J. Nanoparticle Res.* **2013**, *15* (11), 2048. <https://doi.org/10.1007/s11051-013-2048-9>.
- (101) Liu, Z. Self-Organization of Metallic Nanoparticles in Waveguides by Laser : Mechanisms Modelling and New Approaches. phdthesis, Université de Lyon, 2016. <https://theses.hal.science/tel-02018273> (accessed 2023-05-30).
- (102) Liu, Z.; Siegel, J.; Garcia-Lechuga, M.; Epicier, T.; Lefkir, Y.; Reynaud, S.; Bugnet, M.; Vocanson, F.; Solis, J.; Vitrant, G.; Destouches, N. Three-Dimensional Self-Organization in Nanocomposite Layered Systems by Ultrafast Laser Pulses. *ACS Nano* **2017**, *11* (5), 5031–5040. <https://doi.org/10.1021/acsnano.7b01748>.
- (103) Sharma, N.; Destouches, N.; Florian, C.; Serna, R.; Siegel, J. Tailoring Metal-Dielectric Nanocomposite Materials with Ultrashort Laser Pulses for Dichroic Color Control. *Nanoscale* **2019**, *11* (40), 18779–18789. <https://doi.org/10.1039/C9NR06763A>.
- (104) Destouches, N.; Sharma, N.; Vangheluwe, M.; Dalloz, N.; Vocanson, F.; Bugnet, M.; Hébert, M.; Siegel, J. Laser-Empowered Random Metasurfaces for White Light Printed Image Multiplexing. *Adv. Funct. Mater.* **2021**, *31* (18), 2010430. <https://doi.org/10.1002/adfm.202010430>.
- (105) Dalloz, N.; Le, V. D.; Hebert, M.; Eles, B.; Flores Figueroa, M. A.; Hubert, C.; Ma, H.; Sharma, N.; Vocanson, F.; Ayala, S.; Destouches, N. Anti-Counterfeiting White Light Printed Image Multiplexing by Fast Nanosecond Laser Processing. *Adv. Mater.* **2022**, *34* (2), 2104054. <https://doi.org/10.1002/adma.202104054>.
- (106) Boissiere, C.; Grosso, D.; Lepoutre, S.; Nicole, L.; Bruneau, A. B.; Sanchez, C. Porosity and Mechanical Properties of Mesoporous Thin Films Assessed by Environmental Ellipsometric Porosimetry. *Langmuir* **2005**, *21* (26), 12362–12371. <https://doi.org/10.1021/la050981z>.

- (107) Redjala, S.; Aït Hocine, N.; Ferhoum, R.; Gratton, M.; Poirot, N.; Azem, S. UV Aging Effects on Polycarbonate Properties. *J. Fail. Anal. Prev.* **2020**, *20* (6), 1907–1916. <https://doi.org/10.1007/s11668-020-01002-9>.
- (108) Kaplan, S. L.; Rose, P. W. Plasma Surface Treatment of Plastics to Enhance Adhesion. *Int. J. Adhes. Adhes.* **1991**, *11* (2), 109–113. [https://doi.org/10.1016/0143-7496\(91\)90035-G](https://doi.org/10.1016/0143-7496(91)90035-G).
- (109) Hofrichter, A.; Bulkin, P.; Drévilion, B. Plasma Treatment of Polycarbonate for Improved Adhesion. *J. Vac. Sci. Technol. Vac. Surf. Films* **2002**, *20* (1), 245. <https://doi.org/10.1116/1.1430425>.
- (110) Tjandraatmadja, G. F.; Burn, L. S.; Jollands, M. J. The Effects of Ultraviolet Radiation on Polycarbonate Glazing. In *8th International Conference on Durability of Building Materials and Components*; Canada, 1999; pp 884–898.
- (111) Clark, D. T.; Abu-Shbak, M. M. Surface Aspects of the Heat Treatment of Polyethylene Terephthalate as Revealed by ESCA. *Polym. Degrad. Stab.* **1984**, *9* (4), 225–237. [https://doi.org/10.1016/0141-3910\(84\)90051-X](https://doi.org/10.1016/0141-3910(84)90051-X).
- (112) Tricot, F. Films réinscriptibles sur supports souples, Université de Lyon, 2016. <https://theses.hal.science/tel-01767573>.
- (113) Vasconcelos, D. C. L.; Costa, V. C.; Nunes, E. H. M.; Sabioni, A. C. S.; Gasparon, M.; Vasconcelos, W. L. Infrared Spectroscopy of Titania Sol-Gel Coatings on 316L Stainless Steel. *Mater. Sci. Appl.* **2011**, *2* (10), 1375–1382. <https://doi.org/10.4236/msa.2011.210186>.
- (114) Zakaria, M. B.; Suzuki, N.; Torad, N. L.; Matsuura, M.; Maekawa, K.; Tanabe, H.; Yamauchi, Y. Preparation of Mesoporous Titania Thin Films with Well-Crystallized Frameworks by Using Thermally Stable Triblock Copolymers. *Eur. J. Inorg. Chem.* **2013**, *2013* (13), 2330–2335. <https://doi.org/10.1002/ejic.201201305>.
- (115) Almeida, L. A.; Dosen, A.; Viol, J.; Marinkovic, B. A. TiO<sub>2</sub>-Acetylacetone as an Efficient Source of Superoxide Radicals under Reduced Power Visible Light: Photocatalytic Degradation of Chlorophenol and Tetracycline. *Catalysts* **2022**, *12* (2), 116. <https://doi.org/10.3390/catal12020116>.
- (116) Iswar, S.; Galmarini, S.; Bonanomi, L.; Wernery, J.; Roumeli, E.; Nimalshantha, S.; Ben Ishai, A. M.; Lattuada, M.; Koebel, M. M.; Malfait, W. J. Dense and Strong, but Superinsulating Silica Aerogel. *Acta Mater.* **2021**, *213*, 116959. <https://doi.org/10.1016/j.actamat.2021.116959>.
- (117) Fateh, R.; Ismail, A. A.; Dillert, R.; Bahnemann, D. W. Highly Active Crystalline Mesoporous TiO<sub>2</sub> Films Coated onto Polycarbonate Substrates for Self-Cleaning Applications. *J. Phys. Chem. C* **2011**, *115* (21), 10405–10411. <https://doi.org/10.1021/jp200892z>.
- (118) Nieto, D.; Gómez-Varela, A. I.; Martín, Y. C.; O'Connor, G. M.; Flores-Arias, M. T. Improvement of the Optical and Morphological Properties of Microlens Arrays Fabricated by Laser Using a Sol–Gel Coating. *Appl. Surf. Sci.* **2015**, *351*, 697–703. <https://doi.org/10.1016/j.apsusc.2015.05.177>.

- (119) Sharma, N. Self-Organization of Silver Nanoparticles with Femtosecond Laser in TiO<sub>2</sub> Matrix : Applications to Plasmonic Colours, Multiple Hidden Images and Colour Image-Multiplexing. These de doctorat, Lyon, 2020. <https://www.theses.fr/2020LYSES032> (accessed 2023-06-23).
- (120) Florian, C.; Skoulas, E.; Puerto, D.; Mimidis, A.; Stratakis, E.; Solis, J.; Siegel, J. Controlling the Wettability of Steel Surfaces Processed with Femtosecond Laser Pulses. *ACS Appl. Mater. Interfaces* **2018**, *10* (42), 36564–36571. <https://doi.org/10.1021/acsami.8b13908>.
- (121) *Commission internationale de l'éclairage ... huitième session, Cambridge--Septembre 1931*; University Press: Cambridge, 1932.
- (122) *RGB/XYZ* *Matrices.*  
[http://brucelindbloom.com/index.html?Eqn\\_RGB\\_XYZ\\_Matrix.html](http://brucelindbloom.com/index.html?Eqn_RGB_XYZ_Matrix.html) (accessed 2023-06-29).